

CARDIFF UNIVERSITY
SCHOOL OF PHYSICS AND ASTRONOMY



**THE SILICON
COLD-ELECTRON BOLOMETER**

by

THOMAS LEONARD ROBERT BRIEN

March 2015

A THESIS SUBMITTED TO CARDIFF UNIVERSITY FOR THE
DEGREE OF DOCTOR OF PHILOSOPHY

To my Father

Acknowledgements

While there is only one person's name on the front of a thesis, in reality, it is the culmination of the hard work and dedication of many people and, as such, it is only right that a thesis should start by acknowledging the contributions and sacrifices made by others on behalf of the author.

First and foremost, I must thank my supervisor Phil Mauskopf; without whose encouragement and belief in me, I simply would not have reached this stage. Working in Phil's lab during the summers of my undergraduate degree taught me that research can be as rewarding as it can be infuriating, however, it is ultimately addictive.

During my PhD, several others have also acted as my advisors and co-supervisors. Gao Min, Dan Reed, Simon Doyle and Peter Ade have always had a seemingly unlimited supply of time for me and for this I am exceedingly grateful.

I am indebted to my collaborators from other institutes, particularly Professors Evan Parker and Terry Whall from Warwick. Their group's ability to grow the strained and highly-doped material used here not only made the detectors work but do so impressively well. They have always been on the phone and striving to push this technology as far as humanly possible.

For all but the final few months of my studies, I was lucky enough to share an office and lab with Dmitry Morozov. While at times bizarre, it was a great deal of fun and, after Dmitry humming it for over four years, I don't think I will ever truly get *Popcorn* by Gershon Kingsley out of my head; thanks for that!

Rob Tucker and Rashmi Sudiwala for their support with electronics, grounding issues, and answering all those questions beginning "I've tried everything I can think of but...". Also, thanks must go to Rashmi for teaching me that there is only one way to do something: the correct way, and then you only do it once. Working with you has certainly been an experience. I am indebted to Chris Dunscombe for

his support in the clean room fabricating the detectors tested here and explaining how to design photomasks that might actually be of use. Amber Hornsby for operating the FTS during most of my runs. Richard Frewin you are, I can only deduce, some kind of magic computing wizard.

I have been lucky enough to spend a great deal of time—perhaps more than I should have—as a member of the Cardiff University Fencing Club and the Men’s First IX. To all the members of the club and my teammates; the days spent training and travelling all over the country with you have been a pleasure. Abi, Amy, Chris W, Drew, Ed, Eryn, Flavia, Jack, James, Jon, Josie, Lauren, Lydia, Mark, Miguel, Pete G, Pete R, Reggie, Rosie, Sarah G, Sarah E, Steve, Tedi, Tessa, Tim, Tom, Zoë, and anyone one I have terribly, inevitably forgotten, I wish you all the best. A special mention has to go to Andy McLeod who, by some strange twist of fate, I seem to have been crossing paths with, in various walks of life, for well over a decade now. You have been an outstanding friend and I hope we continue to stumble into each other for many decades to come.

To my fellow PhD students, both past and present, you have been excellent providers of weekly cake, buyers of beer, and, of course, very dear friends. Adam, Andrew, Andy, Camilo, Chris C, Chris F, Ciara, Craig, Ezzy, George F, George S, Geraint, Gwen, Ian, Jess, Kane, Laura, Mark, Mat, Matt, Olly, Olivia, Patricia, Paul, Pete, Peter, Ryan, Sam, Sarah, Scott, Scotty, Seb, Simon, Tom A, and Tom B (the other one). To all of you who have finished your PhD, wherever you may now be, you have my congratulations; to the rest of you, you can have my reassurance that the final months and weeks are most certainly an experience.

To my Mum, who has supported me through so much, it is impossible to express in writing how very grateful I am for everything you have done for me. I am, however, in no doubt that you know this and, as such, I will simply say ‘thank you’. Thank you.

Finally, and without a shadow of a doubt most importantly, to my amazing wife Sarah; you have supported me throughout the last three-and-a-half years and through everything that a PhD throws at a person. You have shown me unconditional love and patience, which must border on insanity. I consider myself immeasurably lucky to simply call you my friend, however, to call myself your husband is an honour. While this journey for me is coming to a close, I cannot wait for all the adventures we will share together.

Abstract

This thesis describes the development and testing of two cold-electron bolometers using highly-doped silicon as the absorber. These detectors exhibit both high sensitivity and low time constants. High sensitivity is achieved due to the weak thermal-link between the electrons and the phonons in the silicon absorber at low temperature (< 1 K). Schottky barriers form naturally between the highly-doped silicon absorber and the superconducting contacts. Selective tunnelling of electrons across these Schottky barriers allows the electron temperature in the silicon absorber to be cooled to below the thermal bath temperature. This direct electron-cooling acts as thermoelectric feedback, reducing the time constant of a cold-electron bolometer to below 1 μ s. In this work, the underlying physics of these devices is discussed and two devices are presented: one with a highly-doped silicon absorber and the other with strained highly-doped silicon used as the absorber. The design of these detectors is discussed and results are found from numerous characterisation experiments, including optical measurements. These measurements show that a prototype device, using a strained and highly-doped silicon absorber, has a noise-equivalent power of 6.6×10^{-17} W $\text{Hz}^{-1/2}$. When photon noise (which dominated this measurement) and noise from the amplifier are disregarded, the underlying device-limited noise-equivalent power is 2.0×10^{-17} W $\text{Hz}^{-1/2}$. By measuring the photon noise, the time constant of this detector has been determined to be less than 1.5 μ s. When compared to the device using unstrained silicon, it is clear that the straining of the silicon absorber, which reduces the electron-phonon coupling, produces a notable improvement in detector performance. Furthermore, a novel amplifier-readout technique, whereby the outputs of two matched amplifiers are cross correlated is introduced; this technique reduces the input-referred amplifier noise from 1 nV $\text{Hz}^{-1/2}$ to 300 pV $\text{Hz}^{-1/2}$.

Declaration

This work has not been submitted in substance for any other degree or award at this or any other university or place of learning, nor is being submitted concurrently in candidature for any degree or other award.



Signature (candidate)

26/3/2015

Date

Statement One

This thesis is being submitted in partial fulfilment of the requirements for the degree of PhD.



Signature (candidate)

26/3/2015

Date

Statement Two

This thesis is the result of my own independent work/investigation, except where otherwise stated. Other sources are acknowledged by explicit references. The views expressed are my own.



Signature (candidate)

26/3/2015

Date

Statement Three

I hereby give consent for my thesis, if accepted, to be available online in the University's Open Access repository and for inter-library loan, and for the title and summary to be made available to outside organisations.



Signature (candidate)

26/3/2015

Date

Contents

Acknowledgements	i
Abstract	iii
Contents	vii
List of Figures	xi
List of Tables	xv
Acronyms	xvii
1 Introduction	1
1.1 Motivation	1
1.1.1 Astronomy	1
1.1.2 Security	5
1.2 Bolometric Detectors	6
1.2.1 The Principle of a Bolometer	7
1.3 The History of Cold-Electron Bolometer Development	8
1.4 The Advantages & Disadvantages of Cold-Electron Bolometers . . .	12
1.5 Thesis Summary	13
2 The Theory of Cold-Electron Bolometers	17
2.1 Introduction	17
2.2 Tunnelling Barriers	18
2.2.1 Formation of Insulating Layers	18
2.3 The Tunnelling Current	23
2.4 The Cooling Power	31

2.5	Electron-Phonon Interactions	36
2.6	The Responsivity	39
2.7	The Sources of Electrical Noise	44
2.8	The Noise-Equivalent Power	49
2.8.1	Photon Noise	54
3	The Properties of Doped and Strained Silicon	57
3.1	Introduction	57
3.2	Intrinsic Semiconductors	57
3.3	Doped Semiconductors	59
3.4	Carrier Mobility	62
3.5	Strained Semiconductors	65
4	Detector Design & Fabrication	67
4.1	Introduction	67
4.2	Detector Design	67
4.2.1	Antenna Design	68
4.3	Detector Fabrication	71
4.4	Material Properties	75
5	Cryogenic Testbeds	77
5.1	Introduction	77
5.2	Sorption Refrigerators	78
5.3	Systems Used in This Work	81
5.3.1	Pulse-Tube-Cooled Cryostat with He10 Sorption Refrigerator	81
5.3.2	Liquid Helium Cryostat with He7 Sorption Refrigerator . . .	84
5.4	Detector Holder	86
6	Detector Readout	91
6.1	Introduction	91
6.2	Requirements of the Readout System	92
6.3	Initial Testing System	93
6.3.1	Initial Readout System	93
6.3.2	Initial Bias System	99
6.4	Revisions to the Initial Bias System	102
6.4.1	Changes Made and Advantages	102

6.4.2	Performance of the Updated Bias System	105
6.5	Final Testing System	108
6.5.1	Reason for Replacement	108
6.5.2	Final Readout System	108
6.5.3	Final Bias System	115
6.6	Cross-Correlated Noise Measurement	119
6.6.1	Convolution	119
6.6.2	Cross Correlation	120
6.6.3	Application of Cross Correlation to Detector Readout	120
6.7	Summary of Readout and Biasing Systems	126
7	Results: Dark Measurements	129
7.1	Introduction	129
7.2	Unstrained Silicon	130
7.3	Strained Silicon	135
7.4	Comparison of Unstrained & Strained Detectors	138
8	Results: Optical Measurements	141
8.1	Introduction	141
8.2	Unstrained Silicon	142
8.2.1	Current-Voltage Measurements	142
8.2.2	Responsivity	145
8.2.3	Noise Measurements	147
8.2.4	Spectral Response	154
8.3	Strained Silicon	154
8.3.1	Current-Voltage Measurements	154
8.3.2	Responsivity	157
8.3.3	Noise Measurements	158
8.3.4	Spectral Response	163
8.3.5	Chopped-Source Measurements	164
8.4	Detailed Antenna Simulations	166
8.4.1	Basic Model: Lumped Port, Infinite Silicon	167
8.4.2	Modelling the Antenna and Lens	168
8.4.3	Polarisation Model using Wave Port	169
8.4.4	Introduction of DC Cuts	170

8.4.5	Allowing for Loss in the Aluminium	171
8.4.6	Summary of Findings	172
8.5	Spectral Study of Silicon Material	173
8.6	Summary of Detector Performance	177
9	Conclusions	179
	Bibliography	187

List of Figures

1.1	Atmospheric transmission at the summit of Mauna Kea in Hawaii	2
1.2	All-sky map of the cosmic microwave background produced by the <i>Planck</i> mission	3
1.3	Image of a concealed firearm taken with the Cardiff passive terahertz-imaging instrument	6
1.4	Schematic of a simple bolometer	8
2.1	Growth and chemical fabrication of a metal-oxide layer	19
2.2	Formation of a Schottky barrier	21
2.3	Possible tunnelling of charges in a SiCEB	24
2.4	Tunnelling in of charges across a positively biased device	25
2.5	Tunnelling in of charges across a negatively biased device	26
2.6	BCS model of the superconducting energy gap	30
2.7	Dependence of tunnelling current on electron temperature	32
2.8	Most likely route for charges to tunnel in a two-junction system.	33
2.9	Examples of the physical effects of various signal-to-noise ratios	50
3.1	Band structure of an intrinsic semiconductor	58
3.2	Crystal lattice of silicon with an n-type dopant inserted.	59
3.3	Crystal lattice of silicon with a p-type dopant inserted.	60
3.4	Energy level diagrams for doped semiconductors	61
3.5	Change in electron mobility with increasing donor concentration	64
3.6	Introducing strain into a silicon lattice	65
4.1	Model of silicon cold-electron bolometer detector chip	68
4.2	Key dimensions of a twin-slot antenna	69

4.3	Model of Silicon Cold-Electron Bolometer (SiCEB) detector chip with DC cuts in the ground plane	70
4.4	Dimensions of bolometer bridge in a coplanar waveguide	71
4.5	Example sections from photomask	72
4.6	Cross sections of strained and unstrained SiCEB structures and photograph of a fabricated detector	74
5.1	Simplified model of the cross section of a sorption refrigerator	79
5.2	Computer-generated model of the pulse-tube cooled cryostat	83
5.3	Filters used for optical measurement in the pulse-tube cooled cryostat .	84
5.4	Filter profile of filters used in the optical measurement cryostat	85
5.5	Optical components housed in cryostat used for optical measurements .	86
5.6	Photograph of cryostat used for optical measurements	87
5.7	Detector holder	88
6.1	Initial readout system using RTD amplifier and programmable current source	93
6.2	Noise model of series amplifiers	94
6.3	Gain measurement of original amplifier	96
6.4	Bandwidth measurement of original amplifier	97
6.5	Input referred noise of original amplifier	98
6.6	Jitter from a Keithley 220 Current Source	100
6.7	Noise spectrum from a Keithley 220 Current Source	102
6.8	Internal bias generator used with initial amplifier	103
6.9	Rejection of common-mode noise in a differential bias and readout system	105
6.10	Jitter from initial, custom-made current bias system.	106
6.11	Noise spectrum from original bias generator system, used in conjunction with the initial amplifier.	107
6.12	Final voltage Readout Amplifier	109
6.13	Gain measurement of final amplifier	110
6.14	Asymmetric limit to input of the final amplifier	111
6.15	Bandwidth measurement of final amplifier	113
6.16	Measurement of the internal noise, referred to the input, for the final amplifier.	114
6.17	Differential bias generator used with final readout system	116

6.18 Measurement of jitter from the bias generator used in conjunction with the final readout system.	117
6.19 Noise measurement for bias generator used in conjunction with the final readout system.	118
6.20 Graphical representation of convolution in the time domain	121
6.21 Convolution in the frequency domain.	122
6.22 Cross-correlated noise measurement process flow	124
6.23 Removal of amplifier noise from a measurement by the use of cross correlation.	125
6.24 Reduction in input-referred noise with increased number of averaged acquisitions for cross-correlated amplifiers	126
7.1 Current-voltage characteristics for a SiCEB with an unstrained absorber	131
7.2 Differential resistance for a SiCEB with an unstrained absorber	132
7.3 Electron-temperature fitting for SiCEB with an unstrained absorber . .	134
7.4 Current-voltage characteristics for a SiCEB with a strained absorber . .	136
7.5 Differential resistance of a SiCEB with a strained absorber	137
7.6 Electron temperature for a strained-silicon cold-electron bolometer . .	138
7.7 Comparison of current-voltage (<i>I-V</i>) curves for the unstrained and strained devices	139
7.8 Superconducting gap size as a function of temperature for the unstrained and strained devices	140
8.1 Current-voltage measurements for an optically-loaded unstrained SiCEB	143
8.2 Electron temperature for an optically-loaded unstrained SiCEB	145
8.3 Responsivity of an unstrained-SiCEB	146
8.4 Noise spectrum, measured at optimum bias, for the unstrained SiCEB .	148
8.5 Summary of the change in noise voltage with bias current for the unstrained SiCEB	149
8.6 Noise-equivalent power of an unstrained-SiCEB biased at various currents around the optimum bias	150
8.7 Noise modelling for the unstrained-SiCEB observing a room-temperature source	151
8.8 Noise modelling for the unstrained-SiCEB observing a 77-Kelvin source	152
8.9 Spectral response of the control-SiCEB	153

8.10 Current-voltage measurements for an optically-loaded strained-SiCEB	155
8.11 Electron temperature of strained-SiCEB under optical loading	156
8.12 Responsivity of the strained-SiCEB device	158
8.13 Noise spectrum for the strained-SiCEB	159
8.14 Summary of the change in noise voltage with bias current for the strained-SiCEB	160
8.15 Noise modelling for the strained-SiCEB observing a room-temperature source	161
8.16 Noise modelling for the strained-SiCEB observing a 77-Kelvin source . .	162
8.17 Spectral response of the strained-SiCEB	164
8.18 Time stream of the voltage signal resulting from the strained SiCEB observing a chopped signal	165
8.19 Voltage spectrum measured in the presence of a 160-GHz source chopped at 1,945 Hz	166
8.20 Initial model of the antenna, performed by measuring reflected power . .	167
8.21 Model of the antenna and lens performed by measuring reflected power	168
8.22 Model of antenna and lens using a wave port	169
8.23 Model of antenna, lens and DC cuts using a wave port	170
8.24 Model of antenna, lens, DC cuts and lossy aluminium using a wave port	171
8.25 Transmission spectrum of unstrained doped silicon	174
8.26 Transmission spectrum of strained doped silicon	175
8.27 Transmission of silicon material over a narrow frequency range	176
9.1 Comparison between device-limited noise-equivalent power for silicon cold-electron bolometers made with unstrained and strained silicon . . .	182

List of Tables

1.1	Detector requirements for various current and future astronomical instruments working in the far-infrared	4
3.1	Carrier mobility curve-fitting parameters from Caughey and Thomas (1967)	64
4.1	Dimensions of the designed antennae	70
4.2	Dimensions and expected contact resistance for different bolometer bridge designs	72
4.3	Summary of key material properties for unstrained (control) and strained silicon materials	75
6.1	Summary of detector bias systems	127
6.2	Summary of detector readout systems	127
7.1	Parameters used in electron-temperature fitting of unstrained-silicon detector with optical loading	135
7.2	Parameters used in electron-temperature fitting of strained-silicon detector with optical loading	138
8.1	Parameters used in electron-temperature fitting of unstrained-silicon detector with optical loading	144
8.2	Parameters used in electron-temperature fitting of strained-silicon detector with optical loading	157
9.1	Comparison of the optical performance of various cold-electron bolometer reported in recent years	183

Acronyms

CEB Cold-Electron Bolometer.

CMB Cosmic Microwave Background.

DAQ Data Acquisition unit.

DUT Device Under Test.

ESA European Space Agency.

FDM Frequency-Division Multiplexing.

FFT Fast Fourier Transform.

FTS Fourier Transform Spectrometer.

He7 A helium-based sorption refrigerator consisting of one ^4He pump and one ^3He pump.

He10 A helium-based sorption refrigerator consisting of one ^4He pump and two ^3He pumps.

HEB Hot-Electron Bolometer.

HFI High-Frequency Instrument, an instrument aboard *Planck*.

IR Infrared.

I-V Current-voltage measurement where one of the quantities is varied and the response in the other is recorded.

JAXA Japanese Aerospace Exploration Agency.

JFET Junction Field-Effect Transistor.

KID Kinetic Inductance Detector.

LPE Low-Pass Edge.

NASA National Aeronautics and Space Administration for the United States of America.

NEP Noise-Equivalent Power.

NIS Normal metal-Insulator-Superconductor.

PCB Printed Circuit Board.

PTFE Polytetrafluoroethylene, commonly known by the trademark Teflon (™ DuPont).

RMS Root Mean Square.

RTD Resistance Temperature Detector, a form of thermometer.

SiCEB Silicon Cold-Electron Bolometer.

SINIS Superconductor-Insulator-Normal metal-Insulator-Superconductor.

SIS Superconductor-Insulator-Superconductor.

SIS' Superconductor-Insulator-(different) Superconductor, sometimes written as S_1IS_2 .

SIS'IS Superconductor-Insulator-(different) Superconductor-Insulator-Superconductor, sometimes written as $S_1IS_2IS_1$.

SmS Semiconductor-Superconductor.

SNR Signal-to-Noise Ratio.

SQUID Superconducting Quantum Interference Device.

SSmS Superconductor-Semiconductor-Superconductor, a type of tunnelling structure used to make SiCEBs.

TDM Time-Division Multiplexing.

TES Transition-Edge Sensor.

UHMWPE Ultra-High Molecular-Weight Polyethylene.

Chapter One

Introduction

'Space,' it says, 'is big. Really big. You just won't believe how vastly, hugely, mindbogglingly big it is. I mean, you may think it's a long way down the road to the chemist's, but that's just peanuts to space'

—The Hitchhiker's Guide to the Galaxy,
DOUGLAS ADAMS

From astronomy to security and screening, there is a need for extremely fast, highly-sensitive detectors operating in the mid to far infrared. In this work, one such detector—the silicon cold-electron bolometer—is introduced, tested and appraised.

1.1 MOTIVATION

1.1.1 ASTRONOMY

Millimetre and sub-millimetre wavelengths are of particular interest to several fields of astronomy, such as: studying the **Cosmic Microwave Background (CMB)**, galactic astrophysics (including the study of cold dust), star formation, and cosmology. This is due to the emission of black-body radiation from cold sources at these wavelengths (for example the cosmic microwave background has an average temperature of 2.73 K, with a spectrum peaking at 2 mm). While the recent *Herschel* and *Planck* missions have provided a plethora of high-quality data in these

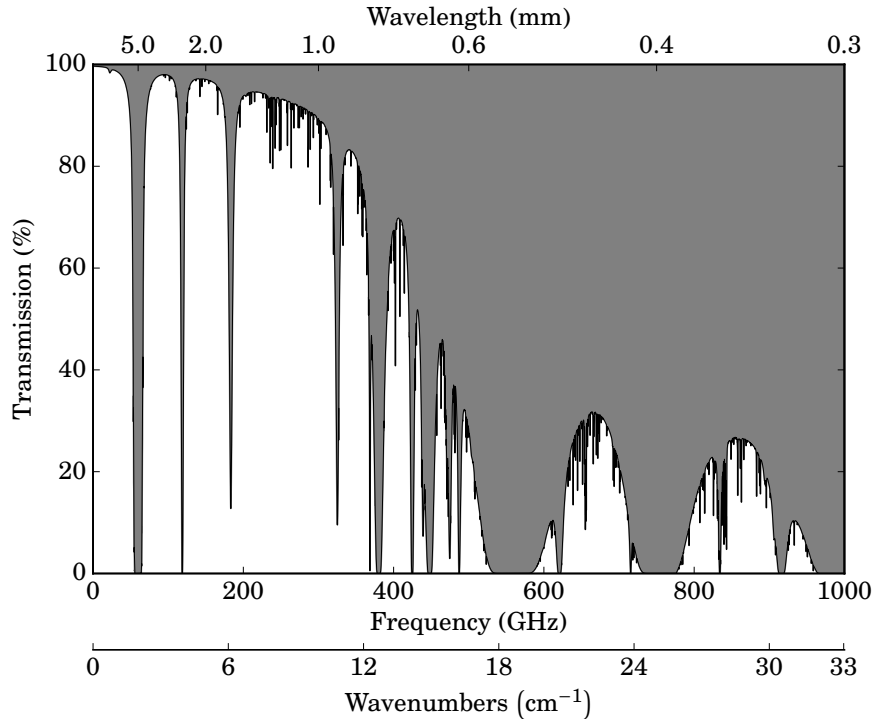


Figure 1.1: Atmospheric transmission at the summit (4,200 m above sea level) of Mauna Kea in Hawaii. Calculated using the model presented by [Pardo et al. \(2001\)](#), assuming 1 mm precipitable water vapour.

fields recently, such missions are incredibly expensive; for example the cost of the entire four year *Herschel* mission was €1.1 billion ($\approx \$1.2$ billion; [ESA, 2015](#)). This is comparable to the \$1.4 billion spent to develop the sixty six telescope Atacama Large Millimeter Array (ALMA) in Chile ([European Southern Observatory, 2013](#)), which, due to being ground based, has the potential to run indefinitely and is upgradeable.

The ability to carry out astronomy at ground-based facilities is restricted by two main factors. Firstly, the black-body emission from the optical components of the telescope results in a high background power (i.e. brighter than the source). Secondly, the atmospheric transmission in the mid to far infrared is not perfect, in fact, for several frequency bands, the atmospheric transmission is essentially zero. Figure 1.1 shows the transmission of light with frequencies below 1 THz at the summit of the Mauna Kea Mountain in Hawaii, the site of the James Clerk

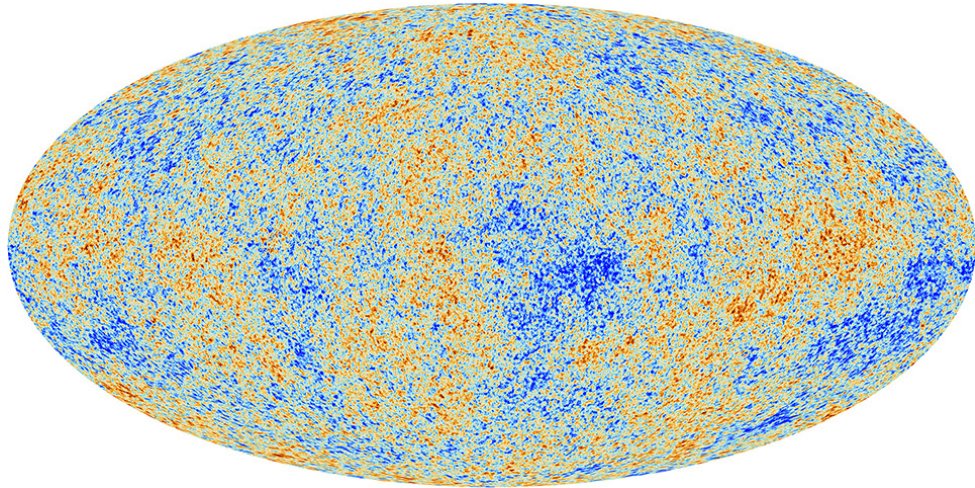


Figure 1.2: All-sky map of the cosmic microwave background produced by the *Planck* mission. © [ESA](#) and the *Planck* Collaboration.

Maxwell Telescope (JCMT), regarded to be one of the best sites in the world for observations at these frequencies. This figure assumes 1 mm of perceptible water vapour in the atmosphere; this is equivalent to approximately the best 25 % of all nights.

This attenuation of radiation by the Earth's atmosphere is a key reason for launching space-based observatories. Such observatories are not only immune to the issues of attenuation from the atmosphere but also need not contest with the high backgrounds that ground-based telescopes are subjected to. This allows space-based telescopes to study faint sources that are inaccessible to ground-based telescopes.

An example of science which can be performed with both ground- and space-based instruments is the measurement of the cosmic microwave background. Some key frequencies used to observe this phenomenon are 70, 150, 220, and 350 GHz; these frequencies are given by the specifications for the low- and high-frequency instruments on the *Planck* satellite ([Valenziano et al., 2007](#); [Lamarre et al., 2003](#)). Figure 1.1 shows that these frequencies are not heavily attenuated by the atmosphere and thus, can be observed from the ground as well as from space. An example of this work is the all-sky survey performed by *Planck*, shown in Figure 1.2. Similar work has been performed by the ground-based Keck and BICEP arrays.

Table 1.1: Detector requirements for various current and future astronomical instruments working in the far-infrared. For simplicity, where different instrument bands have different requirements, the highest (lowest **NEP**) is given.

Instrument	NEP ($\text{W Hz}^{-1/2}$)	Locale	Reference
<i>Planck</i> : HFI	9.7×10^{-18}	Space (L_2)	a
<i>Herschel</i> : SPIRE	5.3×10^{-17}	Space (L_2)	b
<i>Herschel</i> : PACS	2×10^{-16}	Space (L_2)	c
<i>SPICA</i> : SAFARI	2×10^{-19}	Space (L_2)	d
<i>SAFIR</i>	$< 10^{-20}$	Space (L_2)	e
IRAM: NIKA	1×10^{-15}	Earth (Pico Veleta)	f

^a [Lamarre et al. \(2010\)](#)
^b [Griffin et al. \(2006\)](#)
^c [Poglitsch et al. \(2008\)](#)
^d [Jackson et al. \(2012\)](#)
^e [Leisawitz \(2004\)](#)
^f [Monfardini et al. \(2010\)](#)

Such measurements require highly-sensitive detectors capable of accurately measuring very faint optical sources or very small changes in source temperature. For example, the anisotropies in the cosmic microwave background (seen in Figure 1.2) are on the order of 10^{-5} ([Hu and Dodelson, 2002](#)). In the field of instrumentation, a key figure of merit for a detector’s sensitivity is the **Noise-Equivalent Power (NEP)**, which can be thought of as defining the minimum detectable power (this is discussed to greater depth in Section 2.8). To give an impression of the sensitivity requirements for such astronomy, the detector specification (or achieved performance) for several recent and proposed instruments is given in Table 1.1. From this table, it can be seen that the most recent generation of space observatories (such as *Herschel* and *Planck*) used detectors with noise-equivalent powers mostly around $10^{-17} \text{ W Hz}^{-1/2}$. The next generation of such missions (such as *SPICA* or *SAFIR*) are aiming to deliver detectors with noise-equivalent powers approaching $10^{-20} \text{ W Hz}^{-1/2}$, in order to facilitate high-quality (narrow-band) spectral studies ([Benford and Moseley, 2004](#)). For ground-based instruments, the sensitivity requirements are lower (higher **NEP**), due to the inevitability of photon noise from the background limiting performance.

1.1.2 SECURITY

One of the defining characteristics of the 21st Century will be the need for increased security on all fronts. One of these fronts is the screening of people at airports and at sensitive buildings. The techniques and devices described above can be adapted to this purpose readily, since, in the far infrared, clothing is, at least partially, transparent. This allows for concealed objects, whose emission at these wavelengths is different to that of the human body, to be imaged.

A key issue faced by such imagining systems is that the emission from such sources is very faint (similar to the astronomical scenarios described previously). To combat this, the current generation of commercial scanners (such as Rohde & Schwarz's QPS scanner¹) seen in many airports, use active sources whereby the subject is illuminated by a high-power terahertz source, allowing reflection to be measured. Such detectors are unpopular due to the perceived health risk and the requirement for the subject to remain still during the exposure (Topham, 2012; Rich, 2013). An alternative to such technologies is passive detection, where the black-body emission of the subject (or any concealed article) is used as the optical source. This is entirely analogous to the astronomical observations described above (although the focusing optics may be more complex since the object length is not fixed at infinity). An advantage of such a system is that it avoids the requirement for high-power sources. However, due to the high background power and the small thermal variation between the subject and the background, highly-sensitive detectors are required for useful imaging and these systems inevitably require cooling to cryogenic temperatures. A further advantage of using such detectors is the potential to capture images at video-speed frame rates; this means that a subject need not *pose* for the images but may instead be imaged while passing through existing screening infrastructure.

The sensitivity (the noise-equivalent power) of such systems need not be at the ultra-low levels utilised by space-bourne instruments. This is because, as was the case for ground-based astronomical instruments, the temperature of the background components (such as the optics) will cause substantial contamination of the signal due to photon noise. In reality, noise-equivalent powers on the order of $10^{-15} \text{ W Hz}^{-1/2}$ should suffice for this application. Indeed Luukanen et al. (2010)

¹Rohde & Schwarz, Muehldorfstraße 15, 81671 Munich, Germany. Website: <http://www.rohde-schwarz.com/>

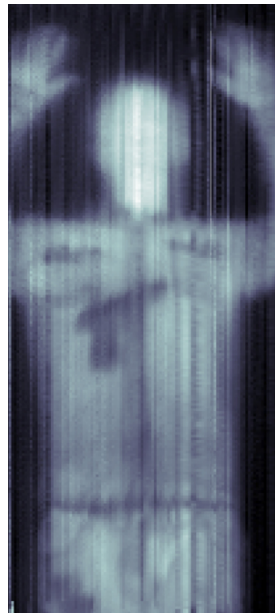


Figure 1.3: Image of a concealed firearm taken with the Cardiff passive terahertz-imaging instrument, as described by [Rowe et al. \(2015\)](#). © 2015 Cardiff University and QMC Instruments Ltd. Reproduced with permission.

describe a system using an array of niobium air-bridge microbolometers which achieve a noise-equivalent power of 8×10^{-15} W Hz $^{1/2}$.

Another prototype of such a system is currently being developed at Cardiff and uses a one-dimensional array of **Kinetic Inductance Detectors (KIDs)** and a scanning mirror to image a subject, as reported by [Rowe et al. \(2015\)](#). Figure 1.3 shows an image taken with this system, in which a firearm, concealed beneath clothing, can be clearly seen.

1.2 BOLOMETRIC DETECTORS

Bolometric detectors operate by accurately measuring the temperature of an absorbing element. Incoming radiative power causes the temperature of this element (the absorber) to increase and it is this increase which is measured. From this, it follows that the greater the incident power, the larger the increase in temperature. It can also be seen that, for a bolometric detector to have a very high sensitivity (i.e.

produce a measurable change in temperature for very low levels of incident power), it must be well isolated from its surroundings. It is also clear that the thermometer used must be capable of measuring extremely small changes in temperature; in practice, this can mean changes as low as one millikelvin. The silicon cold-electron bolometer offers benefits in both of these areas: the use of highly-doped silicon as an absorber allows the charge carriers (the actual absorbers) to be extremely well decoupled from the atomic lattice and, when electrically biased appropriately, the current flowing through the structure is highly dependant on the temperature of these carriers. A further benefit of these devices is that the natural isolation of charge carriers from their surroundings removes the requirements for more complicated arrangements often used to produce the same result. This removes the need for complicated structures to be fabricated; furthermore, because the current flowing through a cold-electron bolometer preferentially removes the most energetic electrons (the hottest), these devices can offer extremely small thermal time constants.

1.2.1 THE PRINCIPLE OF A BOLOMETER

Bolometers operate by measuring, to a high sensitivity, the temperature of an absorbing element. Light incident upon this absorber results in the temperature of the absorber increasing. The greater the level of incident power, the larger the increase in the temperature of the absorber. In order to produce a sensitive bolometer, two properties need be optimised: the change in temperature per unit power absorbed (the thermal responsivity, S_T) needs to be as large as possible; this can be achieved by decoupling the absorber from its surroundings (such as to reduce the thermal mass of the absorber); or ensuring that the thermometer used to measure the change in the absorber's temperature is capable of measuring extremely small changes in temperature.

Figure 1.4 illustrates a basic form of bolometer. A simple electrical thermometer (such as a piece of germanium) is suspended from a heat sink via its wiring. When power is absorbed, the temperature of the material increases accordingly, which results in a change in the material's electrical resistance. Heat is removed to the heat sink via the thermometer's wiring. This leads to one common issue experienced when designing a bolometric detector: it is highly desirable for the time constant of the detector (the minimum time between measurable detection

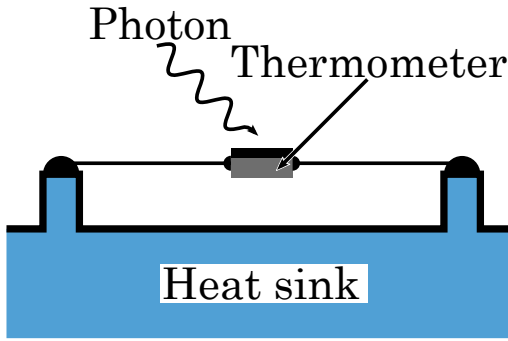


Figure 1.4: Schematic of a simple bolometer. An electrical thermometer is suspended above a heat sink by its wiring, which acts as a weak thermal link to the heat sink. One side of the thermometer is painted black to increase the absorption of incidental radiation. Incident power on the painted surface of the thermometer causes an increase in temperature, which can be measured. Heat is removed from the thermometer via its wiring.

events) to be as small as possible²; this requires the absorbed power to be removed from the absorbing element as rapidly as possible, which in turn necessitates a strong thermal link between the absorber and the heat sink. However, increasing the thermal link between the heat sink and the absorber also has the effect of decreasing the sensitivity, since the change in temperature within the absorber, for a given amount of absorber power, is also reduced. In most cases, one has to find a trade-off between speed of operation and the sensitivity of the detector (as discussed by [Griffin, 2000](#)).

1.3 THE HISTORY OF COLD-ELECTRON BOLOMETER DEVELOPMENT

Development of cold-electron bolometers has combined the developments of two fields to produce small, sensitive and fast bolometers. These fields are those of **Hot-Electron Bolometers (HEBs)** and tunnel-barrier superconducting electron refrigerators (also referred to as microrefrigerators or e-fridges).

²For example, see the discussion of the requirements for the *SPIRIT* mission, as given by [Benford and Moseley, 2004](#).

Although first proposed in [Parmenter \(1961\)](#), enhancement of superconductivity through the use of **Superconductor-Insulator-Superconductor (SIS)** junction was first observed by [Chi and Clarke \(1979\)](#). However, [Manninen et al. \(1999\)](#), who used a slightly different arrangement whereby the central superconductor is sandwiched by insulating contacts to a different superconductor (**SIS'IS**), were the first to show directly that, in this arrangement, the electrons were being cooled below the temperature of the lattice.

[Nahum et al. \(1994\)](#) demonstrated heat extraction from electrons in a normal metal island (copper in this case) to a superconductor via an insulator (**NIS**). From this point, several improvements were made, notably including the work of [Leivo et al. \(1996\)](#) who used a symmetric structure in which the normal island is sandwiched between the insulator-superconductor contacts (**SINIS**); this allowed for replacement of the extracted electrons by carriers of lower energy, improving the cooling power of such a device, while also allowing for operation in both polarities. This approach of symmetric junctions allowed for electrons to be cooled from the lattice temperature of 300 mK to close to 100 mK. An interesting development in this field, although not directly applicable to cold-electron bolometers, was the work of [Clark et al. \(2005\)](#), who used **Normal metal-Insulator-Superconductor (NIS)**-based electron coolers to cool a membrane, as well as its contents, from 320 mK to 225 mK; this work was also reported in *Nature* by [Pekola \(2005\)](#).

The increasing interest in these electron refrigerators led to the work of [Savin et al. \(2001\)](#), who first demonstrated that an effective electron refrigerator could be formed by replacing the normal metal island in a **SINIS** with a highly-doped semiconductor (**SSmS**). One immediate advantage of such a device was that, since it used naturally forming Schottky barriers in place of the oxide layers used in other types of device, fabrication was made simpler. [Savin et al.](#) showed that such a device was capable of cooling the electrons in the semiconductor from the lattice temperature of 160 mK to 120 mK. While this initial cooling was minimal, by [2003](#) [Savin et al.](#) had improved these devices such that they were now capable of cooling from 150 mK to less than 75 mK. Further improvements to **SSmS** coolers were made by [Prest et al. \(2011\)](#) who—by using a strained, highly doped semiconductor as the central island—were able to cool the electrons in the semiconductor from 300 mK to 174 mK.

While the use of the so-called *hot-electron effect* to create a mixing heterodyne

type detector was first described by Arams et al. (1966), the hot-electron bolometer was first envisaged by Nahum et al. (1993), who described a detector where incoming optical power heated the electrons in a normal metal absorber above the temperature of the lattice. The thermal isolation required to enable this independent heating of electrons comes from the fact that, at low temperatures (typically less than 1 K), the inelastic collisions between the electrons and the atomic lattice are extremely infrequent; this is also factor in the effectiveness of the electron refrigerators described above. Nahum proposed the use of an insulating tunnel contact to a superconducting electrode to measure the temperature of the charges in the absorber. This is the same arrangement of a **Normal metal-Insulator-Superconductor (NIS)** structure, as used in the electron refrigerators described above. They noted that, since the tunnelling current in a **NIS** junction is exponentially dependant on the temperature of the charges (as will be shown in Section 2.3 of Chapter 2), this arrangement acts as an extremely sensitive thermometer.

There have been many notable publications and developments in the field of hot-electron bolometers. Of particular note is the work of Karasik and Cantor which has shown that devices similar to those described by Nahum et al., but using a thin strip of superconductor as the absorber, are capable of operating with a noise-equivalent power of $3 \times 10^{-20} \text{ W Hz}^{-1/2}$ (Karasik et al., 2007; Karasik and Cantor, 2011). These levels of sensitivity make hot-electron bolometers an extremely exciting prospect for the next generation of both space and ground based telescopes. However, the speed of these devices is limited by the electron-phonon relaxation time (Karasik et al., 2007, reports a time constant of 30 μs). Furthermore, in order to achieve the thermal isolation required for highly sensitive detectors, these devices require the fabrication of absorbing islands with dimensions on the order of $1 \times 1 \mu\text{m}$ or smaller, with the need for contacts much smaller than this to be fabricated (Karasik and Cantor, 2011). The final undesirable feature of hot-electron bolometers is the need to degrade (slow) the thermal time constant to achieve high sensitivities (Karasik et al., 2000). In order to increase the speed of the device, electrothermal feedback (as described by Irwin, 1995) can be used. While this use of electrothermal feedback allowed microsecond scale thermal constants to be achieved, it also increased the complexity of the detector operation and restricted the biasing signal to a voltage bias.

One important difference between the work of Nahum et al. and Karasik et al. is how their respective detectors were read out. As mentioned above, Nahum

et al. used a **NIS** tunnelling contact to act as an extremely sensitive electron thermometer. **Karasik et al.** on the other hand, simply used the change in the resistance of the superconducting absorber (which was biased such that it was held on the superconducting transition) as the means of measuring the absorbed power (this is the same technique as used for the **Transition-Edge Sensor (TES)**).

The concept of using the *cold-electron effect* that had been shown with electron refrigerator devices, combined with the thermal isolation of the electrons from the phonons used in hot-electron bolometers, was first proposed in 1998 by **Kuzmin et al.**, who further elaborated on his idea in 2000 and 2003. They described how using **NIS** junctions could be used to lower the temperature of the electrons in a normal metal absorber to a rest temperature. Incident power absorbed within the absorber causes the electrons to heat up above the established rest temperature (much as in the case of the hot-electron bolometer). **Kuzmin et al.** explained that the same **NIS** junctions used to cool the electrons could be used as highly sensitive electron thermometers (as had been used by **Nahum et al., 1993**). Finally, **Kuzmin et al.** showed that the time constant of such a detector would be limited by the electron tunnelling time as opposed to the thermal conductance between the electron and phonon systems. This integrated solution for both cooling and readout formed the first example of what could be called a cold-electron bolometer.³

Since the original description of a cold-electron bolometer, there have been numerous publications on the topic. The most prolific author on the subject has been Leonid Kuzmin, who has shown the potential of such detectors to reach speeds in the order of nanoseconds (**Kuzmin, 2004**) and has been involved in the first optical measurement of the sensitivity of a metallic **CEB** detector (**Otto et al., 2013**), which was shown to have an amplifier-limited noise-equivalent power of $3.5 \times 10^{-17} \text{ W Hz}^{-1/2}$.

The work of Kuzmin et al. concentrated on cold-electron bolometers where the absorbing element was made from either a normal metal or a superconductor. As such, these devices are analogous to the **NIS** and **SIS'** types of electron refrigerator described earlier in this section. Due to the success of **Prest et al. (2011)** in achieving excellent levels of electron cooling, a logical step in the development of cold-electron bolometers was to replace the normal metal or superconducting absorber with a

³For this definition of a **CEB**, the selection criterion was that the detector must be consciously designed to utilise direct electron cooling, with absorbed power heating the electrons above their cooled temperature.

highly-degenerately-doped semiconductor. Such a device was first described and characterised by [Brien et al. \(2014\)](#) and is further described in this thesis.

1.4 THE ADVANTAGES & DISADVANTAGES OF COLD-ELECTRON BOLOMETERS

Cold-electron bolometers have been shown to have several advantages over other forms of bolometric detectors. Amongst these are: an extremely small thermal time constant ([Kuzmin, 2004](#), shows that there is the potential for this to be as low as 10 ns); high optical sensitivities ([Otto et al., 2013](#), achieved a noise-equivalent power of $3.5 \times 10^{-17} \text{ W Hz}^{-1/2}$, although this was limited by the readout amplifier); robust construction, since no suspended membrane or back etching is required to produce thermal isolation; and (as shown by [Salatino et al., 2014](#)) a low susceptibility to cosmic rays.

One key disadvantage of cold-electron bolometers is that they cannot be connected together into an array in a way that facilitates a simple readout of the array. This is the case for all bolometric detectors since there is no trivial way of reading the resistance of a number of elements on a single readout line. While being a broad issue in the field of bolometric detectors, several schemes have been proposed and utilised to allow large arrays of bolometric detectors—up to ten thousand pixels in the case of the SCUBA-2 instrument on the James Clark Maxwell Telescope, [Holland et al. \(2013\)](#). The two most common schemes adopted are: **Frequency-Division Multiplexing (FDM)** and **Time-Division Multiplexing (TDM)**, whereby the signals from the various detectors are combined such that the signal from any individual detector only contributes a small part of the total signal received at the readout electronics. Time-division multiplexing operates by the signal switching sequentially between the sources in time intervals. For example, if ten devices are to be read in one second then every 100 ms the readout system would switch to measuring the next device; this requires that each detector has an amplifier or other component which can be switched on and off. Frequency-division multiplexing, on the other hand, works by modulating a carrier wave, which has a specific frequency. This modulation is typically in the carrier's frequency (i.e. shifting the frequency of the signal from the carrier's rest frequency), although parameters such as the carrier's amplitude or phase may also be used. As the value of the measured

quantity varies, so too does the level of modulation. The frequency of the carrier wave associated with each device is different and is distributed across a frequency range. All the carrier waves in the frequency range are summed together, allowing the information from several devices to be read on a single line. At a following stage in the readout system, these signals are demultiplexed by mixing the signal with a signal from a local oscillator whose frequency is the same as the original carrier. Using this approach, multiple signals are read simultaneously using a single line.

Multiplexing techniques have been used to allow larger arrays of bolometric detectors to be deployed. Some major (historical, current, or planned) instruments of particular note which have used these techniques include: the Keck array of telescopes measuring the polarisation of the **Cosmic Microwave Background (CMB)** at the South Pole—each telescope uses time-division multiplexing to readout 512 transition-edge sensors across 16 channels ([Orlando et al., 2010](#)); SCUBA-2, a UK lead instrument at the John Clark Maxwell Telescope (JCMT) in Hawaii, which also utilises time-division multiplexing to readout an array of 10,240 transition-edge sensors across only eight channels ([Holland et al., 2013](#)); the XMS instrument on **NASA** and **ESA**'s jointly proposed *IXO* mission plans to use frequency-division multiplexing to read 1,600 pixels across 40 channels ([Hartog et al., 2011](#)); finally the SAFARI instrument on **JAXA** and **ESA**'s joint *SPICA* mission will use frequency-division multiplexing to readout arrays of 6,000 detectors using 160 channels.⁴

Of particular interest to the field of cold-electron bolometers is the work of [Schmidt et al. \(2005\)](#), who has proposed a scheme where frequency-division multiplexing is used to readout arrays of up to 10,000 hot-electron bolometers. While the scheme devised by [Schmidt et al.](#) was intended for use with hot-electron bolometers, due to the similarities between the two detector types, it should prove compatible with cold-electron bolometers as well.

1.5 THESIS SUMMARY

The preceding chapter has introduced the aim of this work. This is to introduce a new type of detector, the silicon cold-electron bolometer, and to characterise the performance and potential of such a detector. Two potential applications

⁴In 2013 it was decided that the current scheme for delivering *SPICA* would not produce ‘a robust and timely implementation’ and **ESA** ceased to fund the development as of Autumn 2013 ([ESA, 2014](#)). However, work is continuing ([SRON, 2014](#)) with the hope of launching *SPICA* in 2025.

(astronomy and security) have been identified and briefly discussed. The general concepts relating to bolometric detectors and the current status of cold-electron bolometers has been presented and the advantages and disadvantages of such detectors have also been discussed.

Chapter Two presents the theory of cold-electron bolometers. Key concepts are introduced, such as: tunnelling barriers and their fabrication, and detector response and sensitivity. In addition to this, the tunnelling current of a cold-electron bolometer is derived and, from this, it is shown that such a device is capable of direct electron cooling, the power associated with this electron cooling is then derived. The various sources of electrical noise present in such a system is discussed. This leads to the derivation of the ultimate sensitivity, the Noise-Equivalent Power (NEP), of such a detector.

Chapter Three discusses the key properties of the two silicon materials used to fabricate the detectors studied in this thesis. This starts from a brief introduction to the energy structure of a semiconductor and continues to describe how this can be altered by the introduction of dopants. The mobility of charge carriers is discussed as are the key governing parameters of this mobility. Finally, the concept of strained semiconductors is introduced and an explanation as to how this can be utilised to improve the performance of a cold-electron bolometer is presented.

Chapter Four describes the design and fabrication processes followed to produce the detectors studied in this thesis. The system used to couple radiation to the detector (a twin-slot antenna) is introduced. The general fabrication process flow used to manufacture to detectors is described, as are the defining parameters of the materials used to create the absorbers of these detectors.

Chapter Five describes the cryogenic systems used to reach the low temperatures required by these detectors. A general description of each system is given and the basic working principles of the refrigeration system used within these cryostats is covered. The applications to which each system was best suited are also described. Finally, the design and manufacture of a device holder, incorporating a silicon lens, are described.

Chapter Six describes the process of creating a readout and bias system for these detectors. Several iterations are described and each one is characterised to determine its suitability for the measurements in hand. In addition to these, a novel concept of cross correlating the outputs of two matched amplifiers, operating in parallel, to reduce the effect of amplifier noise in a measurement, is presented.

Both experimental data and a model are presented.

Chapter [Seven](#) presents results from the dark characterisation of these detectors. The current-voltage relationship is studied and, from this, the electron cooling is computed. This is performed for a detector with an unstrained-silicon absorber and a detector with a strained-silicon absorber. The mathematical stages needed to analyse the collected data are discussed.

Chapter [Eight](#) describes the results found when the work described in Chapter [Seven](#) was repeated in the presence of incidental optical power. From this, the responsivity of the detectors is found. The sensitivity of the detectors is found by measuring the noise generated within the detectors. In addition to this, the spectral response of the detectors is examined using a [Fourier Transform Spectrometer \(FTS\)](#). Discrepancies from the expected form of this response are discussed and the initial modelling work of the antennae is revisited. Finally, a brief spectral study of the optical transmission of doped and strained silicon samples at terahertz frequencies is presented; from this, any limits to the usefulness of this material in these applications are discussed.

Chapter [Nine](#) concludes the thesis by summarising the key results found throughout this work and commenting on the overall performance of the detectors tested. Brief suggestions for further work in this field are presented.

Chapter Two

The Theory of Cold-Electron Bolometers

'An experiment is a question which science poses to Nature, and a measurement is the recording of

Nature's answer.'

—MAX PLANCK

2.1 INTRODUCTION

As with all areas of study within physics, the fabrication and testing of cold-electron bolometers draws together elements from several fields. These include electronics, concepts from quantum mechanics (such as electron tunnelling), cryogenics, and low temperature physics, as well as solid-state physics. The study and testing of a cold-electron bolometer requires a strong understanding of these areas, as well as a general grounding in the field of instrumentation and its associated vocabulary. Furthermore, it is important to arrive at a model that might be used not only to describe the observed behaviour of the devices being studied but may, when applied with common sense, be used to extrapolate the performance of a device in various scenarios. The following chapter describes the physics which underlies cold-electron bolometer and then details how this is applied to arrive at models which describe the performance of such a detector. Particular note is given to the phenomena which limit the sensitivity of a detector and how such sensitivity might be quantified.

2.2 TUNNELLING BARRIERS

As will be explained in the following sections, the cold-electron bolometer directly removes hot electrons from the detector's absorber. This thermally selective removal of charges is made possible through the use of a tunnelling barrier. This tunnelling barrier allows the electron systems on either side to be separated (i.e. the energy levels in the two do not have to be aligned).

Several types of tunnelling barriers exist, however only those involving a superconductor shall be considered here, since this is a requirement of the thermal selection required for a cold-electron bolometer. The four main types of contact used in cold-electron bolometers are:

Normal metal-Insulator-Superconductor (NIS) The simplest (at least conceptually); the two sides (the normal metal and the superconductor) are separated by an insulating layer (typically an oxide layer).

Superconductor-Insulator-Superconductor (SIS) This is essentially the same as the arrangement described above, except that the normal metal is replaced by the same material as is used on the other side of the barrier.

Superconductor-Insulator-(different) Superconductor (SIS') A further progression of the systems already described; here the materials on either side of the insulator are both superconductors but have different energy gaps (they are different superconductors).

Semiconductor-Superconductor (SmS) This structure replaces the insulator with a Schottky barrier, which forms naturally between the semiconductor and a metal (or superconductor). Typically (and for all the work described in this thesis), a highly doped semiconductor, which can be thought of as being metallic (since there is no discernible band gap), is used.

2.2.1 FORMATION OF INSULATING LAYERS

From the above list, it can be seen that only two types of insulating barriers are typically used in the fabrication of cold-electron bolometers. These are: oxide layers and Schottky barriers. While both of these can be thought of as performing the same function, their formation is very different. An oxide layer requires an additional stage during the device fabrication process, where oxygen is introduced to the evacuated deposition chamber. A Schottky barrier, on the other hand, will

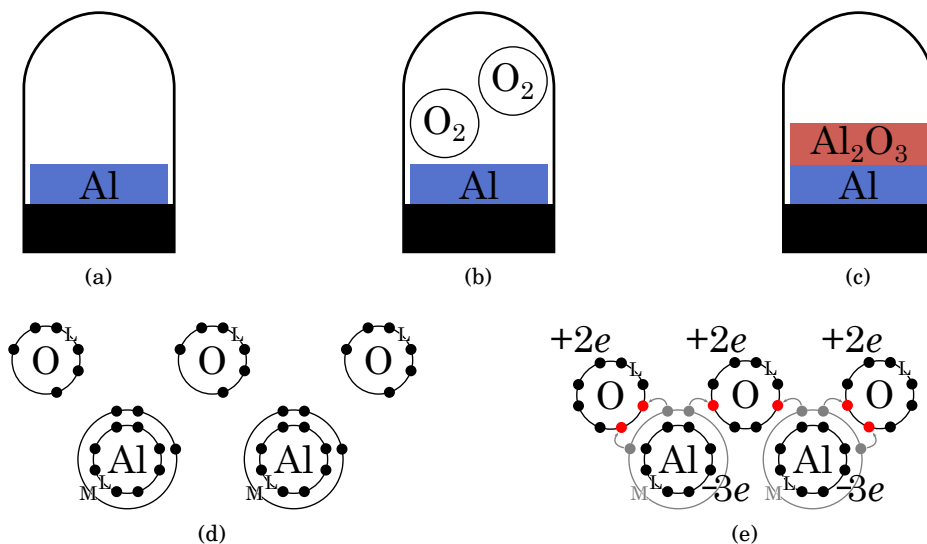


Figure 2.1: Growth (a)–(c) and ionic bond formation (d) and (e) of an aluminium oxide (Al_2O_3) layer. (a) Aluminium has been deposited (usually via evaporation) in a vacuum. (b) Oxygen is introduced into the evaporation chamber. (c) The oxygen atoms form ionic bonds with the aluminium, this causes the growth of an aluminium oxide layer at the surface of the deposited aluminium. (d) Oxygen and aluminium atoms prior to bonding; oxygen contains six electrons in the L electron shell ($1s^2 2s^2 2p^4$), aluminium contains a full L electron shell and has three electrons in its M shell ($1s^2 2s^2 2p^6 3s^2 3p^1$). (e) The electrons from the M shells in the aluminium atoms (shown in grey for clarity) move to the L shell of the oxygen atoms (shown as the red electrons); this is the formation of ionic bonds and results in both the oxygen and aluminium atoms having their L shells filled (for tidiness, the full K shell is not shown).

form naturally between a semiconductor and a metal (or superconductor); this means that no additional fabrication stages are required.

An oxide insulating layer forms ionic bonds between the atoms of the metal and the oxygen atoms. This prevents the outer electrons in the metal, which previously were *free* and available for current flow, from being able to flow as current and thus the resistance of the material is greatly increased.

The formation of an oxide layer is conceptually simple. Since aluminium is commonly used (for example those described by Clark et al., 2005; Pekola et al.,

2004; Prest et al., 2011) as one side of a tunnelling contact, aluminium oxide often forms the insulating oxide. Figure 2.1 and the following explain the growth of an aluminium-oxide layer, however, other oxide layers are sometimes used in similar devices, for example the tantalum oxide based devices described by Chaudhuri and Maasilta (2014). After the metal has been deposited, by evaporation or other means (Figure 2.1a), oxygen is introduced into the deposition chamber (Figure 2.1b). The outermost electrons from the aluminium (those in the third shell, the M shell) move to the vacant states in the outer shell of the oxygen atoms (oxygen has two vacant electron states in its second shell, the L shell), forming ionic bonds between the aluminium and the oxygen; this is shown in Figures 2.1d and 2.1e. This results in a layer of aluminium oxide (Al_2O_3) forming on top of the deposited aluminium (Figure 2.1c).

While conceptually simple, in order to produce an even, high quality layer of a desired thickness, great care needs to be taken regarding both the quantity of gas introduced and the temperature of the chamber during the introduction of the oxygen gas (Cabrera and Mott, 1949; Jaeger et al., 1991). The addition of an oxide layer also necessitates an additional step in the fabrication, along with the required equipment to add and monitor the flow of gas into the deposition chamber.

As opposed to an oxide layer, a Schottky barrier will form naturally between a metal and a semiconductor. The barrier is formed as the electrons in the two materials move to cause the Fermi-energy in the two materials to be aligned. The concept of a naturally forming potential barrier between a semiconductor and a metal was first suggested by Schottky (1939) whose original explanation is illustrated in Figure 2.2

Schottky's explanation was that, after the semiconductor has been brought into contact with the normal metal, the electrons in the conduction band of the semiconductor (the most energetic) are able to move to the lower (energetically favourable) states above the Fermi-level in the metal (illustrated in Figure 2.2b), leaving behind positively charged *donor* ions. This causes the Fermi level within the semiconductor to decrease, since there are fewer electrons in the conduction band. This movement of electrons continues until there is an equilibrium established between the electron systems in the two materials (i.e. when the Fermi levels are aligned). Away from the interface between the metal and the semiconductor, the valence and conduction bands move relative to the Fermi level; however, at the interface, the bands move differently, since it is these electrons which have moved.

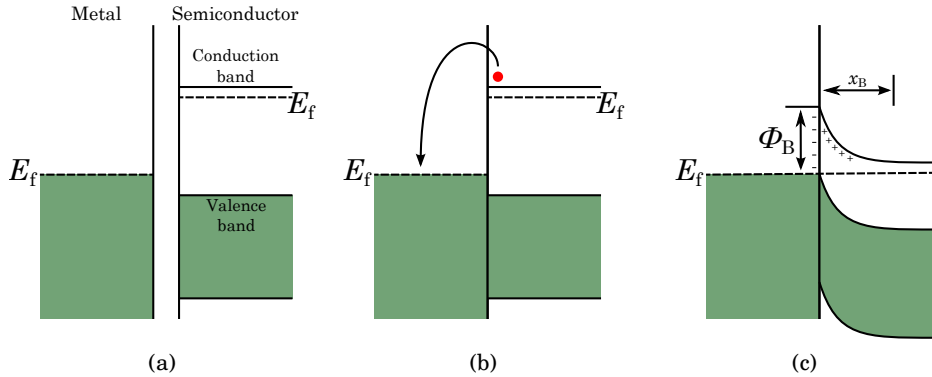


Figure 2.2: Formation of a Schottky barrier between a metal and an n-doped semiconductor. (a) Before being brought into contact, the energy distribution in the metal and the semiconductor are independent, with the Fermi-level (E_f , shown as the dashed line) sitting at the top of the occupied states in the metal (shown at $T = 0$ K) and just below the conduction band of the semiconductor. (b) Immediately after the metal and semiconductor are brought into contact, the energy levels are unchanged; however, electrons (red circle) start to move from the conduction band of the semiconductor to the vacant lower energy states in the metal. These electrons leave behind positively charged ions or *donor states*. (c) The movement of the most energetic electrons from the semiconductor causes the Fermi-level to move, this continues until the Fermi-level in both the materials is the same. Away from the interface, the band structure of the semiconductor moves relative to the Fermi-level; at the interface, however, this is not the case, which causes the phenomenon known as *band-bending* in the semiconductor. The height of the Schottky barrier established is related to the difference between the vacuum level in the two materials and is given by Φ_B .

This causes the phenomenon of *band-bending* and the formation of a depletion region (from E_f to $E_f + \Phi_B$) in the semiconductor at the interface.

Schottky barriers between doped silicon and aluminium typically have a height of $\Phi_B = 0.7$ eV (Yu and Mead, 1970). Archer and Yep (1970) show that increasing the doping of the silicon to very high levels (on the order of say $N_D = 10^{19}$ cm $^{-3}$), as is the case in the materials used in this work, lowers the barrier height by a factor of up to 1.5 from the undoped level (which remains constant up to doping concentrations of $\sim 10^{16}$ cm $^{-3}$). In either case this value is still substantially large than the energy gap of the superconducting aluminium, which has a nominal value

of $2\Delta = 364 \text{ } \mu\text{eV}$ at 0 K.

The width of the barrier, x_B , on the other hand depends heavily on the level of doping in the semiconductor. As shown in Figure 2.2 the formation of a Schottky barrier requires enough electrons to move from the semiconductor to the metal to bring the Fermi levels into alignment. In a lightly-doped semiconductor, where free electrons are sparse, electrons must move from further into the semiconductor to achieve this, resulting in a wider barrier compared to the highly-doped case where sufficient electrons can be found close to the interface. [Kittel \(2005\)](#) provides a rough approximation of the barrier width to be:

$$x_B = \sqrt{\frac{2\epsilon\epsilon_0 |\Phi_B|}{N_D e}}, \quad (2.1)$$

where ϵ and ϵ_0 are the relative and vacuum permittivity. Using typical values for the materials studied in this work of $\epsilon = 11.68$ and $N_D = 4 \times 10^{19} \text{ cm}^{-3}$, along with the value of $\Phi_B = 0.7 \text{ eV}$ from above, yields a barrier width of $x_B = 4.7 \text{ nm}$ in this case. Simplistically the barrier width changes as:

$$x_B \propto \sqrt{\frac{1}{N_D}}. \quad (2.2)$$

Schottky barriers are, in theory, simple to fabricate. All that is required is for the two materials to be deposited sequentially. An important caveat is that one must ensure that the first material deposited (often the semiconductor) is free of impurities or unwanted surface films (such as oxide layers). This is simple if the entire fabrication process can be performed in a single system under continuous vacuum. If, however, the device needs to be removed from the protection of the evacuated deposition system (to be patterned, for example), then it is important to ensure that the surface is thoroughly cleaned prior to the deposition of the second material (a good description of surface preparation requirements is given by [Roccaforte et al., 2003](#)). Should the surface of the first material not be sufficiently cleaned, contamination may either cause an insulating layer to form which, while itself acting as a tunnelling barrier, will inhibit or stop the development of a Schottky barrier; or alter the Fermi-level of the material and thus alter the Schottky barrier height (as discussed in the following paragraph).

One cannot simply choose any combination of semiconductor and metal to create a Schottky barrier. As can be seen from the description above and Figure 2.2, there

needs to be a difference between the inherent Fermi-levels in the two materials. If this is not the case, when the two materials are brought together, there will be minimal movement of electrons from the semiconductor's conduction band to the metal. This will cause the barrier height, Φ_B , to be very small. A similar effect is observed when the Fermi level of the metal is higher than that of the semiconductor; this results in the band-bending, seen in Figure 2.2c, to be downwards. This means that electrons do not encounter a barrier. Contacts of this type are known as *ohmic contacts*. A more detailed description of the formation and criteria for ohmic contacts is given by [Rhoderick and Williams \(1988\)](#) who also offer an excellent overview on the concepts relating to Schottky barriers.

2.3 THE TUNNELLING CURRENT

In order to understand the behaviour of a cold-electron bolometer, it is important to understand the movement of charges, at different energies, across the tunnelling barrier. To do this, we need to consider four directions of charge transfer, these are¹:

1. Charges in the superconductor with energies above the superconducting bandgap ($E > E_{f_S} + \Delta$) tunnelling into the central semiconductor island.
2. Quasiparticles in the superconductor whose energies are below the Fermi-energy ($E < E_{f_S} - \Delta$) tunnelling into the central island.
3. Charges in the central island, with energy levels corresponding to the normal states in the superconductor ($E > E_{f_S} + \Delta$), tunnelling into these states.
4. Charges in the central island, with energies corresponding to below the superconducting states in the superconductor ($E < E_{f_S} - \Delta$), tunnelling into these states.

Since the movement of charges in terms 3 and 4 is the opposite of those in the first two terms, these act to suppress the total current.

Figure 2.3 shows these four possible forms of tunnelling when there is no bias across the structure. It can be seen that the tunnelling routes represented by numbers 1 and 3 are possible (providing there is sufficient thermal broadening of

¹In the following list E_{f_S} is used to denote the Fermi energy in the superconductor.

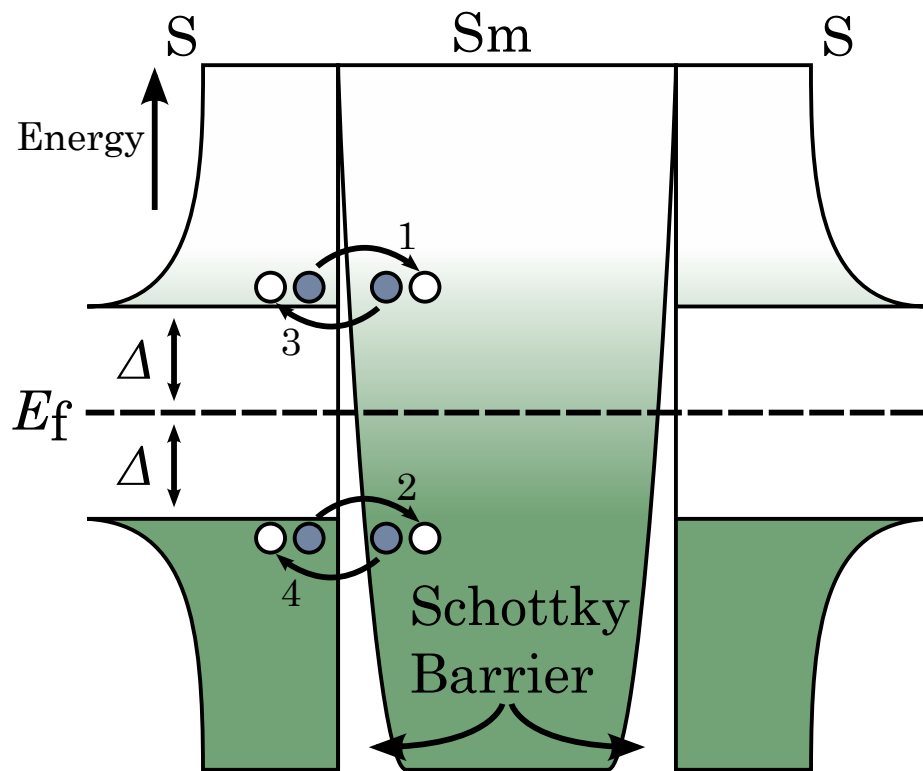


Figure 2.3: Possible tunnelling of charges in a **SSmS** structure, shown at non-zero temperature, without any external bias across this system and for only one junction. The density of the shading represents the number of occupied states. Numbering as listed on Page 23.

the density of states), since there are charges and vacant states on both sides of the Schottky barrier. The tunnelling shown by numbers 2 and 4 are less likely, since there are very few vacant states for electrons to tunnel to.

By applying an external bias across the structure, it is possible to shift the distribution of charges in the three layers relative to each other. This biasing causes the probability of tunnelling via each of the routes to be altered. Figure 2.4 shows the effect of biasing a single junction structure such that the energy levels in the semiconductor (right) are raised above the energy levels in the superconductor (left). This has a notable effect to the probability of tunnelling via each of the described routes. Charges are less likely to tunnel from the superconductor into the semiconductor (routes one and two), since there are fewer states available in the

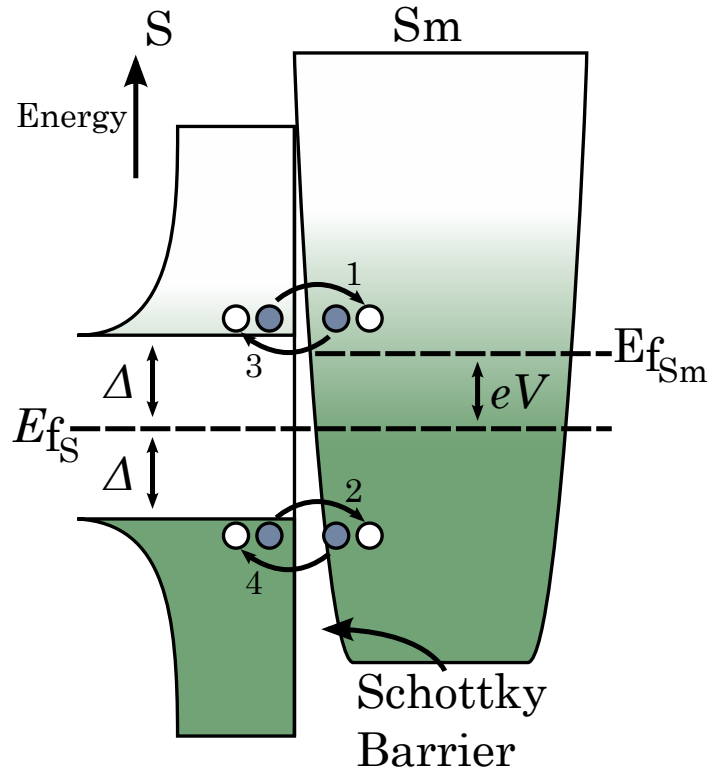


Figure 2.4: Tunnelling of charges across a single superconductor-semiconductor junction when biased by a voltage, V , such that the Fermi level in the semiconductor, E_{fSm} , is raised above that of the superconductor, E_{fS} .

semiconductor. Conversely, charges are more likely to move from the semiconductor into the superconductor (routes three and four) as there are a greater number of occupied states in the semiconductor with energies corresponding to the vacant states in the superconductor.

Figure 2.5 illustrates a single junction system biased in the opposite polarity to the structure shown in Figure 2.4. In this case, when compared to the unbiased state, charges are more likely to tunnel from the superconductor into the semiconductor (routes one and two), since the occupied states in the superconductor correspond to a greater number of vacant states in the semiconductor. Likewise, fewer charges will tunnel from the semiconductor into the superconductor (routes three and four), as there are fewer occupied states in the semiconductor aligned

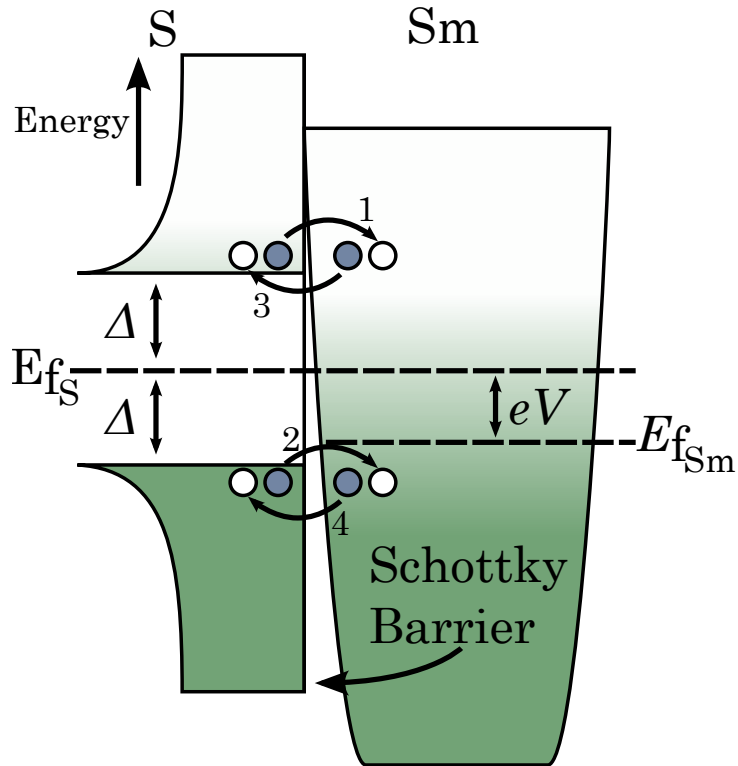


Figure 2.5: Tunnelling of charges across a single superconductor-semiconductor junction when biased in the opposite polarity to that shown in Figure 2.4. The biasing voltage, V , causes the Fermi level in the superconductor, E_{fS} , to be raised above the Fermi level in the semiconductor, E_{fSm} .

with vacant states in the superconductor.

When modelling the current in a two junction system, it is useful to note that, since the two junctions can be thought of as resistors in series, we need only consider the current through one junction, since the current through each of the junctions will be the same. This leads to two important definitions in the following derivation: the voltage used in these equations is defined to be the voltage dropped across a two junction system. The following equations assume that there is no resistance to current flow from either the semiconductor or superconductor, hence the voltage dropped across each junction will be $V/2$. The second definition to note is that the tunnelling resistance, R_N , is defined to be the resistance of a single junction.

For each of these movements of charge, it is possible to define a Fermi distribution, q_n , where the subscript n corresponds to the number of the term in the list on Page 23.

$$q_1 \sim \frac{1}{e^{\frac{|E|}{k_B T_S}} + 1}, \quad (2.3)$$

$$q_2 \sim \frac{1}{e^{\frac{-|E|}{k_B T_S}} + 1}, \quad (2.4)$$

$$q_3 \sim \frac{1}{e^{\frac{(|E|+eV/2)}{k_B T_e}} + 1}, \quad (2.5)$$

$$q_4 \sim \frac{1}{e^{\frac{-(|E|-eV/2)}{k_B T_e}} + 1}. \quad (2.6)$$

In these equations, E is the energy of a carrier, k_B is Boltzmann's constant, T_S and T_e are the temperatures of the charge carriers in the superconductor and the central island respectively, e is the electron charge and V is the voltage across the structure. q_1 is the Fermi-distribution for charges in the superconductor with energy above the superconducting bandgap, q_2 relates to charges in the superconductor with energies below the bandgap, q_3 and q_4 are the distributions of charges in the central island with energies above and below the superconductor's bandgap respectively.

For each of the terms in the above list, we can define a probability p_{1-4} that a charge will tunnel in the stated manner. This probability is related to the likelihood of an occupied state on one side of the tunnelling barrier corresponding to an empty state on the other side. For each of the forms of tunnelling defined above, this probability is:

$$p_1 = q_1 \times (1 - q_3), \quad (2.7)$$

$$p_2 = q_2 \times (1 - q_4), \quad (2.8)$$

$$p_3 = q_3 \times (1 - q_1), \quad (2.9)$$

$$p_4 = q_4 \times (1 - q_2). \quad (2.10)$$

The total movement of charges between the superconductor and the superconducting contact is related to the sum of these probabilities integrated over all energies and, if movement from the superconductor to the semiconductor is taken

to be the positive direction, is given by:

$$p_T = \int_0^\infty [p_1 + p_2 - p_3 - p_4] dE. \quad (2.11)$$

Substituting the terms for p_{1-4} from Equations 2.7–2.10 gives:

$$p_T = \int_{-\infty}^\infty [q_1 \times (1 - q_3) + q_2 \times (1 - q_4) - q_3 \times (1 - q_1) - q_4 \times (1 - q_2)] dE. \quad (2.12)$$

Expanding the brackets and cancelling the like terms yields:

$$p_T = \int_{-\infty}^\infty [q_1 - q_1 q_3 + q_2 - q_2 q_4 - q_3 + q_3 q_1 - q_4 + q_4 q_2] dE, \quad (2.13)$$

$$p_T = \int_{-\infty}^\infty [q_1 + q_2 - q_3 - q_4] dE. \quad (2.14)$$

It is possible to simplify this result further by looking at the sum of various combinations of the q terms in Equation 2.14. Of most interest is the result of $q_1 + q_2$.

$$q_1 + q_2 = \frac{1}{e^{\frac{|E|}{k_B T_S}} + 1} + \frac{1}{e^{\frac{-|E|}{k_B T_S}} + 1}, \quad (2.15)$$

$$= \frac{e^{\frac{-|E|}{k_B T_S}} + 1 + e^{\frac{|E|}{k_B T_S}} + 1}{\left(e^{\frac{|E|}{k_B T_S}} + 1\right) \times \left(e^{\frac{-|E|}{k_B T_S}} + 1\right)}, \quad (2.16)$$

$$= \frac{e^{\frac{|E|}{k_B T_S}} + e^{\frac{-|E|}{k_B T_S}} + 2}{e^{\frac{|E|}{k_B T_S}} e^{\frac{-|E|}{k_B T_S}} + e^{\frac{|E|}{k_B T_S}} + e^{\frac{-|E|}{k_B T_S}} + 1}, \quad (2.17)$$

$$q_1 + q_2 = 1. \quad (2.18)$$

A useful result can also be found from examining the result of sum $q_1 + q_2 - q_3$ and using the result of Equation 2.18 above.

$$q_1 + q_2 - q_3 = 1 - q_3, \quad (2.19)$$

$$= 1 - \frac{1}{e^{\frac{|E|+eV/2}{k_B T_e}} + 1}, \quad (2.20)$$

$$= \frac{e^{\frac{|E|+eV/2}{k_B T_e}}}{e^{\frac{|E|+eV/2}{k_B T_e}} + 1}, \quad (2.21)$$

$$= \frac{1}{e^{-\frac{|E|+eV/2}{k_B T_e}} \left(e^{\frac{|E|+eV/2}{k_B T_e}} + 1 \right)}, \quad (2.22)$$

$$q_1 + q_2 - q_3 = \frac{1}{e^{\frac{-(|E|+eV/2)}{k_B T_e}} + 1}. \quad (2.23)$$

Substituting this result into Equation 2.14 gives:

$$p_T = \int_{-\infty}^{\infty} [q_1 + q_2 - q_3 - q_4] dE, \quad (\text{2.14 revisited})$$

$$= \int_{-\infty}^{\infty} \left[\frac{1}{e^{\frac{-(|E|+eV/2)}{k_B T_e}} + 1} - q_4 \right] dE, \quad (2.24)$$

$$= \int_{-\infty}^{\infty} \left[\frac{1}{e^{\frac{-(|E|+eV/2)}{k_B T_e}} + 1} - \frac{1}{e^{\frac{-(|E|-eV/2)}{k_B T_e}} + 1} \right] dE, \quad (2.25)$$

$$p_T = \int_{-\infty}^{\infty} \left[\frac{1}{e^{\frac{(|E|-eV/2)}{k_B T_e}} + 1} - \frac{1}{e^{\frac{(|E|+eV/2)}{k_B T_e}} + 1} \right] dE. \quad (2.26)$$

The total number of charges tunnelling can be found by multiplying this probability by the density of states in the superconductor $N_S(E)$ which, from Bardeen et al. (1957), is given by:

$$N_S(S) = \frac{E}{\sqrt{E^2 - \Delta^2}}, \quad (2.27)$$

where Δ is half the size of the superconducting energy gap. The energy gap is a function of the electron temperature, increasing from zero at just above the superconducting critical temperature, T_c , to a maximum value of $1.764k_B T_c$ at 0 K. The size of the energy gap with decreasing temperature is shown in Figure 2.6.

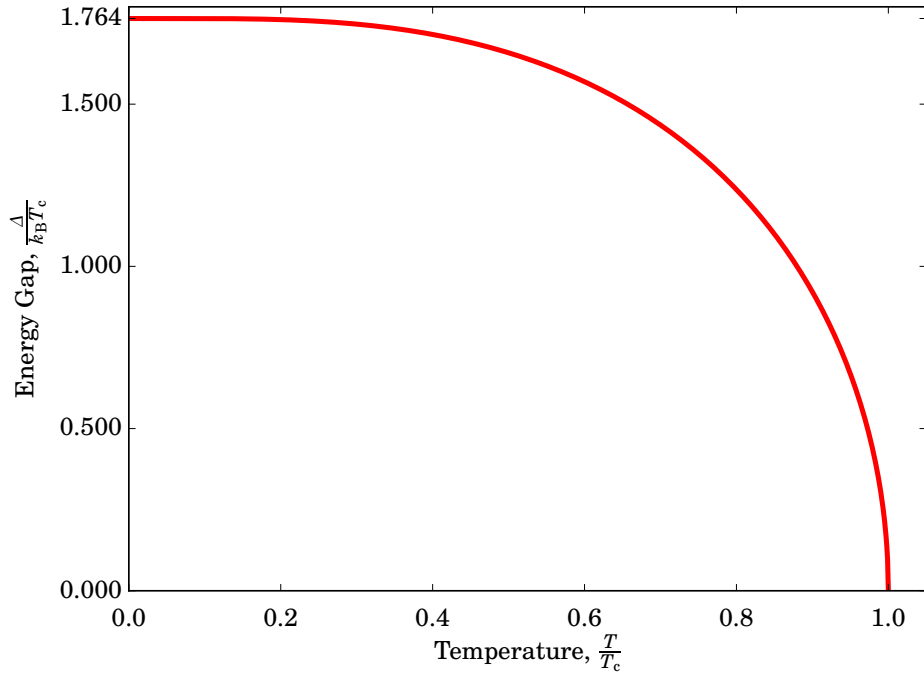


Figure 2.6: Increase in the superconducting energy gap with decreasing temperature as described by Bardeen et al. (1957).

Using Equation 2.27 in the result from Equation 2.26 gives the total number of charges, n , tunnelling across the barrier:

$$n = \int_{-\infty}^{\infty} \frac{|E|}{\sqrt{|E|^2 - \Delta^2}} \left[\frac{1}{e^{\frac{(|E|-eV/2)}{k_B T_e}} + 1} - \frac{1}{e^{\frac{(|E|+eV/2)}{k_B T_e}} + 1} \right] dE. \quad (2.28)$$

Finally, it is possible to convert this number of charges into a tunnelling current, I , by converting Equation 2.28 to a voltage by dividing by the electron charge, e , and using Ohm's Law with the tunnelling resistance R_N , giving:²

$$I = \frac{1}{eR_N} n. \quad (2.29)$$

²The subscript N denotes that this is the *normal state* resistance of a current-voltage (I - V) curve.

Substituting the term for n from Equation 2.28 gives the final result:

$$I = \frac{1}{eR_N} \int_{-\infty}^{\infty} \frac{E}{\sqrt{E^2 - \Delta^2}} \left[\frac{1}{e^{\frac{(E-eV/2)}{k_B T_e}} + 1} - \frac{1}{e^{\frac{(E+eV/2)}{k_B T_e}} + 1} \right] dE. \quad (2.30)$$

Using this result, and if the current and the voltage of a particular device have been measured, it is possible to use a parameter fitting program to calculate the electron temperature.

Inspection of Equation 2.30 shows that there is an exponential dependance on the electron temperature for the tunnelling current. It is this dependency which makes the tunnelling contacts described here highly sensitive thermometers. The relationship between the electron temperature and the tunnelling current (at a constant voltage bias) is shown in Figure 2.7. The tunnelling current increases rapidly with the electron temperature until the temperature of the electrons is greater than the critical temperature; at which point the tunnelling current remains constant.

2.4 THE COOLING POWER

Each time a charge leaves the central island by tunnelling into one of the superconducting contacts, as described in Section 2.3, it must be replaced by a charge from one of the superconductors. When the device is biased, the most likely flow of charge will be from the semiconductor into the lower energy contact ($E_{f_S} - E_{f_{Sm}} = -eV/2$) and for a charge from the superconductor at a higher energy ($E_{f_S} - E_{f_{Sm}} = eV/2$) to fill this vacant state. This is illustrated in Figure 2.8. Since the charges which tunnel out are replaced by less energetic charges, the overall energy (and thus temperature) of the charges in the central island is reduced. It is this process which is utilised to create the microrefrigerator type of device (Nahum et al., 1994).

This cooling of charges in the central island of the structure can be expressed as a cooling or heating power, P . Depending on the exact route by which charges pass through the structure, this term will either be positive, meaning that energy is added to the semiconductor and there is net heating; or it will be negative, due to energy being removed and the temperature of the charges is lowered.

To derive an expression for this power, it is possible to follow a similar derivation to that given in Section 2.3 to find the tunnelling current (Equation 2.30). To do this, the probability, p_T , of an occupied state on one side of the barrier corresponding

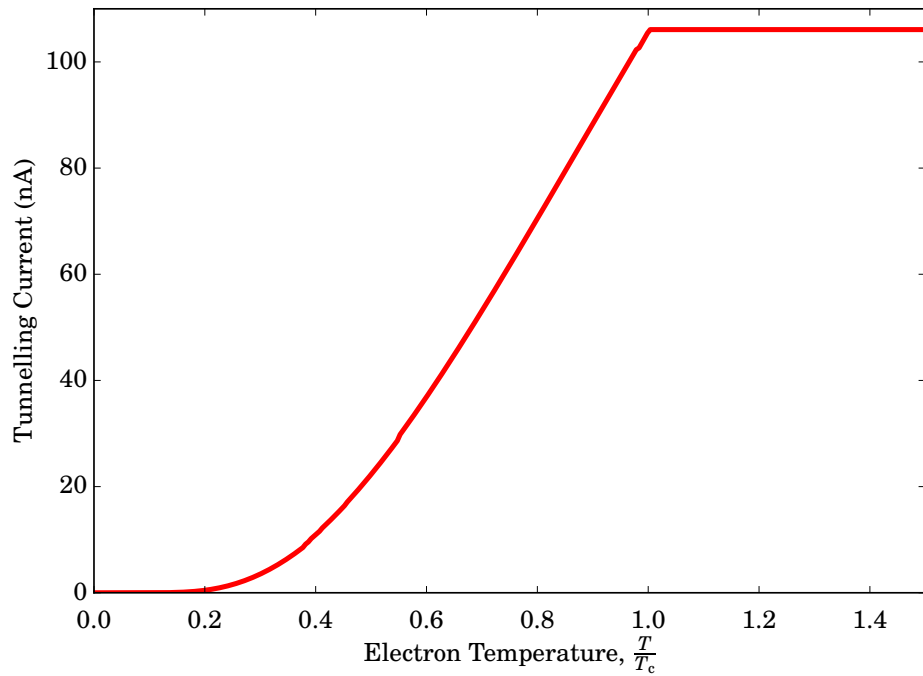


Figure 2.7: The relationship between the tunnelling current and the electron temperature. This was modelled using Equation 2.30 for a superconductor with a critical temperature of 1.2 K, biased by a voltage $V = \Delta_{T=0}$ and a tunnelling resistance, per junction, of $1\text{ k}\Omega$.

to a vacant state on the other is again calculated. There are four possible routes by which charges can tunnel to or from the semiconductor. These were illustrated in Figures 2.3, 2.4 and 2.5. In order to calculate the total energy added to the semiconductor, each of these probabilities needs to be multiplied by the energy of the charges tunnelling.

p_1 transfers charges with energy $E + eV/2$ from the superconducting contact into the semiconductor.

p_2 transfers charges with energy $-(E - eV/2)$ from the superconductor into the semiconductor.

p_3 removes charges with energy $E + eV/2$ from the central semiconductor, this means the energy contribution to the semiconductor is $-(E + eV/2)$.

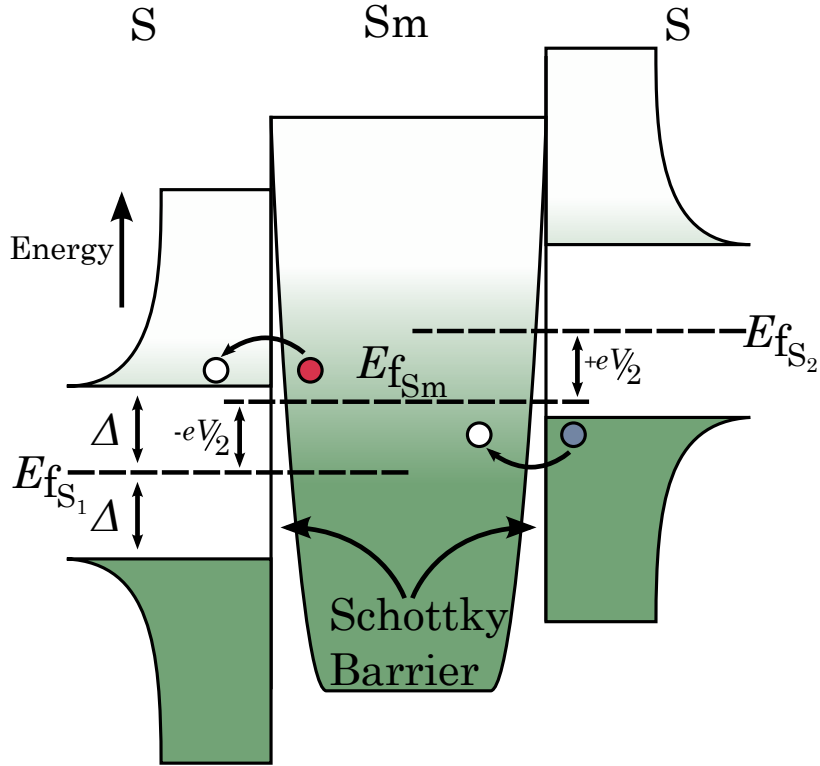


Figure 2.8: The most likely route for charges to tunnel in a biased two-junction system. If the system is biased such that the energy levels in the left hand superconductor are lowered with respect the semiconductor and the states in the right hand contact are raised (as shown), the most likely movement of charges from the semiconductor will be to above the energy gap in the left hand superconductor. This will create a vacant state, which will be filled by a charge from the top of the superconducting state in the right hand superconductor.

p_4 removes charges with energy $-(E - eV/2)$ from the semiconductor, this results in an energy change of $E - eV/2$ in the semiconductor.

To find the total energy transferred through this tunnelling E_{tun} , the summation of these terms needs to be integrated over all energies and multiplied by the superconducting density of states, given by:

$$N_S(S) = \frac{E}{\sqrt{E^2 - \Delta^2}}, \quad (\text{2.27 revisited})$$

This gives:

$$E_{\text{tun}} = \int_{-\infty}^{\infty} \frac{E}{\sqrt{E^2 - \Delta^2}} \left[E(p_1 - p_2 - p_3 + p_4) + \frac{eV}{2}(p_1 + p_2 - p_3 - p_4) \right] dE. \quad (2.31)$$

One important definition which can be taken from this is that the change in energy, due to movement of charges, is defined such that an increase in this term corresponds to the overall energy of the charges in the semiconductor increasing (i.e. heating of the charges).

To calculate the power, P , associated with this change in energy, Equation 2.31 needs to be divided by the tunnelling resistance, R_N , (as defined on Page 30) and the square of the electron charge. This additional electron charge, compared to Equation 2.28, is the result of multiplying by the energy of the carriers as opposed to their charge. One further observation needs to be made prior to arriving at a term for the tunnelling power. When deriving Equation 2.30 for the tunnelling current, it sufficed to examine only a single junction. This was due to the fact that since the two junctions are in a series configuration, the current through the two must be the same. In the case of the tunnelling power, heat can flow through either of the two junctions; this means that for symmetrical junctions, Equation 2.31 needs to be further multiplied by a factor of two. This gives:

$$P = \frac{2}{e^2 R_N} \int_{-\infty}^{\infty} \frac{E}{\sqrt{E^2 - \Delta^2}} \left[E(p_1 - p_2 - p_3 + p_4) + \frac{eV}{2}(p_1 + p_2 - p_3 - p_4) \right] dE. \quad (2.32)$$

It is useful to split this in two terms, P_1 and P_2 , such that:

$$P_1 = \frac{2}{e^2 R_N} \int_{-\infty}^{\infty} \frac{E}{\sqrt{E^2 - \Delta^2}} [E(p_1 - p_2 - p_3 + p_4)] dE, \quad (2.33)$$

$$P_2 = \frac{2}{e^2 R_N} \int_{-\infty}^{\infty} \frac{E}{\sqrt{E^2 - \Delta^2}} \left[\frac{eV}{2}(p_1 + p_2 - p_3 - p_4) \right] dE, \quad (2.34)$$

$$P = P_1 + P_2. \quad (2.35)$$

Equation 2.34 for P_2 can be rewritten as:

$$\begin{aligned} P_2 &= \frac{eV}{2} \frac{2}{e^2 R_N} \int_{-\infty}^{\infty} \frac{E}{\sqrt{E^2 - \Delta^2}} (p_1 + p_2 - p_3 - p_4) dE, \\ P_2 &= V \frac{1}{eR_N} \int_{-\infty}^{\infty} \frac{E}{\sqrt{E^2 - \Delta^2}} (p_1 + p_2 - p_3 - p_4) dE. \end{aligned} \quad (2.36)$$

By noting that tunnelling current, I , can be rewritten as:

$$I = \frac{1}{eR_N} \int_{-\infty}^{\infty} \frac{E}{\sqrt{E^2 + \Delta^2}} [p_1 + p_2 - p_3 - p_4] dE, \quad (2.30 \text{ rewritten})$$

and comparing this to Equation 2.36, it can be seen that the latter can be simply written as:

$$P_2 = IV. \quad (2.37)$$

It is possible to slightly simplify Equation 2.33, in a way similar to that performed to simplify Equation 2.11 to Equation 2.26 in Section 2.3. This starts by recalling that p_{1-4} can be written as:

$$p_1 = q_1 \times (1 - q_3), \quad (2.7 \text{ revisited})$$

$$p_2 = q_2 \times (1 - q_4), \quad (2.8 \text{ revisited})$$

$$p_3 = q_3 \times (1 - q_1), \quad (2.9 \text{ revisited})$$

$$p_4 = q_4 \times (1 - q_2). \quad (2.10 \text{ revisited})$$

Thus, the term in square brackets in Equation 2.33 (which, for the sake of tidiness, we will temporarily call A) can be written as:

$$A = E(p_1 - p_2 - p_3 + p_4), \quad (2.38)$$

$$\therefore P_1 = \frac{2}{e^2 R_N} \int_{-\infty}^{\infty} \frac{E}{\sqrt{E^2 - \Delta^2}} \times A dE, \quad (2.39)$$

$$A = E(q_1 \times (1 - q_3) - q_2 \times (1 - q_4) - q_3 \times (1 - q_1) + q_4 \times (1 - q_2)). \quad (2.40)$$

Multiplying out these terms gives:

$$A = E(q_1 - q_1q_3 - q_2 + q_2q_4 - q_3 + q_3q_1 + q_4 - q_4q_2), \quad (2.41)$$

$$A = E(q_1 - q_2 - q_3 + q_4). \quad (2.42)$$

This gives:

$$P_1 = \frac{2}{e^2 R_N} \int_{-\infty}^{\infty} \frac{E}{\sqrt{E^2 - \Delta^2}} [E(q_1 - q_2 - q_3 + q_4)] dE. \quad (2.43)$$

Since it is not possible to further simplify this, the final form of P_1 can be written as:

$$P_1 = \frac{2}{e^2 R_N} \int_{-\infty}^{\infty} \frac{E^2}{\sqrt{E^2 - \Delta^2}} \left[\frac{1}{e^{\frac{E}{k_B T_S}} + 1} - \frac{1}{e^{\frac{-E}{k_B T_S}} + 1} - \frac{1}{e^{\frac{(E+eV/2)}{k_B T_e}} + 1} + \frac{1}{e^{\frac{-(E-eV/2)}{k_B T_e}} + 1} \right] dE. \quad (2.44)$$

Using this result, along with that of Equation 2.37, in Equation 2.35 gives the final result of the tunnelling power as:

$$P = IV + \frac{2}{e^2 R_N} \int_{-\infty}^{\infty} \frac{E^2}{\sqrt{E^2 - \Delta^2}} \left[\frac{1}{e^{\frac{E}{k_B T_S}} + 1} - \frac{1}{e^{\frac{-E}{k_B T_S}} + 1} - \frac{1}{e^{\frac{(E+eV/2)}{k_B T_e}} + 1} + \frac{1}{e^{\frac{-(E-eV/2)}{k_B T_e}} + 1} \right] dE. \quad (2.45)$$

2.5 ELECTRON-PHONON INTERACTIONS

As a conduction electron moves through a material, such as the lattice of a semiconductor, it will experience interaction with the ion cores created by the vacation of electrons. The simplest result of these interactions is the scattering of electrons due to collisions with the lattice as they move through the lattice, this is the origin of electrical resistance. These collisions result in an exchange of energy between the electrons and phonons, which can be expressed as a thermal conduction, G_{e-ph} ,

between the two systems. As will be seen later in this section, this thermal conduction plays a large part in determining the limit of a cold-electron bolometer's sensitivity.

The fluctuation-dissipation theorem presented by Nyquist (1928b) shows that this thermal conduction will have fluctuations on the order of $k_B T$ and having a power spectral density of $S_G = 4k_B T^2 G$. From this, it is clear that the energy transferred between an electron and a phonon in a collision is directly proportional to temperature in the case of a *clean* metal or T^2 in a *dirty* thin-film metal or highly-doped semiconductor, where there are a large number of impurities. Further dependencies of the power on temperature arise from the rate of collision between the electrons and the phonons (see Ziman, 2001), which contributes an additional dependency on T , and the Bose-Einstein distribution governing the number of states filled, which yields a further T^3 dependency. In total, it has been shown that for a metal, the power flow between the two systems depends on the temperature to the power 5 (Ziman, 2001), whereas for a degenerately-doped semiconductor, the dependence has a T^6 relationship (Prunnila, 2007), as will be used later in this chapter.

These relatively high-order dependencies on the temperature indicate clearly that at low temperatures, one should expect the interaction between the two systems to be weak. When the electrons and phonons are at different temperatures, these collisions will result in a net flow of power from the more energetic (hotter) system to the other. This power flow is given by:

$$P = \Sigma \Omega \left(T_e^\beta - T_{ph}^\beta \right), \quad (2.46)$$

where Ω is the volume of the material in which the collisions occur, T_e and T_{ph} are the temperature of the electrons and phonons respectively, β is the power dependency of the interactions on temperature (nominally 5 for a metal and 6 for a highly-doped semiconductor, as already discussed), and Σ is a material parameter. Wellstood et al. (1994) present an approximation for Σ for a metal ($\beta = 5$) given by:

$$\Sigma = \frac{\hbar}{2\rho c_s} \left(\frac{2E_F}{3} \right)^2 \frac{D(E_F) k_B^5 \Gamma(5) \zeta(5)}{2\pi \hbar^5 c_s^3 v_F \Omega}, \quad (2.47)$$

where ρ lattice density, c_s is the speed of sound in the lattice, E_F and v_F are the Fermi energy and velocity, $D(E)$ is the density of states at energy E , and Γ and ζ are the Gamma and Riemann zeta functions respectively. It should, however, be

noted that when tested by Wellstood et al. (1994) and Qu et al. (2005), both found that the model presented in Equation 2.47 produced values differing by in excess of an order of magnitude compared to measured values and thus it is concluded that Equation 2.47 produces, at best, a rough approximation of Σ .

Muhonen et al. (2011) present a discussion of the effect of straining a semiconductor's lattice on the interaction between electrons and phonons. A simplistic interpretation of their results is that, as strain is introduced in two dimensions of the lattice (the in-plane dimensions), the energy levels for interactions between the in-plane atoms and electrons are increased with strain, to the degree that they are effectively depopulated and electrons only interact via the out-of-plane energy bands (which are not affected by the straining of the lattice). Muhonen et al. tested two materials, one with a straining layer consisting of $\text{Si}_{0.8}\text{Ge}_{0.2}$ (resulting in a strain factor of around 0.95 % in the doped silicon), and one unstrained control sample. Both samples used silicon doped with phosphorus to a concentration of $4 \times 10^{19} \text{ cm}^{-3}$. Note that these two materials are, to all intents and purposes, identical to the materials used to fabricate the devices examined in this work. Examining the same samples, Prest et al. (2011) found that the strained material showed substantially weaker coupling of the electrons and phonons compared to the unstrained control sample, with a Σ value of $2 \times 10^7 \text{ WK}^{-6} \text{ m}^{-3}$ for the strained material and $5.2 \times 10^8 \text{ WK}^{-6} \text{ m}^{-3}$ for the control sample. This is also shown by Muhonen et al. (2011) who, while not calculating values of Σ , do present graphs of $G_{\text{e-ph}}$ vs T_e for both materials in Figure 2b of their manuscript. Muhonen et al. explain that the power loss in interactions between the electrons and phonons can be expressed as:

$$P_{\text{e-ph}} = F(T_e) - F(T_{\text{ph}}), \quad (2.48)$$

where $F(T)$ is the energy loss function, which, according to Prunnila (2007), may be written as:

$$F(T) = F_S(T) + F_A(T), \quad (2.49)$$

where $F_S(T)$ and $F_A(T)$ are the symmetric and asymmetric parts of the energy loss function. Following the rigorous mathematical treatment presented by Prunnila (2007), Muhonen et al. show that, for their control sample, both the symmetric and asymmetric components contribute to the energy loss function and, furthermore, it

can be said that $F_A \gg F_S$ and thus for the unstrained sample:

$$G_{e-ph} \approx \frac{\partial F_A}{\partial T_e}. \quad (2.50)$$

They go on to explain that, if the in-plane energy bands are fully depopulated, then $F_A = 0$ and thus the thermal conduction between the electrons and phonons in the strained device (under this assumption) is given by:

$$G_{e-ph} = \frac{\partial F_S}{\partial T_e}, \quad (2.51)$$

which, when computed, is found to be a factor of several thousand times smaller than the result of Equation 2.50. Looking at the results presented in Figure 2b of [Muhonen et al. \(2011\)](#), it is clear that Equation 2.50 produces a close fit to their experimental results. However, the results for the strained sample agree with Equation 2.51 only in that G_{e-ph} is less for the strained material compared to the control. The magnitude of the reduction is only a factor 20–50 across the entire temperature range studied (0.2–0.5 K). This is many orders of magnitude less than the change predicted by Equation 2.51. From this, it can be concluded that the in-plane energy bands have not been fully depopulated at this level of strain and the assumption that $F_A = 0$ does not hold. This also implies that there is a great deal of potential to decrease the electron-phonon coupling further through the introduction of additional strain into the doped silicon. At the time of writing, this has not been explored and the materials used in this work are essentially identical to those described by [Muhonen et al. \(2011\)](#) and [Prest et al. \(2011\)](#).

2.6 THE RESPONSIVITY

Like all bolometric detectors, it is possible to bias a cold-electron bolometer with either a voltage or a current. In either case, the quantity which is not providing the bias is monitored and it is in this signal that the response to a change in incident optical power will be measured. The responsivity, S , of a detector is defined as the ratio of the change in the measured signal to the change in the power absorbed in the detector. This is written as:

$$S = \frac{dsignal}{dP_{abs}}, \quad (2.52)$$

where *signal* is the quantity being monitored and P_{abs} is the absorbed power. Since a bolometric detector is biased by either a voltage or a current, we can define two types of responsivity. In the case of a voltage-biased detector, where the current flowing through the detector is monitored, the current responsivity, S_I , is given by:

$$S_I = \frac{dI}{dP_{\text{abs}}}, \quad (2.53)$$

where I is the current being measured. For a detector biased by a current, the voltage responsivity, S_V , is given by:

$$S_V = \frac{dV}{dP_{\text{abs}}}, \quad (2.54)$$

where V is the measured voltage.

These terms are general expressions and need to be rewritten such that their values can be calculated. In order to derive useful expressions for the responsivity, it is important to understand the relative contributions to the heating (or cooling) of the electrons in the detector's absorber. Along with tunnelling power (Equation 2.45), which adds or removes heat via the tunnelling current, the electrons in the absorber are also affected by various other sources of heating or cooling. The most significant of which are: Joule heating, P_J , due the resistance experienced by the current within the absorber; the energy from a radiative source which is absorbed by the detector, P_{abs} ; and the flow of energy directly between the electron and the phonon systems, $P_{\text{e-ph}}$. Joule heating was first described by Joule (1837); it is caused by the collisions between the charges flowing in the current and the atomic ions in the conductor. The heating power from these collisions is given by:

$$P_J = I^2 R, \quad (2.55)$$

where I is the current flowing through a resistance R .

Unless the electron and phonon systems are at thermal equilibrium, there will be a flow of heat between the two due to the thermal link between the systems. The heating (or cooling) power resulting from this flow of heat is given by:

$$P_{\text{e-ph}} = \Sigma \Omega \left(T_e^\beta - T_{\text{ph}}^\beta \right), \quad (2.56)$$

where Σ is a material constant relating to how strong the thermal link between the electrons and phonons is; Ω is the volume in which the electrons and phonons are

not in thermal equilibrium; T_e and T_{ph} are the temperatures of the electrons and the phonons respectively; and β is the power dependance on the temperature of the heat flow. Unlike all of the other terms mentioned (including the tunnelling power), this term is positive for the removal of energy (cooling) from the electrons and negative for heating of the electrons.

For the absorber to be at a constant temperature, these terms must add up to zero. This is referred to as the heat balance equation (or the heat balance condition) and can be expressed as:

$$P + P_{abs} + P_J - P_{e-ph} = 0, \quad (2.57)$$

where P is the tunnelling power given in Equation 2.45 (note that P is negative for electron cooling); P_{abs} is the power absorbed in the detector due to incident optical power; I is the current flowing through the absorber of the detector; R_{abs} is the resistance of the detector's absorber; Σ is the material constant of the absorber; Ω is the volume of the absorber; T_e and T_{ph} are the temperatures of the electrons and phonons respectively; and β is the power of temperature dependency of electron-phonon cooling power, this has been found by Prest et al. (2011) to be 6. This equation is simply the equilibrium condition for the temperature of the electrons in the absorber; the first three terms are defined as being positive for heating of the electrons, whereas the final term is defined as being positive for cooling of the charges. The meaning of the first two terms has already been covered, the third term is simply the Joule heating of the electrons in the absorber due to the current flowing through the absorber. The final term is the cooling of the electrons due to their thermal link to the phonons; this is positive when the temperature of the phonons is less than that of the electrons and is thus a cooling power as opposed to a heating power.

In the case of a voltage-biased detector, the current responsivity, S_I , can be derived by noting that Equation 2.53 can be rewritten as:

$$S_I = \frac{dI}{dP_{abs}} = \frac{\frac{\partial I}{\partial T_e}}{\frac{\partial P_{abs}}{\partial T_e}}. \quad (2.58)$$

The denominator of this can be found by differentiating the heat balance equation (Equation 2.57).

$$0 = \frac{\partial P}{\partial T_e} + \frac{\partial P_{\text{abs}}}{\partial T_e} + \frac{\partial}{\partial T_e} I^2 R_{\text{abs}} - \beta \Sigma \Omega T_e^{\beta-1}, \quad (2.59)$$

$$\frac{\partial P_{\text{abs}}}{\partial T_e} = \beta \Sigma \Omega T_e^{\beta-1} - \frac{\partial P}{\partial T_e} - \frac{\partial}{\partial T_e} I^2 R_{\text{abs}}. \quad (2.60)$$

Substituting this result into Equation 2.58 gives the final result:

$$S_I = \frac{\frac{\partial I}{\partial T_e}}{\beta \Sigma \Omega T_e^{\beta-1} - \frac{\partial P}{\partial T_e} - \frac{\partial}{\partial T_e} I^2 R_{\text{abs}}}. \quad (2.61)$$

This differs slightly from Equation 10 of [Golubev and Kuzmin \(2001\)](#), who do not consider the Joule heating of the absorber in their model but who do consider the effects of operating in an AC regime.³

It is possible to derive the voltage responsivity (S_V) similarly, by starting with:

$$S_V = \frac{dV}{dP_{\text{abs}}} = \frac{\frac{\partial V}{\partial T_e}}{\frac{\partial P_{\text{abs}}}{\partial T_e}}. \quad (2.62)$$

Since, in the current-biased regime, the current across the detector cannot change it is possible to write:

$$\frac{dI}{dT_e} = 0 = \frac{\partial I}{\partial V} \frac{\partial V}{\partial T_e} + \frac{\partial I}{\partial T_e}, \quad (2.63)$$

$$\frac{\partial V}{\partial T_e} = -\frac{\frac{\partial I}{\partial T_e}}{\frac{\partial I}{\partial V}}. \quad (2.64)$$

Using this in the numerator of Equation 2.62 yields:

$$S_V = \frac{-\frac{\frac{\partial I}{\partial T_e}}{\frac{\partial I}{\partial V}}}{\frac{\partial P_{\text{abs}}}{\partial T_e}}. \quad (2.65)$$

As in the case for the current responsivity, the numerator can be found by differentiating the heat balance equation. In the current-biased regime, there are two subtle differences to that of Equation 2.60. The first being that the Joule heating

³Also note that [Golubev and Kuzmin](#) define the tunnelling power to be positive for cooling of the electrons.

term no longer depends on the electron temperature, since the current is constant and thus:

$$\left(\frac{\partial}{\partial T_e} I^2 R_{\text{abs}} \right)_I = 0. \quad (2.66)$$

The second is the that the tunnelling power (given by Equation 2.45) is a function of both the electron temperature and the voltage (along with the temperature of the charges in the superconductor). In the voltage-biased case, the voltage was not a function of the electron temperature. In the current-bias regime, since the current is fixed, the voltage across the tunnelling contacts must vary with the temperature of the charges, this means that:

$$\frac{dP}{dT_e} = \frac{\partial P}{\partial V} \frac{\partial V}{\partial T_e} + \frac{\partial P}{\partial T_e}. \quad (2.67)$$

Substituting the result of Equation 2.64 gives:

$$\frac{dP}{dT_e} = \frac{\partial P}{\partial T_e} - \frac{\frac{\partial I}{\partial T_e}}{\frac{\partial I}{\partial V}} \frac{\partial P}{\partial V}. \quad (2.68)$$

Noting this, along with the differential of the Joule heating power from Equation 2.66, the differential of the heat balance equation is now:

$$0 = \frac{\partial P_{\text{abs}}}{\partial T_e} + \frac{\partial P}{\partial T_e} - \frac{\frac{\partial I}{\partial T_e}}{\frac{\partial I}{\partial V}} \frac{\partial P}{\partial V} - \beta \Sigma \Omega T_e^{\beta-1}, \quad (2.69)$$

giving:

$$\frac{\partial P_{\text{abs}}}{\partial T_e} = \beta \Sigma \Omega T_e^{\beta-1} + \frac{\frac{\partial I}{\partial T_e}}{\frac{\partial I}{\partial V}} \frac{\partial P}{\partial V} - \frac{\partial P}{\partial T_e}. \quad (2.70)$$

Substituting this for the denominator of Equation 2.65 gives the final form of the voltage responsivity to be:

$$S_V = \frac{-\frac{\frac{\partial I}{\partial T_e}}{\frac{\partial I}{\partial V}}}{\beta \Sigma \Omega T_e^{\beta-1} + \frac{\frac{\partial I}{\partial T_e}}{\frac{\partial I}{\partial V}} \frac{\partial P}{\partial V} - \frac{\partial P}{\partial T_e}}. \quad (2.71)$$

This is the same, in the DC limit, as Equation 30 of [Golubev and Kuzmin \(2001\)](#).

2.7 THE SOURCES OF ELECTRICAL NOISE

In order for incoming optical radiation to be measured by a detector system, the output signal produced must be greater than the noise signal of the detector or the readout system used. This means that a detector with a high level of inherent noise is less sensitive than a detector with a lower level of noise. When developing a detector, there are two main goals. The first is to prove that the underlying principles are in fact valid and that a functioning detector can be made. The second is to make the detector as sensitive as possible.⁴ Because of this, it is important to have a strong understanding of the noise processes involved in a detector.

There are several physical phenomena that cause noise. These can be roughly grouped into two categories: noise due to some form of fluctuation and noise resulting from the contamination of one signal by another. It is usually possible to shield electrical wiring and components to eliminate contamination of a signal, however, some sources may be more problematic to remove; for example 50 Hz or *mains noise* is caused by the switching AC voltage used to power electrical equipment and, since it is most likely essential to use some form of mains-powered equipment to monitor a detector, this noise may prove impossible to fully eradicate. Noise due to fluctuations in the energy of the charges within the detector are inevitable and can, at best, only be partially reduced through cleverly designing the detector or the materials used.

In deriving a term for the expected noise measured for a silicon cold-electron bolometer, three types of noise will be considered. Firstly, internal noise within the detector; these terms are due to various internal factors which cause the energy of the charges to fluctuate. Secondly, noise which is the result of incident power absorbed by the device. Finally, amplifier or readout noise, which is added to the signal by the electronic systems used to monitor the detector. It is worth noting here that (as will be seen in Chapter 6) the noise of an amplifier, or the readout system as a whole, is often higher at low frequencies (typically below 10 Hz) due to so called $1/f$ noise, whose origin is not well understood.

For the internal noise, two contributions will be considered; these are the current shot noise $\langle \delta I \rangle$ and the power or heat-flow noise $\langle \delta P \rangle$. As can be seen from Section 2.4 (and particularly Equation 2.45), these two quantities are not

⁴It is worth mentioning that, depending upon the desired application for a detector, improvements to the detector's speed may be as desirable as improved sensitivity, if not even more so.

uncorrelated; indeed, the tunnelling power depends heavily on the current (as one might expect). To address this correlation between these two quantities, a third term, the correlated noise, $\langle \delta P \delta I \rangle$, is introduced.

For these terms, the fluctuations that cause the corresponding noise will be taken to be governed by Poisson statistics, meaning that:

$$\sigma_x = \sqrt{\bar{x}}, \quad (2.72)$$

where σ_x is the standard deviation of the quantity x and \bar{x} is the mean value of x .

In the case of the current shot noise, the generated noise is due to the fluctuations in the number of electrons tunnelling across the Schottky contacts. The total number of charges, n , tunnelling (in any direction) for a two-junction system is given by:

$$n = 2 \int_{-\infty}^{\infty} \frac{E}{\sqrt{E^2 - \Delta^2}} [p_1 + p_2 + p_3 + p_4] dE, \quad (2.73)$$

where p_{1-4} are the terms defined on Page 27; the factor of two comes from the fact that charges can tunnel through two junctions. This can be converted to a total noise current, I_N , by dividing by the electron charge and the tunnelling resistance to give:

$$I_N = \frac{2}{eR_N} \int_{-\infty}^{\infty} \frac{E}{\sqrt{E^2 - \Delta^2}} [p_1 + p_2 + p_3 + p_4] dE. \quad (2.74)$$

Schottky (1918) provides the general formula for the current shot noise due to the flow of current to be:

$$\langle \delta I \rangle = \sqrt{2eI}. \quad (2.75)$$

Substituting the noise current from Equation 2.74 gives the final equation for the current shot noise, due to current flow, to be:

$$\langle \delta I^2 \rangle = \frac{4}{R_N} \int_{-\infty}^{\infty} \frac{E}{\sqrt{E^2 - \Delta^2}} [p_1 + p_2 + p_3 + p_4] dE, \quad (2.76)$$

or more completely:

$$\langle \delta I^2 \rangle = \frac{4}{R_N} \int_{-\infty}^{\infty} \frac{E}{\sqrt{E^2 - \Delta^2}} \left[\frac{1}{e^{\frac{E}{k_B T_S}} + 1} + \frac{1}{e^{\frac{-E}{k_B T_S}} + 1} + \frac{1}{e^{\frac{(E+eV/2)}{k_B T_e}} + 1} \right. \\ \left. + \frac{1}{e^{\frac{-(E-eV/2)}{k_B T_e}} + 1} - 2 \frac{1}{e^{\frac{E}{k_B T_S}} + 1} \frac{1}{e^{\frac{(E+eV/2)}{k_B T_e}} + 1} \right. \\ \left. - 2 \frac{1}{e^{\frac{-E}{k_B T_S}} + 1} \frac{1}{e^{\frac{-(E-eV/2)}{k_B T_e}} + 1} \right] dE. \quad (2.77)$$

The noise due to the flow of heat, either into or from the semiconducting absorber, is derived similarly. As was the case when deriving Equation 2.45 for the tunnelling power, the power (or heat-flow) noise is essentially the current shot noise multiplied by the energy of the charges tunnelling.

As previously covered on Page 32 of Section 2.4, each of the tunnelling routes (shown on Page 24) contributes a different amount of energy (per charge tunnelling) to the semiconductor. To recap, the energy change in the semiconductor due to each of the four routes is:

- Route 1 causes an energy change of $E + eV/2$,
- Route 2 causes an energy change of $-(E - eV/2)$,
- Route 3 causes an energy change of $-(E + eV/2)$,
- Route 4 causes an energy change of $E - eV/2$.

As was the case when calculating the current shot noise, it is only the magnitude of the fluctuations in the tunnelling power that are of interest when calculating the noise. This means that to find the power (heat-flow) noise, P_N , Equation 2.32 can be rewritten as:

$$P_N = \frac{2}{e^2 R_N} \int_{-\infty}^{\infty} \frac{E}{\sqrt{E^2 - \Delta^2}} \left[E(p_1 + p_2 + p_3 + p_4) \right. \\ \left. + \frac{eV}{2}(p_1 - p_2 + p_3 - p_4) \right] dE. \quad (2.78)$$

As explained by [Golubev and Kuzmin \(2001\)](#), the heat-flow noise, $\langle \delta P \rangle$, is given by:

$$\langle \delta P \rangle = \sqrt{2EP_N}. \quad (2.79)$$

This is the same as Equation 2.75 for the current shot noise but the electron charge (e) is replaced by the energy (E) which is fluctuating. Combining these two

equations gives the heat-flow noise:

$$\langle \delta P^2 \rangle = \frac{4}{e^2 R_N} \int_{-\infty}^{\infty} \frac{E}{\sqrt{E^2 - \Delta^2}} \left[E^2 (p_1 + p_2 + p_3 + p_4) + \left(\frac{eV}{2} \right)^2 (p_1 - p_2 + p_3 - p_4) \right] dE. \quad (2.80)$$

Substituting for p_{1-4} gives the complete result:

$$\begin{aligned} \langle \delta P^2 \rangle = & \frac{4}{e^2 R_N} \int_{-\infty}^{\infty} \frac{E}{\sqrt{E^2 - \Delta^2}} \left[E^2 \left(\frac{1}{e^{\frac{E}{k_B T_S}} + 1} + \frac{1}{e^{\frac{-E}{k_B T_S}} + 1} + \frac{1}{e^{\frac{(E+eV/2)}{k_B T_e}} + 1} \right. \right. \\ & + \frac{1}{e^{\frac{-(E-eV/2)}{k_B T_e}} + 1} + 2 \frac{1}{e^{\frac{E}{k_B T_S}} + 1} \frac{1}{e^{\frac{(E+eV/2)}{k_B T_e}} + 1} \\ & \left. \left. + 2 \frac{1}{e^{\frac{-E}{k_B T_S}} + 1} \frac{1}{e^{\frac{-(E-eV/2)}{k_B T_e}} + 1} \right) \right. \\ & + \left(\frac{eV}{2} \right)^2 \left(\frac{1}{e^{\frac{E}{k_B T_S}} + 1} - \frac{1}{e^{\frac{-E}{k_B T_S}} + 1} + \frac{1}{e^{\frac{(E+eV/2)}{k_B T_e}} + 1} \right. \\ & - \frac{1}{e^{\frac{-(E-eV/2)}{k_B T_e}} + 1} + 2 \frac{1}{e^{\frac{E}{k_B T_S}} + 1} \frac{1}{e^{\frac{(E+eV/2)}{k_B T_e}} + 1} \\ & \left. \left. - 2 \frac{1}{e^{\frac{-E}{k_B T_S}} + 1} \frac{1}{e^{\frac{-(E-eV/2)}{k_B T_e}} + 1} \right) \right] dE. \quad (2.81) \end{aligned}$$

When combining the noise sources, it is important to note that the current shot noise and the heat-flow noise are correlated, since the tunnelling power depends heavily on the current flowing through the junctions. As such, the total noise resulting from these two sources is not simply given by adding them in quadrature; instead a third term, the cross-correlator, needs to be added. For two correlated noise sources (e_1 and e_2), the total noise, e_T can be found by:

$$e_T^2 = e_1^2 + e_2^2 + 2Ce_1e_2, \quad (2.82)$$

where the dimensionless constant C is the *correlation coefficient* which varies between -1 (if the two sources are anti-correlated) and $+1$ (if the two sources are perfectly correlated). This means the correlator (the final term in Equation 2.82) of the current and heat-flow noise sources, $\langle \delta P \delta I \rangle$, is given by:

$$\langle \delta P \delta I \rangle = 2C \langle \delta P \rangle \langle \delta I \rangle. \quad (2.83)$$

The current shot noise and the heat-flow noise have been shown by [Golwala et al. \(1997\)](#) to be anti-correlated so $C = -1$. Using this result and Equations [2.75](#) and [2.79](#) gives the correlator of the current shot and heat-flow noise to be:

$$\langle \delta P \delta I \rangle = -4\sqrt{eEI_N P_N}. \quad (2.84)$$

[Golubev and Kuzmin \(2001\)](#) show that, in the case $T_e = T_S$, the above can be simplified to:

$$\langle \delta P \delta I \rangle = -4eP. \quad (2.85)$$

Substituting Equation [2.45](#) for tunnelling power gives the result:

$$\begin{aligned} \langle \delta P \delta I \rangle = -4eIV - \frac{8}{eR_N} \int_{-\infty}^{\infty} \frac{E^2}{\sqrt{E^2 - \Delta^2}} & \left[\frac{1}{e^{\frac{E}{k_B T}} + 1} - \frac{1}{e^{\frac{-E}{k_B T}} + 1} \right. \\ & \left. - \frac{1}{e^{\frac{(E+eV/2)}{k_B T}} + 1} + \frac{1}{e^{\frac{-(E-eV/2)}{k_B T}} + 1} \right] dE. \end{aligned} \quad (2.86)$$

The quantised flow of heat between the electron and phonon systems causes thermal fluctuations which result in further electrical noise. This noise is given by the well known expression:

$$\langle \delta P \rangle_{e-ph} = \sqrt{4k_B T^2 G_{e,ph}}. \quad (2.87)$$

$G_{e,ph}$ is the non-direction-specific thermal conductance between the two systems and is given by:

$$G_{e,ph} = |G_e| + |G_{ph}|, \quad (2.88)$$

This is true since noise results from heat flow to or from either system and is always positive. G_e and G_{ph} are given by:

$$G_e = \frac{dP_{e-ph}}{dT_e}, \quad (2.89)$$

$$G_{ph} = \frac{dP_{e-ph}}{dT_{ph}}, \quad (2.90)$$

where P_{e-ph} is the heating or cooling power of the electron-phonon link, given by Equation [2.56](#). Substituting these into the above gives:

$$G_{e,ph} = \left| \frac{d}{dT_e} \Sigma \Omega (T_e^\beta - T_{ph}^\beta) \right| + \left| \frac{d}{dT_{ph}} \Sigma \Omega (T_e^\beta - T_{ph}^\beta) \right|, \quad (2.91)$$

$$G_{e,ph} = \beta \Sigma \Omega (T_e^{\beta-1} + T_{ph}^{\beta-1}). \quad (2.92)$$

Substituting this into Equation 2.87 gives the final form of the heat flow noise:

$$\langle \delta P \rangle_{\text{e-ph}} = \sqrt{2\beta k_B \Sigma \Omega (T_e^{\beta+1} + T_{\text{ph}}^{\beta+1})}. \quad (2.93)$$

The factor of $\sqrt{2}$ difference between the above and Equation 2.87 can be explained by setting $T_e = T_{\text{ph}} = T$, in which case the two equations are the same.

The final source of noise to be considered is the system used to readout the detector. Inevitably, this will involve some form of amplifier. Any amplifier will add a certain level of noise to a signal; this is usually the result of Johnson noise from the resistors used to set the amplifier's gain but can also be the result of shot noise due to the currents flowing in the amplifier. While intelligent design of an amplifier system (such as that described by [Horowitz and Hill, 1989](#)) can result in amplifiers with very low noise levels (often of the order of $\text{nV}\text{Hz}^{-1/2}$), it is not possible to completely remove this noise source and as such, it should be included when considering the fundamental limits of a system.

2.8 THE NOISE-EQUIVALENT POWER

The electrical noise is a useful quantity in that it corresponds to what one would measure when characterising a detector; however, the eventual goal of any detector is not to itself be an object of study but instead be used to study other objects. As such the **Noise-Equivalent Power (NEP)** is a more useful figure of merit, since it gives the minimum power that can be detected with a signal-to-noise ratio of one and an integration time of half a second.⁵ This allows someone using the detector to calculate if it is appropriate for an application given restrictions such as: signal power, measurement time or acceptable signal-to-noise ratio.

To derive the noise-equivalent power, it is perhaps most logical to start by specifying exactly what is meant by the **Signal-to-Noise Ratio (SNR)**. The signal-to-noise ratio is (as its name implies) simply the ratio of the amplitude of a signal to the amplitude of any noise on the signal. As such, the signal-to-noise ratio, *SNR*,

⁵The factor of a half comes from the formal definition of NEP being the power needed to achieve a Signal-to-Noise Ratio (SNR) of one with a 1 Hz bandwidth. Because of the Nyquist-Shannon sampling theorem ([Nyquist, 1928a](#); [Shannon, 1949](#)), the bandwidth, $\Delta\nu$, is defined as $1/(2T)$, where T is the integration time.

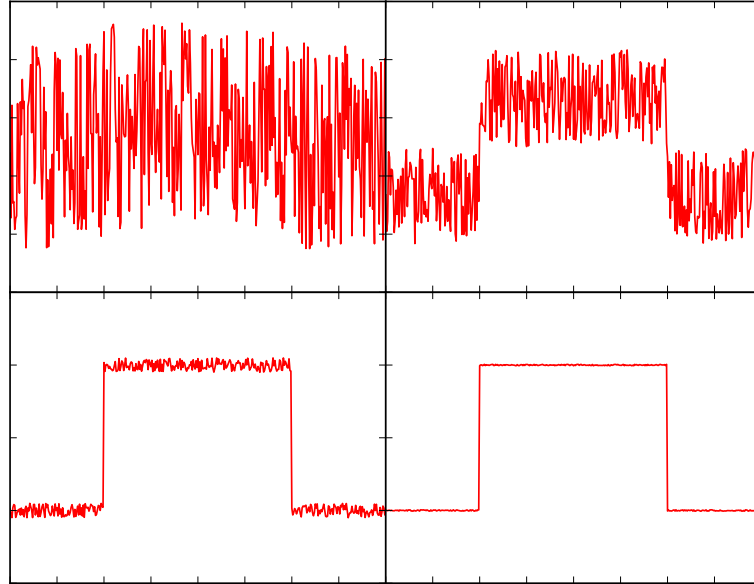


Figure 2.9: The effect of increasing the signal-to-noise ratio of a measurement. Left to right, top to bottom: $SNR = 0.1, 1, 10, 100$.

can be expressed as:

$$SNR = \frac{V_{\text{signal}}}{V_{\text{noise}}}, \quad (2.94)$$

where V_{signal} and V_{noise} are the **Root Mean Square (RMS)** voltages of the signal and the noise respectively.

The physical issues associated with a low signal-to-noise ratio are illustrated in Figure 2.9. It is clear that, with $SNR = 0.1$ (upper-left in Figure 2.9), the signal can barely be seen and neither the width nor the amplitude can be ascertained. When the signal-to-noise ratio is increased to unity (upper right in Figure 2.9), the presence of a signal is clear but there are still significant uncertainties in both the amplitude and the width of the signal. When the signal-to-noise ratio is increased to 10, these uncertainties are greatly reduced and the pulse can be well characterised. Finally, if the ratio is increased further to 100, the fluctuations are reduced to such a level that, except under close examination, they are not noticeable.

The units of noise-equivalent power are $\text{WHz}^{-1/2}$. In order to calculate the noise-equivalent power in the presence of noise sources, such as Johnson noise, which are most commonly measured or calculated as a voltage, these quantities need to be converted into units of Watts. This is done by dividing the noise voltage (units: $\text{VHz}^{-1/2}$) by the voltage responsivity (Equation 2.71, units: VW^{-1}). Should the noise be measured or calculated in units of amperes (as is the case for Equations 2.74 and 2.85), then the noise needs to be divided by the differential of the I - V ($\partial I/\partial V$, units AV^{-1}), as well as the responsivity.⁶

The NEP is given by the total noise, e_{tot} divided by the responsivity (i.e. the incident power that would produce a signal equal in amplitude to the noise). This means it can be written as:

$$\text{NEP} = \frac{e_{\text{tot}}}{S_V}. \quad (2.95)$$

The simplest example of calculating the noise-equivalent power is to take the case where the measured noise is dominated by a single source. In the real world, this is most commonly the case when the amplifier noise in the readout is not low enough. If we take the case where the amplifier noise, $\langle \delta V \rangle_{\text{amp}}$, is very large, i.e.:

$$\langle \delta V \rangle_{\text{amp}} = 100 \text{ nVHz}^{-1/2}. \quad (2.96)$$

Provided that this is significantly larger than any other noise source which contaminates the measurement then:

$$e_{\text{tot}} \approx \langle \delta V \rangle_{\text{amp}}. \quad (2.97)$$

If, in this example, the voltage responsivity was 10^6 VW^{-1} , then the noise-equivalent power would be:

$$\text{NEP} = \frac{\langle \delta V \rangle_{\text{amp}}}{S_V}, \quad (2.98)$$

$$\text{NEP} = \frac{100 \times 10^{-9}}{10^6}, \quad (2.99)$$

$$\text{NEP} = 1 \times 10^{-13} \text{ WHz}^{-1/2}. \quad (2.100)$$

⁶This paragraph assumes the detector is being current biased. Should the biasing signal be a voltage, then sources measured in amperes do not need to be divided by the differential, whereas those measured in volts need to be divided by $\partial V/\partial I$ and the current responsivity is used.

In order to arrive at a term for the total noise-equivalent power of a detector system which includes a non-perfect amplifier, the various noise terms need to be converted into noise-equivalent powers and then added.

Taking the noise terms individually, it is possible to see the specific conversions needed to change them to units of NEP ($\text{WHz}^{-\frac{1}{2}}$).

For a voltage amplifier (as was always used for the experiments in this thesis), the noise is in units of $\text{VHz}^{-\frac{1}{2}}$ so division by the responsivity (which converts between volts and watts) is the only required step to convert the amplifier noise into a noise-equivalent power.

$$NEP_{\text{amp}} = \frac{\langle \delta V \rangle_{\text{amp}}}{S_V}. \quad (2.101)$$

A brief inspection of the units of the heat-flow noise ($\langle \delta P \rangle$) shows that this term, as expected, is already a noise-equivalent power:

$$\langle \delta P \rangle = \sqrt{2EP_N}, \quad (\text{2.79 revisited})$$

$$= \sqrt{JW}, \quad (2.102)$$

$$= \sqrt{WsW}, \quad (2.103)$$

$$= \sqrt{W^2s}, \quad (2.104)$$

$$= \sqrt{W^2\text{Hz}^{-1}}, \quad (2.105)$$

$$\therefore \langle \delta P \rangle = \text{WHz}^{-\frac{1}{2}}, \quad (2.106)$$

$$\therefore NEP_P = \langle \delta P \rangle. \quad (2.107)$$

A similar treatment reveals that the electron-phonon heat-flow noise ($\langle \delta P \rangle_{e-ph}$) is also already in units of noise-equivalent power:

$$\langle \delta P \rangle_{e-ph} = \sqrt{2\beta k_B \Sigma \Omega (T_e^{\beta+1} + T_{ph}^{\beta+1})}, \quad (\text{2.93 revisited})$$

$$= \sqrt{JK^{-1}WK^{-\beta}m^{-3}m^3K^{\beta+1}}, \quad (2.108)$$

$$= \sqrt{JW}, \quad (2.109)$$

which is the same as Equation 2.102. Therefore:

$$\langle \delta P \rangle_{e-ph} = \text{WHz}^{-\frac{1}{2}}, \quad (2.110)$$

$$\therefore NEP_{e-ph} = \langle \delta P \rangle_{e-ph}. \quad (2.111)$$

By dimensional analysis, the units of the tunnelling current noise are shown to be $\text{A Hz}^{-1/2}$:

$$\langle \delta I \rangle = \sqrt{2eI}, \quad (\text{2.75 revisited}) \quad (2.112)$$

$$= \sqrt{CA}, \quad (2.112)$$

$$= \sqrt{AsA}, \quad (2.113)$$

$$\therefore = \text{A Hz}^{-1/2}. \quad (2.114)$$

This means that the tunnelling shot noise-equivalent power, NEP_S , can be found by dividing the current shot noise by both the differential of the current by the voltage and voltage responsivity, i.e.:

$$NEP_S = \frac{\sqrt{2eI}}{\frac{\partial I}{\partial V} S_V}. \quad (2.115)$$

The final noise term to inspect is the correlator of the noise due to the tunnelling power and current ($\langle \delta P \delta I \rangle$). This is found to have units of AW Hz^{-1} :

$$\langle \delta P \delta I \rangle = -4eP, \quad (\text{2.85 revisited}) \quad (2.116)$$

$$= CW, \quad (2.116)$$

$$= AsW, \quad (2.117)$$

$$\therefore \langle \delta P \delta I \rangle = \text{AW Hz}^{-1}, \quad (2.118)$$

which makes sense considering that, dimensionally, this is just the multiplication of $\langle \delta P \rangle$ and $\langle \delta I \rangle$. This means that the noise-equivalent power due to this correlation of terms, NEP_{PI} , is given by:

$$NEP_{PI} = 2C \sqrt{\frac{eP}{\frac{\partial I}{\partial V} S_V}}, \quad (2.119)$$

$$NEP_{PI} = -2 \sqrt{\frac{eP}{\frac{\partial I}{\partial V} S_V}} \quad (2.120)$$

Having converted the various noise sources into units of NEP , it is possible to arrive at a final equation for the total noise-equivalent power of a cold-electron bolometer, NEP_{CEB} . This is found by simply adding the uncorrelated noise terms in quadrature, with the addition of the cross-correlator of the power and current shot

noise. This gives the final result for a current-biased device (i.e. a system using a voltage readout) to be:

$$\begin{aligned} NEP_{\text{CEB}}^2 = & \frac{\langle \delta V^2 \rangle_{\text{amp}}}{S_V^2} + 2\beta k_B \Sigma \Omega \left(T_e^{\beta+1} + T_{\text{ph}}^{\beta+1} \right) \\ & + \langle \delta P^2 \rangle - 2 \frac{\langle \delta P \delta I \rangle}{\frac{\partial I}{\partial V} S_V} + \frac{\langle \delta I^2 \rangle}{\left(\frac{\partial I}{\partial V} S_V \right)^2}, \end{aligned} \quad (2.121)$$

It is not advisable to write this equation more thoroughly (as was done for Equations 2.77 and 2.81) as this would be several pages long.

2.8.1 PHOTON NOISE

In addition to the internal noise sources of the detector and those associated with the readout circuitry, there is another (often limiting) source which it is important to consider. This is the noise associated with the absorption of photons at the detectors. There are two main terms which combine here and these are the photon shot noise and the photon wave noise. The origins of these two terms come from the particle and wave models of light, respectively. At high frequencies, where light is often thought of as distinct particles, it is clear that there should be no correlation between the arrival of one photon and the arrival of the next, but instead, the arrival of photons is governed by Poisson statistics. The noise-equivalent power associated with this model of light is given by the well-known equation:

$$NEP_{\text{ph}_{\text{shot}}}^2 = 2h\nu P_{\text{opt}}, \quad (2.122)$$

where ν is the frequency of the light and P_{opt} is the optical power absorbed by the detector. However, at lower frequencies, such a model of light is not valid and instead, one must think of light as a wave. Clearly, in such a scenario, the arrival of one maximum at the detector heavily determines the arrival of the next—they are highly correlated. Simplistically, what was previously thought of a single photon is now represented by a wave *packet*. These wave packets interfere with one another, causing fluctuations in the power arriving at the detector. This leads to the photon wave noise-equivalent power, which is given by the, also well known, equation:

$$NEP_{\text{ph}_{\text{wave}}}^2 = \frac{P_{\text{opt}}^2}{\Delta\nu}, \quad (2.123)$$

where $\Delta\nu$ is the optical bandwidth. For black-body emission, two regimes exist; these are the Wien region (sometimes called the Wien tail, where $h\nu \gg k_B T$) and the Rayleigh-Jeans region (where $h\nu \ll k_B T$). In the first of these, the photon model is more appropriate and the first term (Equation 2.122) dominates. However, in the Rayleigh-Jeans region, a wave-type model of light is more appropriate and, as such, the second term (Equation 2.123) dominates. However, the most complete treatment may be found by considering both of these terms together and, as such, the total photon noise-equivalent power is given by:

$$NEP_{\text{ph}}^2 = 2h\nu P_{\text{opt}} + \frac{P_{\text{opt}}^2}{\Delta\nu}. \quad (2.124)$$

Chapter Three

The Properties of Doped and Strained Silicon

'Without electrons, there is no Google.'

—JEFF GOODELL

3.1 INTRODUCTION

The work detailed in this thesis explains the development (and hoped improvement) of the already existing cold-electron bolometer by replacing the normal-metal absorbing element used in previous devices (Kuzmin, 2004; Otto et al., 2013) with highly-doped strained silicon. As such, it is useful to address the underlying principle of semiconductors and how their characteristics can be altered by either doping the material or by straining the material's atomic lattice.

3.2 INTRINSIC SEMICONDUCTORS

As is implied by their name, semiconductors are materials which are partially conductive—that is to say, they do not conduct in the same way as a metal but nor do they prevent all current flow, as insulators do. Semiconductors have a crystal lattice of atoms; the formation of this lattice can result in the creation of *free* electrons, these free electrons cease to be tightly bound to their parent nuclei

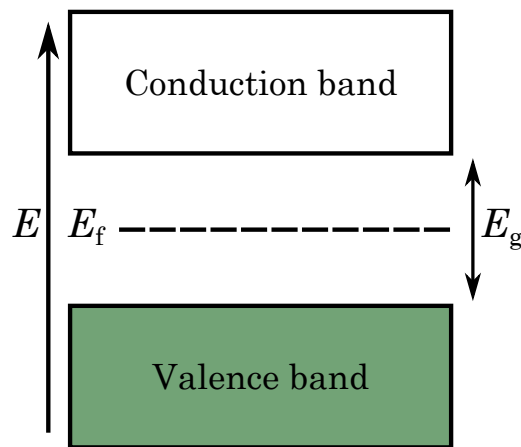


Figure 3.1: Band structure of an intrinsic semiconductor. With no additional energy for the electrons to absorb, all the electrons are bound to their nucleus and exist in the valence band. In order to flow as a current, they must gain enough energy to break their binding to the nucleus. For the most weakly bound electrons, this energy corresponds to the band gap energy, E_g . E_f is the Fermi level, for an intrinsic (undoped) semiconductor, this is located halfway through the energy gap.

(they are referred to as *delocalised*) and can flow (as current) through the crystal lattice of the material. In order for a *delocalised* electron to be able to flow as a current through the material, it must first be removed from the atom to which it belongs by gaining a certain amount of energy (depending upon how tightly bound it is to the atom). This energy can be in the form of thermal energy from heating the crystal (as such semiconductors, unlike metals, have an electrical conductivity which increases with temperature) or by providing an external electrical bias across the material.

The requirement for an energy threshold to be gained before an electron can flow as current can be thought of in terms of a energy band diagram, as shown in Figure 3.1. Without the input of any additional energy, all the electrons are bound to their respective nuclei and are unable to flow as current through the material (the material is an insulator). These electrons have low energies and exist in the valence band shown in Figure 3.1. The top of the valence band corresponds to the energy level of the most weakly bound electrons (that is the energy level of the outer most electron shell). However, this does not mean that any infinitely small increase

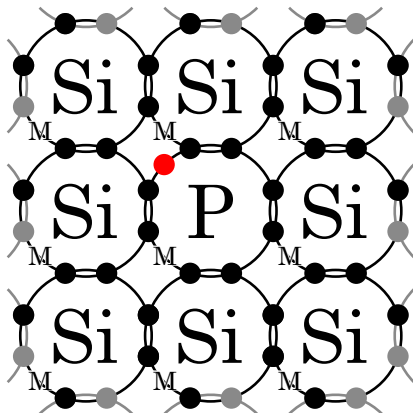


Figure 3.2: Crystal lattice of silicon with an n-type dopant (phosphorus in this case) grown into the lattice. For n-type doping, the dopant has more electrons in its outer shell than are required to form covalent bonds with the surrounding atoms in the lattice, this results in an additional electron (highlighted in red above) which is not bound to the crystal lattice and acts as a *free* electron, increasing conductivity.

in the energy of these electrons will liberate them from their nuclei, instead they must gain enough energy to enter the conduction band. This means that, for the electrons in the outermost electron shells to be able to flow as current, they must gain enough energy to *jump* through the band gap; this is the band gap energy and has a value of E_g .¹

3.3 DOPED SEMICONDUCTORS

The intrinsic semiconductor, explained above and whose energy level diagram is shown in Figure 3.1, is the basis for all forms of semiconductors and can be thought of as being characterised (at least in the sense of its energy distribution) by the size of its energy gap. However, one key advantage of semiconductors is that their conductivity can be controlled by adding impurities to the crystal lattice, this process is called *doping*.

In order for the doping to alter the electrical characteristics of a semiconductor, the impurity added must bond to the crystal lattice in such a way that an unbound

¹Throughout this work E_g will be used to refer to the band gap energy of a semiconductor to avoid confusion with Δ , which is used to denote half of the energy gap in a superconductor.

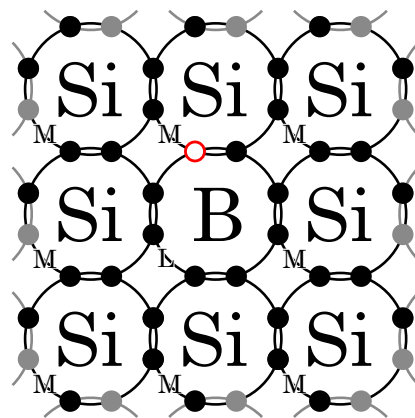


Figure 3.3: Crystal lattice of silicon with a p-type dopant (boron) grown into the lattice. For p-type doping, the dopant has fewer electrons in its outer shell than the neighboring atoms. This means the atom does not form covalent bonds with all of the neighboring atoms and a hole (highlighted red) is created.

electron is added to the crystal or that a vacant electron state is created. Figure 3.2 illustrates the case where an unbound electron is added (referred to as *n-type* doping, since a negative charge is added to the crystal). In this case, the dopant impurity (phosphorus in Figure 3.2) has five electrons in its outer shell; four of these form covalent bonds with neighboring silicon atoms, however, one electron does not form a covalent bond. The impurity is called a *donor* since, when ionised by sufficient energy, the atom *donates* an electron to the conduction band, this has the net effect of increasing the conductivity of the semiconductor.

The opposite of n-type doping is *p-type* doping (the ‘p’ denotes positive charge), where the dopant used has fewer electrons in its outer electron shell than the rest of the atoms in the lattice. This means that there are incomplete covalent bonds (or *holes*) in the crystal structure, which can capture free electrons. This is illustrated in Figure 3.3, where boron has been grown into a lattice of silicon. Boron is a group XIII element and has three electrons in its outer shell, compared to silicon which has four (group XIV); this *missing* electron (shown in Figure 3.3 as an empty red circle) means that a covalent bond is unable to form between the dopant and one of the neighboring silicon atoms. The dopant in this case is referred to as an *acceptor*, since an electron can become bound or *accepted* into the vacant state. Like n-type

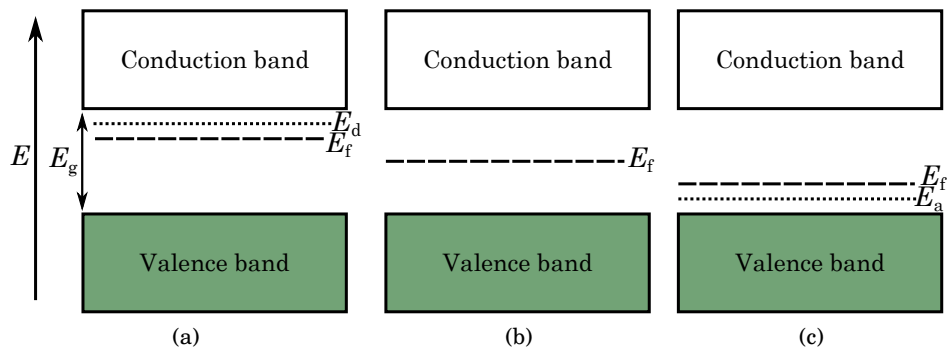


Figure 3.4: Energy level diagrams for doped semiconductor. (a) N-type doped semiconductor—since the dopant adds an additional electron to the lattice, the Fermi energy (E_f) is increased; E_d is the ionisation energy required to unbind the additional electron of the donor dopant from its parent nucleus. (b) Intrinsic semiconductor—since there are no dopants present in the lattice, there are no ionisation levels and the Fermi energy is in the middle of the band gap (as was seen in Figure 3.1). (c) P-type doped semiconductor—the dopant reduces the number of electrons (compared to an intrinsic semiconductor) and thus the Fermi energy is reduced; E_a is the ionisation energy required to unbind the hole state from the acceptor dopant.

doping, p-type doping also has the effect of increasing the conductivity since, when ionised, the hole can become mobile and move through the lattice meaning that electrons switch places with the hole and thus also move through the lattice.

Since doping alters the distribution of electrons in a semiconductor, the energy level diagrams for doped semiconductors differ from that of an intrinsic semiconductor (shown in Figure 3.1). Figure 3.4 shows the energy level diagrams for n- and p-type semiconductors (Figures 3.4a and 3.4c), along with that of an intrinsic semiconductor (Figure 3.4b), for comparison. For doped semiconductors, the energy level diagram includes an additional level corresponding to the ionisation energy of either the additional electron from the donor atom (n-type), E_d , or hole state from the acceptor atom (p-type), E_a . Since n-type doping creates a positively charged region (due to the addition of one or more electrons), the Fermi energy in an n-type semiconductor is increased (moved towards the conduction band) compared to the intrinsic case (Figure 3.4b). In the case of p-type doping, the dopant creates a

positively charged region around it, where there is a shortage of electrons; this has the effect of decreasing the Fermi energy in comparison to the intrinsic case.

One important physical feature of doping worth mentioning is that, since the dopant is added to the lattice during its growth, it does not displace an atom but instead simply forms as part of the lattice.

By increasing the number of dopants present within the lattice, the degree by which the conductivity of the lattice is altered can be carefully controlled. [Pearson and Bardeen \(1949\)](#) showed that introducing phosphorus dopants to a silicon lattice (n-type doping) at a concentration of $4.7 \times 10^{17} \text{ cm}^{-3}$ resulted in decreasing the materials resistivity to $0.3 \Omega\text{cm}$ at room temperature, compared to $\approx 10^6 \Omega\text{cm}$ in the absence of any dopant atoms. Furthermore, increasing the doping concentration further to $4.7 \times 10^{20} \text{ cm}^{-3}$ (equivalent to approximately one per cent phosphorus) resulted in a resistivity of $7 \times 10^{-4} \Omega\text{cm}$.

The terminology of doped semiconductors typically distinguishes four vague levels of doping: *lightly-doped* semiconductors have doping levels $\lesssim 10^{14} \text{ cm}^{-3}$; this can be written as n^- - or p^- -type doping; *moderately-doped* semiconductors have dopant concentrations in the range $10^{14}\text{--}10^{16} \text{ cm}^{-3}$; *heavily-doped* is typically used in relation to doping levels in the approximate range $10^{16}\text{--}10^{18} \text{ cm}^{-3}$ and this level of doping is often expressed as n^+ - or p^+ -type doping; finally, when the doping level is such that the electrical behaviour of the material can be thought of as being analogous to a metal, it is referred to as being *degenerate*, this typically involves doping levels $> 10^{18} \text{ cm}^{-3}$ and is written as n^{++} - or p^{++} -type doping. While—as is true in various areas of physics—there are no exact guidelines or boundaries as to when a material ceases to be classed as lightly-doped and becomes moderately-doped, the term degenerate should be reserved in use for semiconductors which are doped to a sufficient level that they behave (electrically) like a metal.

3.4 CARRIER MOBILITY

The *mobility* of an electron or hole in a semiconducting crystal is defined as the speed at which the charge carrier *drifts* through the lattice per unit electric field. As such, the mobility, μ , is defined by:

$$\mu = \frac{|v|}{E}, \quad (3.1)$$

where $|v|$ is the modulus of the carrier's drift velocity and E is the electric field to which the carrier is subjected. The modulus of the drift velocity is used since mobility of electrons and holes (μ_e and μ_h respectively) are both defined to be positive, despite the fact that for an applied field of given polarity, the two carrier types will move or drift in opposite directions.

It is easy to understand the relationship between the carrier mobility and the doping concentration by considering the movement of the carriers through the lattice. When an electric field is applied, the carrier will be accelerated by the field; if the carrier were moving through free space, then, due to the acceleration, its velocity would continue to increase approaching the speed of light. However, in the crystal structure, the carrier frequently collides with other particles (such as defects or impurities in the lattice), this causes the velocity of the carrier (on scales larger than the mean free path between collisions) to be limited to some equilibrium between the accelerating force from the electric field and rate of collisions experienced. This velocity is the drift velocity referred to in Equation 3.1. After activation, each dopant atom added to the lattice becomes ionised; as the carriers move through the lattice, they collide with these ions and this decreases their drift velocity (and thus their mobility). Clearly, increasing the doping concentration (and thus the number of ions) increases the frequency of collisions experienced by the carriers and accordingly their drift velocity and thus their mobility is decreased.

Data showing the overall relation between the mobility and the doping concentration, for both electrons and holes, was compiled by [Caughey and Thomas \(1967\)](#)² who, in turn, drew heavily on the data of [Irvin \(1962\)](#). [Caughey and Thomas](#) used simple curve fitting techniques to fit the collected data. They showed that, to a reasonable level, the data for both the mobility of electrons and holes could be fitted by:

$$\mu = \frac{\mu_{\max} - \mu_{\min}}{1 + \left(\frac{N}{N_{\text{ref}}}\right)^{\alpha}} + \mu_{\min}, \quad (3.2)$$

where N is the number of dopant atoms per cubic centimetre, μ_{\max} and μ_{\min} are the maximum and minimum measured mobilities, N_{ref} is the total number of atoms per cubic centimetre, and α is a curve-fitting constant. All of these terms are dependent not only on the material but also on the carrier being studied. The

²There is a mistake in [Caughey and Thomas](#)'s manuscript, the captions of Figures 1 and 2 should be switched.

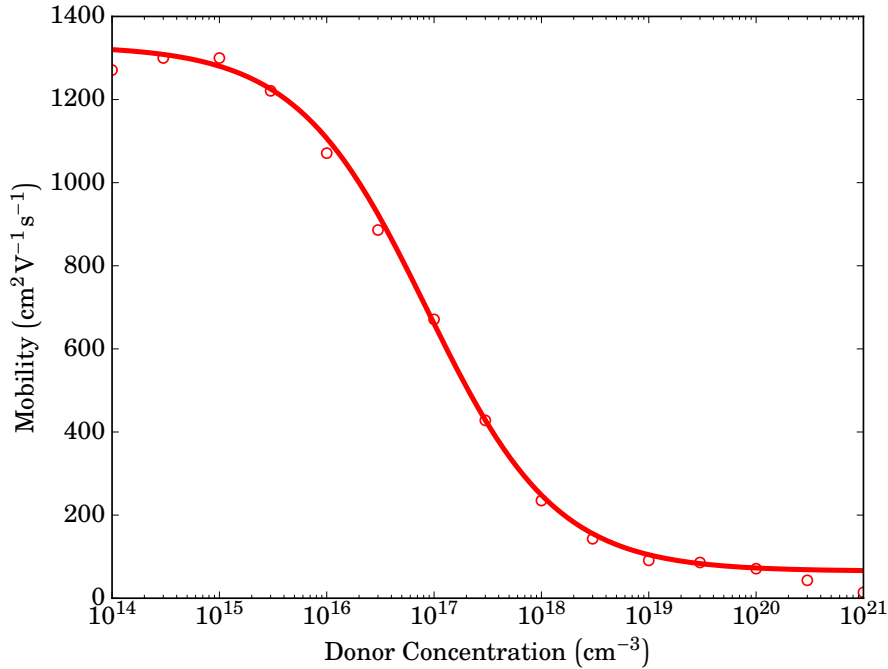


Figure 3.5: Decrease in electron mobility with increasing donor concentration. Circles—data, solid line—model fit. Reproduced, with permission, from [Caughey and Thomas \(1967\)](#). ©1967 IEEE.

fitting parameters found by [Caughey and Thomas \(1967\)](#) are given in Table 3.1 and their graph showing the fit to data collected for electron mobilities is reproduced in Figure 3.5

Table 3.1: Carrier mobility curve-fitting parameters from [Caughey and Thomas \(1967\)](#).

Carrier	μ_{\max} ($\text{cm}^2\text{V}^{-1}\text{s}^{-1}$)	μ_{\min} ($\text{cm}^2\text{V}^{-1}\text{s}^{-1}$)	α	N_{ref} (cm^{-3})
Holes	495	47.7	0.76	6.3×10^{16}
Electrons	1330	65	0.72	8.5×10^{16}

While Equation 3.2, along with the parameters found by [Caughey and Thomas \(1967\)](#), do not produce a complete model of the mobility based on physical processes, they do act as a relatively accurate means of predicting the carrier mobility for a

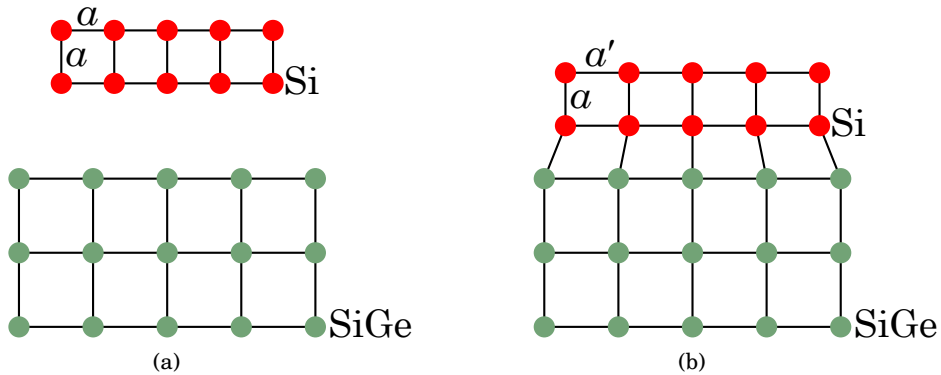


Figure 3.6: Introducing strain into a silicon lattice. (a) Silicon and silicon germanium as isolated lattices; the two materials have independent lattice spacings and, in both cases, the lattice spacing in both directions are the same, which is equal to a for the silicon lattice (a simple two-dimensional model is shown). (b) The effect of growing silicon atop a layer of silicon germanium; the lattice becomes stretched or strained in the plane of the silicon germanium layer, changing the lattice spacing in this plane to a' while the lattice spacing in the vertical direction is unchanged.

particular value of doping concentration.

3.5 STRAINED SEMICONDUCTORS

Straining silicon is the process of forcing the silicon atoms in the lattice to be slightly further apart than they would be naturally (the interatomic spacing is increased). This is achieved by growing silicon atop a buffer layer consisting of a material which has a larger atomic spacing than that of the silicon. Silicon germanium is commonly used as the buffer or straining layer, since it readily forms bonds to the silicon lattice, also the lattice spacing of this layer—and thus the level of strain in the silicon—can be controlled by adjusting the ratio of germanium in the silicon germanium. The concept behind the introduction of strain to a silicon lattice is shown in Figure 3.6.

The most common reason to introduce strain into a silicon lattice is to increase the carrier mobility. This occurs due to the strain forces stretching the crystal lattice, increasing the interatomic spacing and thus increasing the mean free path length between scattering events for the carriers. This is highly advantageous in the

field of semiconducting electronic components where, for example, strained silicon offers substantial increases to the switching speed of transistors, allowing for faster microprocessors. The improvement in carrier mobilities was first demonstrated by [Welser et al. \(1994\)](#), who showed that at low applied electric fields, the electron mobility in n-doped ($N \approx 2 \times 10^{15} \text{ cm}^{-3}$) silicon, strained by a SiGe layer ($\text{Si}_{0.7}\text{Ge}_{0.3}$), was increased to $\approx 1600 \text{ cm}^2\text{V}^{-1}\text{s}^{-1}$ compared to $\approx 600 \text{ cm}^2\text{V}^{-1}\text{s}^{-1}$ for a comparable unstrained system.

Another reason (particularly relevant to the field of detectors) to introduce strain into the silicon is that strained silicon has been shown by [Muhonen et al. \(2011\)](#) to offer decreased coupling between the electrons and the phonons. [Muhonen et al.](#) showed that at sub-Kelvin temperatures, the heat flow between the electrons and the phonons was reduced by a factor of between 20–50, depending on the lattice temperature. In terms of detector performance, this decrease in the electron-phonon coupling can increase a detector’s sensitivity by decreasing the heat flow noise (from Equation 2.93). Furthermore, since the electrons are more thermally isolated from the lattice phonons they can, when cooled as described in Sections 2.3 and 2.4, be cooled further below the lattice temperature compared to electrons in an unstrained material. This was shown by [Prest et al. \(2011\)](#), who used the same material described by [Muhonen et al. \(2011\)](#) as the central island of a microrefrigerator device. [Prest et al.](#) showed that, at a lattice temperature of 300 mK, a device utilising strained silicon was capable of cooling electrons to a minimum temperature of 174 mK, compared to 258 mK for a device using unstrained silicon. This increase in performance is directly applicable to the cold-electron bolometer, not only in decreasing the heat flow noise, but also by allowing the electrons in the absorber to operate at lower temperatures, reducing the majority of noise contributions detailed in Section 2.7.

Chapter Four

Detector Design & Fabrication

'It has long been an axiom of mine that the little things are infinitely the most important.'

—Sherlock Holmes, The Adventures of

Sherlock Holmes: A Case of Identity,

SIR ARTHUR CONAN DOYLE

4.1 INTRODUCTION

This chapter will detail the design of the silicon cold-electron bolometer detectors studied in this work; it will also look at the process by which these devices have been fabricated. It should, however, be stated at the outset that the designs for these detectors had been arrived at prior to the commencement of this work; as such the process by which the detector design was arrived at will not be covered here. The features of the design will, however, be examined, as will some minor modifications which were added to ensure that the detectors were both functional and relatively simple to fabricate with the facilities available in Cardiff at the time.

4.2 DETECTOR DESIGN

The designed detector was a twin-slot antenna-coupled detector. The absorber (the doped-silicon island of the silicon cold-electron bolometer, described in Chapter 2)

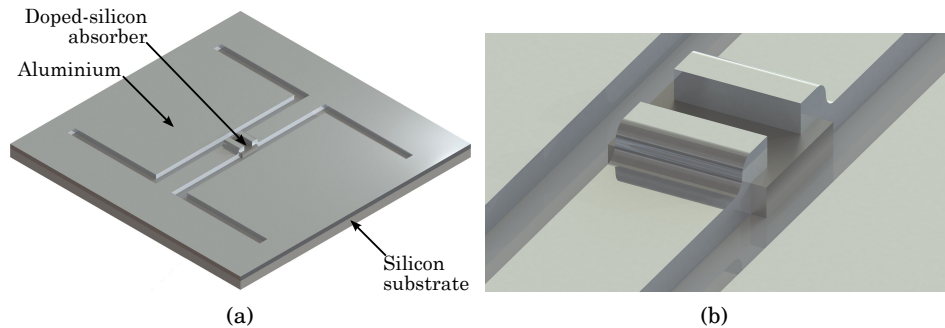


Figure 4.1: Model of silicon cold-electron bolometer chip. (a) Whole detector chip with twin-slot antenna; the strained-silicon absorber is located in middle of a coplanar waveguide which is fed by a twin-slot antenna formed in an aluminium ground plane; (b) zoomed-in view of the strained-silicon mesa which acts as the detector’s absorber. It should be noted that the height of the strained silicon mesa has been greatly exaggerated here in order to make this component visible. In reality, the silicon substrate is in fact 25,000 times thicker than the mesa.

was coupled to the antenna via Schottky contacts to the antenna’s coplanar waveguide, these Schottky contacts served as the tunnelling contacts to the doped-silicon island, as well as capacitively coupling incident radiation from the antenna via the same waveguide. Since the incident radiation typically has a high frequency (> 100 GHz), it couples directly to the absorber, whereas the bias signal is DC and, as such, must tunnel through the Schottky contacts to reach the absorber, thus producing cooling, as described in Chapter 2. A model of the final detector chip is shown in Figure 4.1.

4.2.1 ANTENNA DESIGN

A twin-slot antenna was chosen for coupling radiation to the absorber. The reasons for this included the relatively simple design, along with the fact these twin-slot antennae have a linearly-polarised response which allows for signals coupled to the absorber via the antenna to be differentiated from signals due to direct absorption in the strained-silicon mesa. In terms of a detector in an instrument, an antenna with a polarised response clearly allows for the polarisation of a source to be measured.

The key dimensions of a twin-slot antenna are shown in Figure 4.2. L is the length of the antenna’s slots and corresponds to half the wavelength that the

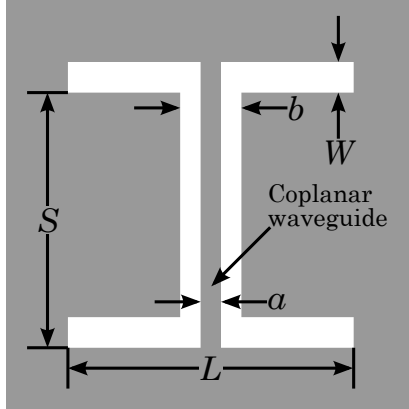


Figure 4.2: Key dimensions of a twin-slot antenna.

antenna is intended to couple to. A caveat to this is that the length corresponds to the wavelength in the medium; in the situation where radiation is coupled to the antenna via a silicon substrate (as indeed was the case in this work), where the refractive index, n , is equal to 3.42–3.48, $L = \lambda_0/2n \approx 0.28\lambda_0$ where λ_0 is the wavelength in free space. S is the separation between the two slots, this has been optimised via finite-element simulation in Ansoft’s HFSS software. W is the width of the slots and is altered to achieve the desired antenna impedance. a and b are the dimensions of the coplanar waveguide and are governed by the desired impedance for the coplanar waveguide.

Three sets of detector design were created, each set had an antenna designed for a different frequency; the selected frequencies were: 160, 225 and 360 GHz. These frequencies were selected due to their similarity to the second to fifth bands of *Planck*’s **High-Frequency Instrument (HFI)** (which are 143, 217 and 353 GHz, as explained by Lamarre et al., 2003) used to study the **Cosmic Microwave Background (CMB)**. The choice of these antenna frequencies was advantageous due to the wealth of expertise—and indeed equipment—at Cardiff for these frequencies; it also allowed for the potential to access silicon cold-electron bolometers for a possible application (studying the cosmic microwave background). The dimensions (as defined in Figure 4.2) of these three designs are given in Table 4.1.

It is clear that if one wishes to either bias or measure (or both) a bridge-type element on the coplanar waveguide, then the design described above, and illustrated

Table 4.1: Dimensions of the designed antennae.

Frequency (GHz)	L (μm)	S (μm)	W (μm)	a (μm)	b (μm)
160	536	333	30	30	58
225	356	230	20	30	58
360	226	155	15	30	58

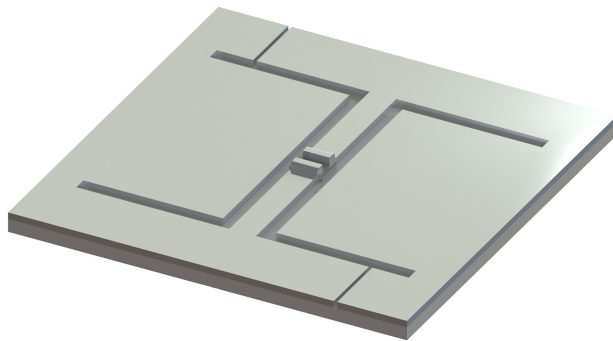


Figure 4.3: Model of silicon cold-electron bolometer chip with DC cuts in the ground plane.

in Figure 4.1, has a major flaw: the metal ground plane is contiguous around the twin-slot antenna and is connected directly to the coplanar waveguide; this means that any attempt to measure a resistive component on the coplanar waveguide would be futile, since such a component would be shorted by the ground plane. In order to address this, it was necessary to add cuts to the ground plane such as to force current to be driven through the coplanar waveguide. These were placed on diagonally opposite slots of the antenna, this design is illustrated in Figure 4.3. While it is clear that these are required for the correct operation of the device, it is fair to say that the placement of these slots was far from optimum since they altered the response of the antenna, this will be seen in greater detail in Section 8.4. With the gift of hindsight and greater study of literature, it would have been better to have added to slots which extended the coplanar waveguide to one of the edges of the chip (similar to those described by [Focardi and McGrath, 2005](#)).

In order for the radiation to be absorbed into the doped-silicon mesa, a break was made in the middle of the coplanar waveguide, where the mesa is situated. The coplanar waveguide overlapped the mesa on both sides and it was at these

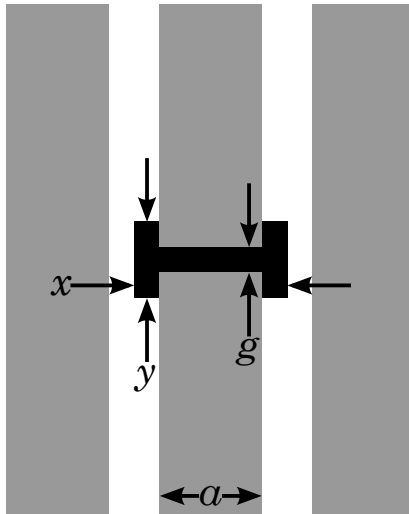


Figure 4.4: Dimensions of bolometer bridge in a coplanar waveguide. The contact length, c , is given by $(y-g)/2$.

points that Schottky contacts were formed. This form of structure is often referred to as a bridge, since the bolometer bridges the gap in the coplanar waveguide. This structure, along with the associated dimensions is illustrated in Figure 4.4.

Four different values for the contact length, c , ($(y-g)/2$ in Figure 4.4) were selected; these were 1, 3, 5 and 7 μm and were selected not only to allow a study of the effect of varying this parameter but also to help ensure successful fabrication. In all cases, the dimensions g and x were 4 and 32 μm . The anticipated contact resistance for these devices was found based on the contact resistivity, which has been measured for both unstrained and strained doped silicon. The measured values for the contact resistivity, ρ_c were $1.28 \times 10^{-4} \Omega\text{cm}^2$ for the unstrained doped silicon and $5.12 \times 10^{-3} \Omega\text{cm}^2$ for the strained silicon. The dimensions of the bridge were not varied with the different antennae frequencies. The dimensions and expected contact resistance, R_c , are given in Table 4.2.

4.3 DETECTOR FABRICATION

The detector chips were fabricated via sputter deposition and photolithographic techniques. In order for the devices to be fabricated, a photomask was created. This

Table 4.2: Dimensions and expected contact resistance for different bolometer bridge designs.

c (μm)	x (μm)	y (μm)	a (μm)	g (μm)	Unstrained R_c (Ω)	Strained R_c ($k\Omega$)
1	32	6	24	4	533	21.3
3	32	10	24	4	178	7.1
5	32	14	24	4	107	4.3
7	32	18	24	4	76	3.0

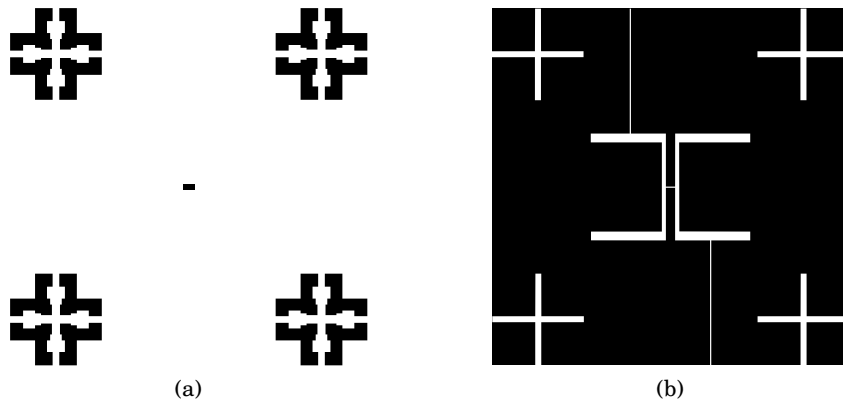


Figure 4.5: Example sections from the photomask used to fabricate silicon cold-electron bolometers. (a) First step, creation of the absorbing mesa; (b) second step, creation of the twin-slot antenna structure. In both stages, the features on the mask in black were protected from the etching process and thus were present on the final detector chip. The features in the corners are alignment marks used to align the mask during the second stage.

mask was used for the two steps in the fabrication process which required etching of a material (covered later in this section); an example of two sections of this mask, used to create a single detector, is shown in Figure 4.5. In this figure, features in black are those protected from the etching process and are those present on the final detector chip. In Figure 4.5a, this corresponds to doped silicon whereas in Figure 4.5b, this corresponds to aluminium.

The fabrication process itself is relatively simple, containing only three etching steps and a single deposition step. The full process flow for the fabrication of the detectors tested in this work is given in the following points:

Initial wafer The starting wafers have been grown at The University of Warwick and have been detailed by [Muhonen et al. \(2011\)](#). The wafers consist of a silicon (001) substrate, followed by a 30 nm layer of epitaxial n⁺⁺ silicon in the case of the unstrained silicon. In the case of the strained silicon, a 2 μm graded layer of Si_{1-x}Ge_x is grown on top of the substrate; this layer is linearly graded from x = 0 at the interface to x = 0.2. This layer is followed by a 500 nm layer of Si_{0.8}Ge_{0.2}. Finally a 30 nm layer of n⁺⁺ silicon is grown on top of the SiGe.

Mesa defined The mesa structure (the absorber) is defined with photoresist. This is applied evenly to the wafer and briefly baked to ensure all excess liquid is removed. The first stage of the photomask (Figure 4.5a) is then placed over the wafer and the photoresist is exposed to ultraviolet light through the photomask. Parts of the mask which are solid (those which are black in Figure 4.5) block the ultraviolet light, protecting the photoresist. The photoresist which has been exposed is weakened and removed with a developer solution.

Mesa etching The mesa structure is created via etching away the undesired parts of the doped-silicon layer. The etching process is unable to etch through the photoresist and thus only the regions exposed to ultraviolet light in the previous step are etched. For the creation of silicon cold-electron bolometers, this etching was performed with a CF₄/O₂ gas etch. The parameters for this etch were: 30 sccm at a pressure of 50 mBar and a power of 100 W.

Surface preparation During early testing of junctions, it was found that in order to create a high-quality Schottky barrier, it was vital to remove the thin layer of silicon oxide (SiO₂) which formed on the doped silicon during storage of the wafer and the above steps. This was performed by briefly etching the wafer in a weak aqueous solution of hydrofluoric acid. This process removed the silicon oxide layer and left hydrogen-terminated silicon at the surface, preventing re-oxidation of the wafer.

Aluminium deposition The aluminium—which created the contacts to the doped-silicon absorber, as well as the ground plane for the antenna—was deposited via sputter deposition. This was performed at a pressure of 5 × 10⁻³ mBar and a sputter power of 150 W. The sputtering gas used was Argon.

Antenna defined The antenna pattern was defined with the second stage of the photomask (Figure 4.5b) and the same process as described above for the mesa.

Antenna etching The antenna structure was etched using a wet etching solution consisting of 26 parts HPO₃, 6 parts H₂O and 2 parts nitric HNO₃. The final

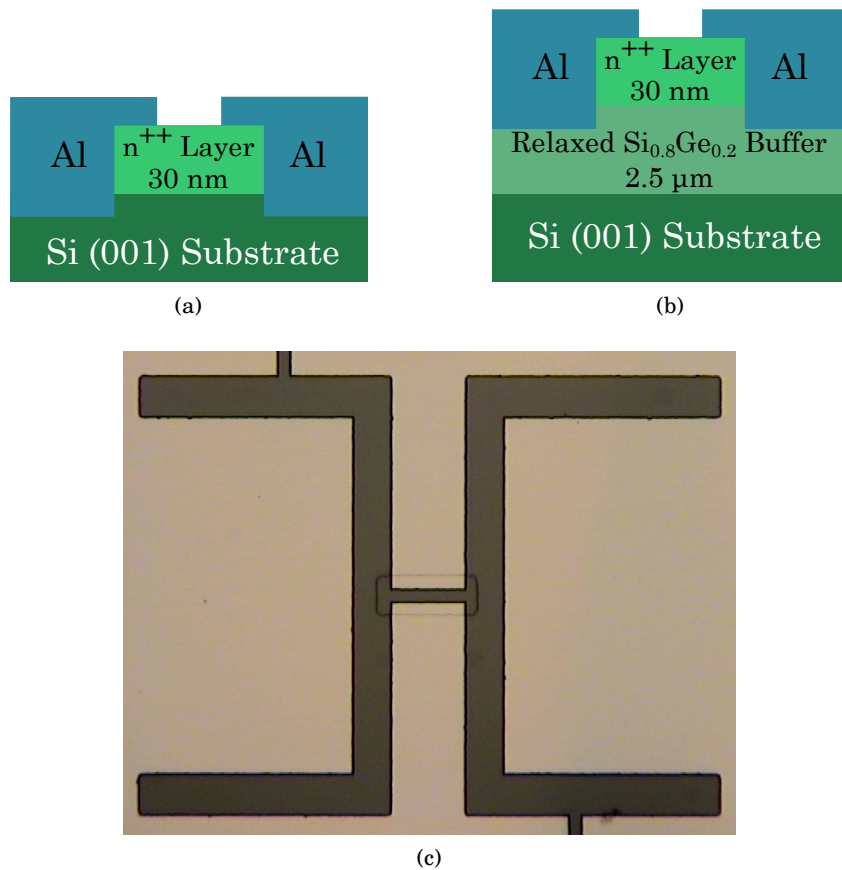


Figure 4.6: (a) Cross section of an unstrained **SiCEB** detector. (b) Cross section of a **SiCEB** detector with a strained-silicon absorber. Both cross sections are along the axis of the coplanar waveguide. (c) Optical photograph of a silicon cold-electron bolometer.

aluminium layer was approximately 100 μm thick.

The process above was used for the fabrication of all devices. The cross sections of the two types of detector fabricated (those with and without a strained absorber) are shown in Figure 4.6, along with a photograph (taken using a microscope) of one of the fabricated devices.

4.4 MATERIAL PROPERTIES

As has been mentioned previously in this chapter, two different silicon wafers have been used to fabricate silicon cold-electron bolometers. These were an unstrained highly-doped silicon (sometimes referred to in literature as the *control* material, wafer reference number: 5365) and a strained highly-doped silicon (wafer reference number: 5362). A detailed study of these two materials has been presented by [Muhonen et al. \(2011\)](#) but a summary of the key properties of these two materials is given in Table 4.3.

Table 4.3: Summary of key material properties for unstrained (control) and strained silicon materials.

Parameter	Unstrained	Strained
Dopant Concentration (cm^{-3}) ^a	4×10^{19}	4×10^{19}
Strain Layer ^a	N/A	$\text{Si}_{0.8}\text{Ge}_{0.2}$
Carrier Density (cm^{-3}) ^a	3.1×10^{19}	2.7×10^{19}
Mobility ($\text{cm}^2\text{V}^{-1}\text{s}^{-1}$) ^a	192	155
Electron-Phonon Coupling, Σ ($\text{WK}^{-6}\text{m}^{-3}$) ^b	5.2×10^8	2.0×10^7
Sheet Resistance (Ω/\square)	384	571
Al-Si Junction Resistance ($\text{k}\Omega\mu\text{m}^2$)	13	512

^a From [Muhonen et al. \(2011\)](#).

^b From [Prest et al. \(2011\)](#).

The sheet resistance and aluminium-silicon junction resistance have been measured at Cardiff.

Chapter Five

Cryogenic Testbeds

*'Some people call it procrastination;
I actually call it thinking.'*
—HANS ZIMMER

5.1 INTRODUCTION

As is the case with all ultra-sensitive mid- to far-infrared detectors (as described by Richards, 1994), the silicon cold-electron bolometer requires cooling to extremely low temperatures in order to operate. This requirement can be seen from the description of cold-electron bolometers given in Chapter 2. Since these detectors incorporate superconducting contacts to select only the most energetic (i.e. the hottest) electrons from the detector's absorber, it is important that the superconductor is cooled sufficiently that the superconducting energy gap is close to its maximum. For the detectors studied in this work, which used aluminium contacts, it was found that cooling to approximately $\sim T_c/4$ (300 mK) allowed the detector to operate reasonably. However, in order to arrive at as complete a study as possible, it was important to measure the electrical properties of the detectors to as low a temperature as possible.

To this end, several different cryogenic systems have been used in the course of this work. The most significant of these (those in which results presented in this thesis were taken) were a $\text{He}10$ sorption refrigerator housed in a cryostat

with a pulse tube cooler, and a He^7 sorption refrigerator mounted on the cold plate of a liquid helium cryostat.¹ The reason for the use of these different systems was essentially due to availability and the associated costs of liquid helium. Primary measurements were carried out in the pulse-tube-cooled cryostat since this had lower running costs (due to not requiring a reservoir of liquid helium to be maintained). However (as will be seen later in this chapter), the system was not designed with the DC readout of sensitive detectors in mind and resulted in lower quality data than would have been desired; however, it did provide a useful facility for ascertaining whether or not a device was functional. The second system, which required the supply of liquid helium, contained optical windows, horns and filters to allow the detector to observe external sources. This chapter will cover the operational principles, along with the cryogenic performance and suitability for the required measurements of each of these systems.

5.2 SORPTION REFRIGERATORS

Sorption refrigerators operate by the adsorption and desorption of a working gas (helium in the case of systems intended to operate at cryogenic temperatures) from a surface or other material (most commonly activated charcoal). The released gas flows through a pipe until it is cooled by a condensation point and liquified. This liquid is collected in a stage called the evaporator. The activated charcoal is then cooled, causing the gas evaporating from the liquid in the evaporator to become reattached to the charcoal, thus decreasing the pressure in the system and thus the temperature of the liquid in the evaporator. A simplified model of a single-stage sorption refrigerator is shown in Figure 5.1.

Before the operation of such a refrigerator is discussed, it is useful to consider the working principles of gas-gap heat switches. Gas-gap heat switches are the most common type of heat switch used in conjunction with sorption refrigerators. This can be thought of simply as a small sorption refrigerator. The heat switch is made of two copper caps connected by an extremely thin-walled stainless steel tube (which has negligible thermal conduction); attached to this, via a second thin tube,

¹Note: He^7 and He^{10} here do not denote strange and exotic isotopes of helium but instead the combination of pumps which make up the sorption refrigerator. Isotopes have been typeset with a leading superscript (i.e. ${}^4\text{He}$). A He^7 refrigerator contains one ${}^4\text{He}$ pump and a ${}^3\text{He}$ pump, a He^{10} refrigerator consists of a He^7 refrigerator used as a buffer stage for a second ${}^3\text{He}$ pump.

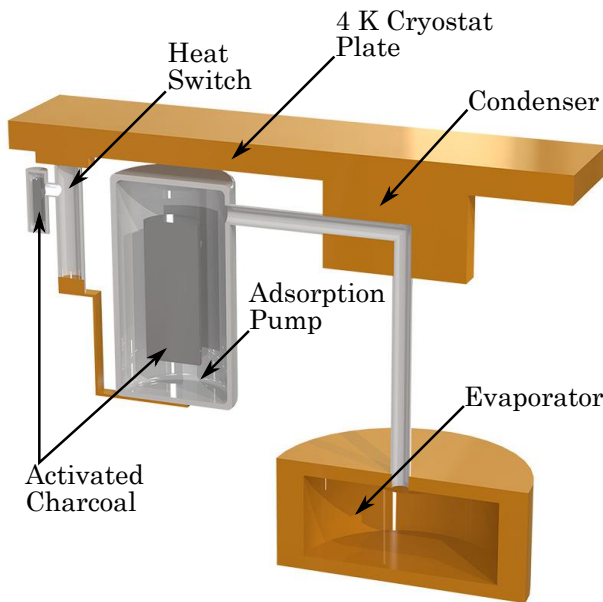


Figure 5.1: Computer-generated model of the cross section of a sorption refrigerator. The 4-Kelvin plate of the cryostat is cooled by either a liquid-helium reservoir or a mechanical cooler (not shown in either case).

is a cylinder containing a charcoal getter. The heat switch also contains helium gas. When the switch is open (off), the helium is attached to the getter and there is little or no thermal conduction between the two copper caps. The heat switch is closed (switched on) by heating the charcoal, causing the helium to be released into the stainless steel tube, which results in the thermal conduction between the two copper caps increasing substantially.

In order to understand a sorption refrigerator, it is perhaps easiest to consider the typical procedure followed to cycle such a system. The general procedure is as follows:

Cool system to working temperature. In order to function, the condensing stage of the system must be cooled to the boiling point of the working gas (this is 4.2 K for ${}^4\text{He}$). This is performed by either: filling the cryostat in which the refrigerator is housed with liquid helium (in the case of *wet* systems) or switching on the cryostat's mechanical cooler (for *dry* systems) and waiting for all the parts of the system to thermalise.

Heat the charcoal in the pump. The pump is heated (usually via a film resistor mounted to the outside of the pump) causing the gas to be released from the activated charcoal (sometimes referred to as the *getter*). As the charcoal is heated to above 10 K, helium will begin to be released and by 25 K the vast majority will have been released.

Helium condenses. Increasing the temperature further causes the pressure within the refrigerator to increase, causing the gas to come into contact with the condenser, where it will condense. This liquid will then collect in the evaporator (situated beneath the condenser).

Charcoal cooled. The charcoal in the pump is then cooled again. This is performed using a heat switch. The heat switch has one side connected to the pump and the other to the cold plate of the cryostat. The closing of the heat switch creates a link between the pump and the cold plate of the cryostat and thus cools the pump.

Pressure reduces. As the charcoal in the pump cools to below 25 K, it is once again able to attract and hold gas. This means that as helium molecules evaporate from the liquid, they become attached to the activated charcoal (through adsorption) which causes the pressure in the system to reduce. This, in turn, lowers the temperature of the liquid in the evaporator along with the walls of the evaporator.

The above process is for a single-stage helium-4 sorption refrigerator; such systems are capable of achieving temperatures of around 1 K at the external walls of the evaporator. To achieve sub-Kelvin temperatures with a sorption refrigerator, one must use helium-3 as the working gas; this necessitates that the condensation point must be at a lower temperature (^3He has a critical point of 3.3 K).

In order to meet this requirement, it is common practice to use a helium-4 pump as a buffer stage to cool a condensation point on a helium-3 pump (this is what is referred to as a $\text{He}7$ system).² This technique was first reported by Dall’Oglio et al. (1991) who, at the time, achieved a minimum temperature of 300 mK at the evaporator of the ^3He pump.

Further cooling can be achieved with sorption refrigerators by using the $\text{He}7$ system described above to cool a further helium-3 pump (thus making a $\text{He}10$ system). This type of system was first introduced by Bhatia et al. (2000) who described a system capable of achieving a minimum temperature of 234 mK for 20

²It is worth mentioning that, as mechanical cooling technology (e.g. pulse tubes) is improving, these systems can, under low to medium thermal loads, offer sufficiently low temperatures to cycle a helium-3 sorption cooler directly, without the need of a buffer stage.

hours under minimal thermal loading ($\approx 0.9 \mu\text{W}$) or 242 mK for 12 hours under a total thermal load of $3.9 \mu\text{W}$. Further improvements to the design of such systems, coupled with the lower starting temperatures offered by pulse tube coolers, has resulted in minimum operating temperatures of lower than 220 mK being achieved under realistic experimental thermal loading.

5.3 SYSTEMS USED IN THIS WORK

Two systems have been used for the majority of the low-temperature measurements presented in this work. These were: a cryostat with a pulse-tube cooler upon which a $\text{He}10$ sorption refrigerator was mounted; and a liquid-helium cryostat, containing windows to facilitate optical measurements, in which a $\text{He}7$ sorption refrigerator was mounted. Each of these systems served a specific role, such as: facilitating optical measurement of detectors or characterisation at extremely low temperatures. These systems are discussed in greater detail in the following subsections.

5.3.1 PULSE-TUBE-COOLED CRYOSTAT WITH HE10 SORPTION REFRIGERATOR

The first system used to characterise silicon cold-electron bolometers was a pulse-tube-cooled cryostat incorporating a $\text{He}10$ sorption refrigerator. This system had a large cold plate (260 mm in diameter), which could be cooled to a minimum temperature of 220 mK, which could be maintained for more than 48 hours. The system also contained a set of windows to enable the measurement of a detector's response to an external source. These windows were not used for the most part, however, since an alternative system (discussed later in this section) enabled a much more complete optical study of a detector.

This cryostat was mainly used for measurements such as the initial verification of the device's function (i.e. whether tunnelling contacts to the silicon absorber had formed correctly), along with dark characterisation of the device (i.e. measuring the current-voltage relationship of the detector at various bath temperatures). It is worth mentioning that pulse tube cooler based cryogenic systems can contribute additional, undesired, components when measuring noise spectra. These are caused by the pulsing of the mechanical cooler introducing movement at various stages of the cryostat. This movement can cause any of the following: thermal oscillations,

movement of wiring (causing electrical variations through either changes to the wiring's capacitance or through induction), or alternations to the optical alignment of components. Clearly, in order to accurately measure the performance of any device mounted within such a system, it is vital not only to discover the magnitude of these effects but also to reduce their presence as much as possible. The various effects of microphonics, along with a considerably more detailed explanation of their introduction, is given by [Bhatia et al. \(1999\)](#). In order to reduce the effect of these microphonics, some form of dampening is required to reduce the force exerted on the various stages of the cryostat.

In the case of this system, microphonics have been reduced by the deployment of four damping stages. Firstly, the pulse tube cooler's motor is electrically decoupled from the cryostat itself; this is performed by sitting the motor on a layer of plastic and by adding PTFE spacers to the lines between the motor and the pulse tube head; on the outside of the cryostat, instead of mounting the pulse tube cooler head directly to the outer vacuum-can, a number of rubber spacer rings (shore hardness 40) are placed between the cryostat and the head, these are sufficiently clamped to ensure a hermetic seal but allow a degree of movement to absorb some of the vibrational energy. Secondly, at the first stage of the pulse tube cooler (nominally at 65 K), the pulse tube cooler is connected to the cold plate via multiple pieces of thin copper shim bent into a c-shape; these act like springs, dampening any vibration, while still creating a good thermal link between the pulse tube cooler and the plate. At the second stage of the pulse tube cooler (nominally 3–4.2 K), a similar technique is used whereby the pulse tube cooler and the cold plate are connected via multiple strands of copper braid; this again affords a good thermal link while damping vibrations. Finally, the coldest stage of the system (that cooled by the second ^3He pump of the He10 sorption cooler) is connected to the pump via more copper shim (similar to that described earlier). All the cold plates of the system, with the exception of the coldest stage, are connected to the cryostat's outer vacuum shield by hollow stainless-steel supports with thin (compared to their length) walls. The coldest stage uses rigid supports containing sapphire-sapphire contacts (these have been described by [Bintley et al., 2007](#)). A computer-generated model of this system, showing these features along with various other components can be seen in Figure 5.2.

For optical measurements in this system, a set of metal-mesh filters (as described by [Ade et al., 2006](#)) were used. These not only reduced the thermal load

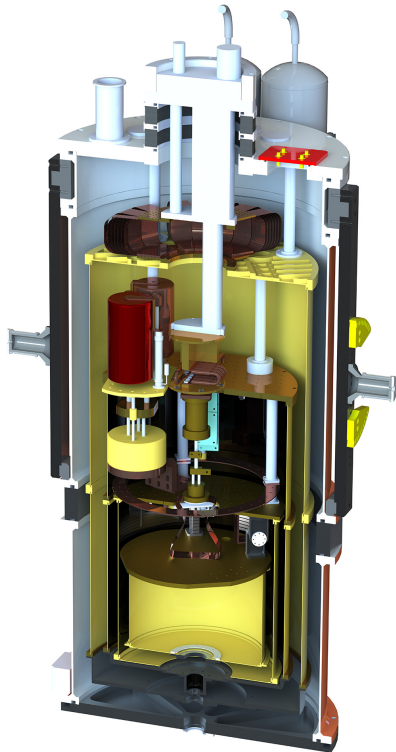


Figure 5.2: Computer-generated model of pulse-tube cooled cryostat. Along with the various sorption pumps and heat switches, the damping stages can also be seen; these are (from top to bottom) the (black) rubber rings via which the pulse tube system is mounted to the cryostat, the bent copper-shim springs, the copper braid connecting the 65 K stage of the pulse tube cooler the plate and copper shim connecting the condenser of the second ^3He sorption pump to the final cold plate.

on the colder stages of the cryostat (those with the least cooling power) but also reduced the out-of-band power on the detector (i.e. radiation with frequencies not of interest for the study being carried out). The transmission profiles of these filters can be seen in Figure 5.3. An additional band-pass filter with 3-dB bandwidth of 50 GHz centred around 150 GHz was also used. This was mounted on the front of the detector holder and is not shown in Figure 5.3.

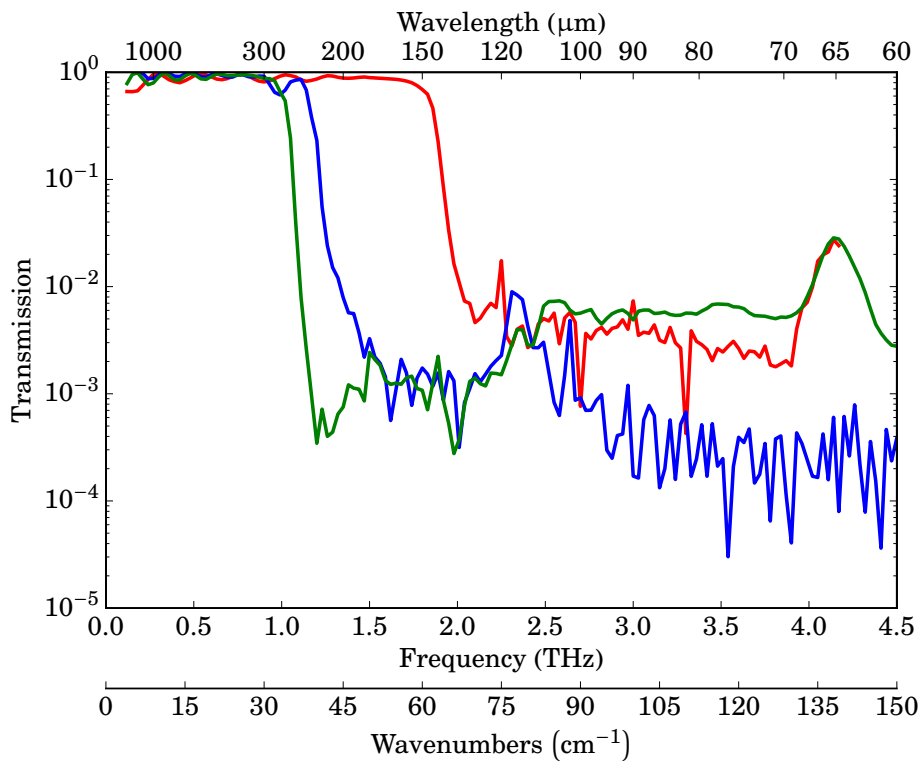


Figure 5.3: Filters mounted at various stages of the pulse-tube cooled cryostat for optical measurements. Red— 60 cm^{-1} low-pass edge filter, mounted on the 60-K shield; blue— 43 cm^{-1} low-pass edge, mounted on the 4-K shield; green— 33 cm^{-1} low-pass edge, mounted on the 350-mK shield.

5.3.2 LIQUID HELIUM CRYOSTAT WITH HE7 SORPTION REFRIGERATOR

The second system used to characterise detectors was a second liquid helium cryostat, this time with a He7 sorption refrigerator. This system was used for the vast majority of optical measurements taken, including measuring the spectral response of the detector. This system was well suited to such measurements, due to the inclusion a set of back-to-back horns, which produced a well defined beam of radiation at the detector stage.

As was the case with the pulse-tube cooled system, a number of filters were used to remove the out-of-band radiation, these are shown in Figure 5.4. The vacuum

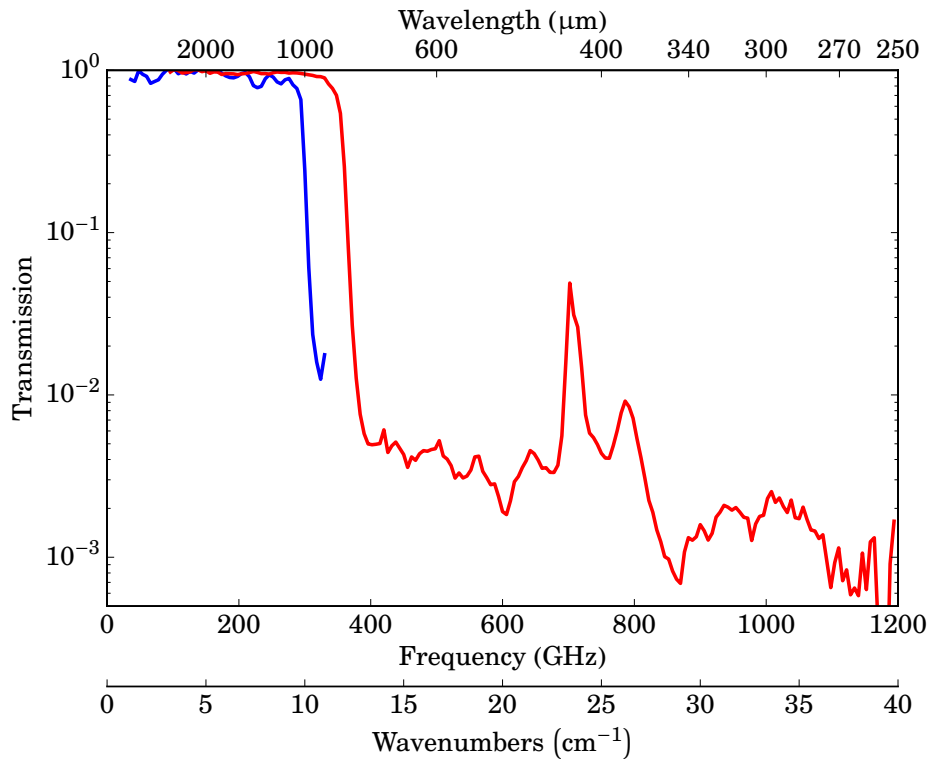


Figure 5.4: Filter profile of filters used in optical measurement cryostat. Red— 12 cm^{-1} low-pass edge filter mounted on the back-to-back horns at 4.2 K; blue— 10 cm^{-1} low-pass edge filter mounted on the device holder at 350 mK. A set of thermal blockers were also used to reduce the power load on the cold stage of the cryostat; these were close to 100 % transparent at the frequencies shown and, as such, have not been included.

jacket of the cryostat contained a large (90 mm) **Ultra-High Molecular-Weight Polyethylene (UHMWPE)** window. This blocked the visible and near-infrared light, as well as ensuring that the vacuum was maintained. The 77-K and 4-K shields contained thermal-blocking filters; these are close to 100 % transparent in the frequency range shown in Figure 5.4 and, as such, the profiles of these have not been plotted. In front of the back-to-back horns (at 4.2 K but after the thermal blocker), a 12 cm^{-1} low-pass edge filter was used (this is the red line in Figure 5.4). The device holder, which was mounted on the 350 mK stage of the cryostat, was fitted with a 10 cm^{-1} low-pass edge filter. No bandpass filters were used to further

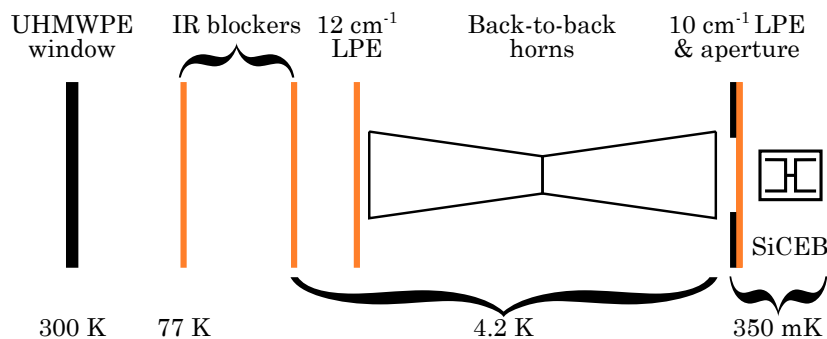


Figure 5.5: Optical components housed in cryostat used for optical measurements.

reduce the spectral range of the incident radiation, since this would obviously prohibit any meaningful study of a detector's spectral response.

The key optical components in this system were a pair of back-to-back corrugated horns, these were mounted at 4.2 mK in a shield surrounding the 350-mK detector stage. These back-to-back horns produced an excellent Gaussian beam with low side-lobes. This horn arrangement is very similar to that used on *Planck's High-Frequency Instrument (HFI)* instrument as described by [Maffei et al. \(2010\)](#). A simplistic schematic of the optical configuration of this cryostat is shown in Figure 5.5. A photograph of this system, in which the outer UHMWPE window can be seen, is shown in Figure 5.6.

5.4 DETECTOR HOLDER

In order for the detectors to be characterised, they needed to be mounted in a holder which not only held them firmly in place, but also facilitated easy electrical connections, along with ensuring that only desired radiation was incident on the detector. Such a holder was manufactured in-house by a computer-numerical-control mill. The holder (shown in Figure 5.7) included an aperture through which light could enter the holder for optical testing; a metal-mesh filter was clamped behind the aperture. For dark measurement, the filter could be replaced by a blank.

The various components of the holder all included lipped edges, which ensured that the holder was reasonably light-tight. A PTFE ring was used to clamp the silicon lens in place, this ring also ensured the lens was correctly aligned. A

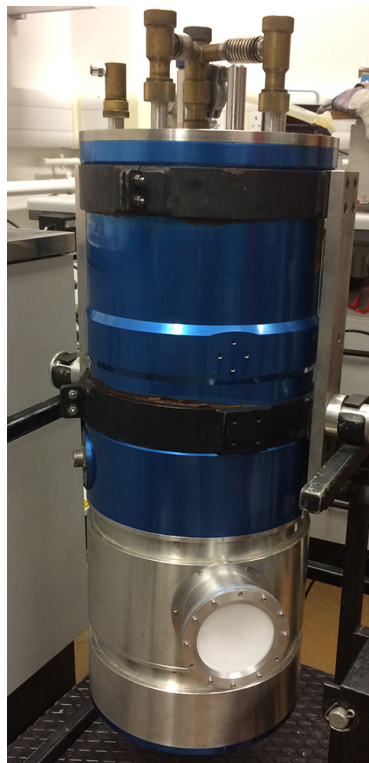


Figure 5.6: Photograph of cryostat used for optical measurements. The relatively large **UHMWPE** window can be seen towards the bottom of the photograph.

Printed Circuit Board (PCB), wired to a micro-miniature D-type connector, allowed for simple connection to the detector holder. The electrical connection from the connector to the detector itself was completed by aluminium wire bonds between the printed circuit board and the detector.³ The detector was secured in the holder via careful glueing, with GE varnish, to a piece of silicon (matched to the lens), which, in turn, was glued to the rear of the circuit board. When glueing the detector to this silicon, it was important to ensure that the GE varnish was only present at the edges and did not seep under the detector chip, since this would interfere with the radiation incident on the detector (which was rear-illuminated through the silicon substrate). A computer-generated model of the device holder can be seen in Figures 5.7a and 5.7b, which show an exploded view of the various components

³The circuit board was gold plated to make the wire bonds more reliable.

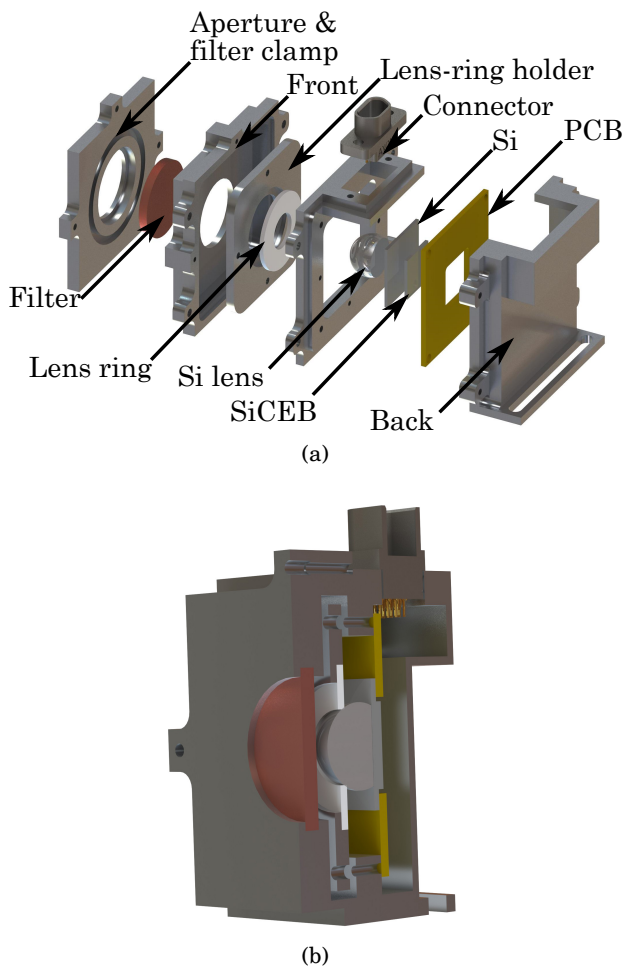


Figure 5.7: Computer-generated model of the detector holder. (a) Exploded view of the detector holder, showing the various components; (b) cross-sectional view of the assembled detector holder.

of the holder (including the detector chip itself) and a cross-section of the fully assembled holder.

At cryogenic temperatures, assemblies of mechanical components, such as the device holder described here, it is vital to pay close attention to how the various components expand or contract relative to each other as they are cooled. The vast majority of the device holder used here was created from machined aluminium and thus the aluminium-aluminium interfaces were not of concern. However, particular attention was needed regarding the silicon lens and its **PTFE** securing ring. While

the ring was clamped firmly to the lens and thin enough that it was capable of deflection while maintaining a firm contact to the lens, it is possible that as the two components were cooled, the ring may become loose and the lens might move. In order to explore this, we examined the coefficients of expansion, α , for the two materials, defined as:

$$\alpha = \frac{1}{x} \frac{dx}{dT}, \quad (5.1)$$

where x is the length of the material and T is the temperature. Values for α are given in many standard reference tables and usually stated for a final temperature. [Kaye and Laby \(1995\)](#) states that for silicon cooled from room temperature (taken to be 293 K) to 100 K is $-0.4 \times 10^{-6} \text{ K}^{-1}$; at the point of clamping the lens diameter was 8.5 mm, so by the use of Equation 5.1 we find that by cooling over this range the lens expands by:

$$\begin{aligned} \Delta x &= 8.5 \times 10^{-3} \times -0.4 \times 10^{-6} \times (100 - 293) \\ &= 0.65 \mu\text{m}. \end{aligned} \quad (5.2)$$

That is to say the lens expands by less than one micrometre at the interface with the clamp. [Corruccini \(1961\)](#) gives a value of $\alpha = 21.1 \times 10^{-3} \text{ K}^{-1}$ for **PTFE** when cooled from room temperature to 20 K; note this is a greater range than is given for silicon by [Kaye and Laby \(1995\)](#), however it serves as a good indication all the same. By again using Equation 5.1, we find that when cooled to 20 K, the silicon ring expands by:

$$\begin{aligned} \Delta x &= 8.5 \times 10^{-3} \times 21.1 \times 10^{-3} \times (20 - 293) \\ &= -49 \mu\text{m}. \end{aligned} \quad (5.3)$$

Meaning that the **PTFE** ring is shrinking by nearly 50 μm . The **PTFE** ring is not mechanically fixed or glued to any other surface and thus is free to contract about its centre. This analysis shows that, when cooled, the lens marginally expands while the clamping ring contracts and so we deduce that at lower temperatures the lens should be clamped to the detector firmly. This justifies the choice of materials here and removes any concerns that the lens may become loose under thermal cycling. It is worth noting that the small values for the relative expansion and contraction discussed here could also be accommodated by ensuring the **PTFE** ring was slightly deflected when clamping the lens.

Chapter Six

Detector Readout

'The audience is the most revered member of the theater. Without an audience there is no theater.'
—VIOLA SPOLIN

6.1 INTRODUCTION

Like all high-sensitivity detectors operating in the far-infrared, cold-electron bolometers need to be readout using amplification (Rieke, 2007). This amplification is of either the voltage or the current, with the quantity not being amplified for readout usually providing the bias. Golubev and Kuzmin (2001) provide a good discussion of the advantages and disadvantages of current-bias versus voltage-bias for use with cold-electron bolometers, along with a basic schematic for each case. When considering the description of Superconducting Quantum Interference Devices (SQUIDs) based readout systems by Golubev and Kuzmin (2001), it should be remembered that this field has made substantial improvements since 2001; the current generation of SQUIDs are capable not only of lower noise and great bandwidth (see, for example, Granata et al., 2015) but have also been multiplexed into large arrays (see, for example, Irwin, 2002). However, the overall bandwidth afforded by such detectors still lags behind that of voltage based amplifiers and, as such, they do not match well with the high speeds afforded by cold-electron bolometers.

In reality, the **SQUIDs** (and their associated electronics) used to amplify current in a voltage bias regime are both more expensive and more complex to set up compared to the voltage amplifiers used for current biased measurements. This means that it is often preferable to use a current biased system for early device development.

During the development of the **SiCEBs** described in this work, numerous iterations of voltage amplifier have been used. Each readout system was designed to offer the possibility of improved device characterisation, from either a lower contribution to the noise measurement or by allowing measurements to higher frequencies of readout.

In addition to changes that were required to the amplification system, it has also been necessary to change the exact technique by which the detector has been biased. The main driver for these changes has been the desire to reduce electrical noise input to the device, as well as to create the most stable and capable testing regime possible.

6.2 REQUIREMENTS OF THE READOUT SYSTEM

In order to specify a readout system, it is important to define a number of desirable goals for its performance. For the early development stage testing of **SiCEBs** the following desired points were set:

- The system had to be as simple as possible. This is to say that the design and operation of the readout should not become a distraction from the testing of devices.
- The system needed to contribute a sufficiently low electrical noise that noise measurements of the detector could be successfully performed.
- The system was capable of measuring the speed of response of the detector by measurement of the roll-off of device noise.

Although it was possible to estimate both the speed and expected noise levels for a **SiCEB**, these estimates were only vague ‘ball-park’ figures. This meant that it was necessary to produce a testing system believed to be capable of meeting these criteria and then to make improvements as required. Further to these requirements,

any system needed to be able to perform DC-measurements, such as recording *I-V* curves with a high degree of stability.

6.3 INITIAL TESTING SYSTEM

6.3.1 INITIAL READOUT SYSTEM

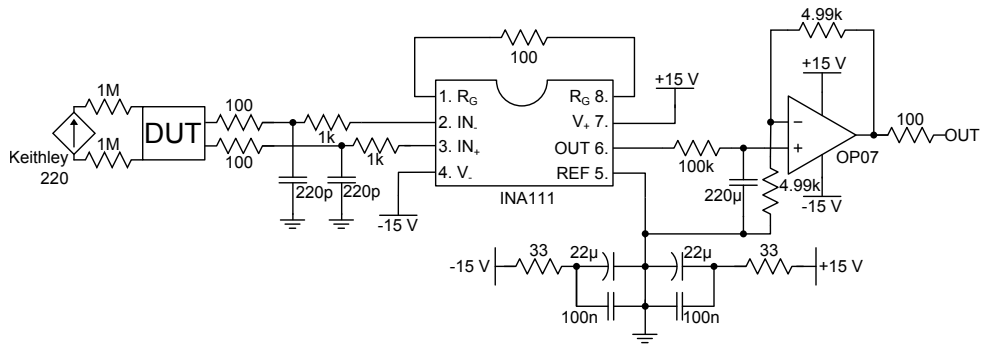


Figure 6.1: Initial bias and readout system using a Keithley 220 Programmable Current Source to bias the **Device Under Test (DUT)**. The voltage is then amplified by the INA111 differential amplifier (configured for a gain factor of 500) and then by the OP07 operational-amplifier (configured to give a gain of two).

The initial amplification system used was heavily based upon an existing circuit designed to readout **Resistance Temperature Detectors (RTDs)**. This was used as it was readily available within the department and early (somewhat optimistic) estimations of device performance indicated that noise measurements would be possible. This amplifier was used in conjunction with a Keithly 220 Programmable Current Source to provide the bias across the device. Figure 6.1 shows the circuit diagram of the amplifier used here, along with the connection to the current source. To perform an *I-V* measurement, the current source, which is controlled by a computer, is stepped through the desired range of values and at each step a **data acquisition unit (DAQ)** records the amplified voltage across the device.

The [INA111 Data Sheet \(2010\)](#) and [OP07 Data Sheet \(2011\)](#) state that both these amplifiers have, when operating in the configuration shown in Figure 6.1, a noise voltage referred to the input of $10 \text{ nV}\text{Hz}^{-\frac{1}{2}}$. In order to understand how

the internal noise of these amplifiers contributes to the total noise measured at the output of the system, we can think of each of the two amplifiers as containing some source which generates a noise voltage with a spectral density of e_n and a *black-box* which provides the gain while generating no noise. This is illustrated in Figure 6.2.

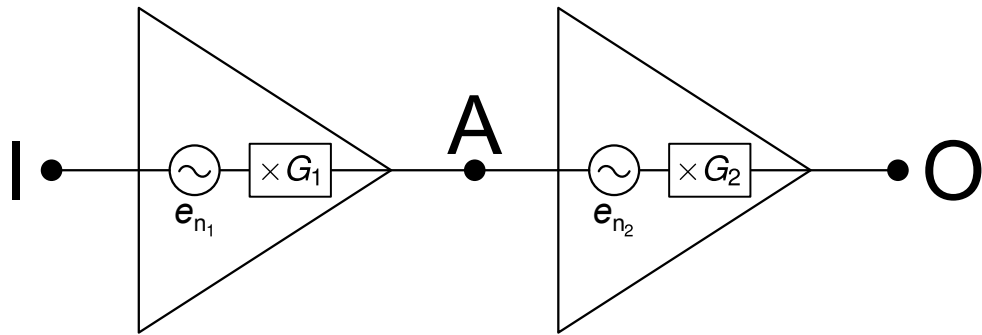


Figure 6.2: Simple model of two amplifiers working in series. Each amplifier contains a component which generates a noise voltage with spectral density e_n before an ideal, noiseless component amplifies the signal by a gain factor of G .

In Figure 6.2, we see that if there is no input signal at point I then the input to the second amplifier, point A, will consist of only the noise generated in the first amplifier, multiplied by that amplifier's gain factor. The uncorrelated noise from the second amplifier is then added to the amplified noise from the first and both are multiplied by the gain of the second amplifier. From this, we can define the total noise, e_{tot} , at the output of this system, in the absence of any input signal, as:

$$e_{\text{tot}} = \sqrt{(e_{n_1} \times G_1)^2 + e_{n_2}^2} \times G_2. \quad (6.1)$$

If, as is the case in Figure 6.1, $e_{n_1} \times G_1 \gg e_{n_2}$ then we can say:

$$e_{\text{tot}} \approx e_{n_1} G_1 G_2. \quad (6.2)$$

We can define the input referred noise voltage spectral density, e_{RTI} , simply as:

$$e_{\text{RTI}} = \frac{e_{\text{tot}}}{G_{\text{tot}}}, \quad (6.3)$$

where G_{tot} is the product of the m gain stages, given by:

$$G_{\text{tot}} = \prod_m G_m . \quad (6.4)$$

By applying Equation 6.1 for the system shown in Figure 6.1 ($e_{n_1} = e_{n_2} = 10 \text{ nVHz}^{-\frac{1}{2}}$, $G_1 = 500$ and $G_2 = 2$), we find that $e_{\text{RTI}} = 10.00002 \text{ nVHz}^{-\frac{1}{2}}$. The above approximation can be verified by calculating e_{RTI} again using Equation 6.2, this gives $e_{\text{RTI}} \approx 10 \text{ nVHz}^{-\frac{1}{2}}$. This shows that, in this case, the internal noise from the second amplifier is contributing only 0.0002 % of the noise at the output.

It is possible to characterise an amplifier by measuring three simple parameters of the amplifier: gain, bandwidth and internal noise. The gain can be found by measuring how much a signal (a simple sinusoidal wave for example) is amplified; the bandwidth of the amplifier can be found by measuring the frequency at which the noise spectral density decreases from $e_{\text{tot}}G_{\text{tot}}$ (this can also serve as a measure of the uniformity of the gain across a wide range of frequencies); finally, the internal noise (referred to the amplifier's input) can be found from the noise spectral density, corrected for the measured gain, when the input of the amplifier is shorted (no input signal).

Figure 6.3 shows the amplification of a 10 Hz sinusoidal wave generated by a signal generator, the output of which was split between the amplifier to be tested and a direct input to a digital oscilloscope. The input signal (red, shown on the primary vertical axis of the upper plot of Figure 6.3) was measured to have a peak amplitude of 10 mV ($V_{\text{rms}} = 7.07 \text{ mV}$). The amplified signal (green, secondary vertical scale) was measured as having a peak amplitude of 10 V ($V_{\text{rms}} = 7.07 \text{ V}$); from this, it is clear that the gain factor of the amplifier is 1000 at the voltage peaks. The uniformity of the gain, for various input amplitudes, was verified by simply taking the ratio of these two signals at all points; the result of this is shown in the lower plot of Figure 6.3. It can clearly be seen that the gain factor of 1000 does not vary with the amplitude of the input signal (up to 10 V). The [INA111 Data Sheet \(2010\)](#) states that the input amplitude range (the range over which the input is amplified by a constant gain) of this device is 12.7 mV when operating at a gain of 1000.

The next stage in characterising this amplifier was to measure the bandwidth, in frequency, over which a signal is consistently amplified. This was performed

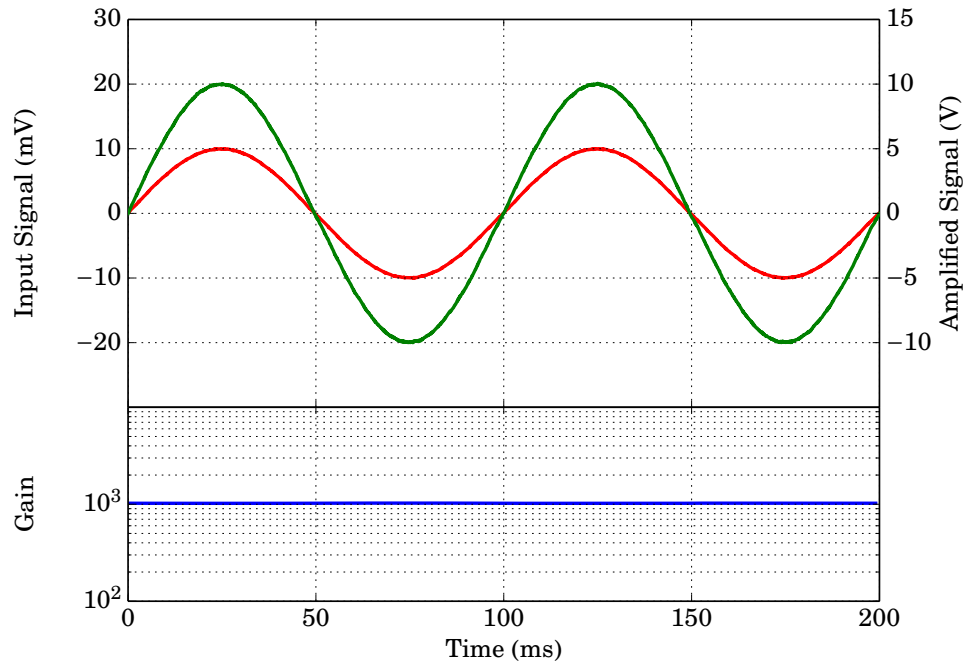


Figure 6.3: Gain measurement of RTD amplifier using a 10 Hz sinusoidal wave. Upper plot—Input signal (red, primary vertical axis) compared to the amplified signal (green, secondary vertical axis). Lower plot—Gain measured from taking the ratio of the amplified and input signals.

by using a signal generator to output a white noise signal of known amplitude.¹ Similarly to the previous test, this signal was then split, with one output being passed directly to a digital oscilloscope and the other being amplified before being passed to the oscilloscope. The digital oscilloscope was also used to process both of these signals by computing the **Fast Fourier Transform (FFT)** of both. When defining the frequency bandwidth of an electronic device, it is usual to take the frequency that the voltage throughput has fallen to a factor of the square root of two times the maximum throughput. This is called the 3-dB bandwidth, since:

$$20\log_{10}\left(\frac{1}{\sqrt{2}}\right) \approx -3 \text{ dB.} \quad (6.5)$$

¹The [Agilent 33220A Function/Arbitrary Waveform Generator Data Sheet \(2011\)](#) states that this device has a bandwidth, when generating noise, of 9 MHz.

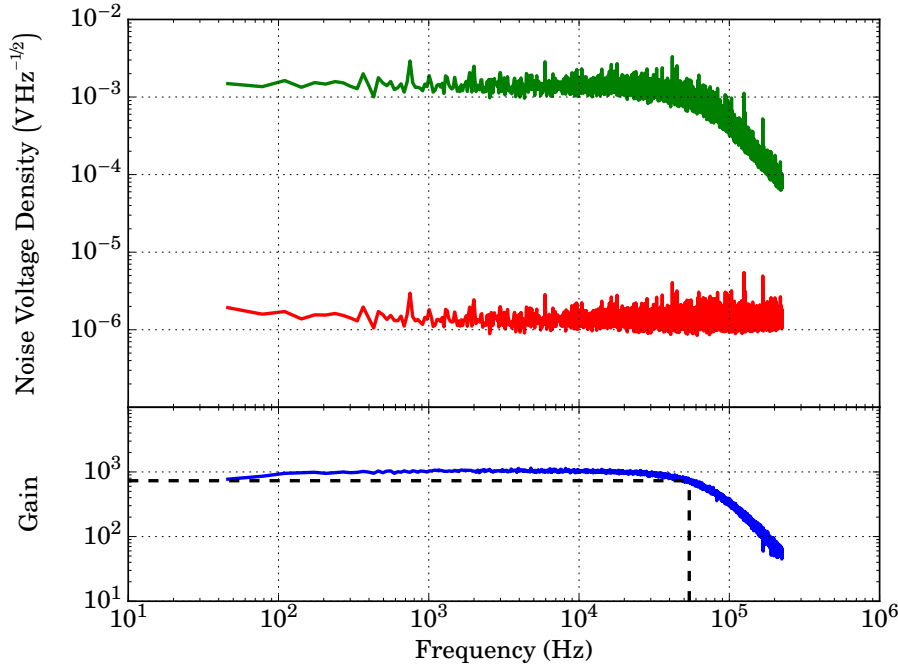


Figure 6.4: Bandwidth measurement of RTD amplifier. A white noise signal was generated by a signal generator, this was split with one feed being fed directly to the oscilloscope (red line) and one feed being amplified first (green line). The ratio (the gain of the amplifier) is shown on the lower plot; the 3-dB level and corresponding frequency limit to the bandwidth are shown by the dashed line in the lower plot.

More correctly, the 3-dB bandwidth is defined as the frequency at which the power throughput has fallen by a factor of one half, i.e.:

$$10 \log_{10} \left(\frac{1}{2} \right) \approx -3 \text{ dB}. \quad (6.6)$$

Figure 6.4 shows the result of the bandwidth measurement. It is clear from the figure that, at frequencies below 10 kHz, the output of the amplifier (green trace on upper plot) differed only from the generated noise (red trace on upper plot) by the gain factor of 1000. As the frequency increased the gain factor (blue trace on lower plot) ceased to be constant and started to decrease. Using Equation 6.5, the 3-dB

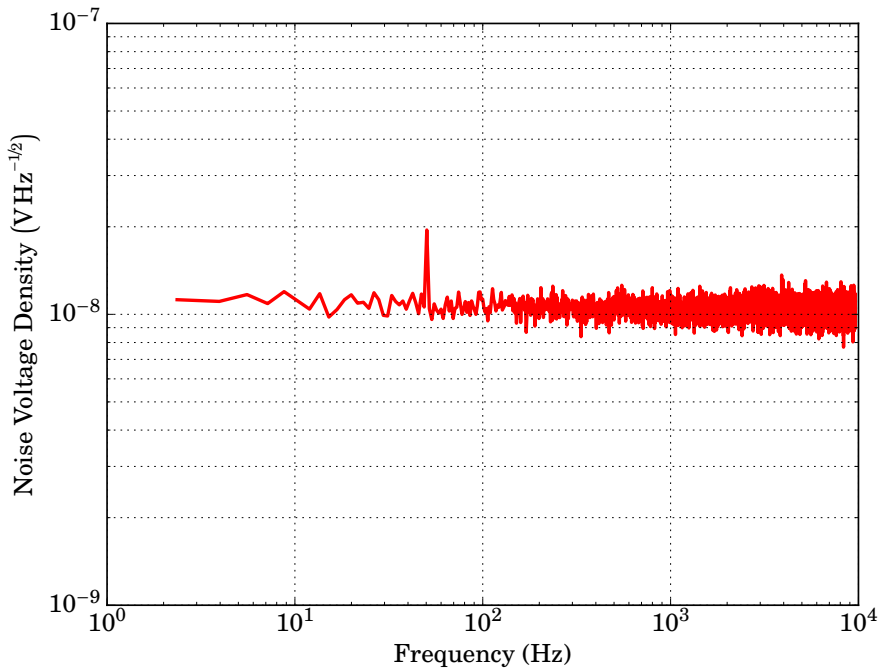


Figure 6.5: Measurement of the internal noise of the original amplifier, referred to the input of the amplifier. The measurement was performed by shorting the input of the amplifier and measuring the output of the amplifier with a digital oscilloscope, which also computed the FFT.

bandwidth corresponds to the gain dropping to 731; this occurred at a frequency of 55 kHz, which is illustrated by the dashed line on the lower plot of Figure 6.4. It should be noted that Figure 6.4 has had the low frequency section (dominated by $1/f$ as discussed in Section 2.7) removed for clarity.

The final part of characterising the amplifier was to measure the input-referred noise. As seen earlier in this section for the configuration of this amplifier (shown in Figure 6.1), the expected input referred noise was $10 \text{ nV}\text{Hz}^{-1/2}$ (explained on Page 95). To measure this quantity, the input of the amplifier was shorted and the output of the amplifier was measured as in the previous tests.

Figure 6.5 shows the measured noise spectrum for the amplifier (as referred to the input), measured up to 10 kHz. From this figure, we can see that the internal noise is equivalent to a noise source of $10 \text{ nV}\text{Hz}^{-1/2}$ at the input of the amplifier.

This is the value which was predicted on Page 95 and this result, along with the results of the other tests carried out thus far, indicated that the amplifier system was performing as designed.

6.3.2 INITIAL BIAS SYSTEM

The amplifier only contributes one part of the total performance of the electronic system. The source of biasing current also plays a substantial role in the final performance. Unlike the amplifier, the speed or bandwidth of this current source is not of high importance since the *I-V* measurements can be performed at a low frequency, and noise measurements are measured with the device at a constant (DC) bias. The bias circuitry can, however, have a negative effect on measurement by either failing to provide a stable bias and thus causing some degree of *jitter* in a measurement, or by adding undesired levels of noise (either as white noise or as finite tones). In the case of the current supply contributing additional noise, this could, in turn, cause additional energy to be dissipated across the device being tested and thus affect the result.

In the first system used, the current bias was provided by a Keithley 220 Programmable Current Source; this unit is capable of providing currents between 500 fA and 100 mA with a peak-to-peak noise level of between 400 ppm and 100 ppm depending on the output range specified.²

In order to test the effect of the current source, two simple measurements were performed using a *dummy* device (typically a resistor with an appropriate value) as the **Device Under Test (DUT)** in Figure 6.1.³ Firstly, a test was carried out to ensure that the output of the device was stable enough to allow for reliable measurements. This was performed in two parts: initially the Keithley 220 current source was set to a constant value (specifically 10 μ A) and the voltage across the *dummy* device (a 1 k Ω resistor) was measured multiple times using a reliable DAQ; after this the current across the resistor was increased in steps through a defined range and the voltage across the **DUT** was measured for each step. These tests were selected as they closely resemble the tests which were to be performed on the eventual SiCEB devices.

²The full specifications of Keithley's 220 current source are stated in the *Keithley 220 Programmable Current Source Data Sheet (2009)*.

³The 1 M Ω resistors shown in Figure 6.1 were used to offer protection to sensitive detectors and were not included in this test.

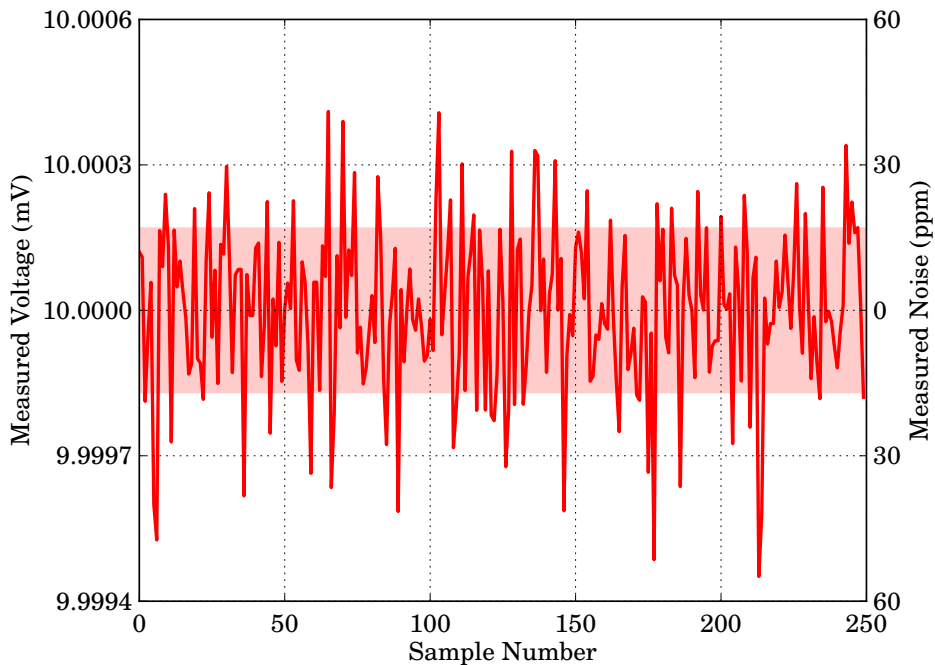


Figure 6.6: Jitter in a measurement caused by current supplied by a Keithley 220 Programmable Current Source. The current source was set to output a constant current of $10 \mu\text{A}$ which was driven across a $10 \text{k}\Omega$ resistor. Multiple measurements were made with a trusted data acquisition system. The primary vertical axis shows the voltage measured across the resistor in each measurement (the expected voltage was 10 mV); the secondary vertical axis shows the jitter or noise about the expected value in terms of noise parts per million; the shaded region shows the standard deviation of the noise about the expected value.

Figure 6.6 shows the measured jitter of a signal caused by the Keithley 200 unit. The signal varied around the expected value of 10 mV by up to 550 nV . The signal was measured by a trusted data acquisition system using shielded cables. This variation is equivalent to a peak-to-peak noise level of 110 ppm . The [Keithley 220 Programmable Current Source Data Sheet \(2009\)](#) states that when outputting a current of $10 \mu\text{A}$, the expected peak-to-peak noise level is 100 ppm ; although this is slightly lower than the measured value and thus indicates either an additional noise source or an issue with the unit, the measured jitter was still sufficiently low

enough for preliminary measurements.

There are several possible reasons for the small amount of additional jitter measured in this test. Both the Keithley 220 unit used and the triaxial cables used as interconnects between the current source and the device under test were several years old and it is entirely possible that a number of small breaks were present in either the cable's inner guard layer or the insulator; this could cause current to be lost between the innermost conductor and the outermost shield layer and thus, for current to be lost between these two. The age of the unit may also have meant that some of the internal components had degraded and were no longer working within their original specification. It is most likely that a combination of these factors caused the additional noise measured. It is also possible that the degrading of the interconnecting cables could have made the system more susceptible to electromagnetic pickup.

The noise voltage spectrum measured across the resistor is shown in Figure 6.7; this did not resemble the *clean* spectrum seen in Figure 6.5, instead there was a substantial tone, due to mains pickup, seen at 50 Hz. Along with several harmonics of this tone, there were various other noise sources evident, including two large clusters of tones at 4 & 8 kHz. These large clusters of noise tones were of particular concern, as they indicated that, in addition to the desired DC biasing signal, there could have been a substantial amount of power dissipated in the device under test from these sources. The cause of this noise was confirmed by repeating the measurement across the resistor, having disconnected the current supply. The result of this closely resembled that shown in Figure 6.5 and showed that the noise was due to the presence of the current supply. By disconnecting the interconnecting triaxial cable from the current supply, while leaving it attached to the device under test, it was found that the two clusters of high frequency tones were no longer present, this indicated that these were due to internal components within the current supply unit. However, many of the lower frequency tones remained, these were attributed to electromagnetic pickup in the cable. This result meant that the Keithley 220 current supply would not be appropriate for use when carrying out noise measurement, since there was substantial contamination of the signal.

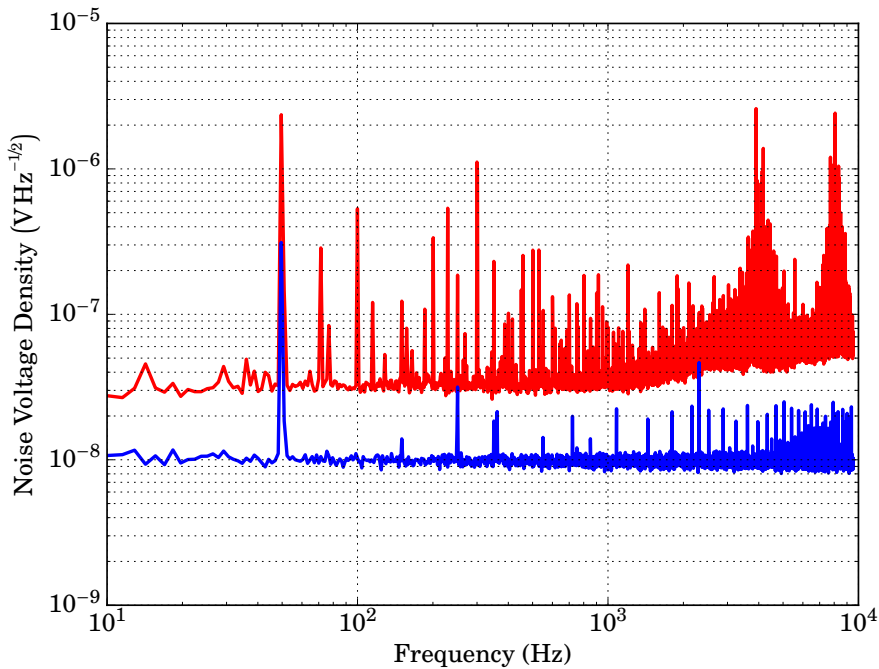


Figure 6.7: Noise spectrum measured across a resistor which was biased by the Keithley 220 Current Supply. A current of $10 \mu\text{A}$ was driven across the resistor and the voltage (and noise spectrum) was measured using a digital oscilloscope. It was expected that the noise spectrum would be dominated by the amplifier noise of $10 \text{ nV}\text{Hz}^{-1/2}$; it is clear that this measurement shows a white noise level greater than this and is dominated by several other sources.

6.4 REVISIONS TO THE INITIAL BIAS SYSTEM

6.4.1 CHANGES MADE AND ADVANTAGES

As was found by the test described in the previous section, the Keithley 220 current source was not appropriate for noise measurement, since there was substantial contamination (at AC frequencies) of the biasing signal from both electromagnetic pickup and the issues within the unit itself. To address this, a simple circuit was constructed which generated a controlled differential signal, which had an amplitude determined by a controllable input signal. This signal could then be

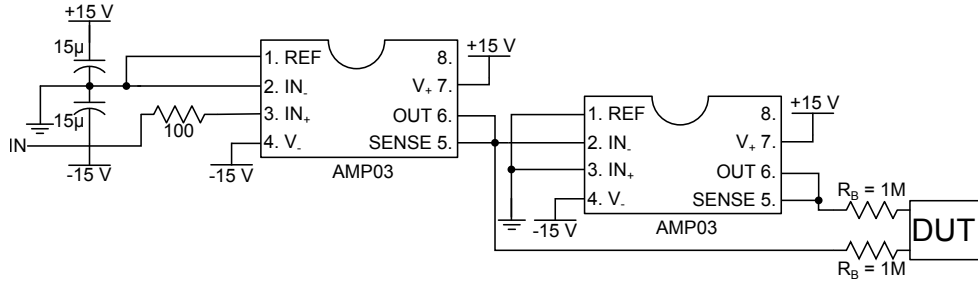


Figure 6.8: Circuit diagram for the custom-made internal bias generator used with the first amplifier. A single-ended input was fed to the non-inverting input of a unity gain amplifier, the output of this amplifier was split with one feed being supplied to the inverting input of a second unity gain amplifier. The output of this amplifier, along with that of the first, was then used to bias the device under test via a pair of biasing resistors.

converted to a biasing current via a pair of resistors and the resulting current was found using Ohm's Law and measuring the voltage dropped across these biasing resistors.

There are several advantages to housing the biasing unit inside the casing of the amplifier, which during device testing was directly mounted to a cryostat. Firstly, since no interconnecting cabling was required, the possibility of electromagnetic pickup was greatly reduced. Secondly, due to the close physical proximity of the amplifier and the current supply, it was possible to have greater control over the grounding of these two components and thus remove any ground loops which could have offset a measurement or contributed to the total noise measured. Further to this, since the biasing signal was now sent using a differential connection, there was no connection to ground across the device under test, so it is fully isolated from any possible ground loops or other contamination from the ground line. Finally, since the amplitude of the current was not directly controlled by the bias generator but instead was governed by an external source, it was possible to produce a smooth range of currents, as opposed to the Keithley unit which was only able to step current, albeit in relatively small steps.

The bias generator worked by using two unity gain amplifiers to generate a differential biasing signal, V_{in} , from a single-ended input. The input was fed into the non-inverting input of the first amplifier, the output of this was equal in

amplitude to the input signal and was then split, with one feed connected to the inverting input of the second amplifier. The output of the second amplifier was again equal in amplitude to the input signal but had the opposite sign; the output of this amplifier, along with that of first amplifier, served as the biasing voltage. This biasing voltage, V_{bias} , formed a differential signal and was given by:

$$V_{\text{bias}} = V_+ - V_-, \quad (6.7)$$

where V_+ and V_- are the outputs of the first and second amplifiers respectively. Since, in this case, the outputs of these amplifiers were $V_+ = +V_{\text{in}}$ and $V_- = -V_{\text{in}}$, the final biasing voltage was given by:

$$V_{\text{bias}} = 2V_{\text{in}}. \quad (6.8)$$

The biasing current, I_{bias} , across the device under test is the same as the current through the two biasing resistors, which from Ohm's Law is given by:

$$I_{\text{bias}} = \frac{V_R}{2R_{\text{bias}}}, \quad (6.9)$$

where V_R is the voltage dropped across the two biasing resistors. By measuring the voltage across the device under test, V_{DUT} , and knowing the voltage generated by the bias circuitry, the voltage dropped across the biasing resistor was given by:

$$V_R = V_{\text{bias}} - V_{\text{DUT}}. \quad (6.10)$$

By using the result of Equation 6.8, the above can be written as:

$$V_R = 2V_{\text{in}} - V_{\text{DUT}}. \quad (6.11)$$

Finally, combining this with Equation 6.9, the biasing current can be calculated by:

$$I_{\text{bias}} = \frac{2V_{\text{in}} - V_{\text{DUT}}}{2R_{\text{bias}}}. \quad (6.12)$$

There were further advantages of this biasing regime, offered by the fact that the system now used a differential signal to bias the device under test; since the device under test was now isolated from the ground line, which is often a source of signal contamination. This regime also offers a dramatic reduction in the effect of

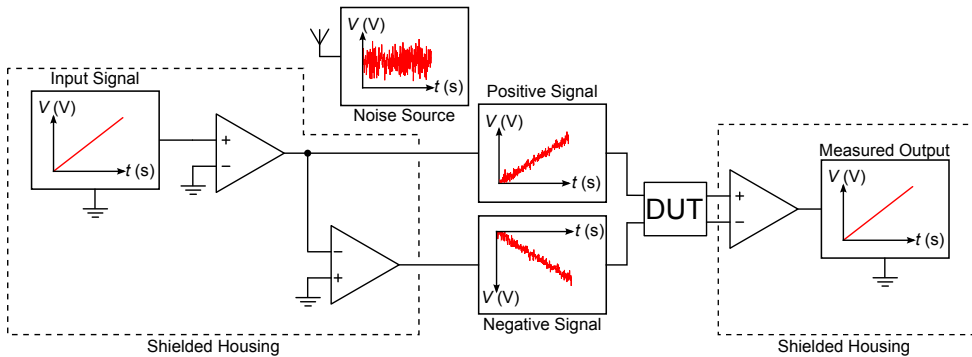


Figure 6.9: Rejection of common-mode noise in a differential-signal bias and readout system. The two amplifiers which make up the differential signal generator produce two signals, which are equal and opposite to each other and related in magnitude to the input signal. This is then carried, by a pair of wires, through an unshielded environment. Any electromagnetic pickup adds to both of these signals as a common mode; this does not affect the difference in amplitude between the two signals and thus is not measured by the final differential amplifier.

electromagnetic pickup. As this differential bias generator produced two signals of equal and opposite voltage and since noise due to electromagnetic pickup would have added to both, this meant that the difference between the two signals, at any given time, remained the same and the output of the final amplifier, which only depended on this difference, was not affected. In terms of differential signals, a change which maintains the same difference between the two signals is referred to as a common mode and when the difference between the two is affected, there is said to be a normal mode. This concept is illustrated in Figure 6.9.

6.4.2 PERFORMANCE OF THE UPDATED BIAS SYSTEM

In order to ascertain whether or not this current generator offered improved performance over the Keithley 220, the same tests that were described in Section 6.3.2 were repeated with the new system. Of particular interest were the results of measuring the noise spectrum produced by this system.

Figure 6.10 shows the jitter measured for the current generator which replaced the Keithley unit. The measured peak-to-peak jitter for this system was 200 ppm, which corresponded to a maximum variation of 1 μ V from the expected value.

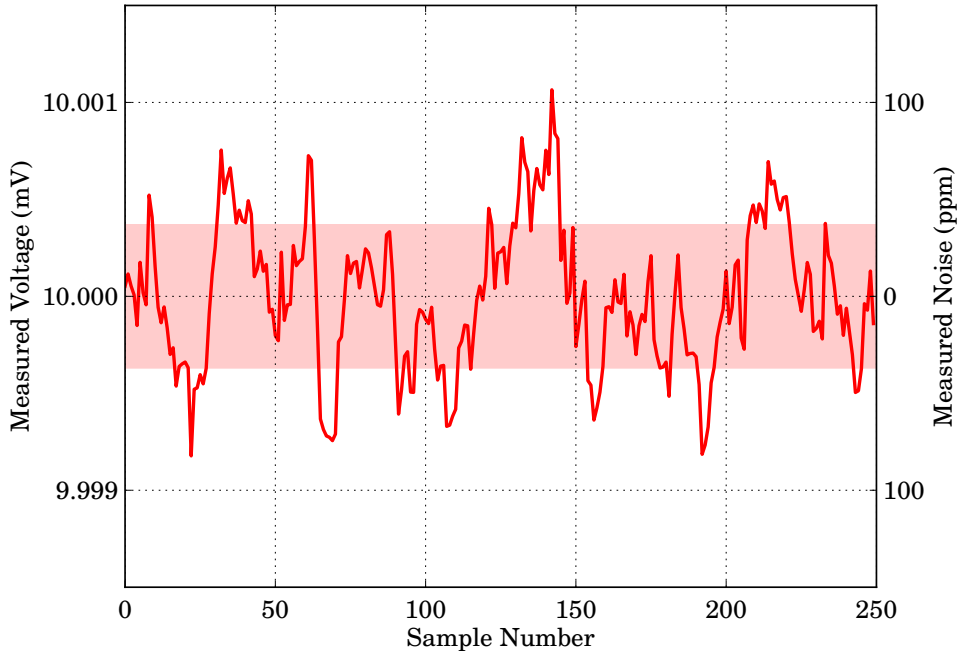


Figure 6.10: Jitter measured from custom-made current bias generator. The input voltage to the system was set such that a current of $10 \mu\text{A}$ flowed through the $1 \text{k}\Omega$ resistor (which took the place of the device under test). The voltage across the resistor was measured using a trusted data acquisition system. The primary vertical axis shows this voltage (which was expected to be 10 mV); the secondary vertical axis shows the jitter or noise about the expected value, in terms of noise parts per million; the shaded region shows the standard deviation of the noise about the expected value.

While this value is approximately twice what was measured in Section 6.3.2 for the Keithley unit (illustrated in Figure 6.6), this level was still deemed to be acceptable for *I-V* characterisation.

The noise spectrum measured across a resistor, biased using the newer current generator, is shown in Figure 6.11. When compared to the corresponding measurement in Section 6.3.1 for the Keithley 220 (Figure 6.7), it is noted that the noise spectrum measured here is much cleaner; there are far fewer noise tones present and the two clusters of tones seen at higher frequencies in Figure 6.7 are no longer

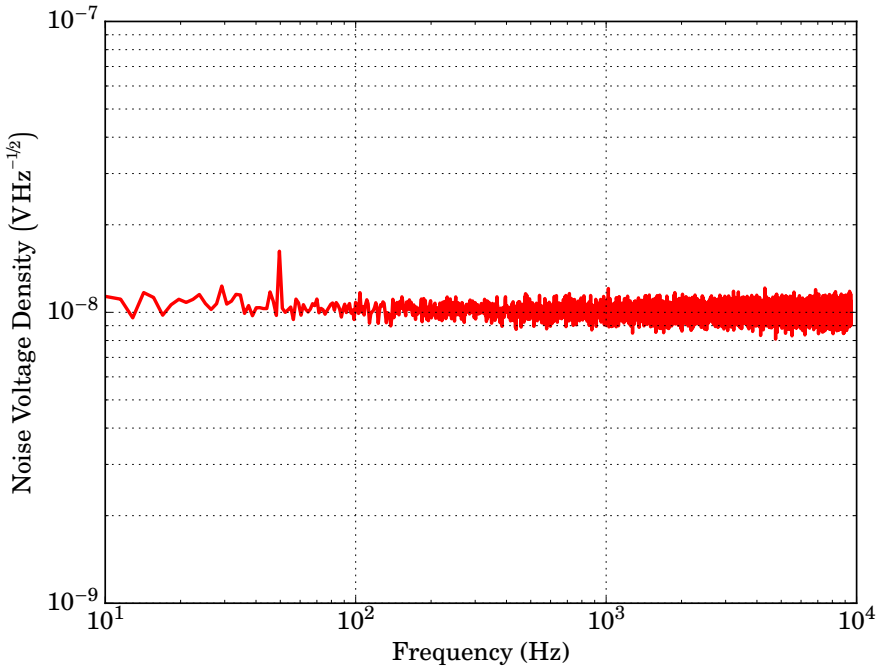


Figure 6.11: The noise spectrum measured across a $1\text{ k}\Omega$ resistor biased using the custom-made bias generator. When compared to the spectrum measured using the Keithley 220, shown in Figure 6.7, it is clear that the newer system showed very little contamination of this signal.

present. In fact, the only undesired feature present within the spectrum is the tone at 50 Hz, this was due to the 50 Hz variation of the mains power. The white noise level measured in this test was $10\text{ nVHz}^{-1/2}$ compared to a minimum value of $30\text{ nVHz}^{-1/2}$ (rising to over $70\text{ nVHz}^{-1/2}$) for the Keithley unit. In fact, when the noise spectrum shown in Figure 6.11 is compared to the measurement made with the input of the amplifier shorted (Figure 6.7), it is clear that the two compare extremely favourably. This showed that this measurement was limited by the internal noise generated by the readout amplifier (as shown in Section 6.3.1).

From these tests, it was clear that the revised biasing system offered a notable overall improvement when compared to the Keithley 220. Despite there being a decrease in the stability of the bias signal produced, the improvements to noise spectrum and the resulting reduction in unwanted power dissipated across the

device under test, meant that this system was used for the preliminary testing of **Cold-Electron Bolometer (CEB)** devices.

6.5 FINAL TESTING SYSTEM

6.5.1 REASON FOR REPLACEMENT

Despite having reached a stage where the initial readout system was performing as well as could have been expected of it, it became clear, as the testing of devices progressed, that its limitations were prohibiting the full characterisation of devices. When compared to list of desirable features for the readout system (as defined in Section 6.2), neither the second nor third points were met. That is to say that measurements of noise spectra were limited by the amplifier's own internal noise and that the amplifier did not offer sufficient bandwidth to allow the response speed of a detector to be measured.

For these reasons, it was decided to replace the initial readout amplifier and bias generator, which had been constructed from non-optimised components and designs already existing within the department, with a new specifically designed system. This system would continue to offer a bias generator similar to the one described in Section 6.4.1 but with the added feature of being able to internally supply the voltage input to the bias generator; this feature was desirable, as it would offer an ultra-low noise DC bias, albeit at the slight cost of functionality.⁴

6.5.2 FINAL READOUT SYSTEM

Figure 6.12 shows the amplifier used for the final stages of testing silicon cold-electron bolometers. The main amplification was performed by a INA103 chip manufactured by Texas Instruments.⁵ However, in order to provide a low-impedance input to the amplifier, as well as isolating the device under test from the amplifier circuitry, a matched pair of **Junction Field-Effect Transistor (JFET)** were used to create a differential source follower to act as the input of the amplifier.

One disadvantage of this configuration was that the addition of the **JFET** source followers meant that an offset voltage was added at the input of the amplifier. As

⁴Since this ultra-low noise level was only required when measuring noise spectra, the system could still be used in a way similar to the method described in Section 6.4.1 without any loss of functionality.

⁵12500 TI Boulevard, Dallas, Texas 75243, USA. Website: <http://www.ti.com>

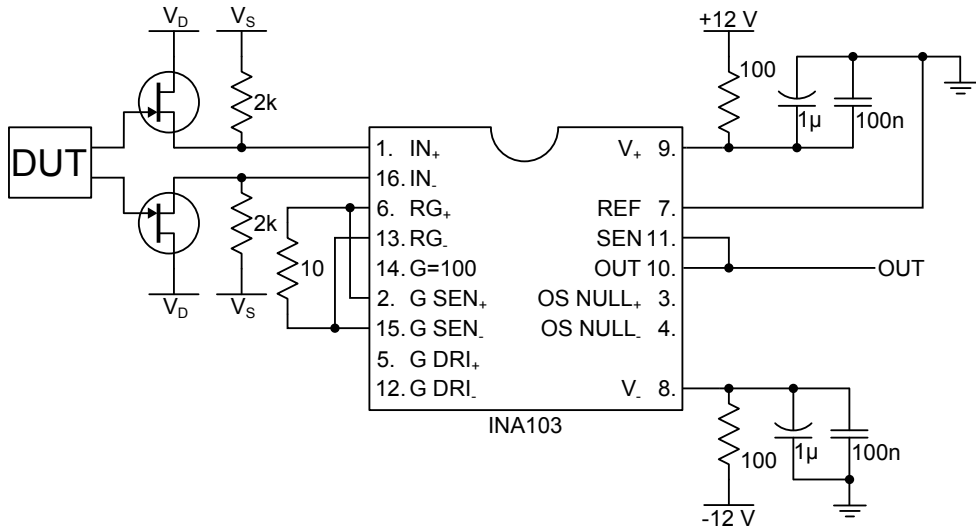


Figure 6.12: Final amplifier used for measuring voltage across devices. As opposed to the previous system (Figure 6.1), only one amplifier stage was used: the Texas Instruments INA103 amplifier, which was configured to offer a gain of 600. In addition to the amplifier, a matched pair of JFETs were used as source followers. This improved coupling to the amplifier by offering a low output impedance. It also isolated the amplifier from the device being measured, thus resulting in a lower noise level.

explained by Horowitz and Hill (1989, chap. 2), this is the result of inconsistencies in the current produced by a given voltage across the gate and source of the JFET. The reason for these inconsistencies is due to this parameter being poorly controlled in the manufacture of JFETs. This could have been addressed by including a second JFET, matched to the existing JFET, that acted to vary the source voltage to the first JFET, such that there would have been no voltage offset at the output (which would have been at the drain terminal of this second JFET). This modification was not however applied, since the differential input to the amplifier already necessitated that the two JFETs be matched and the increase to quad-matched JFETs was prohibitively expensive for a non-critical improvement.

The preliminary testing had indicated that the previous amplifier's gain of 1000 was possibly excessive. To this end, it was decided that a lower gain, of approximately 600, would be used in this case. The *INA103 Data Sheet* (2000) does not provide a table of the required resistance across the gain setting pins to achieve

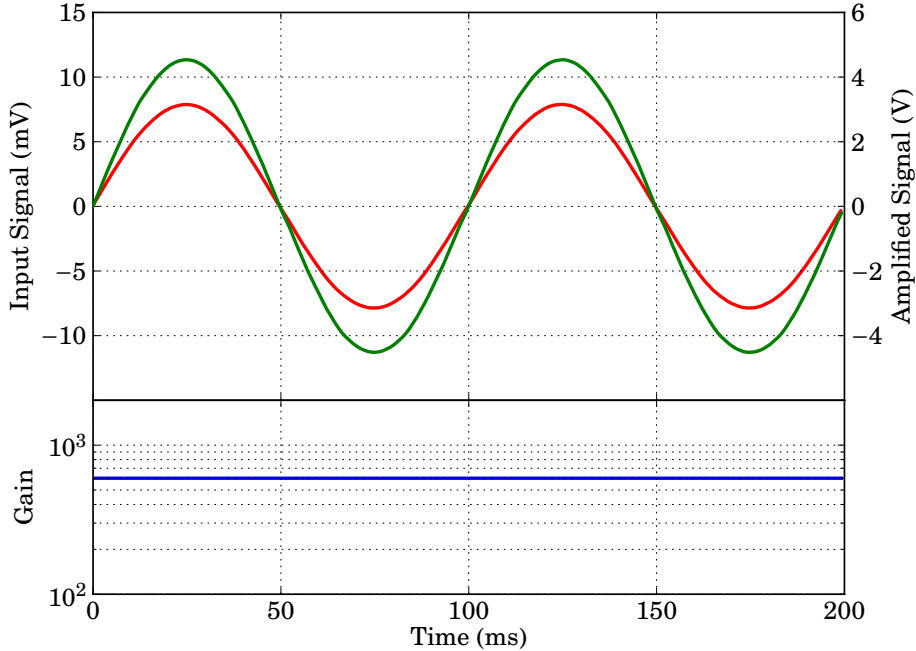


Figure 6.13: Gain measurement for the amplifier used in the final test of silicon cold-electron bolometers. As in Section 6.3.1, a 10 Hz sinusoidal signal was supplied to the input of the amplifier and the output measured. Upper plot—input signal (red, primary vertical axis) compared to the output of the amplifier (green, secondary vertical axis). Lower plot—gain measured from the ratio of the output and input signals.

this value, there is however the equation for the gain, G :

$$G = 1 + \frac{6000}{R_G}, \quad (6.13)$$

where R_G is the value of the gain setting resistor required to achieve a gain of G . Thus, the value of the resistor required for a gain of 600 could be found as:

$$R_{G=600} = \frac{6000}{600 - 1}, \quad (6.14)$$

$$R_{G=600} \approx 10. \quad (6.15)$$

As had been performed for the previous amplifier (Section 6.3.1), a sinusoidal signal was split, with one feed supplied to the input of the amplifier and the other,

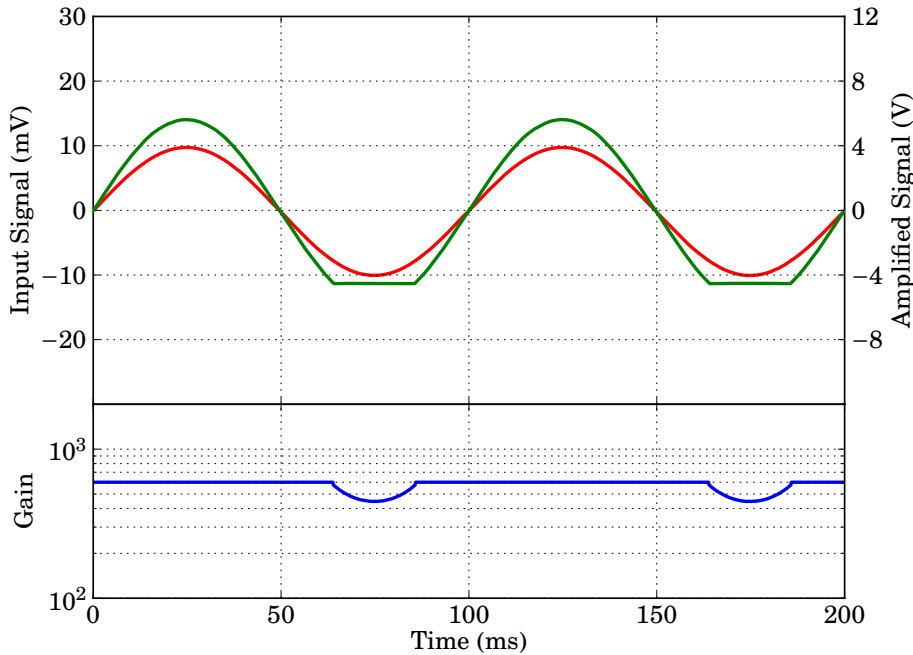


Figure 6.14: When the input to the final amplifier was increased above an amplitude of 7.5 mV, an asymmetric response was noted. While positive signal continued to be amplified, by a gain factor of 600, the negative signal with the same magnitude became limited to a certain minimum value. Upper plot—input signal (red, primary vertical axis) compared to the output of the amplifier (green, secondary vertical axis). Lower plot—gain measured from the ratio of the output and input signals.

along with the output of the amplifier, measured using a digital oscilloscope. The gain of the amplifier could then be calculated by simply taking the ratio of these two values. The results of these measurements are shown in Figure 6.13 where it can be seen that, for an input signal with an amplitude of 7.5 mV, there is uniform amplification at all amplitudes and the gain factor is 600.

The addition of the **JFET** source followers caused a further complication with this amplifier. Figure 6.14 shows what happened when the amplitude of the input signal to the amplifier was increased above the 7.5 mV illustrated in Figure 6.13. In Figure 6.14, it is clear that there is a lower limit to the output voltage (green

line shown on the secondary vertical axis) of approximately -4.5 V. In order to understand the origin of this limit and any significance it might have had on testing, it is important, as always, to fully understand how these data were collected. As has already been mentioned, the presence of the JFET source followers resulted in an (undesired) DC voltage offset to the input of the INA103 amplifier. When measured, this offset was found to be -6.59 V at the output of the amplifier (or -11 mV at the input). In order to correct for this in the measurement, the input of the digital oscilloscope (which was used for all the measurements in this section) was set to AC-coupling. This meant that values which were recorded as 0 V in the AC-coupled measurement corresponded to an output voltage of -6.59 V from the amplifier. The *INA103 Data Sheet (2000)* explains that the amplifier is capable of a maximum voltage output range of ± 11 V. By dividing by the gain of the amplifier (600 in the configuration used), it was possible to calculate the range of input voltages to the amplifier for which a correctly amplified output was attainable (i.e. those which corresponded to an output of less than ± 11 V); this was found to be ± 18.3 mV. As explained earlier however, the JFET source follower used resulted in an offset voltage of -11 mV at the input of amplifier. When this was subtracted from the input range of the amplifier, the effective range of input voltages, $V_{\text{input}_{\text{eff}}}$, was found to be

$$V_{\text{input}_{\text{eff}}} = V_{\text{input}} - V_{\text{offset}}, \quad (6.16)$$

$$= \pm 18.3 \text{ mV} - 11.0 \text{ mV}, \quad (6.17)$$

$$= \frac{+29.3}{-7.3} \text{ mV}. \quad (6.18)$$

While this result had the advantage of meaning the amplifier system had an increased range for positive signals, there was a severe restriction placed on the amplifier's ability to handle negative signals. Fortunately, the required measurable input voltage range for testing SiCEB devices was only of the order of ± 1 mV, with few circumstances existing where signals of greater magnitude were measured and none that would require measuring to as low as 7.3 mV across the device. For comparison, the previous amplifier's input range, which did not suffer from any asymmetry, was ± 13 mV.

Since the restricted range of input voltage did not, in fact, affect the amplifier's suitability for the measurements being undertaken, it was decided that there was no need to address this, despite it being non-ideal. As previously mentioned, the

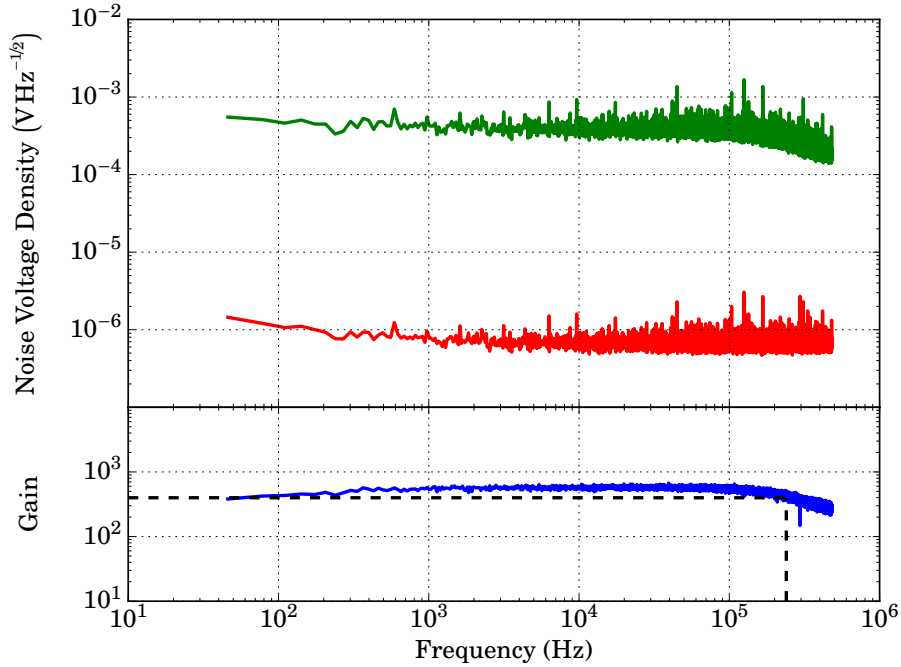


Figure 6.15: Bandwidth measurement of final amplifier. A white noise signal (red trace) was generated and supplied to the amplifier whose output (green trace) was also monitored. The ratio of these two (the gain—blue trace) was also calculated.

DC offset due to the **JFET** could have been removed via the addition of a second **JFET** on each input, if necessary.

In order to measure the 3-dB bandwidth of this amplifier, the same measuring procedure was used as for the initial amplifier (described fully in Section 6.3.1). A signal generator was used to create a white noise signal which was input to the amplifier. The output of the amplifier, along with the output of the signal generator, were monitored using a digital oscilloscope. To measure the bandwidth of the amplifier, the ratio of the input of the amplifier to its output (its gain) was measured; the results of this are shown in Figure 6.15. As explained by Equation 6.5, the edge of the 3-dB bandwidth corresponds to the frequency at which the gain has fallen by a factor of $\sqrt{2}$. The lower plot in Figure 6.15, shows the measured gain with the dashed lines illustrating the 3-dB level, which was a gain

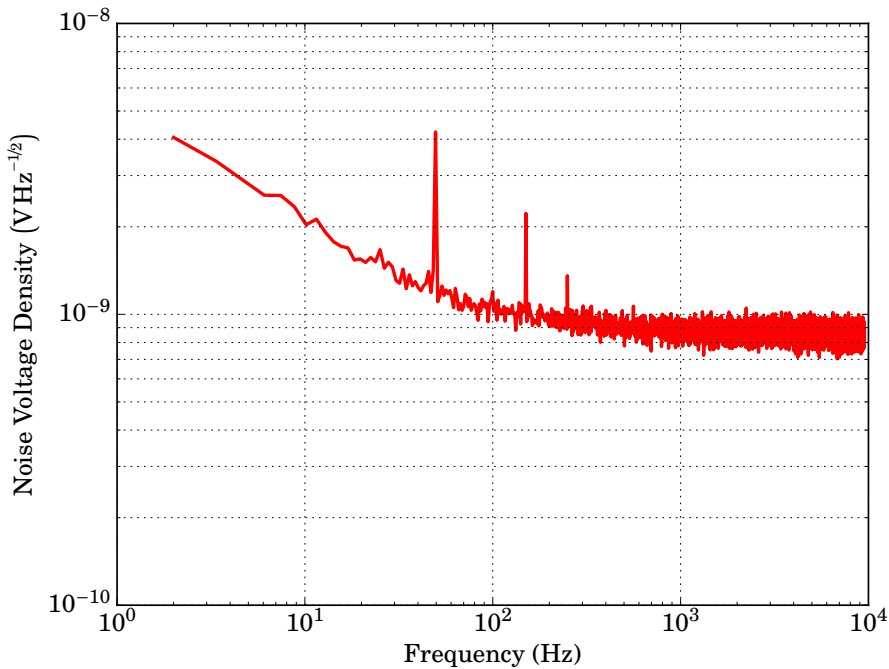


Figure 6.16: Measurement of the internal noise, referred to the input, for the final amplifier. This was measured with a shorted input of the amplifier.

of 424, and the corresponding frequency was found to be 240 kHz. This shows that the amplifier offered a substantial improvement compared to its predecessor, whose 3-dB bandwidth was equal to 55 kHz (calculated on Page 98). Although the [INA103 Data Sheet \(2000\)](#) does not provide a figure for the expected bandwidth of the amplifier when operating with a gain of 600, it does provide values of 6 MHz and 800 kHz for gains of 1 and 100 respectively, this seems to indicate that the value of 240 kHz, at a gain of 600, is to be expected.

Figure 6.16 shows the measurement of the internal noise of the final amplifier. This was measured with the input to the amplifier (the gates of the two **JFET** source followers) shorted such that there was a differential signal of 0 V at the input of the amplifier. The output of the amplifier was fed to a digital oscilloscope, which computed the Fourier transform of the signal. This was then divided by the gain (measured in Figure 6.13), to give the input-referred internal noise of the

amplifier. From Figure 6.16, it can be seen that the white noise level of this noise spectrum is approximately $1.5 \text{ nV}\text{Hz}^{-1/2}$ and that the spectrum is white from a few hundred Hertz up until the end of the measurement at 10 kHz.

When compared to the corresponding measurement for the previous amplifier, shown in Figure 6.5, two key differences are immediately apparent. Firstly, the newer amplifier has a substantially lower noise level, with the white noise floor of the previous amplifier having been $10 \text{ nV}\text{Hz}^{-1/2}$, compared to the newer device's level of $850 \text{ pV}\text{Hz}^{-1/2}$; this notable improvement was the key reason for switching to the newer amplifier. Secondly, there was a more pronounced level of $1/f$ noise visible in the spectrum for the newer amplifier compared to its predecessor. While this increase was indeed undesirable, the *INA103 Data Sheet (2000)* indicates that this is to be expected for this device and it is worth noting that even when allowing for this additional noise, the newer amplifier still offered lower noise at these frequencies than the previous amplifier.

These two tests showed that the replacement amplifier offered a notable improvement, in all areas, over the initial amplifier used and also showed that despite the newer device having some limitations not present in its predecessor (principally the asymmetric limit to the input voltage, shown in Figure 6.14), these limitations did not stop it from being fit for the testing required.

6.5.3 FINAL BIAS SYSTEM

For simplicity, a biasing system, similar to that described in Section 6.4 (which has been shown to function well), was integrated into this final system. The circuitry for this is shown in Figure 6.17. The only difference in operation between this circuit and the system used previously was the relation between the input signal and the differential output. For the previous system, this was 1:2, meaning for an input of 1 V, a differential signal of 2 V was output (as explained on Page 104). The key difference here was that, although both of the OP470 amplifiers (manufactured by Analog Devices and, in fact, housed within a single package) were configured to provide a gain factor of unity, an additional potential was included at the input of the first amplifier. This divider (the two $1.2 \text{ k}\Omega$ resistors seen in Figure 6.17) acted to reduce the input of the first amplifier by a factor of two. This meant that the output of each of the amplifiers was equal to one half of the input voltage, thus the total differential voltage at the output was the same as the input voltage. As in

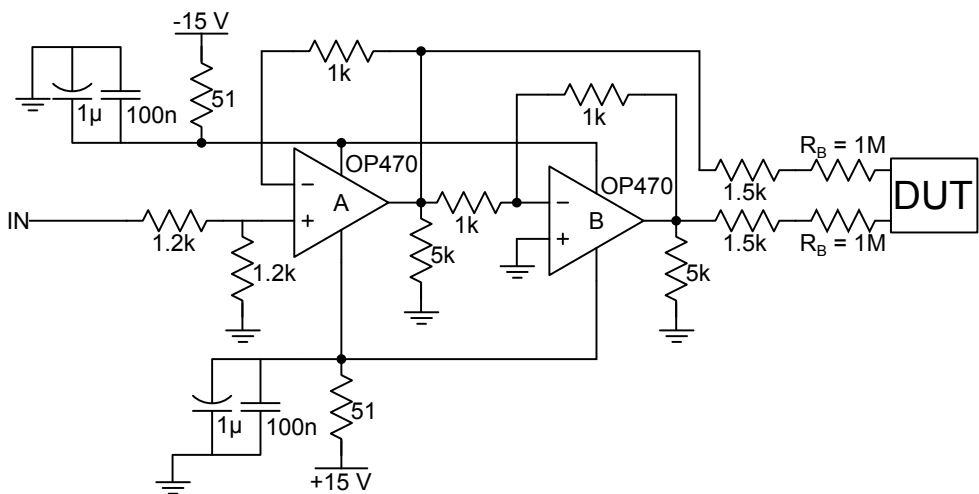


Figure 6.17: Circuitry used to generate a differential signal used to bias the device under test. The principle is the same as described in Section 6.4.

In the previous case, the device was biased via a pair of $1\text{ M}\Omega$ biasing resistors and the biasing current can be calculated similarly to the method on Page 104. For this system, using Equation 6.7, the biasing voltage V_{bias} was given simply by:

$$V_{\text{bias}} = V_{\text{in}}, \quad (6.19)$$

where V_{in} was the input voltage to the bias generator. This meant that the biasing current, I_{bias} , across the device under test was calculated as:

$$I_{\text{bias}} = \frac{V_R}{2R_{\text{bias}}}, \quad (6.9 \text{ revisited})$$

where V_R is again the voltage dropped across the biasing resistors and, given the result shown in Equation 6.19, was calculated by:

$$V_B = V_{in} - V_{DUT}, \quad (6.20)$$

where V_{DUT} is the voltage measured across the device under test. Finally, combining this with Equation 6.9 gave the final relation for the biasing current:

$$I_{\text{bias}} = \frac{V_{\text{in}} - V_{\text{DUT}}}{2R_{\text{bias}}} \quad (6.21)$$

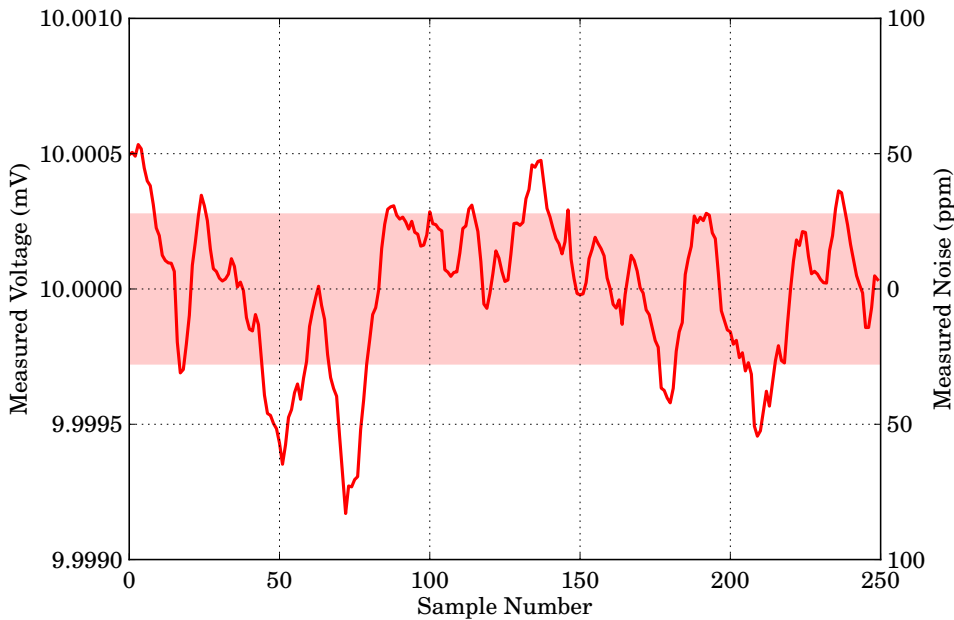


Figure 6.18: Measurement of jitter from the bias generator used with the final readout amplifier. The generator was configured to produce a biasing current of $1 \mu\text{A}$, which was driven across a $10 \text{ k}\Omega$ resistor.

As for the previous biasing systems, it was important to measure the jitter in the current produced. This was performed by configuring the bias generator to produce a current of $1 \mu\text{A}$, which was driven across a $10 \text{ k}\Omega$ resistor.⁶ This meant that the expected voltage measured across the resistor, according to Ohm's Law, was 10 mV . Figure 6.18 shows the results of this measurement. The maximum variation from the expected value was 800 nV which corresponded to a peak-to-peak jitter of 160 ppm . While this was still not as low as the jitter measured for the Keithley 220 unit, which was 110 ppm , it was, in fact, an improvement on the value of 200 ppm which was measured for the previous bias generator in Section 6.4.2. Since the jitter of the previous system had caused no problems, there was no reason to conclude that any issue would be presented here.

⁶The input voltage to the bias generator for this measurement was provided by using the system's on-board voltage (controlled through a potential divider) rather than an external source.

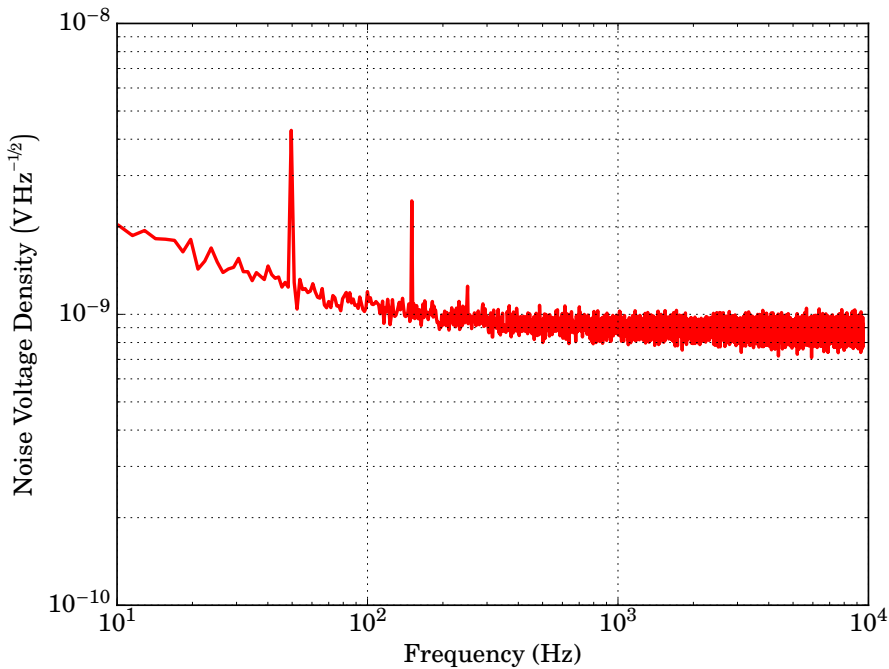


Figure 6.19: Noise measurement for the bias generator used in conjunction with the final readout system. A low value resistor ($\approx 10 \Omega$) was placed across the output generator and the amplifier was used to amplify the signal. The output of the amplifier was read by a digital oscilloscope which computed the noise spectrum.

Figure 6.19 shows the noise spectrum, measured using the amplifier described in Section 6.5.2, for a device (a low resistance resistor) biased by the system shown in Figure 6.17. Comparison between this figure and the noise spectrum shown in Figure 6.16 shows that the dominating noise is from the internal processes in the amplifier and that the bias generator did not contribute any additional noise to this measurement. This is the same as had been found for the previous bias generator system and is not a surprise considering the similarities, in operational principle, between the two systems.

6.6 CROSS-CORRELATED NOISE MEASUREMENT

Despite the improved (lower) noise limit of the system detailed in Section 6.5, this system was, at best, only able to measure noise generated within a device at optimum bias.⁷ To allow a full study of the sensitivity of a device, it was important to be able to measure the noise in the device over the greatest possible range of biases. To this end, an innovative solution was devised to reduce the noise level of the readout system. This was to split the voltage readout of the device between two identical amplifiers and then to use a computer to cross-correlate the output of these to effectively remove the noise contribution of the amplification.

6.6.1 CONVOLUTION

The convolution of two signals or functions is a third function whose amplitude is given by the area overlap of the functions f and g , when one of the functions is reversed and then translated across the other function. Common applications of convolution include: measuring the response function to an impulse function (Callier and Desoer, 1978); in probability, the convolution of two independent variables gives the probability distribution (Hogg et al., 2012); in acoustics and sound-engineering, reverberation is the convolution of an original signal with reflections (echos) from surfaces (Begault, 2007); in signal processing, a weighted average of a signal is a convolution.

In time-space, the convolution of two functions, f and g , is written as $f * g$. Mathematically, this is computed by reversing one of these functions such that $f(t) \rightarrow f(t - \tau)$ and is then translated across the other function. This can be written as an integral:

$$(f * g)(t) \stackrel{\text{def}}{=} \int_{-\infty}^{\infty} f(\tau)g(t - \tau) d\tau. \quad (6.22)$$

Convolution is commutative so $f * g = g * f$ or, more completely:

$$\begin{aligned} (f * g)(t) &\stackrel{\text{def}}{=} \int_{-\infty}^{\infty} f(\tau)g(t - \tau) d\tau, \\ &= \int_{-\infty}^{\infty} f(t - \tau)g(\tau) d\tau. \end{aligned} \quad (6.23)$$

⁷The dependance of various noise sources on the bias, or more correctly the bias dependant responsivity, is explained in Section 2.8.

It is, perhaps, easiest to understand convolution in the time domain graphically. This is shown in Figure 6.20. From this figure, it can be seen that the value of convolution at any time τ is given by the area overlap of the two functions (shown as the highlighted regions in Figures 6.20d to 6.20h), when the leading non-zero value of the reversed function ($g(t)$ in this case) is at τ . Convolution can be thought of, much more simply, in the frequency domain. As explained by Bracewell (2000, chap. 2), Convolution Theory states that the Fourier transform of the convolution of two functions is the multiplication of the Fourier transforms of the functions. This can be written as:

$$\mathcal{F}\{f * g\} = \mathcal{F}\{f\} \cdot \mathcal{F}\{g\} \quad (6.24)$$

where \mathcal{F} is the Fourier transform function, and f and g are functions.⁸ The convolution of two functions in the frequency domain is illustrated in Figure 6.21.

6.6.2 CROSS CORRELATION

Cross correlation is a mathematical process which can be used to measure the similarity of two functions or signals and is closely related to convolution. Mathematically, the cross correlation of two functions, $f(t)$ and $g(t)$, is defined as:

$$(f \star g)(t) \stackrel{\text{def}}{=} \int_{-\infty}^{\infty} f^*(-\tau) g(t - \tau) d\tau, \quad (6.25)$$

where f^* is the complex conjugate of f . A quick comparison to the definition of the convolution (Equation 6.22):

$$(f * g)(t) \stackrel{\text{def}}{=} \int_{-\infty}^{\infty} f(\tau) g(t - \tau) d\tau, \quad (\text{Equation 6.22 revisited})$$

shows that the convolution and cross correlation are simply related by:

$$f(t) \star g(t) = f^*(-t) * g(t). \quad (6.26)$$

6.6.3 APPLICATION OF CROSS CORRELATION TO DETECTOR READOUT

In order to completely characterise a detector, it is important to measure the electronic noise generated within the detector itself; this is because it is this noise

⁸The scalar product symbol (\cdot) is used in Equation 6.24 to avoid confusion with the vector product (\times), since the two Fourier transforms are multiplied on a point-by-point basis.

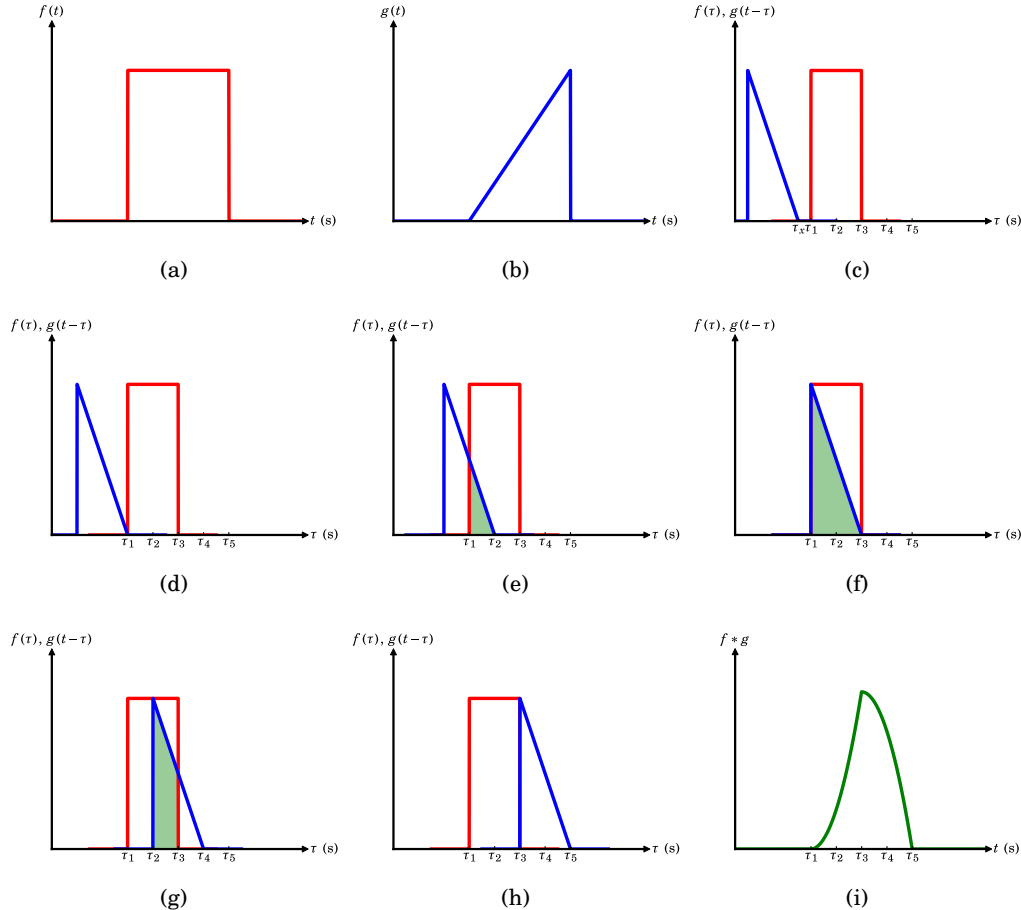


Figure 6.20: Graphical representation of convolution in the time domain. Two functions $f(t)$ and $g(t)$, are shown in parts (a) and (b) respectively. To find the convolution of the two functions, one function is reversed in time—this is shown in part (c) (in this case $g(t)$ was chosen), and it is then translated across the other function, shown in parts (d) through to (h). The value of the convolution at any time, τ , is the area overlap (shown as the highlighted areas in parts (d) through to (h)) of the two functions, when the leading non-zero value of the translated function is at τ . The convolution function is shown in part (i).

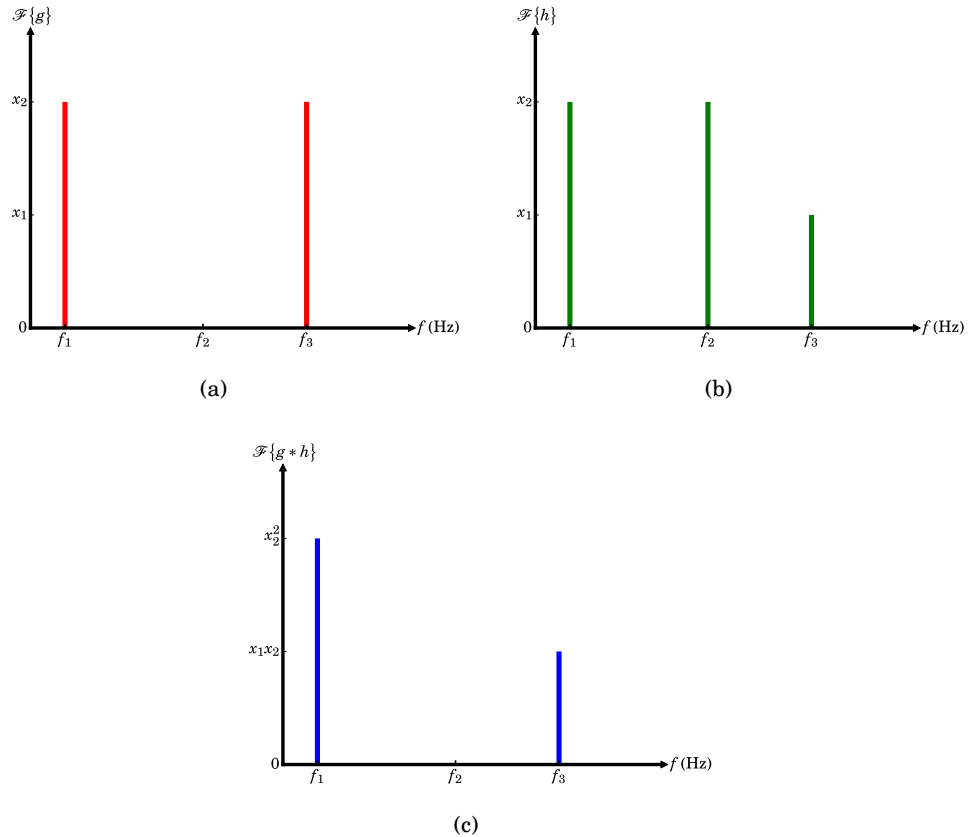


Figure 6.21: Convolution in the frequency domain. Two functions g and h , whose Fourier transforms ($\mathcal{F}\{g\}$ and $\mathcal{F}\{h\}$) are shown in (a) and (b) respectively. (c) shows the Fourier transform of the convolution of g and h ($\mathcal{F}\{g * h\}$); it can be clearly seen that this is the same as the point-by-point multiplication of the two Fourier transforms of g and h (as is expected from the convolution theory).

that will define the ultimate sensitivity of the detector (for a CEB-type detector the various internal noise sources have been covered in Section 2.7). The measurement of a detector's noise is complicated, however, by the fact that the amplitude of internal noise in the detector is, in most cases, much less than the input-referred noise of the readout amplifier. While it is possibly to simply state that in any realistic scenario, the performance of the detector (in terms of sensitivity, at least) will be limited by the amplifier and thus it is justifiable to calculate the sensitivity

of the detector based upon the noise of the readout amplifier; in a study of the detector itself (rather than an instrument utilising the detector), it is important to characterise the detector as completely as possible. This was one of the main reason for the switch from the readout amplifier described in Section 6.3 to that described in Section 6.5.

Unfortunately, the INA103 based amplifier (described in Section 6.5, which had an input-referred noise amplitude of $\sim 1 \text{ nV}\text{Hz}^{-1/2}$) was unable to directly measure the internal noise of the CEB detectors being studied. To address this, a novel readout and data-processing system was devised utilising two parallel JFET-buffered INA103 amplifiers (as shown in Figure 6.12) and cross correlating their outputs. The concept behind the design of this readout system was that, while the average noise amplitude of the two amplifiers would be the same, their noise spectra are not correlated, hence the cross-correlation techniques described above should be capable of removing the noise signal generated by the amplifier.⁹ On the other hand, the signal supplied to both amplifiers will be present and correlated in the output of both amplifiers and thus would be present after the two signals were cross correlated. The voltage output of the detector was split between the two amplifiers, with the output of each amplifier fed into a separate channel of a data acquisition system. Once the signals had been digitised by the data acquisition system, the two signals were cross correlated by National Instruments LabView software.¹⁰ A simplified process flow for the measurement of detector noise using this technique is shown in Figure 6.22.

The effect of using cross correlation to remove electrical noise introduced by readout amplifiers is illustrated in Figure 6.23, which shows simplified examples of the noise power spectrum at various stages of the process flow shown in Figure 6.22—the spectra shown in Figure 6.23 correspond to the points at which the process flow intercepts the dashed lines in Figure 6.22. Figure 6.22 shows that, while the majority of the noise contributed by the amplifiers is successfully removed, some features remain; this is due to the random probability of both amplifiers generating a tone at a given frequency. When both noise spectra contain features at corresponding frequencies, there will also be a tone at the same frequency in the

⁹Since the exact amplitude and frequency spectrum of the amplifier noise is random, it is clear that multiple cross-correlated acquisitions may need to be combined to remove the amplifier noise.

¹⁰National Instruments Corporation, 11500 Mopac Expwy, Austin, TX 78759-3504, USA. Website: <http://www.ni.com>

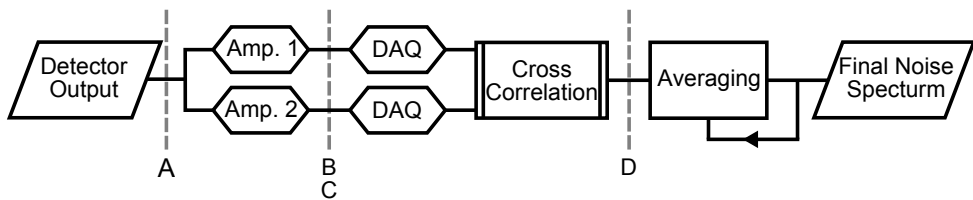


Figure 6.22: Simplified process flow for measurement of low levels of electrical noise by utilising cross correlation of two signals from a common source. Intersections with dashed lines correspond to the example noise power spectra shown in Figure 6.23.

cross-correlated spectrum. While this cannot be avoided, the amplitude of these tones can be substantially reduced with averaging.

The performance of this readout system has been both simulated (using artificial signals generated by National Instruments LabView software) and measured experimentally. Both the simulation and the measurements were of the amplifiers having a shared connection to a short (equivalent to the scenario for measuring the input-referred noise of an amplifier used throughout the work covered in this chapter). Figure 6.24 shows the results of the simulation (solid line), along with experimental data (open circles¹¹) and the expected noise level resulting from one of the amplifiers operating singularly. It can be seen from Figure 6.24 that the simulation and measured data are in excellent agreement. Both the simulation and the measured data start above the specified amplifier noise; this is due to the mechanics of the noise measurement and the possibility of a single cross-correlated acquisition causing an increase in the noise. After a small number of acquisitions (approximately ten), the measured noise level has dropped to that of the input-referred noise of a single amplifier. With continued acquisitions, the noise level continues to drop until a constant level, well below the amplifiers' input-referred noise, is reached. Sampietro et al. (1999), who describe a similar configuration used in a signal analyser,¹² explain that the noise floor is due to stray capacitances in the system which cause each amplifier's noise to weakly couple back into the detector,

¹¹For clarity, the experimental data have been reduced prior to plotting.

¹²Note that to the best of the author knowledge neither the system nor the techniques described by Sampietro et al. (1999) have been used to readout a detector and this work represents the first description of such a measurement.

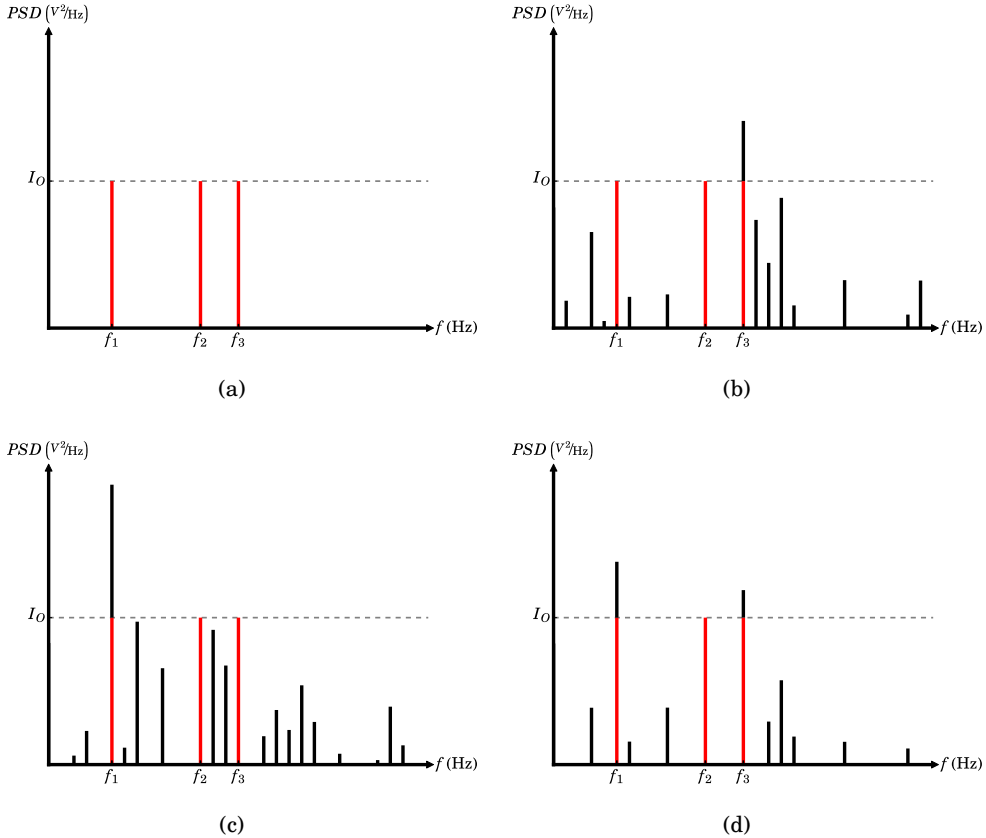


Figure 6.23: Removal of amplifier noise from a measurement by the use of cross correlation. (a) Power spectrum of detector output; the signal consists of three tones, each of intensity I_0 , at frequencies f_1 , f_2 and f_3 . (b) and (c) Outputs of the two parallel amplifiers; the signal (shown in red) is still present however the power spectra now also includes several other features including noise which has affected the signal at f_3 in (b) and f_1 in (c). (d) Output from readout system without any averaging; the majority of the noise introduced by the amplifiers has been removed (some features remain due to the random nature of the noise generated by the amplifiers, meaning that it is possible for features to exist at the same frequency in the outputs of both amplifiers, such features will *survive* the cross correlation). The alteration to the signal at f_1 and f_3 has also been reduced. Subfigure numbering corresponds to the points at which the signal intersects with the dashed lines in Figure 6.22. (Colours for reference only.)

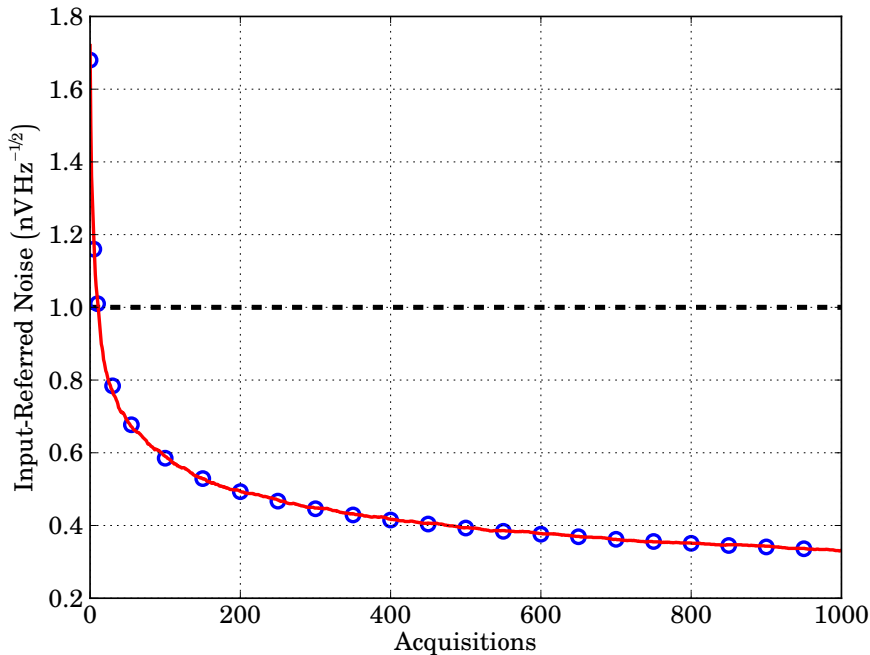


Figure 6.24: Reduction in input-referred noise with increased number of averaged acquisitions for cross-correlated amplifiers. Solid line—simulation performed in National Instruments LabView software. Open circles—Experimental data. Dashed line—Expected input-referred noise for a single INA103 amplifier. It is clear that the simulation and experimental data are in excellent agreement.

resulting in a low level of correlated amplifier noise. The minimum achieved input-referred noise of the cross-correlated amplifier setup was found to be approximately $330 \text{ pVHz}^{-1/2}$.

6.7 SUMMARY OF READOUT AND BIASING SYSTEMS

As has been covered in this chapter, a number of systems have been developed and used to measure SiCEB detectors. While the majority of the measurements presented in this work were performed with the equipment described in Section 6.5 (with successful measurements of the device and photon noise performed using the

techniques described in Section 6.6), some early measurements were performed with the systems described earlier in this chapter (where this is the case, it has been made apparent). A summary of the performance of the various bias systems and readout amplifiers described throughout this chapter is given in Tables 6.1 and 6.2 respectively.

Table 6.1: Summary of detector bias systems.

System	Bias Jitter (μA)	Notes
Keithley 220	0.55	See below ^a
Initial custom bias generator ^b	1.00	
Final custom bias generator ^c	0.80	

^a This unit caused substantial levels of electrical noise to be introduced into the measurement (as seen in Figure 6.7).

^b Based upon Analog Devices' AMP03 amplifier.

^c Based upon Analog Devices' OP470 amplifier.

Table 6.2: Summary of detector readout systems.

System	Gain	Input Range (mV)	3-dB BW (kHz)	IRN ($\text{nV}\text{Hz}^{-1/2}$)
Initial System	1000	± 12.7	55	10.00
Final System	600	$^{+29.3}_{-7.3}$	240	0.85
Final System w/ Cross-Correlation	600	$^{+29.3}_{-7.3}$	240	0.33

Chapter Seven

Results: Dark Measurements

*'The most exciting phrase to hear in science, the one
that heralds new discoveries, is not 'Eureka!' but
'That's funny...?'*
—ISAAC ASIMOV

7.1 INTRODUCTION

The first stage of device testing was to characterise the device in the absence of any optical signal. These tests were performed in the first of the two cryogenic systems described in Chapter 5. The purpose of these tests were: firstly, to ascertain that the detectors had been fabricated correctly, that is to say that a Schottky contact had formed between the aluminium and the doped silicon; the second goal of these measurements was to produce a set of data to which later—optical—data could be compared. The characterisation performed in these measurements concentrated on the current-voltage relationship of the detectors at various different bath temperatures. Attempts were also made to measure the device noise at this point; however, it was found that the amplifier noise of the readout circuitry used at the time dominated these measurements.¹

¹This was the reason the system described in Section 6.6 was devised.

7.2 UNSTRAINED SILICON

It is logical to start the exploration of silicon cold-electron bolometers with the devices fabricated from the unstrained (but still highly-doped) silicon material; the structure of these devices has already been illustrated in Figure 4.6a. This device could be thought of as offering a benchmark to which the performance of a detector utilising strained silicon could be compared. Inspection of Equation 2.121 shows immediately that a key limiting parameter to the noise-equivalent power is the electron-phonon coupling, Σ ; Table 4.3 shows that this parameter is substantially larger for an unstrained detector compared to a detector using strained silicon (by a factor of 26, in fact). From this, it is immediately clear that one should expect the detector described in this section to be less sensitive than the detector utilising strained silicon, which is described later in this chapter. Furthermore, Equations 2.61 and 2.71 show that the responsivity, in either bias regime, is decreased for increased electron-phonon coupling, further increasing the noise-equivalent power (reducing the detectors sensitivity).

The *current-voltage (I-V)* characteristics of the unstrained-SiCEB have been tested in the pulse-tube-cooled system detailed in Section 5.3.1 and were performed with the bias and readout system described in Section 6.5. The current-voltage characteristics at various bath temperatures are shown in Figure 7.1.

Examination of Figure 7.1 shows that, for low bath temperatures, the *I-V* curve is highly non-linear. The low voltage area corresponds to where the Fermi level in the silicon aligns with the energy gap within the superconductor and thus electrons cannot tunnel out of the silicon absorber into the superconducting contacts (this corresponds to the scenario shown in Figure 2.3). As the voltage across the device increases, the energy levels in the semiconductor and superconducting contacts are rearranged, such that the Fermi level within the semiconductor corresponds to the vacant states above the superconducting energy gap, allowing carriers to exit the semiconductor via the tunnelling contacts (the arrangement shown in Figure 2.4). This change is seen in the *I-V* curve by the increased gradient (lower resistance) at higher biases. At the highest biases, where the Fermi level in the semiconductor is well above the superconductor's energy gap, the *I-V* curve is linear, with a resistance determined by the sum of the two tunnelling resistances and the resistance of the silicon absorber itself. It should be mentioned that the data quality in Figure 7.1 is lower than might have been desired; this has been attributed to

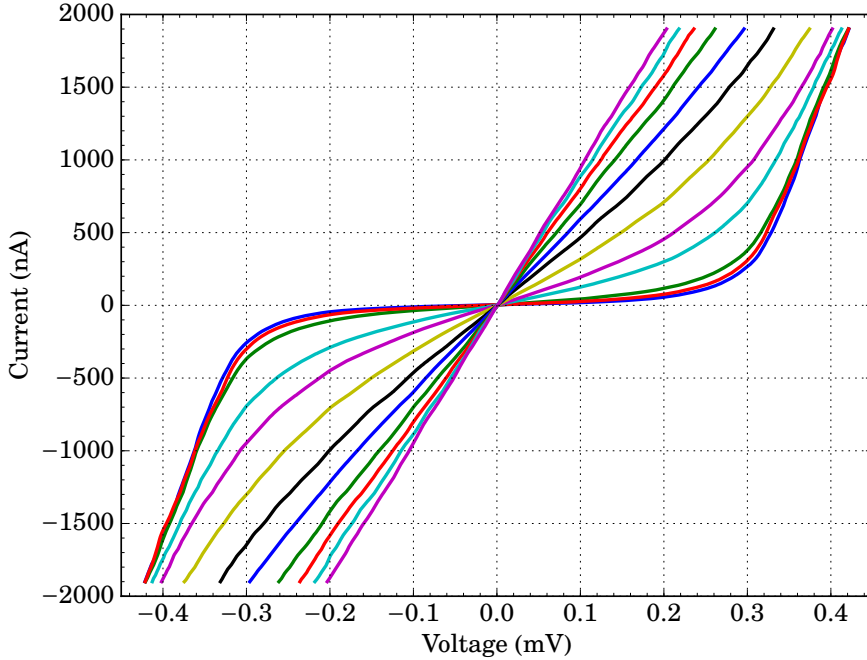


Figure 7.1: Current-voltage characteristics for a **SiCEB** with an unstrained absorber at various bath temperatures. Bath temperature from outermost (blue) to innermost (magenta, second occurrence): 0.30, 0.35, 0.40, 0.45, 0.50, 0.60, 0.70, 0.80, 0.90, 1.00, 1.10, and 1.20 K.

contamination of the signals within the pulse-tube cooled testbed. Specifically, it is believed that this was caused by microphonic noise introduced by the pulse tube cooler, combined with pickup from the refrigerator control and monitoring circuitry. As will be seen later in this chapter, these issues were addressed for later, more critical, measurements.

As the bath temperature was increased (the outermost curve in Figure 7.1 corresponds to the lowest bath temperature), it is clear that the non-linearity of the *I-V* curve diminished. This is due to the reduction of the superconducting energy gap (as shown in Figure 2.6) with increasing temperature. As the gap decreases, the energy needed to align the absorber with the vacant states above the superconducting gap decreases accordingly, until the situation where $T_{\text{bath}} = T_c$; at which point, the gap is diminished to zero and no additional energy is required for

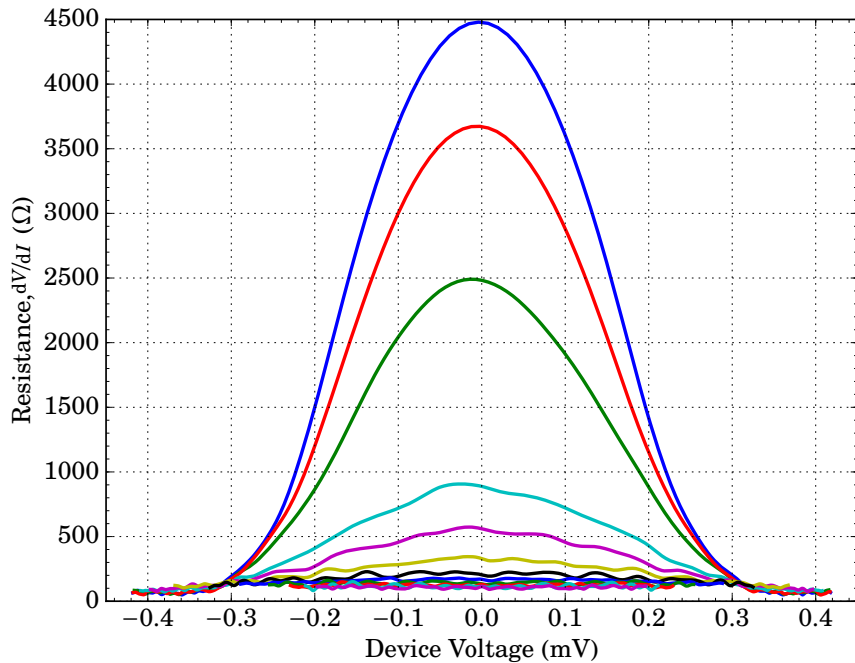


Figure 7.2: Differential resistance for a SiCEB with an unstrained absorber at various bath temperatures. Colours as in Figure 7.1. Bath temperature from outermost (blue) to innermost (magenta, second occurrence): 0.30, 0.35, 0.40, 0.45, 0.50, 0.60, 0.70, 0.80, 0.90, 1.00, 1.10, and 1.20 K.

tunnelling from the absorber to the contacts. The case where $T_{\text{bath}} = T_c$ is shown by the innermost curve of Figure 7.1, which is entirely linear with a resistance corresponding to the tunnelling resistance (along with any contribution from the absorber and the now normal-state contacts) at all biases.

An alternative way of viewing the data shown in Figure 7.1 is to calculate the differential resistance (dV/dI) of the detector as a function of either the voltage across the detector or the current flowing through the detector. This is shown in Figure 7.2.² It is clear from this figure that, as the voltage across the detector increases, the resistance tends to the same value which is independent of the bath temperature, this value is the sum of the two tunnelling (Schottky barrier)

²Device voltage was selected as the x-axis of Figure 7.2 simply because this selection produced a clearer figure.

resistances. Closer inspection of the various data found this value to be of the order 60Ω . This is lower than the anticipated value of 260Ω which was derived from combining the anticipated contact resistance of 107Ω per contact with the absorber resistance of 50Ω . This discrepancy was most likely due to a Schottky contact not being formed evenly throughout the contact area but instead some areas forming Ohmic contacts. From observing these data, and those presented in Figure 7.1, it becomes apparent that the superconducting gap was not, in fact, described by a transition temperature of for the aluminium of $T_c = 1.20 \text{ K}$ as anticipated but instead a value of $T_c = 1.05 \text{ K}$ describes the data better. This was most likely due to contamination of the aluminium during deposition or during storage of the device. This may also be the cause of the lower-than-expected normal-state resistance.

Using the data presented in Figure 7.1, it was possible to compute the electron temperature, T_e as a function of either the voltage across or current through the detector.³ This has been performed by fitting the data using Equation 2.30 with T_e as the only free parameter. In order to do this, the data first needed to be prepared by noting a few facts about Equation 2.30 (previously discussed in Chapter 2). Firstly, Equation 2.30 only computes the current due to electron tunnelling through the barrier, it does not allow for the current drawn due to the series resistance of the detector's absorber, R_{abs} ; to address this, it was necessary to scale the voltage such that the current due to this resistance was removed, this voltage, V_J was simply given by:

$$V_J = V_{\text{CEB}} - IR_{\text{abs}}, \quad (7.1)$$

where V_J is the voltage dropped through the two junctions, V_{CEB} is the total voltage across the detector, I is the current flowing through the detector, and R_{abs} is the resistance of the absorber. Secondly, R_N in Equation 2.30 is the normal-state resistance of the structure (excluding the absorber resistance, as discussed above); that is to say, the resistance of tunnelling through both junctions of the detector as seen at higher biases in Figure 7.1. Equation 2.30 however, computes the current due to a single junction and, as such, it was necessary to simply divide the normal-state resistance by a factor of two.⁴

³As previously mentioned for Figure 7.2, figures have most commonly been plotted as a function of the device voltage for clarity, along with providing a clearer link to the underlying physical processes.

⁴Note that Equation 2.30 already divides the voltage by a factor of two to allow for the series arrangement of two identical junctions.

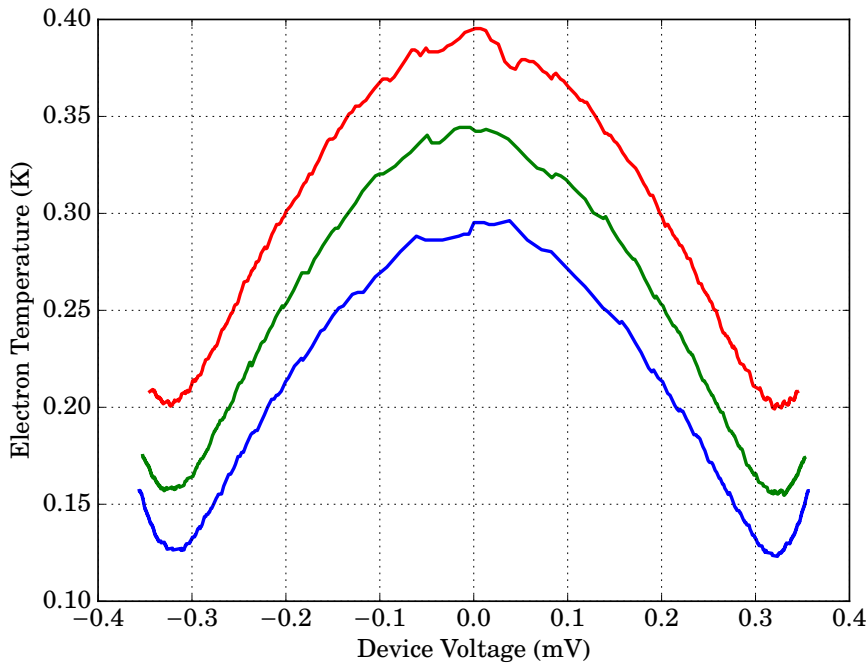


Figure 7.3: Electron-temperature fitting for SiCEB with an unstrained absorber at low bath temperatures. Bath temperatures from bottom to top: 0.30, 0.35, and 0.40 K. Note that $T_e = T_{\text{bath}}$ at $V = 0$.

This electron-temperature fitting has been performed for the data presented in Figure 7.1 (using the parameters given in Table 7.1) and is shown in Figure 7.3 for the three lowest bath temperatures available 0.30, 0.35, and 0.40 K. It is clear from this figure that the electron temperature is equal to the bath temperature at zero bias and falls to a minimum at a voltage slightly below $2\Delta_e$ (≈ 0.30 mV for this device). At voltages beyond $\approx 2\Delta_e$, the temperature of the electrons starts to climb rapidly; this climb corresponds to the situation where a great number of carriers in the absorber have energies corresponding to the vacant states above the superconductor's energy gap and tunnelling becomes decreasingly thermally selective.

Table 7.1: Parameters used in electron-temperature fitting of unstrained-silicon detector without optical loading.

R_{abs}	$2R_N$	V_J	Δ	$\Delta_{T=0}$	T_c
37 Ω	60 Ω	$V_{\text{dev}} - IR_{\text{abs}}$	BCS, $\Delta(T_e, T_c)$	160 μeV	1.05 K

7.3 STRAINED SILICON

The same measurements detailed in the previous section have been performed for a detector utilising a strained-silicon absorber. The expectation for this device was that it should show an ability to access lower electron temperatures, due to reduced power flow between the phonons and the electrons in this material.

The current-voltage characteristics for the strained-silicon devices are shown in Figure 7.4. An immediate comparison which can be made is that the I - V curves measured at the lowest temperatures are much more tightly grouped than was seen in Figure 7.1 for the unstrained device. To illustrate this point, the inset plot in Figure 7.4 shows the current-voltage relationship around the area $V = 2\mathcal{A}_e$, allowing the two coldest measurements ($T_{\text{bath}} = 0.30$ and 0.35 K, the outermost blue and green curves) to be seen distinctly. Closer comparison of the unstrained and strained measurements also shows that the I - V curves in Figure 7.4 are flatter in the sub-gap region ($V = -0.3 - +0.3$ mV); this indicates that a higher quality Schottky junction has been formed and, as a result, the so-called sub-gap leakage is reduced.

Some of the key differences between these data and the previously covered data for the unstrained silicon can be seen by examining the resistance of the detector as a function of the voltage across the device (as was done in Figure 7.2 for the unstrained-silicon device), this is shown in Figure 7.5. Firstly, the data presented in this section indicate a critical temperature of $T_c = 1.2$ mK for the aluminium, as was expected, and as such present an improvement over the results contained in the preceding section. The normal-state resistance of the strained-silicon device was noticeably higher than that of the unstrained detector, 580 Ω compared to 60 Ω measured for the unstrained detector. This increase was to be expected since the aluminium-silicon-junction resistance was shown in Table 4.3 to be higher by a factor of almost 40 for this material than for the unstrained material. The discrepancy between this value and the measured ratio of the two normal-state

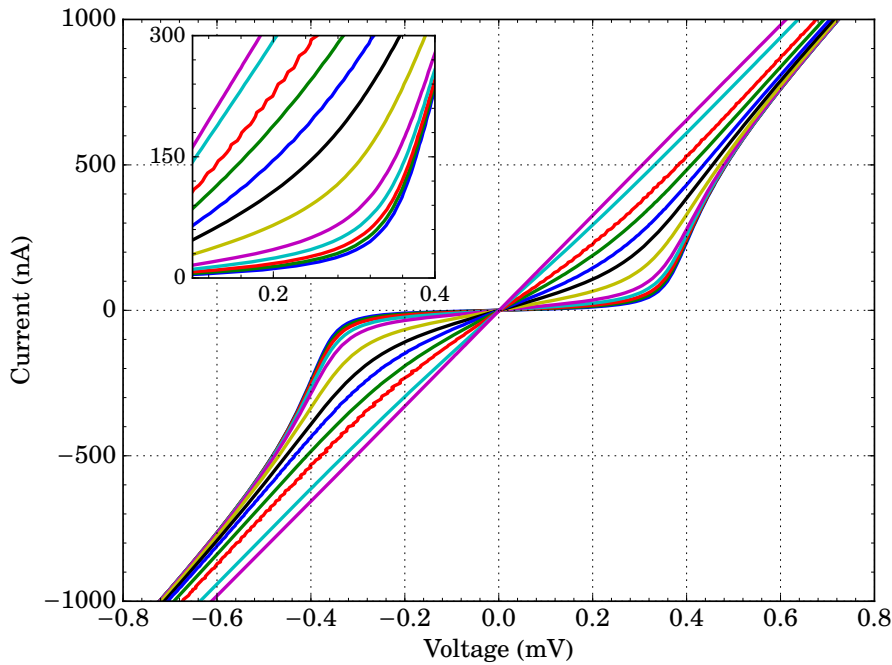


Figure 7.4: Current-voltage characteristics for a **SiCEB** with a strained absorber at various bath temperatures. Inset—zoomed-in plot around voltages corresponding to $2\Delta_e$ to show the difference in the I - V curves at the lowest bath temperatures; the axes are the same as in the main figure. Bath temperature from outermost (blue) to innermost (magenta, second occurrence): 0.30, 0.35, 0.40, 0.45, 0.50, 0.60, 0.70, 0.80, 0.90, 1.00, 1.10, and 1.20 K, inset colours and areas as in main figure.

resistances is further indication that high-quality Schottky contacts may not have formed evenly across the entire contact area during fabrication. A further increase in the normal-state resistance was to be expected, due to the slightly higher sheet resistance of the strained material; this resulted in the absorber resistance being 75Ω (compared to 50Ω for the unstrained detector). This difference, however, is clearly negligible compared to the change in the contact resistance.

As was performed for the unstrained-silicon device, the electron temperature has been calculated (after the previously discussed relevant changes were made) for this device. The results of this are shown for the three lowest bath temperatures

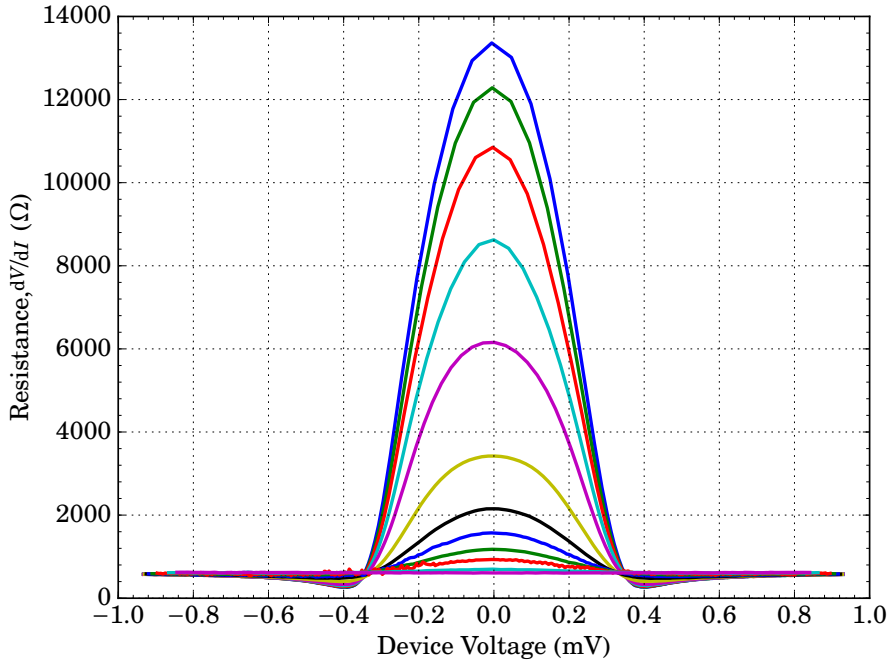


Figure 7.5: Differential resistance of a **SiCEB** with a strained absorber at various bath temperatures. Bath temperature from top (blue) to bottom (magenta, second occurrence): 0.30, 0.35, 0.40, 0.45, 0.50, 0.60, 0.70, 0.80, 0.90, 1.00, 1.10, and 1.20 K.

(0.30, 0.35, and 0.40 K) in Figure 7.6 (the parameters used in this temperature fitting are given in Table 7.2). This figure shows that at optimum bias, the device was able to self-cool to electron temperatures of ≈ 100 mK from an initial bath temperature of 300 mK. The overall behaviour of this device seems much as expected, with the electron temperature at zero bias being set by the temperature of the phonons (the bath temperature); the minimum value of electron temperature again occurs at the situation where the absorber's Fermi level is aligned with the top of the superconducting energy gap.

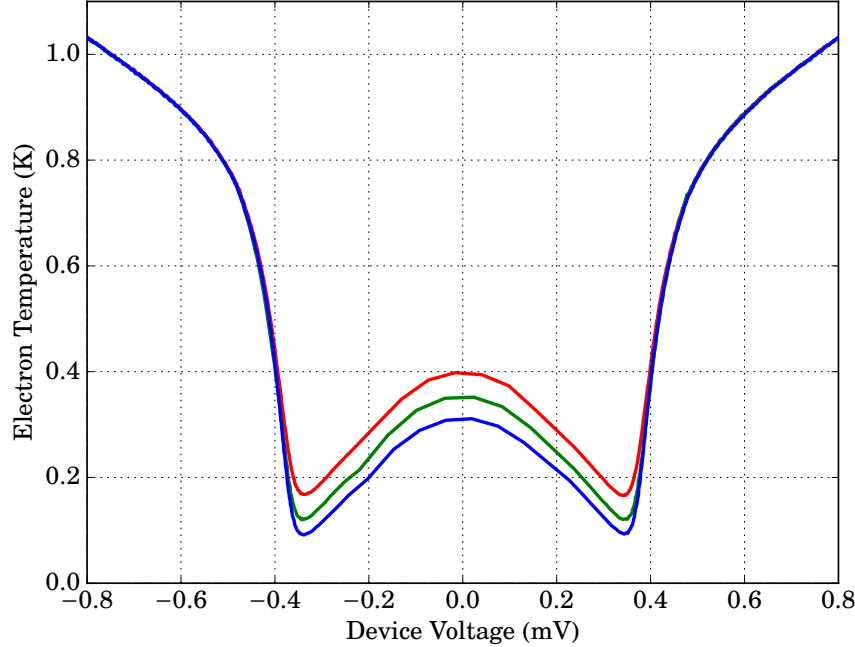


Figure 7.6: Electron temperature for a strained-silicon cold-electron bolometer at low bath temperatures. Bath temperatures from bottom to top: 0.30, 0.35, and 0.40 K. Note that $T_e = T_{\text{bath}}$ at $V = 0$.

Table 7.2: Parameters used in electron-temperature fitting of strained-silicon detector.

R_{abs}	$2R_N$	V_J	Δ	$\Delta_{T=0}$	T_c
75 Ω	580 Ω	$V_{\text{dev}} - IR_{\text{abs}}$	BCS, $\Delta(T_e, T_c)$	182 μeV	1.2 K

7.4 COMPARISON OF UNSTRAINED & STRAINED DETECTORS

A simple comparison between the two devices tested here can be made by comparing the measured characteristics on a like-for-like basis. Comparing the current-voltage curves of the two detectors (Figures 7.1 and 7.4) (as has been done, for 300-mK *I-V* curves in Figure 7.7) it can be seen that the curves for the strained-silicon

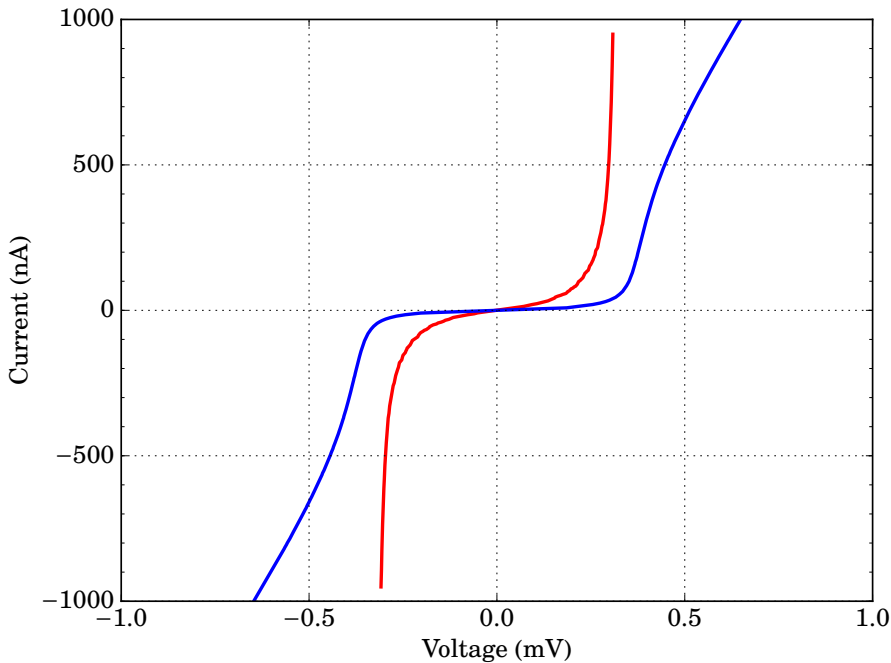


Figure 7.7: Comparison of I - V curves for the unstrained (red) and strained (blue) devices. Using I - V curves measured at 300 mK

detector have a much greater resistance below the superconducting gap (this point is made much more clearly from Figures 7.2 and 7.5, which show the resistance of the device). It can also be seen that tunnelling occurs at slightly lower voltages in the unstrained device compared to the strained detector, this is not a property of the absorber but possibly a sign of a small issue with the aluminium contacts to the detector; this may also explain the lower sub-gap resistance in this device. The lower currents achieved for the strained sample are a result of the higher device resistance. As discussed earlier in this chapter, the two devices exhibit different superconducting gap characteristics, the gap of the unstrained sample was narrower than that of the strained; this is shown clearly in Figure 7.7. Since both devices used aluminium as their superconductor, this should not be the case and is attributed to contamination of the aluminium in the control detector. The difference in superconducting gap has been accounted for in all calculations in this

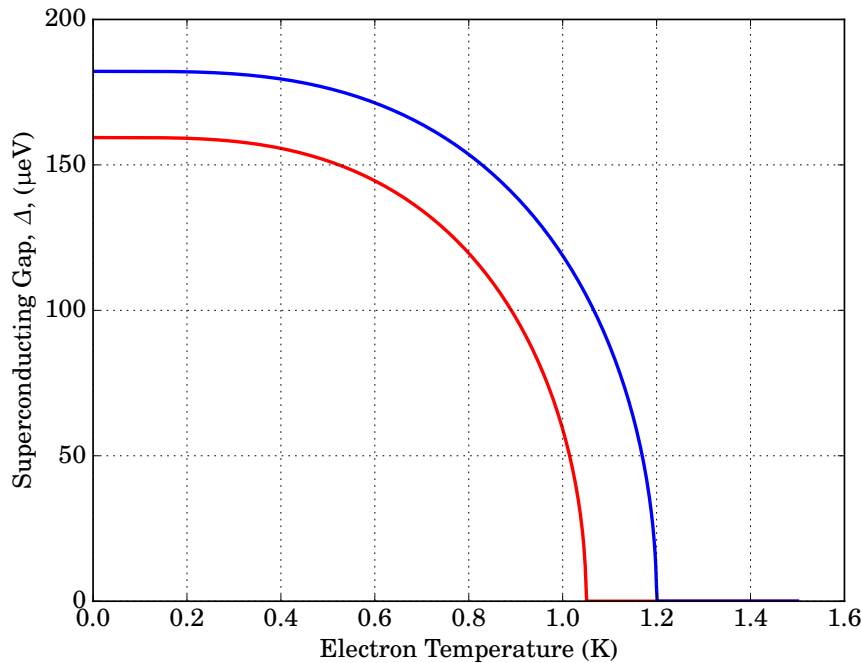


Figure 7.8: Superconducting gap size as a function of temperature for the unstrained (red) and strained (blue) devices. Both devices used aluminium superconductors but the aluminium used in the unstrained device was believed to be contaminated, reducing its gap size.

work and the values used for the two detectors are shown in Figure 7.8.

Comparing the electron-cooling performance of the two detectors (Figures 7.3 and 7.6) shows that the device utilising strained silicon offered a notable reduction in the minimum achieved electron temperature. This device was able to cool carriers to a minimum temperature of 100 mK from a bath temperature of 300 mK, compared to a minimum temperature of 170 mK for the unstrained device operating in the same conditions.

The results collected in this chapter indicate that the optical testing of both devices is merited, in order to compare the two materials in terms of their performance as detectors.

Chapter Eight

Results: Optical Measurements

'Out, vile jelly!'
—The Duke of Cornwall, King Lear,
WILLIAM SHAKESPEARE

8.1 INTRODUCTION

In order to determine the usefulness of any detector, it is obviously necessary to illuminate it with some form of light and measure the changes in the detector's characteristics. This has been performed for both of the detectors detailed in the previous chapter. Three main measurements have been performed to ascertain the performance of these detectors. Firstly, the response to room-temperature and 77 K sources has been measured by recording current-voltage curves while the detector was illuminated by such a source. Secondly, noise spectra have been measured at various bias points for both of these optical loads. Finally, the spectral response of the detectors has been measured using a **Fourier Transform Spectrometer (FTS)** with a mercury arc lamp (with a source temperature of $\approx 1,500$ K) as the optical source. Since the main focus of this work is to characterise a silicon cold-electron bolometer using strained silicon as the absorber, this detector has been subjected to additional tests, where a chopped source has been measured in an attempt ascertain the response time of the detector. In either case, the main goal of these optical measurements was to arrive at the **Noise-Equivalent Power (NEP)** for these detectors in a at least partially, realistic scenario.

The vast majority of the tests detailed in the following chapter have been performed in the final cryostat described in Chapter 5; that is to say a liquid-helium cryostat using a two-stage helium-4 and helium-3 sorption refrigerator. This resulted in the majority of measurements being performed at a thermal bath temperature of 350 mK. The change in optical performance with bath temperature has not been measured. All testing has been performed with radiation coupled to the absorber via a silicon lens and a twin-slot antenna; for all tests the 160-GHz antenna design (detailed in Section 4.2.1) has been used. Radiation from frequency other than those of interest (i.e. radiation with frequencies greater than 300 GHz) has been blocked using the filter stacks shown in Figure 5.3 for the chopped-source measurements and Figure 5.4 for all other measurements.

8.2 UNSTRAINED SILICON

The detector using unstrained silicon for the absorber has been measured in all the situations described above, with the exception that measurements of a chopped source have not been made. When eventually compared to the strained-silicon device, it is expected that this detector will be less sensitive for the reasons outlined at the start of Section 7.2. That is to say that the stronger electron-phonon coupling of this material will decrease the detector's responsivity (as seen in Equation 2.61), which will, in turn, increase the noise-equivalent power (Equation 2.121). Nevertheless, this material makes for an interesting demonstration of the performance of silicon-based cold-electron bolometers compared to metallic devices and, specifically, the advantages the strained material offers.

8.2.1 CURRENT-VOLTAGE MEASUREMENTS

As was performed for the *dark* measurements, the current-voltage characteristic of the detector has been measured. However, whereas during the dark measurements this characterisation was performed for various bath temperatures, in this case, characterisation has been formed at a single bath temperature of 350 mK—the lowest achievable in the system used—and the optical power has been varied. Two main optical sources were used for these measurements, these were a room-temperature black-body source and a 77-Kelvin black-body source. In both cases,

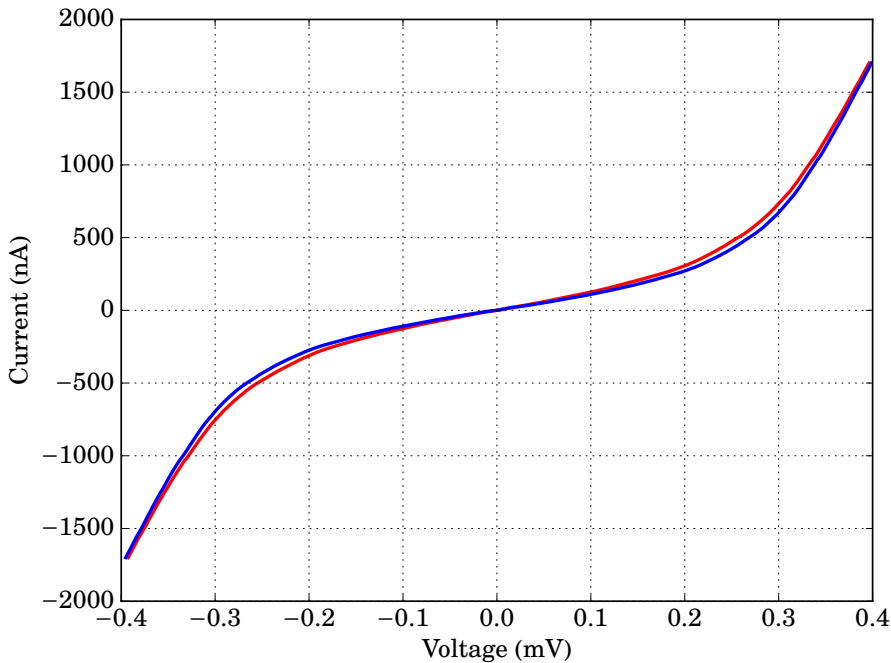


Figure 8.1: Current-voltage measurements for the unstrained detector. *I-V* curves were recorded with the detector *looking* at a 77-Kelvin source (blue) and a room-temperature source (red). Both measurements were made at a bath temperature of 350 mK.

the material used as the source was Eccosorb which is commonly used as a black-body source in millimeter and sub-millimeter measurements (see, for example, Mather et al., 1999).¹

The results of these measurements are shown in Figure 8.1. Firstly, it is clear from this figure that these measurements did not suffer from the contamination which affected those presented in Figure 7.1. More significantly, however, Figure 8.1 shows that there is a measurable difference in the current-voltage characteristics for the two sources. The *I-V* measurement taken with the lower-power source (the blue curve in Figure 8.1) sits outside the measurement made with the higher-power source (red curve). The additional power from the room-temperature source causes

¹Eccosorb is a material produced by Emerson & Cumming Microwave Products Inc., 28 York Avenue, Randolph, MA 02368, USA.

the I - V curve to shift towards the linear, in a similar way to increasing the bath temperature in the dark measurements (see Figure 7.1). This clearly makes sense, as in both scenarios, the energy of the carriers within the absorber was increased. It should, however, be noted that increasing the carrier energy via the optical system is much more efficient, since power is coupled to the carriers directly, as opposed to when the bath temperature increases, where power must flow through the weak thermal link between the electron and phonon systems. In both the cases shown in Figure 8.1, the I - V curve has substantially shifted towards the linear when compared to the 350 mK curve shown in Figure 7.1.

Using Equation 2.30, it was possible to calculate the electron temperature (as was performed for the dark measurements). The results of this electron-temperature fitting are shown in Figure 8.2.

Table 8.1: Parameters used in electron-temperature fitting of unstrained-silicon detector with optical loading.

R_{abs}	$2R_N$	V_J	Δ	$\Delta_{T=0}$	T_c
50 Ω	60 Ω	$V_{\text{dev}} - IR_{\text{abs}}$	BCS, $\Delta(T_e, T_c)$	160 μeV	1.05 K

Electron-temperature fitting was performed using the parameters shown in Table 8.1. Figure 8.2 shows that the electron temperature has been raised substantially from the bath temperature of 350 mK. For the 77-Kelvin source, the electrons have been raised to 400 mK at zero bias, whereas for the higher-power source (room-temperature source), the electrons are warmed to 415 mK in the absence of any bias. This rise in the carrier temperature is entirely due to the optical power and is limited by the thermal link (described in Section 2.5) to the lattice, which remains at the bath temperature of 350 mK. Electron cooling can still be seen in Figure 8.2, with the minimum achieved electron temperature being 290 and 310 mK for the 77-Kelvin and room-temperature sources respectively.

By noting that, in the absence of any bias, Equation 2.57 can be rewritten as:

$$P + P_{\text{abs}} + P_J - P_{\text{e-ph}} = 0, \quad (\text{Equation 2.57 revisited})$$

$$P_{\text{abs}} = P_{\text{e-ph}}, \quad (8.1)$$

it is possible to calculate the power absorbed within the detector by using Equation 2.56. Doing so gave the absorbed power to be 34 pW for the 77-Kelvin source and 43 pW for the room-temperature source.

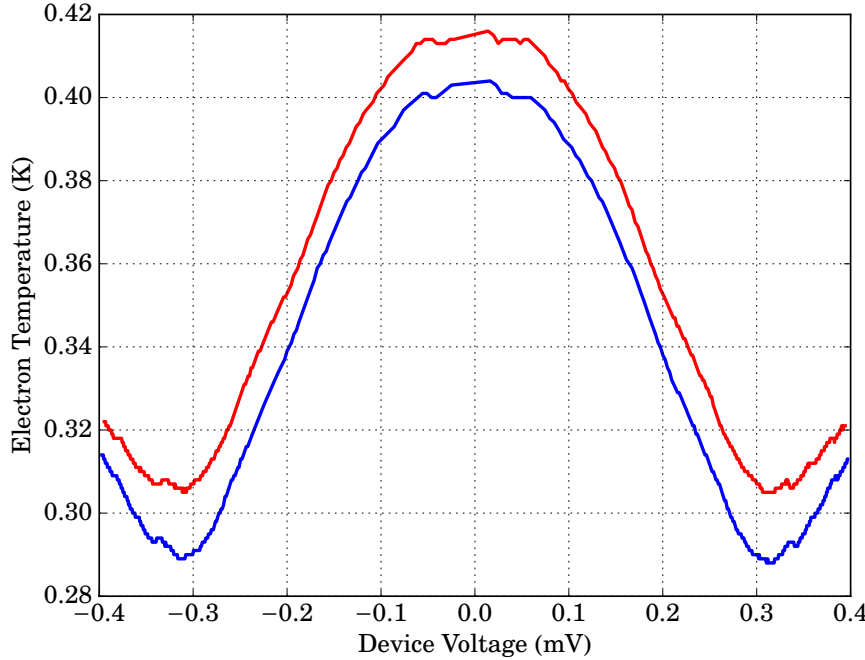


Figure 8.2: Electron-temperature fitting for the unstrained detector. This has been computed from the two optically-loaded I - V curves shown in Figure 8.1. The two curves correspond to the different optical sources. Blue—77-Kelvin source; red—room-temperature source. Note that, due to the optical load in these measurements, T_e at $V = 0$ is not equal to T_{ph} . Measured at 350 mK.

8.2.2 RESPONSIVITY

Given the electron temperature (found above), combined with the physical parameters of the detector, it is possible to calculate the responsivity of the detector using Equation 2.71. This is expected to be different for the two different levels of optical loading, since the tunnelling current (and thus the voltage) is not linearly dependent on the electron temperature (see Figure 2.7 for example). This analysis has been performed and the results are shown in Figure 8.3. In this figure, the absolute value of the responsivity has been plotted since, in a current-biased regime, the responsivity has the opposite sign to that of the bias (i.e. additional incident power always causes the measured voltage to shift towards zero).

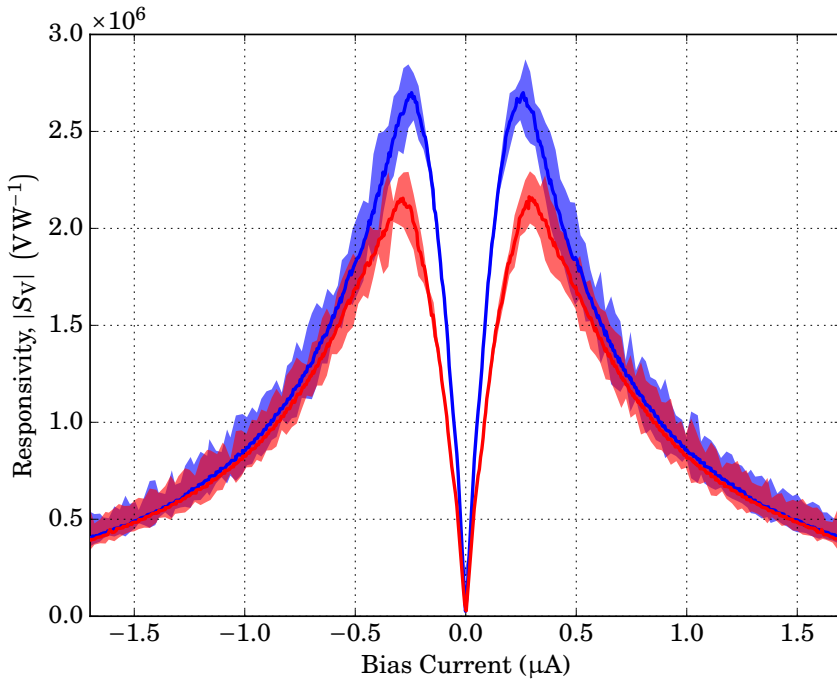


Figure 8.3: Responsivity of an unstrained-silicon cold-electron bolometer. Blue—77-Kelvin Source; red—room-temperature source. Shaded regions—uncertainty in responsivity. Measured at 350 mK.

From Figure 8.3, it can be seen that the maximum responsivity achieved for this detector was $2.7 \times 10^6 \text{ VW}^{-1}$ at a bias of 250 nA for the case where the detector was illuminated with a 77-Kelvin source. For the room-temperature source, the maximum responsivity was $2.1 \times 10^6 \text{ VW}^{-1}$. In both cases, the peak responsivity occurs at the same optimum bias of $\sim \pm 250 \text{ nA}$. It is also worth noting that Equation 2.71 does not depend on a measured optical power.

The error in the responsivity is governed by two main sources. Firstly, the error in the bias current across the device, which, more accurately, is the error in the current calculated for the electron temperature fitting described in Section 8.2.1 and the error in the electron temperature itself. The total error in a measurement

is given by the well-known equation:

$$(\Delta Z)^2 = \left(\frac{\partial Z}{\partial x} \right)^2 (\Delta x)^2 + \left(\frac{\partial Z}{\partial y} \right)^2 (\Delta y)^2 + \dots, \quad (8.2)$$

where Z is the final quantity, x and y are measurements used to obtain Z , and Δx and Δy are their respective uncertainties. Applying this to the situation presented here, we find that the error in the detectors' responsivity is given by:

$$(\Delta S_V)^2 = \left(\frac{\partial S_V}{\partial I} \right)^2 (\Delta I)^2 + \left(\frac{\partial S_V}{\partial T_e} \right)^2 (\Delta T_e)^2. \quad (8.3)$$

To calculate ΔS_V , the differentials have been calculated programmatically in a Python script, ΔI has been taken from the error in the current-fitting script utilised in Section 8.2.1 (which is automatically calculated), and ΔT_e has been taken to be 0.005 K which is due to the electron temperature fitting resolution. The results of this error calculation are shown as the shaded regions in Figure 8.3. This shows that at peak responsivity, the uncertainty is $\pm 1.5 \times 10^6 \text{ VW}^{-1}$ when observing the 77-Kelvin source and $\pm 1.3 \times 10^6 \text{ VW}^{-1}$ when observing the room-temperature source.²

8.2.3 NOISE MEASUREMENTS

The noise voltage of the unstrained detector has been measured using the cross-correlated noise-measurement technique described in Section 6.6. This has been performed for both of the sources described above at current biases around the peak response (250 nA). Averaging was performed on 201 acquisitions, which resulted in a correlated-amplifier-noise level of $500 \text{ pVHz}^{-1/2}$ (as can be seen from Figure 6.24).

An example noise spectrum (in this case measured at optimum bias with the 77-Kelvin source) is shown in Figure 8.4. It can be seen that there is very little $1/f$ noise present in this measurement and that the white-noise level is well established for frequencies of 10 Hz and above. There is some 50-Hz noise present in the measurement; however, harmonics of this are not seen above 300 Hz, after which, the spectrum is flat. This measurement was performed at a sampling rate of 200,000 samples per second with 200,000 samples per acquisition. These settings resulted in a Nyquist frequency of 100,000 Hz and the roll-off due to the data acquisition system has been removed from Figure 8.4.

²Note that while the uncertainty is close to symmetric at peak bias, this is not generally the case.

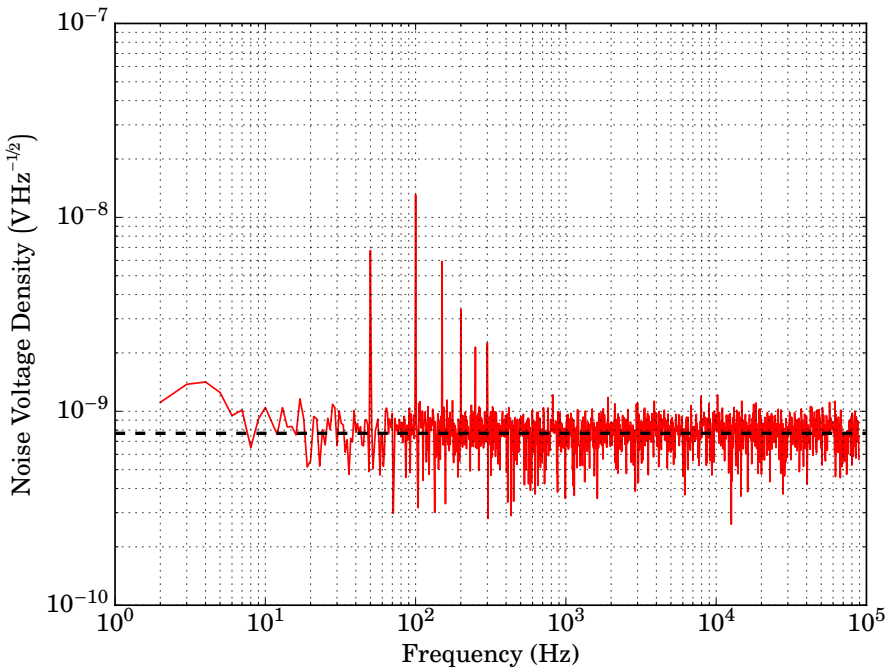


Figure 8.4: Noise spectral density, measured at optimum bias (250 nA), for the unstrained SiCEB. Red—Noise spectrum; dashed line—average noise level across the entire spectrum. Data have been reduced via logarithmic binning to improve the clarity of the figure. Measured at 350 mK.

The average noise levels from the measurements made at different bias levels and for the two optical sources has been collated and is shown in Figure 8.5.

Figure 8.5 shows that the unstrained detector has similar noise properties under both optical loadings. At optimum bias, the noise voltage measured when viewing the 77-Kelvin source is marginally ($6 \text{ pV}\text{Hz}^{-1/2}$) higher than when viewing the room-temperature source; away from the optimum bias, the measured noise voltages are near-identical for the two different sources.

The noise-equivalent power of the detector in these situations can be found by dividing the measured noise voltage by the detectors responsivity and is shown (calculated from the various data above) in Figure 8.6. This figure shows that the noise-equivalent power is not dominated by the small differences seen in the noise voltage (Figure 8.5) but is dominated by the differences in the responsivity

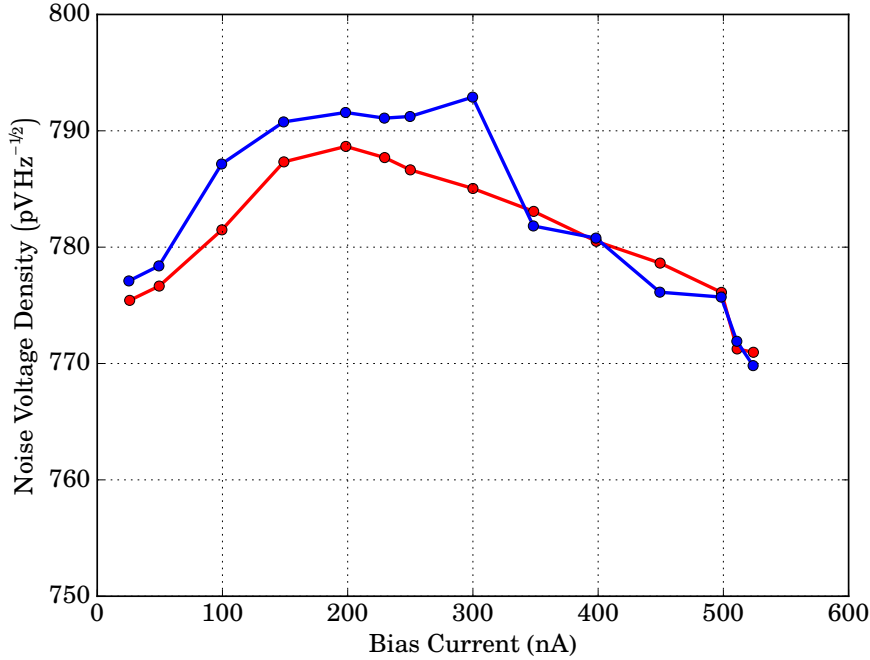


Figure 8.5: Summary of the change in noise voltage with bias current for the unstrained SiCEB. Blue—77-Kelvin Source; red—room-temperature source. Measured at 350 mK.

seen in Figure 8.3. The minimum achieved noise-equivalent power for the 77-Kelvin source was $2.9 \times 10^{-16} \text{ W Hz}^{-1/2}$, whereas for the room-temperature source, the minimum noise-equivalent power was marginally larger at $3.7 \times 10^{-16} \text{ W Hz}^{-1/2}$. This makes sense given the slightly larger responsivity found when the detector was illuminated by the 77-Kelvin source and noting that, in the case where the noise of the detector is hardly changing, $NEP \propto 1/S$.

The noise-equivalent power can be examined in a more complete fashion by using Equation 2.121, combined with the results found previously in this chapter, to calculate the predicted contribution of the various noise sources to the total noise-equivalent power. The results of this noise modelling, for the case where the detector was illuminated by a room-temperature source, are presented in Figure 8.7. From this figure, it can be seen that, despite cross-correlation of the noise, the noise-equivalent power of the this device is mainly dominated by the

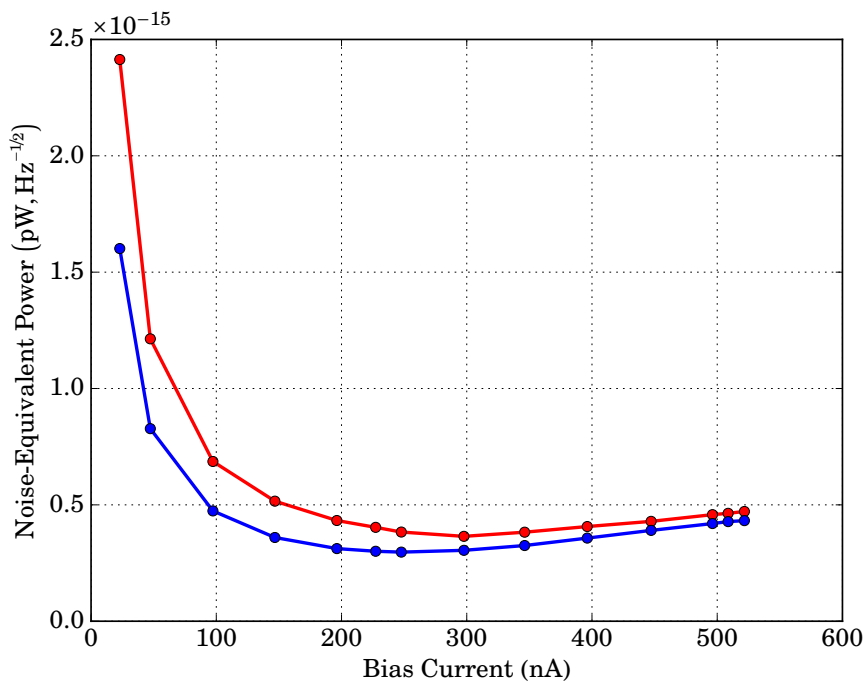


Figure 8.6: Noise-equivalent power of an unstrained-SiCEB biased at various currents around the optimum bias. Blue—77-Kelvin source; red—room-temperature source. Measured at 350 mK.

amplifier noise; however, at the minimum value of the noise-equivalent power, the contribution from photon noise is discernible. The domination of the amplifier noise over the photon noise is due to the low responsivity of the detector—the responsivity decreases the amplifier noise as S_V^{-1} , whereas the photon noise does not depend on the responsivity. The previously calculated NEP data show reasonable agreement with the model within their errors (discussed in the following paragraph). In the absence of any amplifier noise, the detector would have been photon-noise limited. Finally, if the photon noise is also disregarded, the device-limited noise-equivalent power (given by the combination of the tunnelling noise and the electron-phonon heat-flow noise) would have had a minimum value (shown by the dashed-black curve in Figure 8.7) of $4.8 \times 10^{-17} \text{ W}\text{Hz}^{-\frac{1}{2}}$.

The uncertainty in the noise-equivalent power (shown as the error bars on the

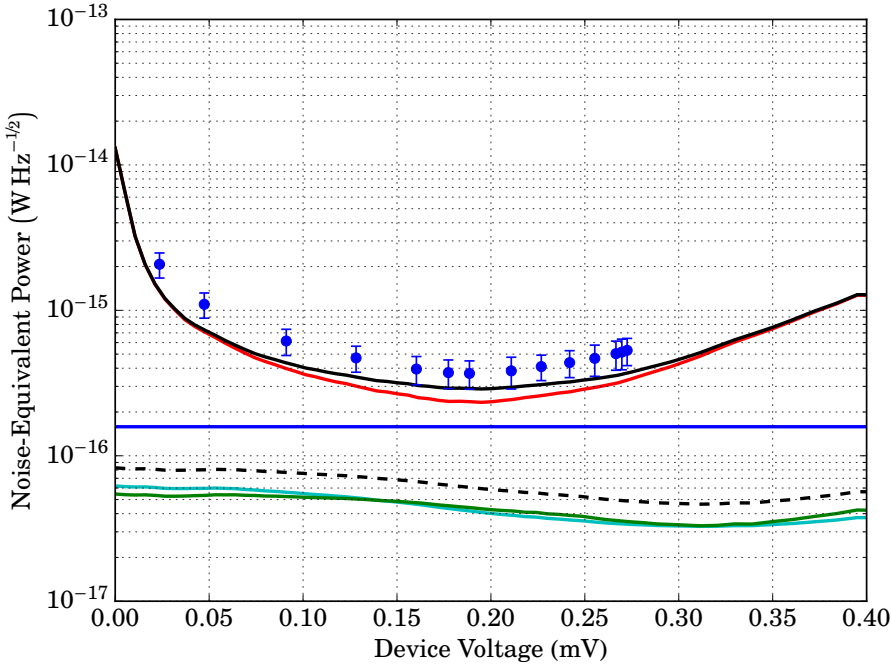


Figure 8.7: Noise modelling for the unstrained-SiCEB observing a room-temperature source. Cyan—Electron-phonon heat-flow noise; green—tunnelling noise, a combination of tunnelling-current noise and the tunnelling-heat-flow noise; blue—photon noise; red—amplifier noise; black (solid)—total noise; black (dashed)—total device noise; circles—data. Measured and calculated at 350 mK.

data points in Figure 8.7) is given by:

$$(\Delta NEP)^2 = \left(\frac{\partial NEP}{\partial S_V} \right)^2 (\Delta S_V)^2 + \left(\frac{\partial NEP}{\partial e_{tot}} \right)^2 (\Delta e_{tot})^2, \quad (8.4)$$

where ΔS_V is the uncertainty in the voltage responsivity, given by Equation 8.3, and e_{tot} is the noise spectral density measured at the oscilloscope. Since the white noise is Gaussian, we can write:

$$\Delta e_{tot} = \sigma(e_{tot}). \quad (8.5)$$

This means that Equation 8.4 can be written as:

$$(\Delta NEP)^2 = \left(\frac{\partial NEP}{\partial S_V} \right)^2 (\Delta S_V)^2 + \left(\frac{\partial NEP}{\partial e_{tot}} \right)^2 (\sigma(e_{tot}))^2. \quad (8.6)$$

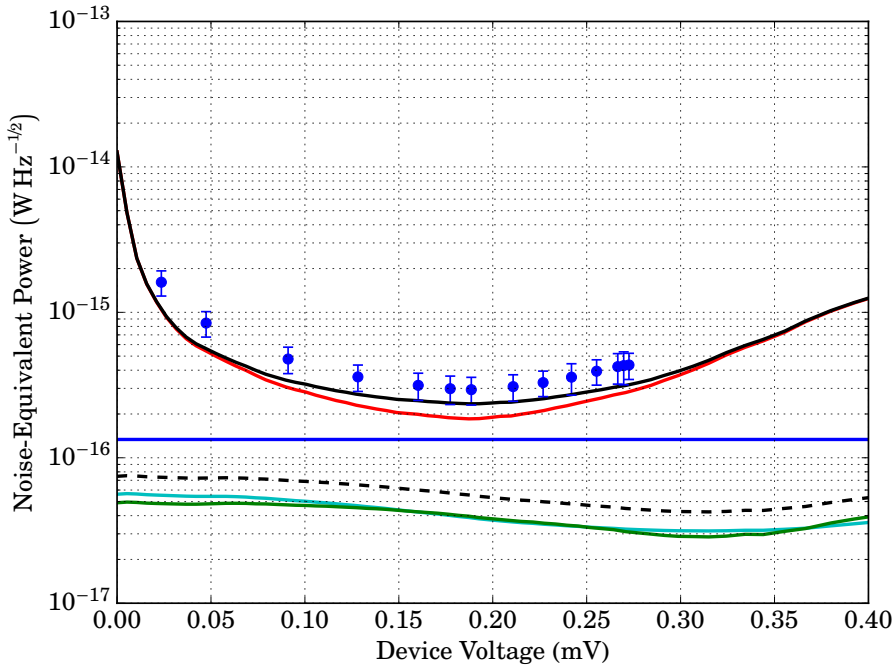


Figure 8.8: Noise modelling for the unstrained-SiCEB observing a 77-Kelvin source. Cyan—Electron-phonon heat-flow noise; green—tunnelling noise, a combination of tunnelling-current noise and the tunnelling-heat-flow noise; blue—photon noise; red—amplifier noise; black (solid)—total noise; black (dashed)—total device noise; circles—data. Measured and calculated at 350 mK.

Using Equation 2.95 for the noise-equivalent power, the uncertainty is given by:

$$(\Delta NEP)^2 = \left(\frac{1}{S_V} \right)^2 (\Delta S_V)^2 + \left(\frac{-e_{\text{tot}}}{S_V^2} \right)^2 (\sigma e_{\text{tot}})^2. \quad (8.7)$$

Examining the contributions of this for the minimum noise-equivalent power shown in Figure 8.7 (3.7×10^{-16} WHz $^{-1/2}$) shows that the uncertainty in NEP due to the responsivity is $^{+5.1}_{-4.7} \times 10^{-18}$ WHz $^{-1/2}$ ³, whereas the error due to measurement of the noise spectrum was $\pm 7.8 \times 10^{-17}$ WHz $^{-1/2}$. From this, it is clear that the total error is dominated by the error associated with the measurement of the noise spectrum.

³Note this error is asymmetric for the reasons discussed in Section 8.2.2.

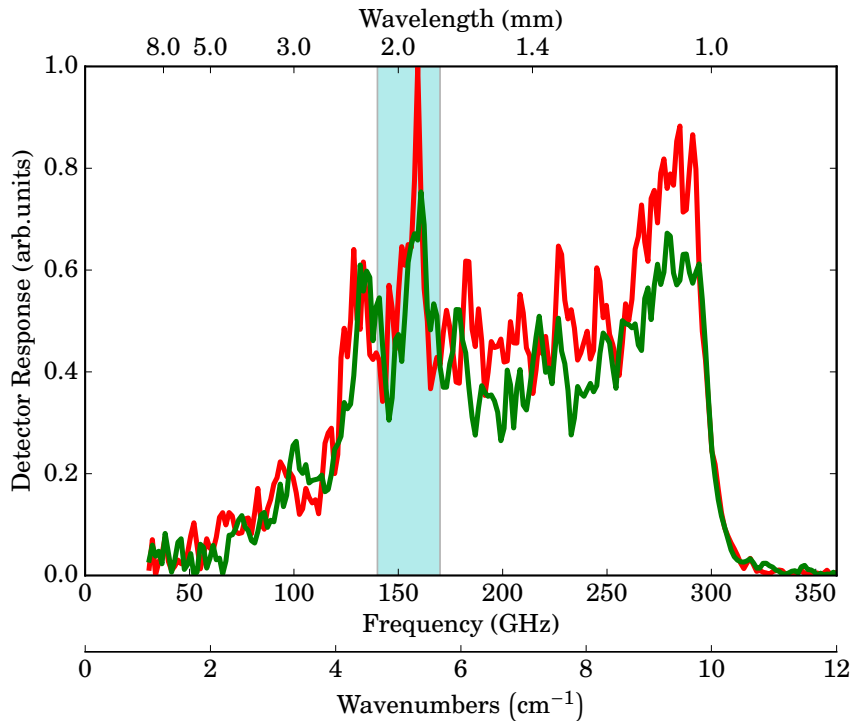


Figure 8.9: Spectral response of the unstrained-SiCEB, measured using a Fourier-transform spectrometer. Red—polarisation vector aligned with antenna polarisation; green—polarisation vector perpendicular to antenna polarisation; highlighted region—expected region of antenna response. In these measurements, a mercury arc lamp was used as the source. Measured at 350 mK.

Repeating the above analysis for the case where the detector was illuminated by a 77-Kelvin source yields similar results with the noise-equivalent power being dominated by the amplifier noise, although, again, the contribution from the photon noise can be observed at optimum bias. The minimum achieved noise-equivalent power in this case was $2.4 \times 10^{-16} \text{ WHz}^{-1/2}$ and the minimum device noise limited noise-equivalent power was $4.2 \times 10^{-17} \text{ WHz}^{-1/2}$. These results are shown in Figure 8.8.

8.2.4 SPECTRAL RESPONSE

The spectral response of the unstrained detector has been measured using Fourier transform spectrometer. This measurement was performed for both linear polarisations and the results are shown in Figure 8.9. When the polarisation of the spectrometer's source (a mercury arc lamp with a linear slot polarising grid) was aligned with that of the antenna (red line in Figure 8.9), a notable response is seen at the anticipated frequencies (shaded region in Figure 8.9). Where the source polarisation was rotated such to be orthogonal to that of the antenna (green line in Figure 8.9), this response was diminished. The overall plateau level seen in Figure 8.9 is most likely due to direct, bolometric, absorption of radiation in the absorber or by the aluminium being slightly lossy and absorbing the radiation. Other features seen in the spectrum can most likely be attributed to reflections from the lens and within the device holder, since none of these surfaces were anti-reflection coated. These issues are explored to greater detail in Section 8.4. The loss of detector response at 300 GHz is simply the result of the low-pass filter used in this measurement.

8.3 STRAINED SILICON

All the characterisation work detailed in the previous section for the unstrained detector has been replicated for the detector with a strained-silicon absorber (previously covered in Section 7.2). The experimental conditions were replicated as closely as possible between the two experiments; with one exception being that the optical configuration was slightly different, in that the back-to-back horn pair were placed slightly further away from the detector, slightly reducing the optical throughput of the optics system. Further to these tests, as mentioned in the introduction to this chapter, the response of this detector to a chopped source (an emitting-diode source tuned to output 150 GHz) has also been measured.

8.3.1 CURRENT-VOLTAGE MEASUREMENTS

As was the case for the unstrained detector, I - V curves have been measured with the detector illuminated by two different sources: room-temperature Eccosorb and Eccosorb cooled in liquid nitrogen to 77 K. As with the previous measurement for the unstrained device, the optical testing was carried out at a bath temperature

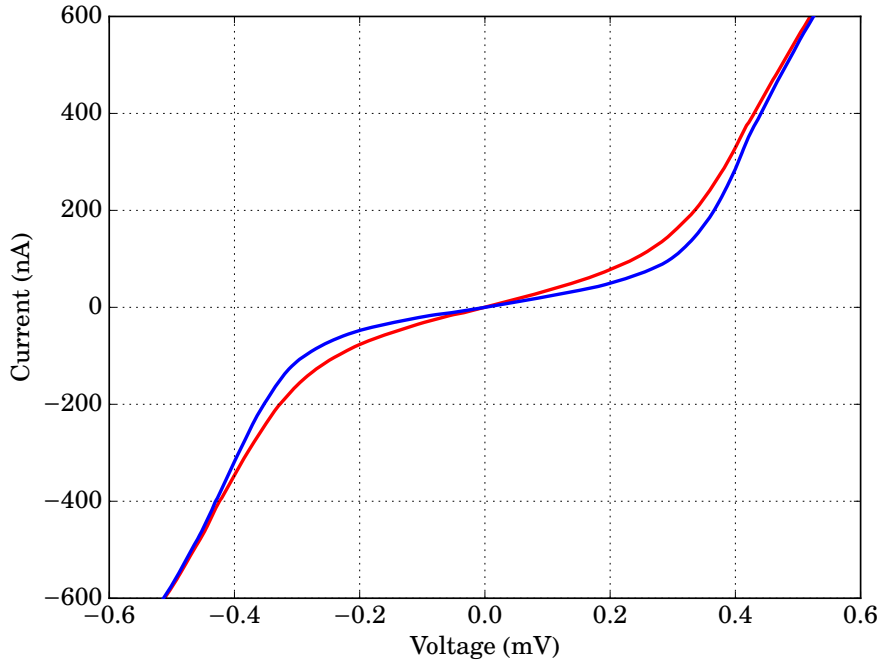


Figure 8.10: Current-voltage measurements for the strained detector. *I-V* curves were recorded with the detector illuminated by both a 77-Kelvin source (blue) and a room-temperature source (red). Both measurements were made at a bath temperature of 350 mK.

of 350 mK. The results of these measurements can be seen in Figure 8.10. From this figure, it can be seen that the general behaviour is similar to the previously tested detector, in that the additional optical power causes the *I-V* curve to tend towards the linear. When a closer comparison to the current-voltage characteristics of the unstrained detector (as shown in Figure 8.1) is made, it is apparent that the response for this detector is noticeably larger (i.e. the *I-V* curve for the room-temperature source is much more clearly distinguished from the curve for the 77-Kelvin source than was seen previously). This is even more impressive considering that, as discussed above, the incident optical power on this detector was expected to be lower than for the unstrained device, due to differences in the optical configuration.

The overall characteristics of the *I-V* curves seen in Figure 8.10 are in line

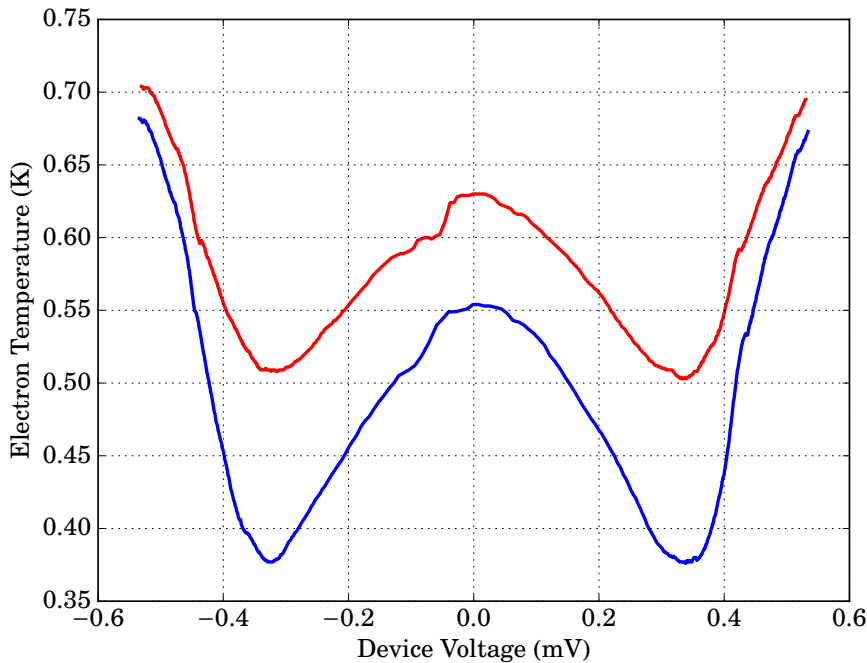


Figure 8.11: Electron temperature of strained-SiCEB under optical loading. Blue—77-Kelvin source; red—room-temperature source. Measured at a thermal bath temperature of 350 mK. Measured at 350 mK.

with those previously measured in the absence of any optical power (shown in Figure 7.4). As has been performed for both sets of dark measurements and the optically loaded *I-V* curves for the unstrained detector, the electron temperature has been calculated as a function of the voltage across the detector by fitting the *I-V* curves to Equation 2.30. This is shown in Figure 8.11. The electron temperature in the absence of any bias was calculated to be 550 mK for the 77-Kelvin source and 630 mK for the room-temperature source. These increases from the bath temperature of 350 mK are greater than was seen for the unstrained detector (Figure 8.2); this is the result of the substantially reduced electron-phonon coupling in this sample ($2.0 \times 10^7 \text{ WK}^{-6} \text{ m}^{-3}$), compared to the unstrained detector ($5.8 \times 10^8 \text{ WK}^{-6} \text{ m}^{-3}$), as discussed in Section 2.5. The parameters used in the electron-temperature fitting are given in Table 8.2.

By using Equation 8.1, the absorbed power in the detector for the two optical

Table 8.2: Parameters used in electron-temperature fitting of strained-silicon detector with optical loading.

R_{abs}	$2R_N$	V_J	Δ	$\Delta_{T=0}$	T_c
75 Ω	580 Ω	$V_{\text{dev}} - IR_{\text{abs}}$	BCS, $\Delta(T_e, T_c)$	182 μeV	1.2 K

sources was found to be 9.2 pW for the 77-Kelvin source and 20.0 pW for the room-temperature source. These values support the assertion at the start of this section that the optical power would be reduced in these measurements compared to those performed for the unstrained detector, due to small changes in the optical setup.

8.3.2 RESPONSIVITY

The responsivity of the strained-silicon device has been found using Equation 2.71 and is shown in Figure 8.12. The maximum responsivity occurred when the detector was illuminated by the 77-Kelvin source and had a peak value of $(1.5^{+0.5}_{-1.0}) \times 10^7 \text{ VW}^{-1}$. The maximum responsivity when the detector was illuminated by the room-temperature source was $(4.6 \pm 0.4) \times 10^6 \text{ VW}^{-1}$. The responsivity was slightly higher under negative biases, this was most likely the result of minor misalignment during the fabrication process, creating slightly asymmetric contacts to the absorber. The optimum bias for this detector was found to be -90 nA with $+90 \text{ nA}$ being the optimum current under positive bias. The uncertainty in these measurements has been calculated as discussed in Section 8.2.2.

It is interesting to note that the relative difference between the two curves shown in Figure 8.12 is greater than that seen in Figure 8.3 for the unstrained detector, where the optical power was higher. This indicates that the responsivity is diminishing with increased optical loading. This can be seen in both Figures 8.3 and 8.12, where, in both cases, the lower optical load (that from the 77-Kelvin source) has resulted in a higher responsivity. While this seems to makes sense when considering the unloaded current-voltage measurements (unstrained: Figure 7.1; strained: Figure 7.4), where for higher bath temperatures the I - V curves become increasingly linear and more closely packed, clearly further study—with a greater range of optical powers—is needed to fully explore this behaviour. The greater responsivity observed here is a clear indication that the reduced interaction between the electrons and phonons has resulted in a more responsive detector. This is, in

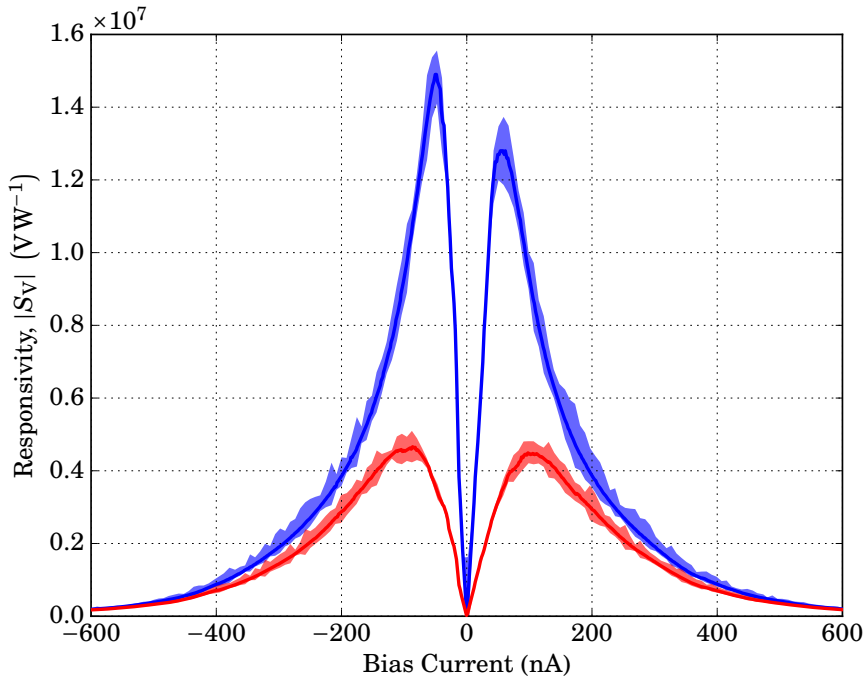


Figure 8.12: Responsivity of the strained-silicon cold-electron bolometer. Blue—77-Kelvin Source; red—room-temperature source. Shaded regions—uncertainty in responsivity. Measured at 350 mK.

part due to the fact that the absorber temperature in the strained sample is higher for an equivalent optical power compared to the unstrained detector; this again is a result of the reduced electron-phonon coupling, as described in Section 2.5.

8.3.3 NOISE MEASUREMENTS

Electrical-noise spectra have been measured at a range of bias currents and with the detector illuminated by both the 77-Kelvin and the room-temperature source. These measurements were performed using the cross-correlated noise readout system used for the unstrained detector (that described in Section 6.6), with a similar number of averages being used in both scenarios.

Figure 8.13 shows a noise spectrum measured away from the optimum bias, where the noise voltage is lowest, for the strained detector. As was seen for the

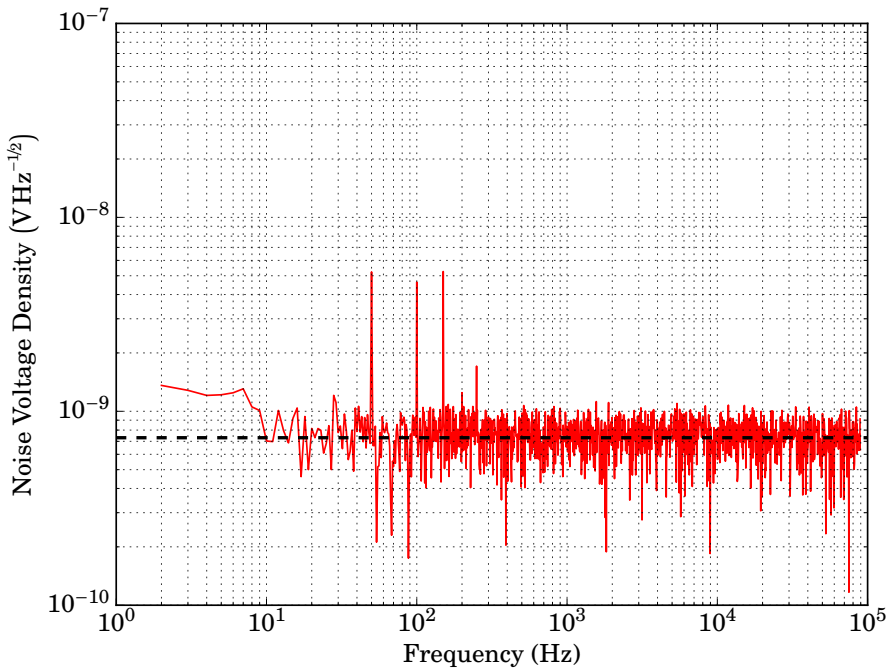


Figure 8.13: Noise spectral density for the strained-SiCEB. This spectrum was measured away from the optimum bias (in terms of response), where the noise voltage was lowest and in the presence of a 77-Kelvin optical source. Red—Noise spectrum; dashed line—average noise level across the entire spectrum. Data have been reduced via logarithmic binning to improve the clarity of the figure. Measured at 350 mK.

unstrained detector (Figure 8.4), the spectrum is almost entirely flat with a $1/f$ component having diminished by 10 Hz and little pickup. Limited 50-Hz pickup is seen from the mains supply but otherwise, there are few features in this spectrum. The roll-off due to the data acquisition system has been removed from the spectrum.

All the noise spectra have been analysed by finding their average white-noise level and the results of this are shown in Figure 8.14. For both optical sources, the peak noise occurred slightly below the optimum bias current ($\approx \pm 90$ nA). Compared to the comparable figure for the unstrained detector (Figure 8.5), not only is a greater difference seen between the two sources but also the variation in the noise voltage is also greater.

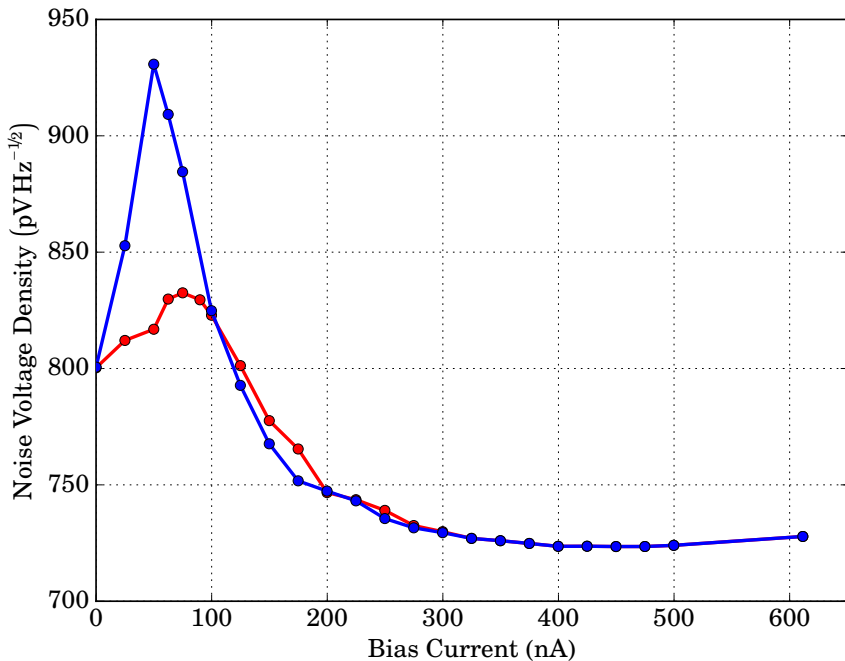


Figure 8.14: Summary of the change in noise voltage with bias current for the strained-SiCEB. Blue—77-Kelvin Source; red—room-temperature source. Measured at 350 mK.

To fully explore the significance of the noise, it is necessary to model the expected contributions of the various noise sources to the final noise. Figure 8.15 shows the modelled noise-equivalent power, along with the measured values, for the strained detector under illumination from the room-temperature source. Firstly, unlike the comparable plot for the unstrained detector (Figure 8.8), it is clear that, for this detector, the amplifier noise has not dominated the measurement. Instead, the photon noise is the dominant noise source for device voltages between 0.15 and 0.30 mV. If only the internal noise mechanisms of the detector are considered, the noise is dominated by the tunnelling noise (the final three terms in Equation 2.121) and has a minimum value of $4 \times 10^{-17} \text{ WHz}^{-1/2}$. If all noise sources are considered, the model is close to the measured noise (circles in Figure 8.15), although the error bars do not bring the two into full agreement. The model has a minimum value of $1.3 \times 10^{-17} \text{ WHz}^{-1/2}$, which is limited by the photon noise.

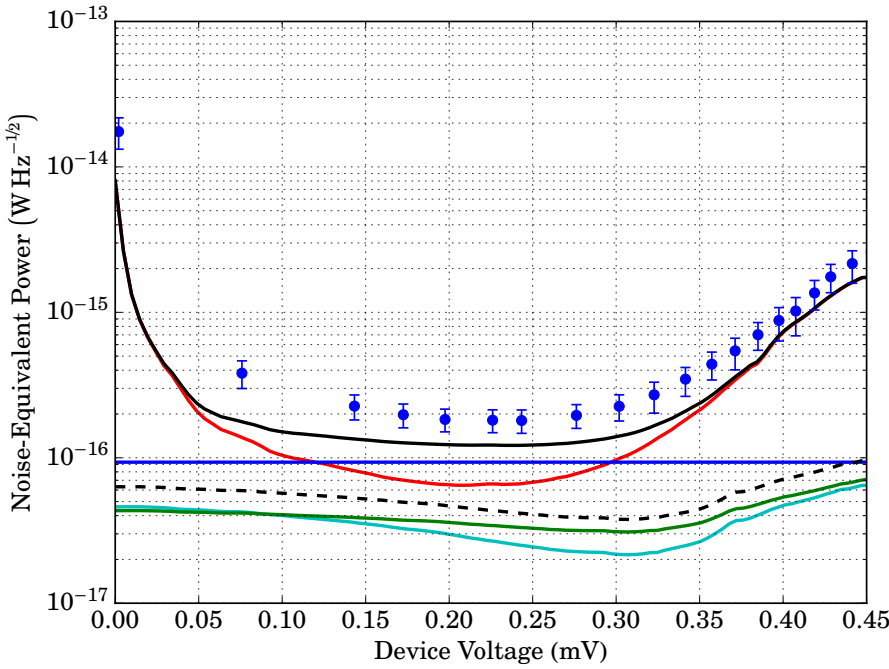


Figure 8.15: Noise modelling for the strained-SiCEB observing a room-temperature source. Cyan—Electron-phonon heat-flow noise; green—tunnelling noise, a combination of tunnelling-current noise and the tunnelling-heat-flow noise; blue—photon noise; red—amplifier noise; black (solid)—total noise; black (dashed)—total device noise; circles—data. Measured and calculated at 350 mK.

Performing the same modelling, for the case where the detector was illuminated by the 77-Kelvin source, gave the model shown in Figure 8.16. Here, it can be seen that the noise-equivalent power is lower overall; this is due to both the optical power being lower in this scenario and the responsivity being higher. The device-limited noise-equivalent power is still limited by the tunnelling noise, although a greater contribution from the electron-phonon noise is now seen. This is due to the electron-phonon noise not being affected by the increased responsivity, only by the slightly reduced electron temperature, whereas the tunnelling noise has decreased more substantially with the responsivity, bringing it towards the electron-phonon noise. The minimum device-limited noise-equivalent power seen in this

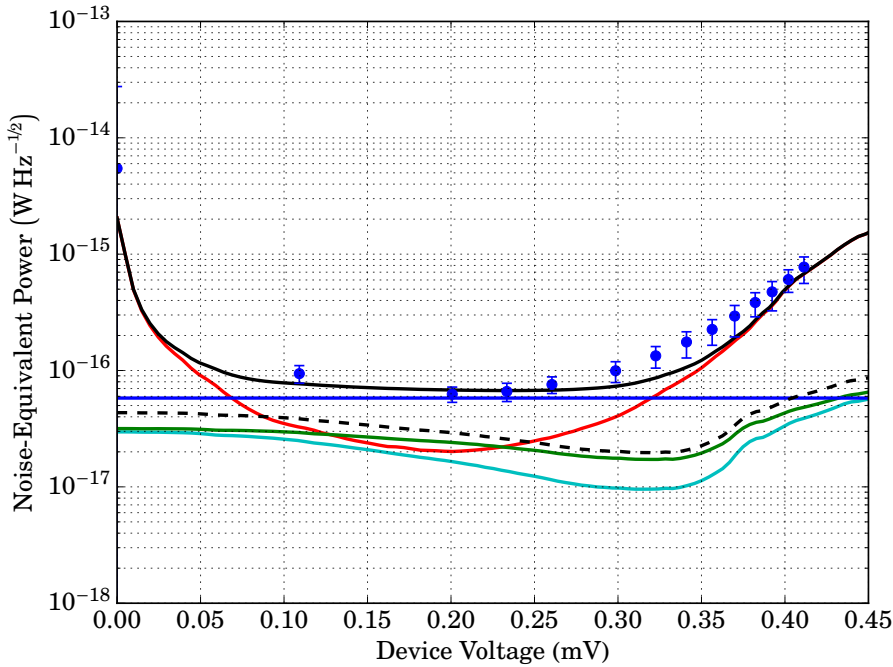


Figure 8.16: Noise modelling for the strained-SiCEB observing a 77-Kelvin source. Cyan—Electron-phonon heat-flow noise; green—tunnelling noise, a combination of tunnelling-current noise and the tunnelling-heat-flow noise; blue—photon noise; red—amplifier noise; black (solid)—total noise; black (dashed)—total device noise; circles—data. Measured and calculated at 350 mK.

model was 2×10^{-17} W Hz $^{-1/2}$. Considering all noise sources (solid black line in Figure 8.16), the model fits the data (circles) very well. The minimum noise-equivalent power when all noise sources were considered was 6.6×10^{-17} W Hz $^{-1/2}$.⁴ Examining the contributions to the error in the noise-equivalent power, we find that the error due the responsivity in for this measurement was $^{+1.3}_{-1.2} \times 10^{-18}$ W Hz $^{-1/2}$ from the responsivity and $\pm 9.3 \times 10^{-18}$ W Hz $^{-1/2}$ due to the measurement of the noise

⁴Note that this value differs from that reported by Brien et al. (2014) (1.1×10^{-16} W Hz $^{-1/2}$), where a value at device voltage of 0.32 mV (bias current of close to 100 nA) was used. This was due to greater confidence in this point at the time of publication, due to being nearer the nominal value of 2Δ . However, since publication of Brien et al. (2014), we have gained confidence in the remainder of the data, allowing for the lower noise-equivalent power to be presented herein.

spectrum, thus, as was the case for the unstrained device, the measurement of the noise spectrum was the main source of error in this measurement.

Roughly speaking, one might have expected the noise-equivalent power of the strained detector to be a factor of thirty lower than the unstrained device, following the reduction in the electron-phonon coupling. However, as has been seen, the difference was nearer a factor of three. This is explained by the fact that, although the electron-phonon noise was reduced for the strained detector, this is slightly undone by the increase in the tunnelling noise (due to the higher contact resistance to the strained silicon). Overall though, the larger responsivity observed in the strained detector (which is the result of lower coupling between the electron and phonon systems) results in the noise-equivalent power being lower for the strained detector. Photon noise limited noise spectra (such as the one presented in Figure 8.13) were white from the (low) $1/f$ -knee to the Nyquist limit (100 kHz), showing no roll-off in the photon noise and thus indicating that the response time of this detector was $< 1.5 \mu\text{s}$.

8.3.4 SPECTRAL RESPONSE

The spectral response of the strained-silicon detector has been measured with a Fourier-transform spectrometer. A spectrum has been measured in each of the two orthogonal polarisations and the results of these measurements are shown in Figure 8.17. There is a clear response from the detector in the polarisation aligned with that of the antenna (red plot in Figure 8.17). There are, however, two other features in these spectra which were not anticipated. Firstly, the broad peak in the perpendicular polarisation (green plot) was not the result of the antenna response and is most likely attributed to either the coplanar waveguide and/or the DC cuts introduced into the ground plane (see Chapter 4); or to reflections from the surfaces of the silicon lens and the device holder. The constant plateau level seen in both polarisations is most likely the result of direct absorption (i.e. not via the antenna) of optical power in the silicon mesa; it is also possible that power absorbed in the aluminium caused this. The loss of signal above 300 GHz, however, is simply due to the 300-GHz low-pass filter placed in front of the detector. The features of this spectrum will be discussed in greater detail in Section 8.4.

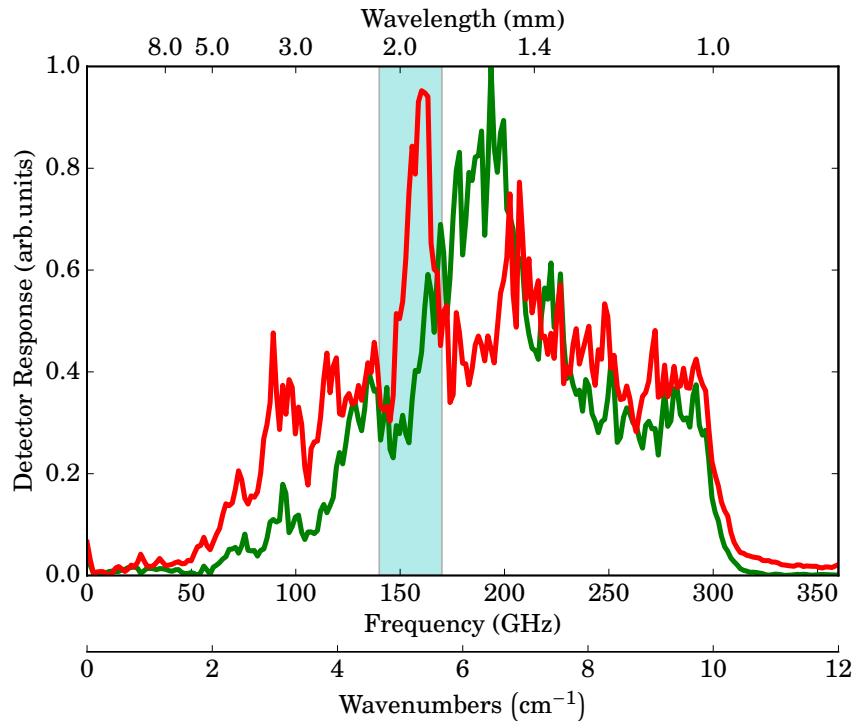


Figure 8.17: Spectral response of the strained-SiCEB, measured using a Fourier-transform spectrometer. Red—polarisation vector aligned with antenna polarisation; green—polarisation vector perpendicular to antenna polarisation; highlighted region—expected region of antenna response. In these measurements, a mercury arc lamp was used as the source. Measured at 350 mK.

8.3.5 CHOPPED-SOURCE MEASUREMENTS

In an effort to measure this detector's time constant, the response to a chopped source has been measured. The source used for this measurement was a diode (emitting radiation at 160 GHz) in a vector network analyser extender which was coupled to free space via a horn. This measurement was performed in the pulse-tube cooled system. The time stream recorded in this measurement is shown in Figure 8.18. The source was configured to emit a 70 μ s long pulse. The two vertical lines in this plot correspond to the source being switched off and the signal return to zero (the measurement was performed with a AC-coupled input). The time between the source being switched off and the signal returning to zero was measured to

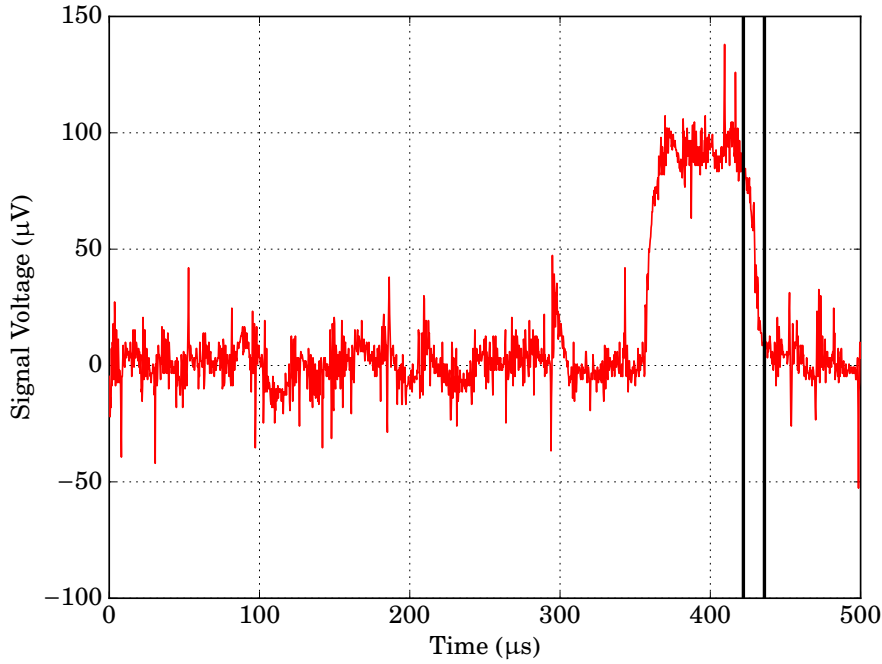


Figure 8.18: Time stream of the voltage signal resulting from the strained SiCEB observing a chopped signal. The source was set to emit a pulse of 70 μs , which was switched off at the first vertical black line; the voltage signal had returned to zero 14 μs later, at the second vertical black line. Measured at 280 mK.

be 14 μs . The same time has also been measured for this source using [Kinetic Inductance Detectors \(KIDs\)](#) and thus, it is clear that this measurement was limited by the time constant of the source as opposed to the detector. This measurement does at least allow an upper limit of 14 μs to be placed on the time constant of this detector.

Figure 8.19 shows a voltage spectrum measured with the detector being illuminated by the same source at a chopping frequency of 1,945 Hz. The response is immediately clear in the spectrum and has a signal-to-noise ratio of close to 1,000.

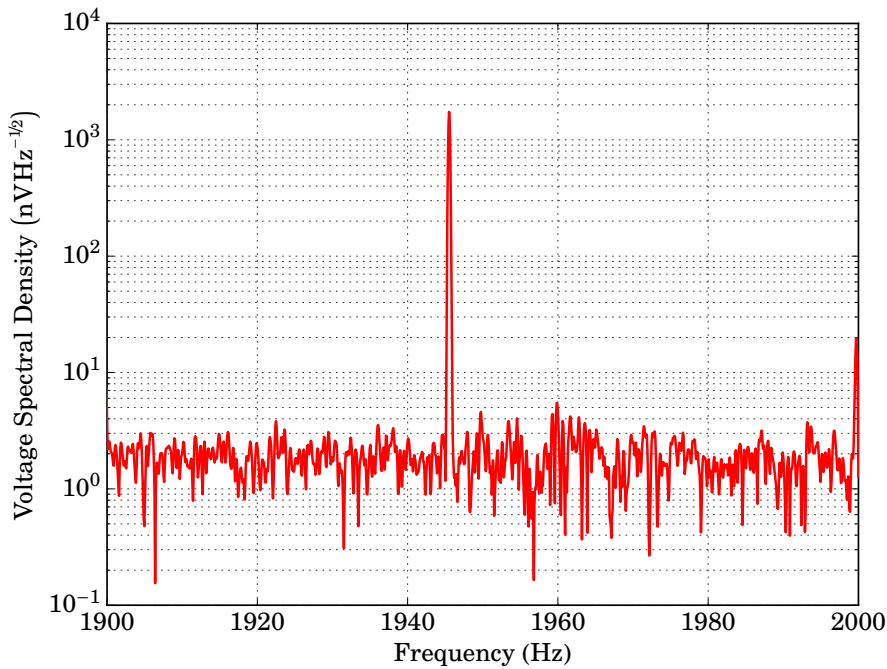


Figure 8.19: Voltage spectrum measured in the presence of a 160-GHz source chopped at 1,945 Hz. Measured at 280 mK.

8.4 DETAILED ANTENNA SIMULATIONS

In order to attempt to explain the spectral response of these detectors (seen earlier in this chapter) which were not as clean as had been hoped, the simulation work for the designed antenna has been revisited and expanded, in an attempt to more accurately model the detector as a whole. This section will look at the processes which have been undertaken to produce a more accurate model of the spectral response of the device. All models presented in this section have been computed using Ansys's HFSS software.⁵

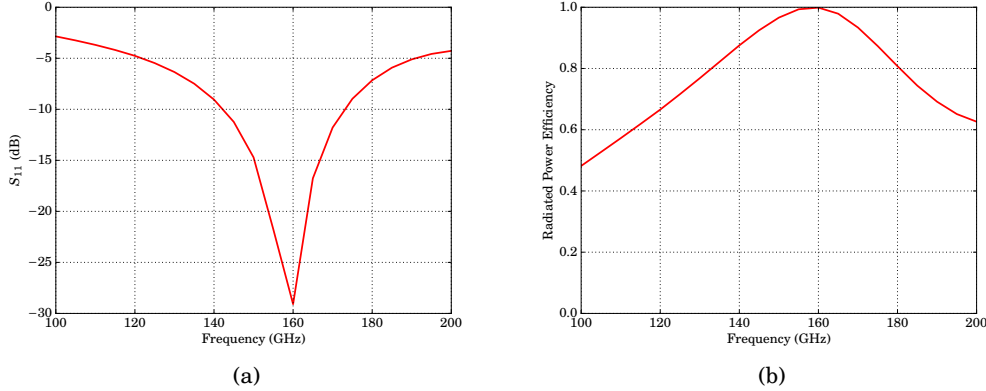


Figure 8.20: Initial model of the antenna performed by measuring reflected power from a lumped port placed at the absorber. (a) S_{11} parameter; (b) radiated power efficiency.

8.4.1 BASIC MODEL: LUMPED PORT, INFINITE SILICON

The starting point for the simulation work was to revisit the initial simulation of the antenna. This rather simplistic model consisted of an emitting lumped port placed at the absorber and the reflection parameter (S_{11}) being calculated. The model was performed with the detector fabricated on infinitely thick silicon. The boundaries of the model were defined as reflective and placed greater than $\lambda/4$ away from the lumped port. The absorption efficiency was also calculated using:

$$Eff = 1 - |S_{11}|^2. \quad (8.8)$$

The results of this measurement are shown in Figure 8.20. Both the reflected power (S_{11} in Figure 8.20a) and the absorption efficiency (Figure 8.20b) showed an excellent response at the desired frequency of 160 GHz. The 3-dB bandwidth can be seen to be ranging from approximately 100 to 200 GHz.

From these results, it is clear that, while the initial simulation may have been incomplete, there are no fundamental issues related to the design of the antenna itself.

⁵ANSYS, Inc., Southpointe, 2600 ANSYS Drive, Canonsburg, PA 15317, USA. Website: <http://www.ansys.com>

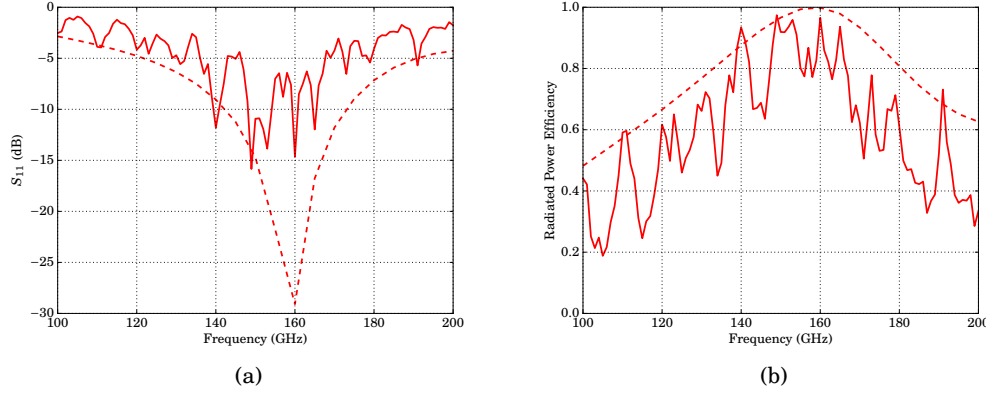


Figure 8.21: Model of the antenna and lens performed by measuring reflected power from a lumped port placed at the absorber. (a) S_{11} parameter; (b) radiated power efficiency. Dashed lines—results of previous model (Figure 8.20) for comparison.

8.4.2 MODELLING THE ANTENNA AND LENS

The next step in this more detailed examination of the system was to include the silicon lens, which had not been included in the initial simulation work. The reason for using the lens was due to following similar configurations used in the measurement of hot-electron bolometers—which are at least partly comparable to the devices tested here—and other detectors using twin-slot antennae (see for example: Ganzevles et al., 2000; Focardi and McGrath, 2005; Karasik and Cantor, 2011, along with other works by Karasik on this topic). This silicon lens replaced the infinite silicon substrate seen in the previous model; other than this, the two models were the same and the results were computed in the same manner. In neither the model nor real life was the lens anti-reflection coated.

The results of this revised model can be seen in Figure 8.21. When these plots are compared to those computed for the previous model (Figure 8.20), it is clear that the presence of the silicon lens has degraded the response of the system. In terms of the plot of the S_{11} parameter (Figure 8.21a), it can be seen that there is now more power reflected to the lumped port at all frequencies compared to previous model (shown as the dashed lines in Figure 8.21). It can also be seen that the 3-dB bandwidth is reduced slightly in this case and ranges from 120 to 170 GHz.

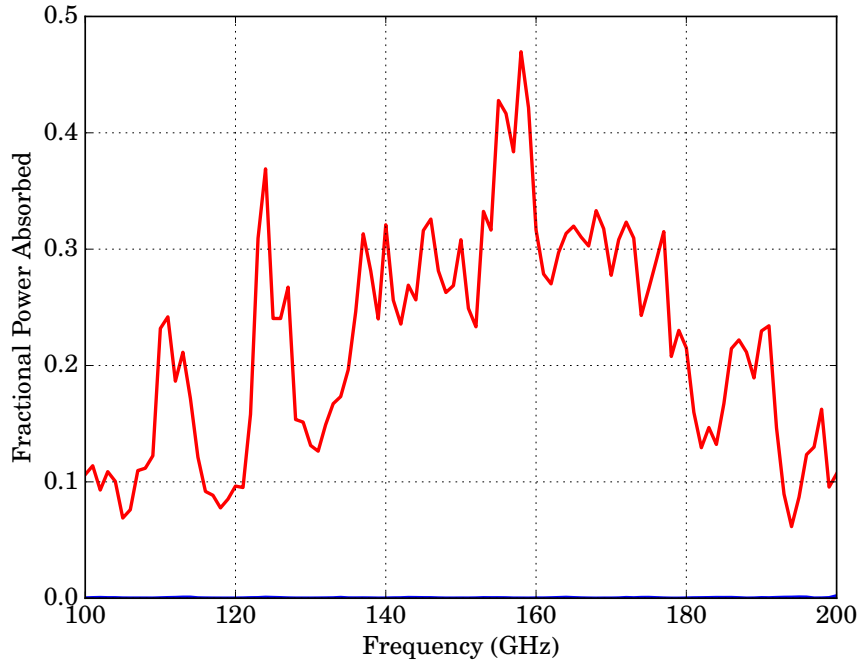


Figure 8.22: Model of antenna and lens using a wave port. Red—polarisation vector aligned with that of the antenna; blue—polarisation vector perpendicular to that of the antenna

8.4.3 POLARISATION MODEL USING WAVE PORT

With the lumped-port modelling used above, it was not easily possible to measure the response of the system to the polarisation of the incoming radiation. To perform such work, the model was revised to use a wave port, placed at the input to the optical system (i.e. in front of the lens); the walls of the model were kept as reflective, as was the base of the model. The wave port was set to have two modes corresponding to the two orthogonal polarisations. In this model, the power (on a fractional basis) was modelled for each of the polarisations.

Figure 8.22 shows the results of this model. When the polarisation vector of the radiation emitted from the wave port is aligned with that of the antenna (red line in Figure 8.22), it can be seen that power is absorbed by the silicon mesa. Although this happens over a broad range of frequencies, there is a maximum in the absorbed

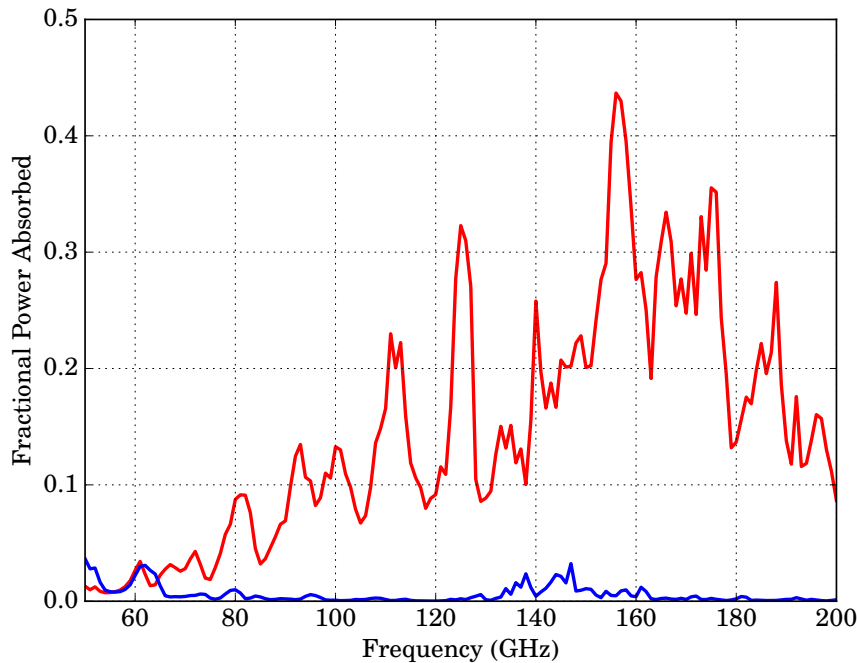


Figure 8.23: Model of antenna, lens and DC cuts using a wave port. Red—polarisation vector aligned with that of the antenna; blue—polarisation vector perpendicular to that of the antenna

power just below the design frequency (160 GHz). When the radiation's polarisation vector is perpendicular to that of the antenna (blue line Figure 8.22), very little power is absorbed.

8.4.4 INTRODUCTION OF DC CUTS

The next stage performed was to include the DC cuts in the ground plane which had not previously been modelled. This amendment was made to the model covered in the previous section and no further changes were made. The results of this model are shown in Figure 8.23. This shows that in the aligned polarisation there is now additional absorption at 125 and 175 GHz but the most power is still absorbed in the silicon just below the design frequency. While there is still only a small amount of power absorbed in the perpendicular polarisation, the level is noticeably higher

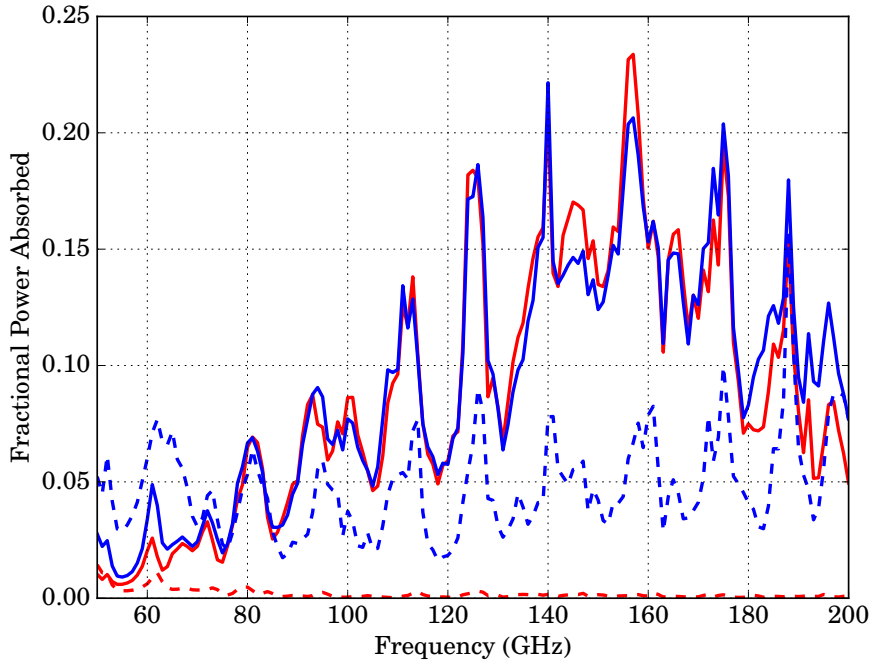


Figure 8.24: Model of antenna, lens, DC cuts and lossy aluminium using a wave port. Red—Absorption in the silicon mesa; blue—absorption in the aluminium; solid lines—radiation polarisation aligned with the antenna; dashed lines—radiation polarisation perpendicular to the antenna.

than in the previous model (Figure 8.22).

8.4.5 ALLOWING FOR LOSS IN THE ALUMINIUM

The final model created was one in which the aluminium was defined to be non-perfectly conductive. This situation was intended to replicate the possible scenario whereby incoming light split Cooper pairs in the aluminium, which in turn resulted in a detector response. Clearly, in such a scenario, one would expect to see a broadband response at all frequencies above that required to split the Cooper pairs ($h\nu > 2\Delta$). In this model, the impedance of the aluminium was set to be $1 \Omega/\square$ and not only has the power absorbed in the silicon been found for polarisation but the aluminium absorption has also been modelled. The results of these measurements

are shown in Figure 8.24.

The results of this model (Figure 8.24) show that there is still sustainably more power absorbed when the polarisation of the incident radiation is aligned with the antenna. When the polarisations of the antenna and wave are aligned the absorption in the silicon and aluminium are comparable and the features seen in the two polarisation-aligned models seem to agree, this indicates the antenna may be coupling (losing) some power into the surrounding aluminium. When the radiation's polarisation vector is perpendicular to that of the antenna these features are also seen in the aluminium, although their magnitude is somewhat reduced. However, in the perpendicular case, very little power is absorbed within the silicon.

8.4.6 SUMMARY OF FINDINGS

The above simulation work has shown that, although the interpretation of the initial model of the antenna was valid and the antenna does indeed respond at the design frequency of 160 GHz, this crude model missed out several features seen when a more realistic model of the system is produced. One of the main issues raised by this work is that the silicon lens used to improve coupling of radiation to the antenna is, in fact, adversely affecting the detector response away from the design frequency. This was most likely due to the lack of an anti-reflection coating to the lens. The modelling has also shown that, should the aluminium become lossy, there would be further broadening of the response spectrum and the power absorbed in the silicon mesa would be reduced. It should be noted that the case presented in Figure 8.24 is, by far, a worse-case scenario, whereby the aluminium has not only become lossy but the sheet resistance is in fact relatively high and matched to the coplanar waveguide. Clearly, from the data collected earlier in this chapter (Figures 8.9 and 8.17), there is an easily distinguishable feature, due to the antenna. It is still most likely that the broadband level seen in these figures is the result of direct, bolometric, absorption by the silicon mesa, although as has been seen in this modelling work, it is possible that loss in the aluminium may have contributed to this.

8.5 SPECTRAL STUDY OF SILICON MATERIAL

The final set of experiments performed in the course of this work were to measure the transmission properties of the silicon material as a function of frequency. The purpose of these measurements was to ascertain if the material would place any limits on the frequency range over which such a detector may be useful (i.e. capable of responding to light). Although such measurements have been carried out for bulk silicon (see for example [Hawkins, 1998](#)), no such measurements have been performed for highly-doped silicon either with or without strain, such as the material used here.

This measurement was performed using the same Fourier-transform spectrometer already used to measure the spectral response of the [SiCEB](#) detectors. For these measurements, a well-characterised bolometric detector (specifically a gold-sapphire composite bolometer operating at 1.5 K) was used to measure the signal transmitted through the material. Two samples were prepared for each of the two silicon materials (the unstrained and the strained material, both of which were highly doped). Firstly, one sample was prepared where the doped layer (along with straining layer, where relevant) was removed, this sample was used to ensure that the bulk silicon (through which the detector was illuminated) did not interfere with the measurement. Secondly, a sample of the complete wafer material was prepared; this, combined with the information already collected about the substrate, would demonstrate the affect of the doped (and strained, in the case of the second device) layer. All samples were mounted in front of the detector at a temperature of 1.5 K.

Figure 8.25 shows the transmission measured for the unstrained-doped silicon (green), along with its substrate alone (red). The substrate is highly transparent from the lowest frequencies measured up to approximately 10 THz, where the transmission has dropped to 0.7, which is maintained for the rest of the spectrum. Considering the whole wafer, there is around 60 % transmission at low frequencies, then the absorption slowly drops to 40 %. This small drop in the absorption should not affect a detector to the extent that it would become unusable and so it may seem reasonable to assert that this material could be used up to 17 THz (the extent over which data have been collected).

Figure 8.26 shows the same spectrums measured with for the wafer with strained silicon. With the straining and doped layers removed (red plot in Figure 8.26), the wafer transmission was, reassuringly, much the same as was seen for

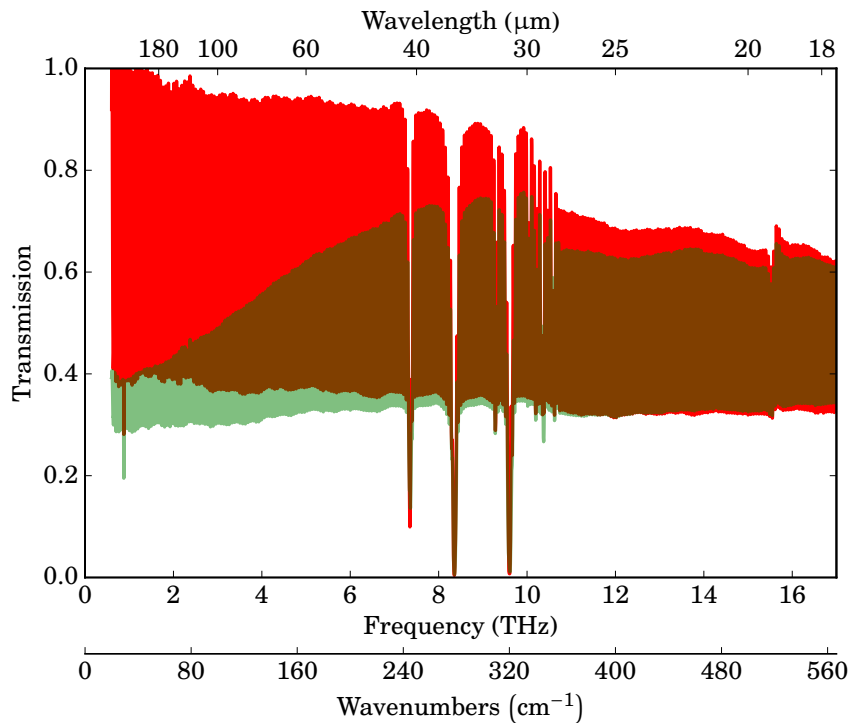


Figure 8.25: Transmission spectrum of unstrained doped silicon. Red—silicon substrate only; green—full wafer (including doped layer).

the previous wafer in Figure 8.25. When the strain and doped layers are considered (green plot in Figure 8.25), absorption at a level of 60 % can be seen from low frequencies up to 3 THz. Above this frequency, the material becomes gradually more transmissive, until at 7 THz, where the absorption has decreased to 40 %, a level which is, for the most part maintained, for the remainder of the measurement. This measurement, as was the case for the unstrained material, still shows that it should be possible to use highly-doped strained silicon as an absorber up to 17 THz.⁶ It should be noted that these measurements start at a frequency of 600 GHz compared to the operating frequency of 160 GHz for the detectors described in this work. While not ideal, this does not present a fundamental issue with these data, since there is no reason to believe the lower-frequency behavior would change from the lowest frequencies measured (as can be seen from the mostly flat behaviour

⁶Note that this is not to say that the material would cease to be useable at 17 THz, simply that the data collected do not allow for the performance of the material above this frequency to be inferred.

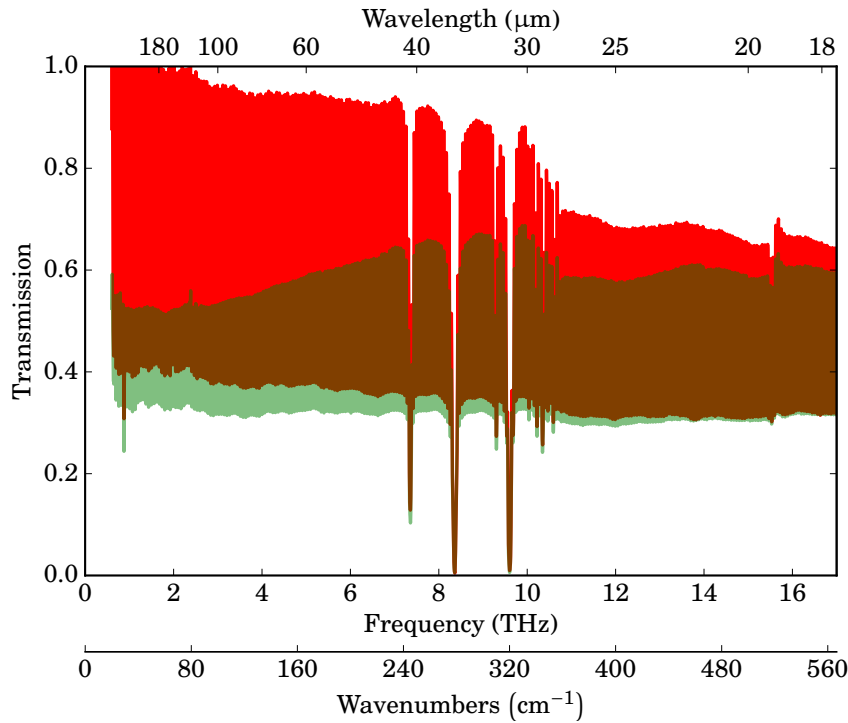


Figure 8.26: Transmission spectrum of strained doped silicon. Red—silicon substrate only; green—full wafer (including doped layer).

at the start of Figures 8.25 and 8.26). This is further justified by the fact that the main cause for the increasing transparency of the material is the roll-off in the kinetic inductance of the carriers which, as seen from the figures in this section, occurs around 6 THz.

It should be noted that while the data contained in Figures 8.25 and 8.26 appear as blocks rather than lines (especially in print) they are, in fact, sinusoidal oscillations in the transmission as a result of Fabry-Perot interference due to multiple surface reflections within the sample, which can be considered to be two parallel reflecting plates. This means that the transmission, T , can be described by:

$$T = \frac{(1-R^2)^2}{1-R^2 \left(2 \cos \left(\frac{4\pi n d}{\lambda} \right) \right) + R^4}, \quad (8.9)$$

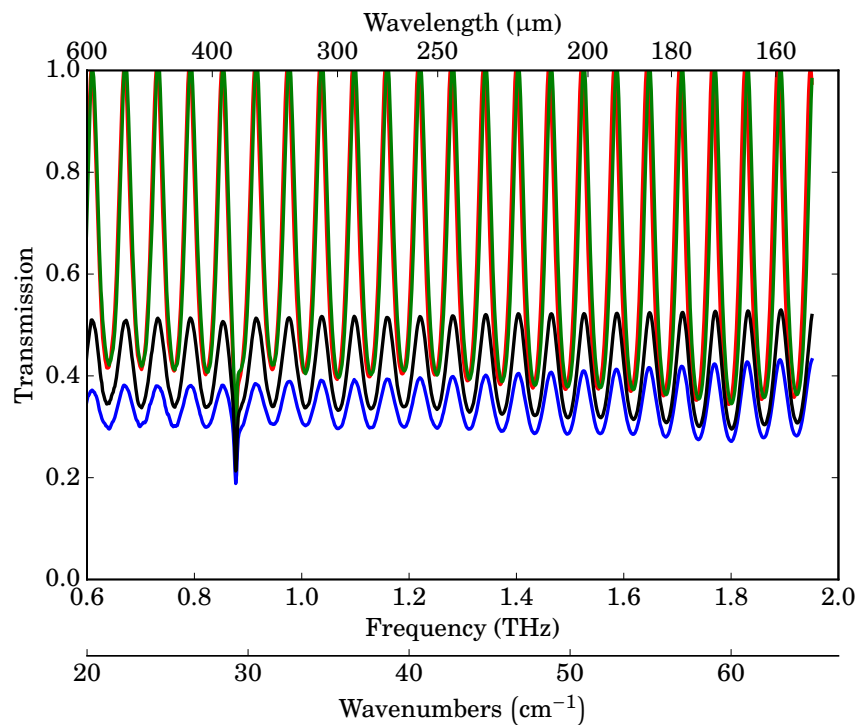


Figure 8.27: Transmission of silicon material over a narrow frequency range. Fabry-Perot interference is clearly shown as the sinusoidal variations in the signal. Red—unstrained material with doped layer removed, green—strained material with doped and straining layers removed, blue—full unstrained wafer, black—full strained wafer. Measured at a temperature of 1.5 K.

where R is the reflectance of the plates (taken to be the same for both planes), n in the order, and d is the distance between the two plates. For clarity Figure 8.27 shows a magnified view of the data presented in this section over a much smaller frequency range. This shows the sinusoidal behaviour clearly.

The absorption lines seen at 0.25, 7.36, 8.36, and 9.60 THz in all the measurements presented in this chapter are simply absorption lines of silicon. As are those seen between 10 and 11 THz (Kramida et al., 2014; Nahar and Pradhan, 1993).

8.6 SUMMARY OF DETECTOR PERFORMANCE

The results in this chapter have shown that the silicon cold-electron bolometer is a sensitive detector capable of achieving sensitivities (noise-equivalent powers) of $\sim 10^{-17} \text{ W Hz}^{-1/2}$. These sensitivities have been achieved for a relatively unrefined, proof-of-concept-type, device. However, these sensitivities are still close to those of the detectors used in the last generation of space-based missions (see Table 1.1) and are already capable of being background limited on any ground-based instrument. To be suitable for the next generation of space based missions (for example *SPICA* or *SAFIR*), improvements will be required. However, as already mentioned, the devices tested throughout this work are first-generation, prototype, detectors and there is great scope for improvement. Firstly, the current absorbing element is much larger than required ($14 \times 32 \mu\text{m}$), reducing the size of this element would lower the noise-equivalent power associated with the interaction between the electron and phonon systems (Equation 2.111). Calculations performed for a comparable device, where the absorber is reduced in size by a factor of ten, give $NEP_{\text{e-ph}} = 2.6 \times 10^{-18} \text{ W Hz}^{-1/2}$. This shrinking is easily attainable with standard photolithography and, if e-beam lithography were to be used, further order-of-magnitude reductions could be made. Furthermore, it should be possible to further increase the strain in the absorbing layer and, as has been seen in this chapter, such a change should further reduce the interaction between the electrons and the phonons. Finally, the current tunnelling contacts could be improved to create more consistent Schottky contacts; greater control over this would allow the tunnelling noise to be lowered.

Chapter Nine

Conclusions

'Difficulties mastered are opportunities won.'

WINSTON CHURCHILL

This work has tested two silicon cold-electron bolometers and assessed their potential, predominately in terms of their sensitivity. The two detectors tested were fabricated to the same designs, differing only in the material used to construct the detector's absorber. The first detector tested used an unstrained *control* silicon material, which was heavily doped (with phosphorus to a concentration of $4 \times 10^{19} \text{ cm}^{-3}$); whereas, in the second device, the absorbing silicon was strained (through a $\text{Si}_{0.7}\text{Ge}_{0.3}$ layer), as well as being doped to the same concentration as in the previous detector (the cross-sections of the two wafers used are shown in Figures 4.6a and 4.6b, respectively). For both detectors, radiation was coupled to the absorber via a twin-slot antennae, designed to couple radiation with a frequency of 160 GHz (the antenna design has been detailed in Section 4.2.1).

Both detectors have been measured in the absence of optical power (dark measurements, Chapter 7) and with incident optical power from black-body sources (Chapter 8). Dark measurements predominately consisted of measuring the current-voltage relationship of the detectors as the phonon (bath) temperature was varied. The results of these measurements (shown in Figures 7.1 and 7.4 for the unstrained and strained devices, respectively) verified that tunnelling junctions had been formed between the silicon absorber and the superconducting (aluminium) contacts. These data also allowed the electron-cooling performance to be calculated (by fitting

to Equation 2.30); by doing so, the ability of these detectors to cool the carriers in the silicon absorber to below the temperature of the lattice has been demonstrated (see Figures 7.3 and 7.6). The electron-temperature fitting showed the benefits of using strained silicon, in that the strained-silicon detector was able to cool the electrons in the silicon to a lower temperature than the unstrained device (the strained detector was able to cool electrons to ≈ 100 mK compared to ≈ 180 mK for the unstrained silicon; in both cases, the bath temperature was 300 mK); this improved performance is the result of the reduced coupling between the electrons and phonons in the strained material.

These tests were repeated with the detectors illuminated by a black-body source. From these measurements, it was clear that a response to a change in optical power (produced by varying the temperature of the black-body source) could be measured in the *I-V* curves and thus, it would be possible to measure a varying optical signal by biasing the device at a constant value (Figures 8.1 and 8.10 show the current-voltage relationship for the unstrained and strained detectors, respectively, for different levels of optical power). By using the same electron-temperature fitting technique used for the dark data, along with Equation 8.1 (the absorbed power) and Equation 2.61 (the responsivity in a current-biased regime), the responsivity was calculated to peak at 2.1×10^6 VW $^{-1}$ for the unstrained detector and 1.5×10^7 VW $^{-1}$ for the strained-silicon detector (these results are taken from Figures 8.3 and 8.12, respectively). This factor of 10 is approaching, but noticeably less than, the difference in the electron-phonon coupling which was 29 (from Table 4.3). This still represents a strong advantage in the performance of the strained detector compared to the unstrained device. This improvement is the result of the weaker electron-phonon coupling (as discussed in Section 2.5) present in the strained detector, which allows the electrons to heat up by a greater amount per unit amount of optical power incident; this is seen by comparing the temperatures of the carriers at zero bias in the case of each detector (see Figures 8.2 and 8.11). There should be no significant difference in the sensitivity of the tunnelling-junction thermometers between the two cases.

As well measuring the current-voltage behavior of the detector under optical loading, the electrical noise was also measured as a function of optical load and bias. These data, combined with those already collected and the various equations presented in Section 2.8, allowed for a complete model of the noise-equivalent power of each detector to be produced (these have been presented in Figure 8.8

for the unstrained detector and Figures 8.15 and 8.16 for the strained-silicon detector). The results of these measurements are summarised for comparison in Figure 9.1. This graph compares the device-limited noise of the two detectors; it is clear that the inherent noise of the strained-silicon detector is lower than that of the unstrained device (by a factor of approximately 3.5). In both cases, the device noise was limited by the flow of charges through the tunnelling contacts, a combination of the final three terms in Equation 2.121. When other noise sources such as the readout amplifier and photon noise—which were the limiting sources for the unstrained and strained detectors, respectively—are considered, the achieved noise-equivalent powers were $1.5 \times 10^{-16} \text{ WHz}^{-\frac{1}{2}}$ and $6.6 \times 10^{-17} \text{ WHz}^{-\frac{1}{2}}$ for the unstrained and strained detectors, respectively. From this, and when considering both the extremely early stage of development and the unoptimised designs used here, it has been shown that silicon cold-electron bolometers have the potential to rival the most sensitive detectors operating in the far infrared (such as those reported by: Suzuki et al., 2014; Visser et al., 2014; Karasik et al., 2015).

Attempts were made to determine the time constant of the strained-silicon detector by measuring the response to a rapidly-chopped source and by measuring the roll-off in photon noise. Neither of these methods were able to accurately determine the time constant, instead only upper limits could be inferred; these were $\tau < 14 \mu\text{s}$ from the chopped optical source and $\tau < 1.5 \mu\text{s}$ from the roll-off in photon noise. These values not only match or better the current state-of-the-art detectors operating in these wavelengths (e.g. Zhang et al., 2015; Visser et al., 2014; Karasik and Cantor, 2011) but also show that such detectors are indeed capable of achieving the anticipated time constant of 10 ns presented by Kuzmin (2004).

These results (which have been, in part, previously published in Brien et al., 2014) represent the first optical measurements for a silicon cold-electron bolometer, as well as some of the first optical result for any type of cold-electron bolometer. To put the results presented in this thesis in the context of the wider field, Table 9.1 compares the results obtained for the two devices studied here with those achieved in recent years for metal-based cold-electron bolometers. It can be seen that, considering the early stage of development, the strained-silicon cold electron bolometer compares well.

As discussed in Chapter 1, it is a goal for the next generation of space-based instruments to operate at noise-equivalent powers of close to $10^{-20} \text{ WHz}^{-\frac{1}{2}}$. While promising for a prototype device, the results presented here, along with those shown

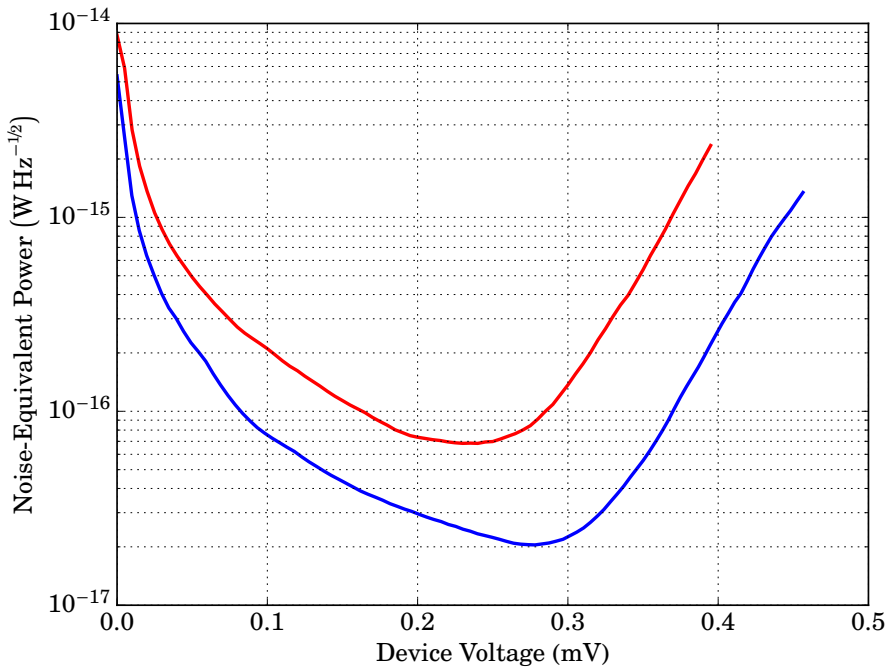


Figure 9.1: Comparison between device-limited noise-equivalent power for silicon cold-electron bolometers made with unstrained (red) and strained (blue) silicon, at a thermal bath temperature of 350 mK.

in Table 9.1, are still orders of magnitude above this. In the absence of noise due to either photons or readout, the limiting noise performance of a silicon cold-electron bolometer is due to the tunnelling noise (Equations 2.107, 2.115 and 2.120) and the noise due to the electron-phonon interactions (Equation 2.111). In order to ascertain if the technology presented here could achieve a NEP of approaching 10^{-20} W Hz^{-1/2}, a similar noise model to those presented in Chapter 8, but with the dimensions of the detector reduced by a factor of a hundred and the operating temperature reduced by a factor of three, has been performed. This model gives a very approximate limit of $1\text{--}2 \times 10^{-18}$ W Hz^{-1/2} for such a device. This is limited by the tunnelling noise; the noise due to the electron-phonon noise-equivalent power in such a detector is estimated to be approximately 6×10^{-20} W Hz^{-1/2}. This shows some promise for such detectors, however improvements are needed to bring the overall noise-equivalent power down to the level of 10^{-20} W Hz^{-1/2}. The current

Table 9.1: Comparison of the optical performance of various cold-electron bolometer reported in recent years.

Detector	Absorber Volume (m ³)	Noise-Equivalent Power (WHz ^{-1/2})	Responsivity (VW ⁻¹)
Unstrained SiCEB	1.3×10^{-17}	2.4×10^{-16}	2.7×10^6
Strained SiCEB	1.3×10^{-17}	6.6×10^{-17}	1.5×10^7
Distributed			
Aluminium CEB ^a	8×10^{-20}	4.8×10^{-17}	8.8×10^8
Titanium CEB ^b	<i>Not given</i>	8.9×10^{-17}	1.1×10^8

^a Tarasov et al. (2011).

^b Otto et al. (2013).

noise contribution to the tunnelling noise reduces with the responsivity (which has not been altered in this model) as S^{-1} , as seen in Equation 2.115. As such, improving the responsivity should bring the over noise-equivalent power down. As discussed in Section 8.3, the presence of strain in the absorber has the effect of increasing the responsivity of a silicon cold-electron bolometer, as the electrons are heated more per unit of power absorbed. As discussed in Section 2.5, the thermal conduction between electrons and phonons in the strained material is currently much higher than models would suggest and, as such, improvements to the straining of the absorber are definitely plausible and should help to improve the overall noise-equivalent power of these detectors.

To perform the measurements described in this work, a bias and readout system has been designed and revised for best performance. To facilitate the measurement of the very low noise voltage associated with these detectors, a novel means of measuring below the amplifier noise floor has been described. This was performed by cross correlating the output of two matched amplifiers to remove the uncorrelated amplifier noise. This technique has been shown to reduced the noise associated with the readout chain from ≈ 1 nVHz^{-1/2} to 300 pVHz^{-1/2} with averaging (shown in Figure 6.24). This technique clearly has great potential for measuring ultra-low noise sources to determine the characteristics of high-end devices.

In order to explain the spectral responses seen in Figures 8.9 and 8.17, the simulation work of the optical system has been revisited in much greater detail than was initially performed. This work showed that the main source degradation in the spectral response was the silicon lens, which was lacking any anti-reflection

coatings. It also showed that the DC cuts in the ground plane (which were essential for biasing the detector) had added to the spectral response at frequencies other than the design frequency.

A brief study has been performed to determine if the silicon material used to fabricate these detectors may place a limit on the usable frequency range of detectors fabricated using it. This work (presented in Section 8.5) showed that while no severe limit exists, both materials exhibited small drops in absorption beyond a few THz. This drop should not by any means make the construction of a silicon cold-electron bolometer operating above this frequency implausible.

This work has only performed an initial study of silicon cold-electron bolometers. Clearly, there is a great scope for further study and refinement of these detectors, to deduce those properties that have not been accurately found in this work and to work towards improving those which already have. It is the opinion of the author that the logical next step in this work is to accurately measure the time constant of such a detector. Based on the findings of this work, the best route to achieve this would be to measure the photon noise to higher readout frequencies than those studied here and to measure the roll-off in this noise.

This work has only studied the behavior of detectors under a very limited set of optical loadings, there should be great interest in a more complete study, from which the dynamic range of these detectors could be ascertained along with constraining, through measurement, the relationship between the responsivity and the absorbed optical power. Beyond this, a more optimised device could be fabricated and tested to compare with the detectors studied in this work. Such detectors should have smaller overall dimensions (reducing the electron-phonon noise), along with more controlled—higher-quality—tunnelling contacts. It is envisaged that such a device should be capable of offering at least an order of magnitude improvement to the sensitivity (if not more), with no tradeoff to other characteristics. In fact, such a device may well improve on the time constant of the designs presented in this work, since their relatively large absorber size may result in the time constant being limited by the diffusion time of the electrons in the absorber, rather than the tunnelling time.

Overall, this thesis has, through thorough testing of two types of silicon cold-electron bolometer, demonstrated that such devices are highly sensitive detectors capable of operating with very short time constants. Furthermore, it has been

shown that this is possible even for a proof-of-concept type detector lacking optimisation. With relatively simple refinements to both design and the fabrication, these detectors clearly present a very exciting opportunity to achieve the ultra-low noise limits which will be required by the next generation of space-based far-infrared observatories.

Bibliography

“If I have seen further, it is by standing on the shoulders of giants.”
—SIR ISAAC NEWTON

- Ade, P. A. R., G. Pisano, C. Tucker, and S. Weaver (2006). “A review of metal mesh filters”. In: vol. 6275, 62750U. DOI: [10.1117/12.673162](https://doi.org/10.1117/12.673162) (Cited on page 82).
- Agilent 33220A Function/Arbitrary Waveform Generator Data Sheet* (2011). Agilent Technologies. URL: <http://cp.literature.agilent.com/litweb/pdf/5988-8544EN.pdf> (Cited on page 96).
- Arams, F., C. Allen, B. Peyton, and E. Sard (1966). “Millimeter mixing and detection in bulk InSb”. In: *Proceedings of the IEEE*. Vol. 54. 4, pp. 612–622. DOI: [10.1109/PROC.1966.4781](https://doi.org/10.1109/PROC.1966.4781) (Cited on page 10).
- Archer, R. J. and T. O. Yep (1970). “Dependence of Schottky Barrier Height on Donor Concentration”. In: *Journal of Applied Physics* 41.1, pp. 303–311. DOI: [10.1063/1.1658340](https://doi.org/10.1063/1.1658340) (Cited on page 21).
- Bardeen, J., L. N. Cooper, and J. R. Schrieffer (1957). “Theory of Superconductivity”. In: *Phys. Rev.* 108 (5), pp. 1175–1204. DOI: [10.1103/PhysRev.108.1175](https://doi.org/10.1103/PhysRev.108.1175) (Cited on pages 29, 30).
- Begault, D. R. (2007). *3-D Sound: For Virtual Reality and Multimedia*. Academic Press (Cited on page 119).
- Benford, D. J. and S. H. Moseley (2004). “Cryogenic detectors for infrared astronomy: the Single Aperture Far-InfraRed SAFIR Observatory”. In: *Nuclear Instruments and Methods in Physics Research A* 520.1–3. Proceedings of the 10th International Workshop on Low Temperature Detectors, pp. 379–383. DOI: [10.1016/j.nima.2003.11.295](https://doi.org/10.1016/j.nima.2003.11.295) (Cited on pages 4, 8).

- Bhatia, R. S., J. J. Bock, P. A. R. Ade, A. Benoît, T. W. Bradshaw, B. P. Crill, M. J. Griffin, I. D. Hepburn, V. V. Hristov, A. E. Lange, P. V. Mason, A. G. Murray, A. H. Orlowska, and A. D. Turner (1999). "The susceptibility of incoherent detector systems to cryocooler microphonics." In: *Cryogenics* 39.8, pp. 701–715. DOI: [0.1016/S0011-2275\(99\)00071-5](https://doi.org/10.1016/S0011-2275(99)00071-5) (Cited on page 82).
- Bhatia, R. S., S. T. Chase, S. F. Edgington, J. Glenn, W. C. Jones, A. E. Lange, B. Maffei, A. K. Mainzer, P. D. Mauskopf, B. J. Philhour, and B. K. Rownd (2000). "A three-stage helium sorption refrigerator for cooling of infrared detectors to 280 mK". In: *Cryogenics* 40.11, pp. 685–691. DOI: [10.1016/S0011-2275\(00\)00072-2](https://doi.org/10.1016/S0011-2275(00)00072-2) (Cited on page 80).
- Bintley, D., A. L. Woodcraft, and F. C. Gannaway (2007). "Millikelvin thermal conductance measurements of compact rigid thermal isolation joints using sapphire-sapphire contacts, and of copper and beryllium-copper demountable thermal contacts". In: *Cryogenics* 47.5–6, pp. 333–342. DOI: [10.1016/j.cryogenics.2007.04.004](https://doi.org/10.1016/j.cryogenics.2007.04.004) (Cited on page 82).
- Bracewell, R. N. (2000). *The Fourier Transform and its Applications*. 3rd ed. McGraw-Hill Higher Education (Cited on page 120).
- Brien, T. L. R., P. A. R. Ade, P. S. Barry, C. Dunscombe, D. R. Leadley, D. V. Morozov, M. Myronov, E. H. C. Parker, M. J. Prest, M. Prunnilla, R. V. Sudiwala, T. E. Whall, and P. D. Mauskopf (2014). "A strained silicon cold electron bolometer using Schottky contacts". In: *Applied Physics Letters* 105.4, p. 043509. DOI: <http://dx.doi.org/10.1063/1.4892069> (Cited on pages 12, 162, 181).
- Cabrera, N. and N. F. Mott (1949). "Theory of the oxidation of metals". In: *Reports on progress in physics* 12.1, p. 163 (Cited on page 20).
- Callier, F. M. and C. A. Desoer (1978). "An algebra of transfer functions for distributed linear time-invariant systems". In: *Circuits and Systems, IEEE Transactions on* 25.9, pp. 651–662. ISSN: 0098-4094. DOI: [10.1109/TCS.1978.1084544](https://doi.org/10.1109/TCS.1978.1084544) (Cited on page 119).
- Caughey, D. M. and R. E. Thomas (1967). "Carrier mobilities in silicon empirically related to doping and field". In: *Proceedings of the IEEE*. Vol. 55. 12, pp. 2192–2193. DOI: [10.1109/PROC.1967.6123](https://doi.org/10.1109/PROC.1967.6123) (Cited on pages 63, 64).
- Chaudhuri, S. and I. J. Maasulta (2014). "Superconducting tantalum nitride-based normal metal-insulator-superconductor tunnel junctions". In: *Applied Physics Letters* 104.12. DOI: [10.1063/1.4869563](https://doi.org/10.1063/1.4869563) (Cited on page 20).
- Chi, C. C. and J. Clarke (1979). "Enhancement of the energy gap in superconducting aluminum by tunneling extraction of quasiparticles". In: *Phys. Rev. B* 20 (11), pp. 4465–4473. DOI: [10.1103/PhysRevB.20.4465](https://doi.org/10.1103/PhysRevB.20.4465) (Cited on page 9).
- Clark, A. M., N. A. Miller, A. Williams, S. T. Ruggiero, G. C. Hilton, L. R. Vale, J. A. Beall, K. D. Irwin, and J. N. Ullom (2005). "Cooling of bulk material by electron-tunneling refrigerators". In: *Applied Physics Letters* 86.17, p. 173508. DOI: [10.1063/1.1914966](https://doi.org/10.1063/1.1914966) (Cited on pages 9, 19).

- Corruccini, R. J. (1961). *Thermal Expansion of Technical Solids at Low Temperatures: A Compilation From the Literature*. Monograph. National Bureau of Standards (Cited on page 89).
- Dall’Oglio, G., L. Pizzo, L. Piccirillo, and L. Martinis (1991). “New $^3\text{He}/^4\text{He}$ refrigerator”. In: *Cryogenics* 31.1, pp. 61–63. DOI: [10.1016/0011-2275\(91\)90193-Z](https://doi.org/10.1016/0011-2275(91)90193-Z) (Cited on page 80).
- ESA (2015). *Herschel Fact Sheet*. URL: <http://esamultimedia.esa.int/docs/herschel/Herschel-Factsheet.pdf> (visited on 03/05/2015) (Cited on page 2).
- ESA (2014). *SPICA - A SPACE INFRARED TELESCOPE FOR COSMOLOGY AND ASTROPHYSICS*. Press Release. URL: <http://sci.esa.int/cosmic-vision/53635-spica/> (Cited on page 13).
- European Southern Observatory (2013). *ALMA Inauguration Heralds New Era of Discovery*. Press Release. URL: <http://www.eso.org/public/news/eso1312/> (Cited on page 2).
- Focardi, P. and W. R. McGrath (2005). “Design guidelines for terahertz mixers and detectors”. In: *Infrared and Millimeter Waves and 13th International Conference on Terahertz Electronics, 2005. IRMMW-THz 2005. The Joint 30th International Conference on*. Vol. 2, pp. 624–625. DOI: [10.1109/ICIMW.2005.1572696](https://doi.org/10.1109/ICIMW.2005.1572696) (Cited on pages 70, 168).
- Ganzevles, W. F. M., L. R. Swart, J. R. Gao, P. A. J. de Korte, and T. M. Klapwijk (2000). “Direct response of twin-slot antenna-coupled hot-electron bolometer mixers designed for 2.5 THz radiation detection”. In: *Applied Physics Letters* 76.22, pp. 3304–3306. DOI: [10.1063/1.126614](https://doi.org/10.1063/1.126614) (Cited on page 168).
- Golubev, D. and L. S. Kuzmin (2001). “Nonequilibrium theory of a hot-electron bolometer with normal metal-insulator-superconductor tunnel junction”. In: *Journal of Applied Physics* 89.11, pp. 6464–6472. DOI: [10.1063/1.1351002](https://doi.org/10.1063/1.1351002) (Cited on pages 42, 43, 46, 48, 91).
- Golwala, SR, J Jochum, and B Sadoulet (1997). “Noise considerations in low resistance NIS tunnel junctions”. In: *Proceedings of the Seventh International Workshop on Low Temperature Detectors*, pp. 56–59 (Cited on page 48).
- Granata, C., A. Vettoliere, R. Russo, M. Fretto, N. Leo, E. Enrico, and V. Lacquaniti (2015). “Ultra High Sensitive Niobium NanoSQUID by Focused Ion Beam Sculpting”. In: *Journal of Superconductivity and Novel Magnetism* 28.2, pp. 585–589. DOI: [10.1007/s10948-014-2693-y](https://doi.org/10.1007/s10948-014-2693-y) (Cited on page 91).
- Griffin, M. J. (2000). “Bolometers for far-infrared and submillimetre astronomy”. In: *Nuclear Instruments and Methods in Physics Research Section A: Accelerators, Spectrometers, Detectors and Associated Equipment* 444.1–2, pp. 397–403. DOI: [10.1016/S0168-9002\(99\)01413-8](https://doi.org/10.1016/S0168-9002(99)01413-8) (Cited on page 8).
- Griffin, M. J. et al. (2006). “Herschel-SPIRE: design, performance, and scientific capabilities”. In: *Proc. SPIE*. Vol. 6265, 62650A. DOI: [10.1117/12.670783](https://doi.org/10.1117/12.670783) (Cited on page 4).

- Hartog, R. den, J. Beyer, D. Boersma, M. Bruijn, L. Gottardi, H. Hoevers, Rui Hou, M. Kiviranta, P. de Korte, J. van der Kuur, B. van Leeuwen, M. Lindeman, and A. Nieuwenhuizen (2011). “Frequency Domain Multiplexed Readout of TES Detector Arrays With Baseband Feedback”. In: *Applied Superconductivity, IEEE Transactions on* 21.3, pp. 289–293. DOI: [10.1109/TASC.2010.2101998](https://doi.org/10.1109/TASC.2010.2101998) (Cited on page 13).
- Hawkins, Gary J (1998). “Spectral characterisation of infrared optical materials and filters.” PhD thesis. University of Reading (Cited on page 173).
- Hogg, R. V., J. McKean, and A. T. Craig (2012). *Introduction to mathematical statistics*. 2nd ed. Pearson (Cited on page 119).
- Holland, W. S. et al. (2013). “SCUBA-2: the 10 000 pixel bolometer camera on the James Clerk Maxwell Telescope”. In: *Monthly Notices of the Royal Astronomical Society* 430.4, pp. 2513–2533. DOI: [10.1093/mnras/sts612](https://doi.org/10.1093/mnras/sts612) (Cited on pages 12, 13).
- Horowitz, P. and W. Hill (1989). *The art of electronics*. 2nd ed. Cambridge University Press (Cited on pages 49, 109).
- Hu, W. and S. Dodelson (2002). “Cosmic Microwave Background Anisotropies”. In: *Annual Review of Astronomy and Astrophysics* 40.1, pp. 171–216. DOI: [10.1146/annurev.astro.40.060401.093926](https://doi.org/10.1146/annurev.astro.40.060401.093926) (Cited on page 4).
- INA103 Data Sheet* (2000). Texas Instruments. URL: <http://www.ti.com/product/ina103> (Cited on pages 109, 112, 114, 115).
- INA111 Data Sheet* (2010). Texas Instruments. URL: <http://www.ti.com/lit/ds/symlink/ina111.pdf> (Cited on pages 93, 95).
- Irvin, J. C. (1962). “Resistivity of Bulk Silicon and of Diffused Layers in Silicon”. In: *Bell System Technical Journal* 41.2, pp. 387–410. ISSN: 1538-7305. DOI: [10.1002/j.1538-7305.1962.tb02415.x](https://doi.org/10.1002/j.1538-7305.1962.tb02415.x) (Cited on page 63).
- Irwin, K. D. (1995). “An application of electrothermal feedback for high resolution cryogenic particle detection”. In: *Applied Physics Letters* 66.15, pp. 1998–2000. DOI: [10.1063/1.113674](https://doi.org/10.1063/1.113674) (Cited on page 10).
- Irwin, K. D. (2002). “SQUID multiplexers for transition-edge sensors”. In: *Physica C: Superconductivity* 368.1–4, pp. 203–210. DOI: [10.1016/S0921-4534\(01\)01167-4](https://doi.org/10.1016/S0921-4534(01)01167-4) (Cited on page 91).
- Jackson, B. D. et al. (2012). “The SPICA-SAFARI Detector System: TES Detector Arrays With Frequency-Division Multiplexed SQUID Readout”. In: *Terahertz Science and Technology, IEEE Transactions on* 2.1, pp. 12–21. DOI: [10.1109/TTHZ.2011.2177705](https://doi.org/10.1109/TTHZ.2011.2177705) (Cited on page 4).
- Jaeger, R.M., H. Kuhlenbeck, H.-J. Freund, M. Wuttig, W. Hoffmann, R. Franchy, and H. Ibach (1991). “Formation of a well-ordered aluminium oxide overlayer by oxidation of NiAl (110)”. In: *Surface science* 259.3, pp. 235–252 (Cited on page 20).

- Joule, J. P. (1837). "On the Production of Heat by Voltaic Electricity." In: *Abstracts of the Papers Printed in the Philosophical Transactions of the Royal Society of London*. Vol. 4. The Royal Society, pp. 280–282 (Cited on page 40).
- Karasik, B. S. and R. Cantor (2011). "Demonstration of high optical sensitivity in far-infrared hot-electron bolometer". In: *Applied Physics Letters* 98.19, p. 193503. DOI: [10.1063/1.3589367](https://doi.org/10.1063/1.3589367) (Cited on pages 10, 168, 181).
- Karasik, B. S., W. R. McGrath, M. E. Gershenson, and A. V. Sergeev (2000). "Photon-noise-limited direct detector based on disorder-controlled electron heating". In: *Journal of Applied Physics* 87.10, pp. 7586–7588. DOI: [10.1063/1.373026](https://doi.org/10.1063/1.373026) (Cited on pages 10, 11).
- Karasik, B. S., C. B. McKitterick, T. J. Reck, and D. E. Prober (2015). "Normal-Metal Hot-Electron Nanobolometer With Johnson Noise Thermometry Readout". In: *Terahertz Science and Technology, IEEE Transactions on* 5.1, pp. 16–21. DOI: [10.1109/TTHZ.2014.2370755](https://doi.org/10.1109/TTHZ.2014.2370755) (Cited on page 181).
- Karasik, B. S., D. Olaya, J. Wei, S. Pereverzev, M. E. Gershenson, J. H. Kawamura, W. R. McGrath, and A. V. Sergeev (2007). "Record-Low NEP in Hot-Electron Titanium Nanobolometers". In: *Applied Superconductivity, IEEE Transactions on* 17.2, pp. 293–297. DOI: [10.1109/TASC.2007.897167](https://doi.org/10.1109/TASC.2007.897167) (Cited on page 10).
- Kaye, G. W. C. and T. H. Laby (1995). *Tables of physical and chemical constants*. 16th ed. Harlow: Longman (Cited on page 89).
- Keithley 220 Programmable Current Source Data Sheet* (2009). Keithley. URL: <http://www.keithley.com/support/data?asset=367> (Cited on pages 99, 100).
- Kittel, Charles (2005). *Introduction to solid state physics*. 8th ed. Wiley New York (Cited on page 22).
- Kramida, A., Yu. Ralchenko, J. Reader, and NIST ASD Team (2014). URL: <http://physics.nist.gov/asd> (visited on 23/03/2015) (Cited on page 176).
- Kuzmin, L. S. (2000). "On the concept of a hot-electron microbolometer with capacitive coupling to the antenna". In: *Physica B: Condensed Matter* 284–288, pp. 2129–2130. DOI: [10.1016/S0921-4526\(99\)03032-X](https://doi.org/10.1016/S0921-4526(99)03032-X) (Cited on page 11).
- Kuzmin, L. S. (2003). "Superconducting cold-electron bolometer with proximity traps". In: *Microelectronic Engineering*. Vol. 69. 2–4. Proceedings of the Symposium and Summer School on: Nano and Giga Challenges in Microelectronics Research and Opportunities in Russia, pp. 309–316. DOI: [10.1016/S0167-9317\(03\)00314-9](https://doi.org/10.1016/S0167-9317(03)00314-9) (Cited on page 11).
- Kuzmin, L. S. (2004). "Ultimate cold-electron bolometer with strong electrothermal feedback". In: *Proc. SPIE*. Vol. 5498, pp. 349–361. DOI: [10.1117/12.554317](https://doi.org/10.1117/12.554317) (Cited on pages 11, 12, 57, 181).
- Kuzmin, L. S., I. A. Devyatov, and D. Golubev (1998). "Cold-electron bolometer with electronic microrefrigeration and general noise analysis". In: *Proc. SPIE*. Vol. 3465, pp. 193–199. DOI: [10.1117/12.331165](https://doi.org/10.1117/12.331165) (Cited on page 11).

- Lamarre, J. M. et al. (2003). "The Planck High Frequency Instrument, a third generation CMB experiment, and a full sky submillimeter survey". In: *New Astronomy Reviews* 47.111112, pp. 1017–1024. DOI: [10.1016/j.newar.2003.09.006](https://doi.org/10.1016/j.newar.2003.09.006) (Cited on pages 3, 69).
- Lamarre, J. M. et al. (2010). "Planck pre-launch status: The HFI instrument, from specification to actual performance". In: *A&A* 520, A9. DOI: [10.1051/0004-6361/200912975](https://doi.org/10.1051/0004-6361/200912975) (Cited on page 4).
- Leisawitz, D. (2004). "NASA's far-IR/submillimeter roadmap missions: *SAFIR* and *SPECS*". In: *Advances in Space Research* 34.3. Astronomy at IR/Submm and the Microwave Background, pp. 631–636. DOI: [10.1016/j.asr.2003.06.023](https://doi.org/10.1016/j.asr.2003.06.023) (Cited on page 4).
- Leivo, M. M., J. P. Pekola, and D. V. Averin (1996). "Efficient Peltier refrigeration by a pair of normal metal/insulator/superconductor junctions". In: *Applied Physics Letters* 68.14, pp. 1996–1998. DOI: [10.1063/1.115651](https://doi.org/10.1063/1.115651) (Cited on page 9).
- Luukanen, Arttu, Leif Grönberg, Markus Grönholm, Petteri Lappalainen, Mikko Leivo, Anssi Rautiainen, Aleksi Tamminen, Juha Ala-Laurinaho, Charles R. Dietlein, and Erich N. Grossman (2010). "Real-time passive terahertz imaging system for standoff concealed weapons imaging". In: *Proc. SPIE*. Vol. 7670, p. 767004. DOI: [10.1117/12.850369](https://doi.org/10.1117/12.850369) (Cited on page 5).
- Maffei, B. et al. (2010). "Planck pre-launch status: HFI beam expectations from the optical optimisation of the focal plane". In: *A&A* 520, A12. DOI: [10.1051/0004-6361/200912999](https://doi.org/10.1051/0004-6361/200912999) (Cited on page 86).
- Manninen, A. J., J. K. Suoknuuti, M. M. Leivo, and J. P. Pekola (1999). "Cooling of a superconductor by quasiparticle tunneling". In: *Applied Physics Letters* 74.20, pp. 3020–3022. DOI: [10.1063/1.124051](https://doi.org/10.1063/1.124051) (Cited on page 9).
- Mather, J. C., D. J. Fixsen, R. A. Shafer, C. Mosier, and D. T. Wilkinson (1999). "Calibrator Design for the COBE Far Infrared Absolute Spectrophotometer (FIRAS)". In: *The Astrophysical Journal* 512.2, p. 511. DOI: [10.1086/306805](https://doi.org/10.1086/306805) (Cited on page 143).
- Monfardini, A. et al. (2010). "NIKA: A millimeter-wave kinetic inductance camera". In: *A&A* 521, A29. DOI: [10.1051/0004-6361/201014727](https://doi.org/10.1051/0004-6361/201014727) (Cited on page 4).
- Muhonen, J. T., M. J. Prest, M. Prunnila, D. Gunnarsson, V. A. Shah, A. Dobbie, M. Myronov, R. J. H. Morris, T. E. Whall, E. H. C. Parker, and D. R. Leadley (2011). "Strain dependence of electron-phonon energy loss rate in many-valley semiconductors". In: *Applied Physics Letters* 98.18, p. 182103. DOI: [10.1063/1.3579524](https://doi.org/10.1063/1.3579524) (Cited on pages 38, 39, 66, 73, 75).
- Nahar, S. N. and A. K. Pradhan (1993). "Atomic data for opacity calculations. XVIII. Photoionization and oscillator strengths of Si-like ions Si^0 , S^{2+} , Ar^{4+} , Ca^{6+} ". In: *Journal of Physics B: Atomic, Molecular and Optical Physics* 26.6, p. 1109. DOI: [10.1088/0953-4075/26/6/012](https://doi.org/10.1088/0953-4075/26/6/012) (Cited on page 176).

- Nahum, M., T. M. Eiles, and J. M. Martinis (1994). "Electronic microrefrigerator based on a normal-insulator-superconductor tunnel junction". In: *Applied Physics Letters* 65.24, pp. 3123–3125. DOI: [10.1063/1.112456](https://doi.org/10.1063/1.112456) (Cited on pages 9, 31).
- Nahum, M., P. L. Richards, and C. A. Mears (1993). "Design analysis of a novel hot-electron microbolometer". In: *Applied Superconductivity, IEEE Transactions on* 3.1, pp. 2124–2127. DOI: [10.1109/77.233921](https://doi.org/10.1109/77.233921) (Cited on pages 10, 11).
- Nyquist, H. (1928a). "Certain topics in telegraph transmission theory". In: *American Institute of Electrical Engineers, Transactions of the* 47.2, pp. 617–644. DOI: [10.1109/T-AIEE.1928.5055024](https://doi.org/10.1109/T-AIEE.1928.5055024) (Cited on page 49).
- Nyquist, H. (1928b). "Thermal Agitation of Electric Charge in Conductors". In: *Phys. Rev.* 32 (1), pp. 110–113. DOI: [10.1103/PhysRev.32.110](https://doi.org/10.1103/PhysRev.32.110) (Cited on page 37).
- OP07 Data Sheet (2011). Analog Devices. URL: http://www.analog.com/static/imported-files/data_sheets/OP07.pdf (Cited on page 93).
- Orlando, A. et al. (2010). "Antenna-coupled TES bolometer arrays for BICEP2/Keck and SPIDER". In: *Proc. SPIE*. Vol. 7741, 77410H. DOI: [10.1117/12.857914](https://doi.org/10.1117/12.857914). arXiv: [1009.3685 \[astro-ph.IM\]](https://arxiv.org/abs/1009.3685) (Cited on page 13).
- Otto, E., M. Tarasov, P. K. Grimes, A. Chekushkin, L. S. Kuzmin, and G. Yassin (2013). "Optical response of a titanium-based cold-electron bolometer". In: *Superconductor Science and Technology* 26.8, p. 085020. DOI: [10.1088/0953-2048/26/8/085020](https://doi.org/10.1088/0953-2048/26/8/085020) (Cited on pages 11, 12, 57, 183).
- Pardo, J.R., J. Cernicharo, and E. Serabyn (2001). "Atmospheric transmission at microwaves (ATM): an improved model for millimeter/submillimeter applications". In: *Antennas and Propagation, IEEE Transactions on* 49.12, pp. 1683–1694. DOI: [10.1109/8.982447](https://doi.org/10.1109/8.982447) (Cited on page 2).
- Parmenter, R. H. (1961). "Enhancement of Superconductivity by Extraction of Normal Carriers". In: *Phys. Rev. Lett.* 7 (7), pp. 274–277. DOI: [10.1103/PhysRevLett.7.274](https://doi.org/10.1103/PhysRevLett.7.274) (Cited on page 9).
- Pearson, G. L. and J. Bardeen (1949). "Electrical Properties of Pure Silicon and Silicon Alloys Containing Boron and Phosphorus". In: *Phys. Rev.* 75 (5), pp. 865–883. DOI: [10.1103/PhysRev.75.865](https://doi.org/10.1103/PhysRev.75.865) (Cited on page 62).
- Pekola, J. P. (2005). "Low-temperature physics: Tunnelling into the chill". In: *Nature* 435.7044, pp. 889–890. DOI: [10.1038/435889a](https://doi.org/10.1038/435889a) (Cited on page 9).
- Pekola, J. P., T. T. Heikkilä, A. M. Savin, J. T. Flyktman, F. Giazotto, and F. W. J. Hekking (2004). "Limitations in Cooling Electrons using Normal-Metal-Superconductor Tunnel Junctions". In: *Phys. Rev. Lett.* 92 (5), p. 056804. DOI: [10.1103/PhysRevLett.92.056804](https://doi.org/10.1103/PhysRevLett.92.056804) (Cited on page 19).

- Poglitsch, A., C. Waelkens, O. H. Bauer, J. Cepa, H. Feuchtgruber, T. Henning, C. van Hoof, F. Kerschbaum, O. Krause, E. Renotte, L. Rodriguez, P. Saraceno, and B. Vandenbussche (2008). “The Photodetector Array Camera and Spectrometer (PACS) for the Herschel Space Observatory”. In: *Proc. SPIE*. Vol. 7010, p. 701005. DOI: [10.1117/12.790016](https://doi.org/10.1117/12.790016) (Cited on page 4).
- Prest, M. J., J. T. Muhonen, M. Prunnila, D. Gunnarsson, V. A. Shah, J. S. Richardson-Bullock, A. Dobbie, M. Myronov, R. J. H. Morris, T. E. Whall, E. H. C. Parker, and D. R. Leadley (2011). “Strain enhanced electron cooling in a degenerately doped semiconductor”. In: *Applied Physics Letters* 99.25, p. 251908. DOI: [10.1063/1.3670330](https://doi.org/10.1063/1.3670330) (Cited on pages 9, 11, 20, 38, 39, 41, 66, 75).
- Prunnila, M. (2007). “Electron-acoustic-phonon energy-loss rate in multicomponent electron systems with symmetric and asymmetric coupling constants”. In: *Phys. Rev. B* 75 (16), p. 165322. DOI: [10.1103/PhysRevB.75.165322](https://doi.org/10.1103/PhysRevB.75.165322) (Cited on pages 37, 38).
- Qu, S.-X., A. N. Cleland, and M. R. Geller (2005). “Hot electrons in low-dimensional phonon systems”. In: *Phys. Rev. B* 72 (22), p. 224301. DOI: [10.1103/PhysRevB.72.224301](https://doi.org/10.1103/PhysRevB.72.224301) (Cited on page 38).
- Rhoderick, E. H. and R. H. Williams (1988). *Metal-semiconductor contacts*. 2nd ed. Clarendon Press Oxford (Cited on page 23).
- Rich, N. (2013). “Showdown at the Airport Body Scanner”. In: *The New York Times*. URL: <http://opinionator.blogs.nytimes.com/2013/05/25/showdown-at-the-airport-body-scanner/> (Cited on page 5).
- Richards, P. L. (1994). “Bolometers for infrared and millimeter waves”. In: *Journal of Applied Physics* 76.1, pp. 1–24. DOI: [10.1063/1.357128](https://doi.org/10.1063/1.357128) (Cited on page 77).
- Rieke, G. H. (2007). “Infrared Detector Arrays for Astronomy”. In: *Annual Review of Astronomy and Astrophysics* 45.1, pp. 77–115. DOI: [10.1146/annurev.astro.44.051905.092436](https://doi.org/10.1146/annurev.astro.44.051905.092436) (Cited on page 91).
- Roccaforte, F., F. La Via, V. Raineri, P. Musumeci, L. Calcagno, and G.G. Condorelli (2003). “Highly reproducible ideal SiC Schottky rectifiers: effects of surface preparation and thermal annealing on the Ni/6H-SiC barrier height”. In: *Applied Physics A* 77.6, pp. 827–833. DOI: [10.1007/s00339-002-1981-8](https://doi.org/10.1007/s00339-002-1981-8) (Cited on page 22).
- Rowe, S. et al. (2015). “A passive THz video camera based on lumped element kinetic inductance detectors”. In: *Review of Scientific Instruments*. In preparation (Cited on page 6).
- Salatino, M., P. de Bernardis, L. S. Kuzmin, S. Mahashabde, and S. Masi (2014). “Sensitivity to Cosmic Rays of Cold Electron Bolometers for Space Applications”. In: *Journal of Low Temperature Physics* 176.3–4, pp. 323–330. DOI: [10.1007/s10909-013-1057-5](https://doi.org/10.1007/s10909-013-1057-5) (Cited on page 12).

- Sampietro, M., L. Fasoli, and G. Ferrari (1999). "Spectrum analyzer with noise reduction by cross-correlation technique on two channels". In: *Review of Scientific Instruments* 70.5, pp. 2520–2525. DOI: [10.1063/1.1149785](https://doi.org/10.1063/1.1149785) (Cited on page 124).
- Savin, A., M. Prunnila, J. Ahopelto, P. Kivinen, P. Törmä, and J. Pekola (2003). "Application of superconductor-semiconductor Schottky barrier for electron cooling". In: *Physica B: Condensed Matter* 329–333, Part 2. Proceedings of the 23rd International Conference on Low Temperature Physics, pp. 1481–1484. DOI: [10.1016/S0921-4526\(02\)02400-6](https://doi.org/10.1016/S0921-4526(02)02400-6) (Cited on page 9).
- Savin, A., M. Prunnila, P. P. Kivinen, J. P. Pekola, J. Ahopelto, and A. J. Manninen (2001). "Efficient electronic cooling in heavily doped silicon by quasiparticle tunneling". In: *Applied Physics Letters* 79.10, pp. 1471–1473. DOI: [10.1063/1.1399313](https://doi.org/10.1063/1.1399313) (Cited on page 9).
- Schmidt, D. R., K. W. Lehnert, A. M. Clark, W. D. Duncan, K. D. Irwin, N. Miller, and J. N. Ullom (2005). "A superconductor-insulator-normal metal bolometer with microwave readout suitable for large-format arrays". In: *Applied Physics Letters* 86.5, p. 053505. DOI: [10.1063/1.1855411](https://doi.org/10.1063/1.1855411) (Cited on page 13).
- Schottky, W. (1918). "Über spontane Stromschwankungen in verschiedenen Elektrizitätsleitern". German. In: *Annalen der Physik* 362.23, pp. 541–567. ISSN: 1521-3889. DOI: [10.1002/andp.19183622304](https://doi.org/10.1002/andp.19183622304) (Cited on page 45).
- Schottky, W. (1939). "Zur Halbleitertheorie der Sperrsicht- und Spitzengleichrichter". German. In: *Zeitschrift für Physik* 113.5–6, pp. 367–414. DOI: [10.1007/BF01340116](https://doi.org/10.1007/BF01340116) (Cited on page 20).
- Shannon, C. E. (1949). "Communication in the presence of noise". In: *Proceedings of the IRE*. Vol. 37. 1. IEEE, pp. 10–21. DOI: [10.1109/JRPROC.1949.232969](https://doi.org/10.1109/JRPROC.1949.232969) (Cited on page 49).
- SRON (2014). *A new start for the SPICA mission*. Press Release. URL: <http://www.sron.nl/news-mainmenu-588/press-releases-mainmenu-686/3927-a-new-start-for-the-spica-mission> (Cited on page 13).
- Suzuki, T., P. Khosropanah, R. A. Hijmering, M. Ridder, M. Schoemans, H. Hoevers, and J.-R. Gao (2014). "Performance of SAFARI Short-Wavelength-Band Transition Edge Sensors (TES) Fabricated by Deep Reactive Ion Etching". In: *Terahertz Science and Technology, IEEE Transactions on* 4.2, pp. 171–178. DOI: [10.1109/TTHZ.2014.2298376](https://doi.org/10.1109/TTHZ.2014.2298376) (Cited on page 181).
- Tarasov, M. A., L. S. Kuzmin, V. S. Edelman, S. Mahashabde, and P. deBernardis (2011). "Optical Response of a Cold-Electron Bolometer Array Integrated in a 345-GHz Cross-Slot Antenna". In: *Applied Superconductivity, IEEE Trans. on* 21.6, pp. 3635–3639. DOI: [10.1109/TASC.2011.2169793](https://doi.org/10.1109/TASC.2011.2169793) (Cited on page 183).
- Topham, G. (2012). "Airport scanners 'here to stay'". In: *The Guardian*. URL: <http://www.theguardian.com/world/2012/may/04/airport-scanners-here-to-stay> (Cited on page 5).

- Valenziano, L. et al. (2007). "The low frequency instrument on-board the Planck satellite: Characteristics and performance". In: *New Astronomy Reviews* 51.3–4, pp. 287–297. DOI: [10.1016/j.newar.2006.11.030](https://doi.org/10.1016/j.newar.2006.11.030) (Cited on page 3).
- Visser, P. J. de, J. J. A. Baselmans, J. Bueno, N. Llombart, and T. M. Klapwijk (2014). "Fluctuations in the electron system of a superconductor exposed to a photon flux". In: *Nature Communications* 5. DOI: [10.1038/ncomms4130](https://doi.org/10.1038/ncomms4130) (Cited on page 181).
- Wellstood, F. C., C. Urbina, and John Clarke (1994). "Hot-electron effects in metals". In: *Phys. Rev. B* 49 (9), pp. 5942–5955. DOI: [10.1103/PhysRevB.49.5942](https://doi.org/10.1103/PhysRevB.49.5942) (Cited on pages 37, 38).
- Welser, J., J. L. Hoyt, and J. F. Gibbons (1994). "Electron mobility enhancement in strained-Si n-type metal-oxide-semiconductor field-effect transistors". In: *Electron Device Letters, IEEE* 15.3, pp. 100–102. DOI: [10.1109/55.285389](https://doi.org/10.1109/55.285389) (Cited on page 66).
- Yu, A.Y.C. and C.A. Mead (1970). "Characteristics of aluminum-silicon Schottky barrier diode". In: *Solid-State Electronics* 13.2, pp. 97–104. DOI: [10.1016/0038-1101\(70\)90039-0](https://doi.org/10.1016/0038-1101(70)90039-0) (Cited on page 21).
- Zhang, W., J. Q. Zhong, W. Miao, W. Y. Duan, Q. J. Yao, S. C. Shi, J. Martino, F. Pajot, D. Prele, F. Voisin, and M. Piat (2015). "Characterization of a Superconducting NbSi Transition Edge Sensor for TeSIA". In: *Applied Superconductivity, IEEE Transactions on* 25.3, pp. 1–4. DOI: [10.1109/TASC.2014.2364138](https://doi.org/10.1109/TASC.2014.2364138) (Cited on page 181).
- Ziman, J. M. (2001). *Electrons and Phonons: The Theory of Transport Phenomena in Solids*. New. Oxford (Cited on page 37).